Karlsruher Institut für Technologie

INE-004/11

Final Report of the BMWi Joint Research Project: Actinide Migration in Natural Clay Rock

Dezember 2011

Sub-Project: Influence of Clay Organic Substances on the retardation of Actinide Ions in the Clay Barrier

N. Banik, E. Hartmann, C.M. Marquardt, P. Panak, Th. Schäfer, A. Skerencak

Das diesem Bericht zugrunde liegende Vorhaben wurde mit Mitteln des Bundesministeriums für Wirtschaft und Technologie unter dem Förderkennzeichen 02E10206 gefördert. Die Verantwortung für den Inhalt dieser Veröffentlichung liegt bei den Autoren.

KIT – Universität des Landes Baden-Württemberg und
nationales Forschungszentrum in der Helmholtz-Gemeinschaft

Zusammenfassung

Die Arbeiten innerhalb dieses Projektverbundes beschäftigten sich mit dem Migrationsverhalten von Actiniden in der natürlichen Tonbarriere. Hierzu wurden natürliche Tongesteinsproben - Opalinuston aus dem Mont Terri (Schweiz) und Callovo-Oxfordian-Ton aus Bure (Frankreich) - im Hinblick auf die für die Migration von Actiniden relevanten Eigenschaften charakterisiert. Die Sorptionseigenschaften von Opalinuston und COx-Ton gegenüber Europium (Eu(III)), Curium (Cm(III)), Neptunium(V) und Plutonium(V) wurden in zahlreichen Experimenten untersucht. Hierbei konnte für Eu(III) und Cm(III) gezeigt werden, dass die Tonmineralien in den natürlichen Tongesteinen hauptsächlich verantwortlich sind für die Sorption der Metallkationen. Mittels eines einfachen Modells, dass eine Sorption nur an den Tonmineralien berücksichtigt und die Tonminerale Illit und Montmorillonit und den Calcit in einem für das jeweilige Tongestein speziellen Verhältnis beinhaltet, konnten die experimentellen Ergebnisse gut beschrieben werden. Hierzu wurde das Oberflächenkomplexierungsmodell von [Bradbury und Baeyens, 2002, 2005a,b] angewendet.

Eine Unterscheidung nicht-sorbierter Aquoionen von „outer-sphere“ sorbierten Kationen und eine Quantifizierung der „Outer-sphere“-Komplexbildung war mit Hilfe fluoreszenzspektroskopischer Methoden – Time-resolved laser fluorescence spectroscopy (TRLFS) - bislang nicht möglich, da diese auf Veränderungen im Ligandenfeld des fluoreszierenden Kations basieren. Beide Spezies behalten jedoch ihre vollständige erste Hydrathülle. Für die Identifikation der „Outer-sphere“-Komplexierung des Cm(III) wurde der quenchende Effekt des Eisens in der Kristallstruktur der Tone zur Hilfe genommen. Die in unterschiedlichen Tonsuspensionen (I = 0,01 mol/l, pH = 4) gemessenen Cm(III)-Fluoreszenzemissionslebensdauern korrelieren mit dem entsprechenden Eisengehalt des verwendeten Tones und sind signifikant kürzer (H_2O: ≥ 27 µs; D_2O: ≥ 85 µs) als die des Aquoions (65 - 68 µs bzw. 1250 µs). „Outer-sphere“ sorbiertes Cm^{3+} wurde in H_2O und D_2O mit Hilfe der TRLFS quantifiziert, indem das charakteristische Abklingverhalten der Fluoreszenzemission – hier vor allem der kurzlebige Anteil - analysiert wurden. Modellrechnungen zur Cm(III)-Outer-sphere-Komplexbildung an Tonen mit unterschiedlichen Kationenaustauschkapazitäten (KAK) ergeben eine sehr gute Übereinstimmung mit den experimentell ermittelten Werten. Dabei muss für die Sorption an Illit die Konkurrenz um Sorptionsplätze durch andere Kationen (insbesondere Al^{3+} und Ca^{2+}/Mg^{2+}) berücksichtigt werden. Diese werden durch teilweise Auflösung des Tons bei niedrigem pH aus der Kristallstruktur freigesetzt. Bei Montmorillonit hingegen muss die partielle Auflösung aufgrund ihrer ca. 4-fach höheren KAK nicht berücksichtigt werden.

Im Gegensatz zu den dreiwertigen Eu und Cm sind Np und Pu redoxsensitiv. Deshalb lag der Fokus der Untersuchungen in den Np- und Pu-Sorptionsexperimenten auf der Redoxspeziation beider Elementen. Hierzu wurden XANES, EXAFS, XPS für die Speziation auf der Tonmineraloberfläche sowie UV/Vis/NIR-Absorptions-Spektroskopie, Kapillarelektrophorese (CE) und Flüssig-flüssig-Extraktion für die Speziation in der wässrigen Phase eingesetzt. Die CE gekoppelt an eine ICP-MS ist für zukünftige Aufgaben, speziell für die Redoxspeziation bei sehr geringen Konzentrationen, eine vielversprechende Methoden. Deshalb wurden in einer Zusammenarbeit mit der Universität

Köln weitere Entwicklungsarbeiten unternommen um diese Methode zukünftig einsetzen zu können.
Bei dem redoxsensitiven Actinid Np zeigte sich, dass Np(V) bei geringen Konzentrationen von $3x10^{-7}$ M teilweise zu Np(IV) reduziert wird. Der relativ kleine Kd-Wert von 33±9 L/kg bestätigt, dass Np(V) noch vorhanden sein muss. Eine Reduktion konnte in den Versuchen zur spektroskopischen Bestimmung des Oxidationszustands auf der Tonoberfläche bei höherer Konzentration nicht festgestellt werden. Auf der Tongesteinsoberfläche befindet sich auch nach 4 Monaten Reaktionszeit Np(V). Ein signifikanter Unterschied zwischen OPA und COx konnte in den Versuchen nicht festgestellt werden. Die Reduktion zu Np(IV) läuft kinetisch sehr langsam ab. Im Gleichgewichtszustand sollte allerdings gemäß thermodynamischen Rechnungen basierend auf den gemessenen Eh-Werten fast ausschließlich vierwertiges Np zu finden sein. Eine Modellierung der Ergebnisse mit dem Oberflächenkomplexierungsmodell von [Bradbury und Bayens, 2002, 2005a,b] sind für COx in guter Übereinstimmung, für OPA gibt es noch deutliche Abweichungen, die im Moment nicht erklärt werden können.
Fünfwertiges Plutonium (Pu(V)) war im Tongesteinssystem nicht stabil und wurde zu Pu(IV) innerhalb der ersten Wochen reduziert. Auf der Oberfläche des Tongesteins wurde vierwertiges Pu nachgewiesen. Das Ergebnis steht im Einklang mit thermodynamischen Rechnungen basierend auf den gemessenen Eh-Werten. Erwartungsgemäß wird auch ein höherer Kd-Wert gemessen von bis zu 500 L/kg. Allerdings ist der Kd-Wert abhängig vom gewählten Feststoff-zu-Lösungsmittel-Verhältnis (K_d = 43 – 517 L/kg). Es stellt sich die Frage im Falle von Experimenten mit Pu-Konzentrationen nahe der Löslichkeit, ob ein Kd-Wert für vierwertiges Pu eine vernünftige Größe ist, da das vierwertige Pu löslichkeitskontrolliert in Lösung vorliegt. Das bedeutet, dass es sich hier nicht um eine Sorption, sondern vornehmlich um eine Oberflächenausfällung handelt, die in einem dem Sorptionsmodell berücksichtigt werden muss. Erste EXAFS-Auswertungen geben in der Tat Hinweise auf eine Oberflächenausfällung. Sorptionsexperimente bei niedrigeren Pu-Konzentrationen ergeben deutlich höhere K_d-Werte als für Np, die innerhalb eines Jahres um eine Größenordnung angestiegen sind (log K_d(12 d) = ~4.0 (L/kg); log K_d(1 y) = ~5.3 (L/kg)). Die bisherigen Resultate zeigen deutlich, dass die Pu-Sorption unbedingt an reinen Tonmineralien untersucht werden muss, um das komplexe Verhalten im natürlichen System erklären zu können.

Der Einfluss von natürlichem organischem Material (NOM) auf die Sorption von Actiniden an Ton wurde in weiteren Experimenten untersucht. Das natürliche organische Material (NOM) ist zwar in natürlichen Tongesteinen oft nur in geringen Mengen enthalten, kann jedoch aufgrund seiner sorptionsrelevanten Eigenschaften (große spezifische Oberfläche, hohe Kationenaustauschkapazität KAK, niedriger pKs Wert) und wegen der relativ hohen log ß-Werte für die Komplexbildung mit Actiniden deren Sorption erheblich beeinflussen. Unter bestimmten Bedingungen können lösliche huminartige Säuren in natürlichen Tongesteinen mobilisiert werden. Dies ist z. B. der Fall beim Auftreten von Hoch-pH-Lösungen, wie sie bei der Zementkorrosion in einem Endlager entstehen können. Hierzu wurden Experimente mit synthetischen Mischungen aus Montmorillonit und Huminsäure (HS) durchgeführt. In Gegenwart von HS (10 mg/l) nimmt die Eu(III)-Sorption an Montmorillonit im pH-Bereich 7 bis 9 ab, während sie in HS-freier Tonsuspension unverändert hoch

bleibt. Unter den in dieser Arbeit verwendeten experimentellen Bedingungen wurden aus dem natürlichen Tongestein jedoch keine signifikanten HS-Konzentrationen mobilisiert. Rechnungen zeigen, dass die verfügbaren Daten zur Ln(III)/An(III)-Komplexierung mit HS für das NICA-Donnan-Modell die Humatkomplexierung insbesondere im hohen pH-Bereich deutlich überschätzen.

Die Ergebnisse der vorliegenden Arbeit zeigen, dass bei einer Endlagerung in Ton mit einer Rückhaltung von dreiwertigen Actiniden vornehmlich an den Tonmineralen zu rechnen und die Sorption an anderen Mineralphasen vernachlässigbar ist. Außerdem hat die Komplexierung von An(III) mit Carbonat, das überwiegend aus dem Calcit der natürlichen Tongesteine stammt, einen großen Einfluss auf deren Sorption. Die Komplexbildung mit anderen anorganischen sowie organischen Liganden scheint hingegen bei der Endlagerung in Tongesteinen kaum eine Rolle zu spielen. Auch konnte dargestellt werden, dass die TRLFS als spektroskopische Methode zur Charakterisierung und Quantifizierung von Sorptionsprozessen, wie der Cm(III)/Ton-Outer-sphere-Komplexbildung hervorragend geeignet ist. Im Falle der redoxsensitiven Actiniden Np und Pu sind die erhaltenen Resultate für eine Beschreibung ihrer Rückhaltung im natürlichen Tongestein noch nicht zufriedenstellend. Die Ergebnisse verdeutlichen auch, dass eine aussagekräftige und allgemeingültige Beschreibung der Wechselwirkung zwischen Actiniden und der Lösung/Mineral-Grenzfläche nur auf der Grundlage eines molekularen Prozessverständnisses erfolgen kann.

Die Diffusion von Pu und HTO in OPA wurde mittels der “Through-diffusion”-Methode studiert. Die erhaltenen Diffusionskoeffizienten stimmen gut überein mit Werten anderer “Through-diffusion”-Experimenten. Allerdings zeigten sich auch experimentelle Schwierigkeiten: 20-40% des Pu wurde an den Oberflächen der Diffusionszelle sorbierte. Das nicht-sorbierte und in Lösung verbleibende Pu liegt in der fünfwertigen Oxidationsstufe vor und kann als mobiler Pu-Anteil bezeichnet werden. Das vierwertige Pu befindet sich auf oder im Tonkern, zeigt aber keinen bevorzugten Transportpfad, sondern findet sich an wenigen Stellen konzentriert wieder. Warum das Pu gerade an diesen Stellen konzentriert wird, konnte nicht geklärt werden; eine Korrelation zwischen Pu und z.B. Fe(II) im Ton konnte nicht gefunden werden. Allerdings zeigte sich, das eine verlässliche Post-Mortem-Analyse schwieriger ist als gedacht. Deswegen wurde auf weitere Post-Mortem-Analysen verzichtet, um zunächst eine verlässliche Technik zu entwickeln. Diese konnten in dieser Projektphase noch nicht verwirklicht werden. In einem sogenenannten “Out-of-diffusion”-Experiment konnte gezeigt werden, dass das Pu nicht in die wässrige Phase desorbiert wird und quasi irreversibel im Tongestein sorbiert bleibt. Damit kann Tongestein für Plutonium unter reduzierenden Bedingungen als sehr gute Rückhaltebarriere angesehen werden.

Um das Verhalten von Actiniden in natürlichen Tongesteinen besser verstehen zu können, vor allem auf der geologischen Zeitskala, wurde als natürliches Analogon eine Uran-Ablagerung in einer argillaceous-reichen Formation (Lodève Basin, Frankreich) betrachtet. Die Speziation von Uran hinsichtlich der Wechselwirkung mit der vorhandenen Tonorganik und den vorherrschenden Tonmineralien (Chlorit, Illit) war der Fokus dieser Untersuchung, um Rückschlüsse auf einen Rückhaltemechanismus zu erhalten. μ-XANES und μ-EXAFS-Resultate zeigen, dass Uran in der vierwertigen

Oxidationsstufe im Sediment vorliegt. U(IV) bildet dabei nano-kristalline UO_2-ähnliche Phasen. Aus den Elementkorrelationen mittels verschiedener Techniken (μ-XRF, STXM and μ-FTIR) kann man die folgenden vorläufige Hyphothese einer Uran-Immobilisierung entwickeln. Es existiert keine Korrelation zwischen Fe und U und damit kann man Fe-Mineralien als Reduktionsort von U(VI) zu U(IV) weitgehend ausschließen. Uran ist korreliert mit Kalium, das als ein Indikatorelement für Illit gilt. Weiterhin sind die Tonmineralien vom Illit-Typ mit organischen Komponenten des Tons assoziiert. Daraus könnte man schließen, dass U(VI) in der wässrigen Phase durch Tonorganik in schwerlösliches U(IV) reduziert wird und durch Oberflächenausfällung oder Sorption an der Tonoberfläche immobilisert wird. Allerdings muss diese Schlussfolgerung noch bewiesen werden, da noch einige offene Fragen gegen diese Hypothese noch nicht beantwortet sind.

Ein weiteres Arbeitspaket war die Grundlagenuntersuchungen zur Wechselwirkung von Actiniden mit Tonorganik und Huminstoffen. Eine mengenmäßig relevante organische Komponente im Ton ist das Kerogen, was durch Grundwasser mit hohem pH-Wert extrahiert werden kann. Zur Komplexierung von Cm(III) durch Kerogen, welches aus natürlichem Tongestein extrahiert wurde, wurden erste Experimente durchgeführt. Die Resultate zeigen eine eindeutige Wechselwirkung des Cm(III) mit dem Kerogen-Extrakt mittels TRLFS. Allerdings konnte nicht geklärt werden, ob diese Komplexierung von dem Kerogen selbst oder durch anorganische Verunreinigungen im Kerogenextrakt wie Pyrit hervorgerufen wird. Da es unmöglich war ein reines Kerogen zu extrahieren ohne die organische Struktur zu zerstören, wurde auf ein ausgedehntes experimentelles Programm zu diesem Zeitpunkt verzichtet. Die Bestimmung einer Komplexierungskonstante hätte keine Aussagekraft und würde nur zu falschen Schlüssen führen.

Eine zweite Studie beschäftigte sich mit der Fulvat-Komplexierung von vierwertigem Np. Bekanntlich hydrolisiert Np(IV) sehr leicht und bildet Hydroxokomplexe und Kolloide. Ausgedehnte XAFS und XPS-Analysen sollten klären, ob man mit gemischten ternären Komplexen rechnen muss oder ob es sich um einfache binäre Komplexe handelt. Die Untersuchungen zeigten aber, dass man mittels XAFS- und XPS-Ergebnissen nicht eindeutig zwischen den ternären und den binären Komplexen unterscheiden kann. Auch gibt es keine eindeutigen Korrelationen zwischen den Ergebnissen der spektroskopischen Methoden und dem pH-Werten, der Reaktionsdauer und der Art der Präparation von Np(IV)-Fulvat-Komplexen. In einigen Versuchen wurden zwei Np-O-Abstände gefunden (~2.22 Å und ~2.42 Å), in anderen Versuchen erhielt man nur einen Np-O-Abstand der zusätzlich noch zwischen 2.30 und 2.38 Å variierte. Allerdings kann man aus den Ergebnissen deutlich folgern, dass das Np eine Bindung zu einer Carboxylgruppe (monodentat oder bidentat) bildet und dass man keine Oligomere oder Kolloide findet. Geht man von einem reinen NpFA(IV)-Komplex aus, erhält man unter Berücksichtigung der sogenannten Beladungskapazität oder dem Deprotonierungsgrad der Fulvinsäure bei pH 1 und 1.5 eine Komplexierungskonstante für eine Ionenstärke von 0.1 M NaCl von $\log\beta = 7.0$ bzw. 7.6. Die pH-Abhängigkeit lässt sich aber durch das gegenwärtige Komplexierungs-Modell nicht kompensieren, reiht sich aber gut in die Literaturwerte für Huminstoff-Komplexe der vierwertigen Actiniden als Funktion des pH-Wertes ein.

Die Nachbildung eines natürlichen Tonsystems aus reinen Komponenten fokusierte in diesem Projekt auf die Polymerisation von niedermolekularen organischen Molekülen in der Gegenwart von reinem Quellton unter klar definierten Bedingungen. Dieser Ansatz der Kerogen-Synthese aus Komponenten bestehend aus C, O, H und N-Atomen hat den Vorteil, dass man anorganische Verunreinigungen vermeidet – diese konnten aus den natürlichen Extrakten niemals vollständig entfernt werden – und wichtige Erkenntnisse gewinnt über den Reaktionsweg, mögliche katalytische Effekte der Tonphasen sowie den Einfluss der Zusammensetzung austauschbarer Kationen. Mittels einer Maillard-Reaktion von D-Glukose, Glycin oder Katechol in Gegenwart von Na-/Ca-reichen Bentonit (Ibeco) wurde über eine Reaktionszeit von einem Monat bei 80 °C und verschiedenen Trocknungs- und Befeuchtungszyklen ein braunes polymeres Organik-Ton-System hergestellt. Die Komponenten wurden mit verschiedenen analytischen Methoden (Pyrolyse-Gaschromatographie-Massenspektrometrie (Py-GC/MS), μFT-IR, XRD, TEM, STXM, NEXAFS) untersucht. Die Pyrolyseschritte wurden aufgrund der Analysenergebnisse schrittweise verändert um das organische Endprodukt hinsichtlich des H/C- und O/C-Verhältnis dem Kerogen aus Bure bzw. Tournemire anzupassen. Die letzten erhaltenen Produkte stimmten im O/C-Verhältnis gut überein, waren aber im H/C-Verhältnis zu niedrig und ähnelten eher Holzkohle/Ruß-Komponenten. In einem neuen Ansatz muss die Pyrolyse deshalb weiter angepasst werden, sodass ein COx-ähnliches Kerogen synthetisiert werden kann. Damit hätte man dann die Möglichkeit die Wechselwirkung eines reinen Kerogens mit Actiniden zu untersuchen.

Eine Literaturstudie wurde durchgeführt, um einen Überblick über die Komplexierung von Actinides in verschiedenen Oxidationsstufen mit kleinen organischen Liganden zu erhalten, die im natürlichen Tonsystem gefunden wurden. Durch die Verfügbarkeit von zahlreichen Studien und eine breite Palette von Daten, wurden nur ausgewählte Ligand-Systeme mit systematischen Variationen ihrer momolekularen Struktur diskutiert, um einen grundlegenden Einblick in die Komplexierungs-Mechanismen zu bekommen. Der Vergleich der gegebenen Stabilitätskonstanten zeigte, dass die Komplexbildung durch eine Reihe von Faktoren beeinflusst wird, wie die Alkalität des Liganden und seiner molekularen Struktur. Im Falle der aliphatischen Carbonsäure-Liganden erhöhen funktionelle Gruppen in α-, β-oder γ-Position zur bindenden COOH-Gruppe die Stabilität der Komplexe deutlich. Dieser Effekt wird einem zusätzlich bindenden Beitrag der zusätzlichen funktionellen Gruppe zugeschrieben, was teilweise eine chelatbildende Wirkung hervorruft. Die verfügbaren thermodynamischen Daten sind jedoch mit verschiedenen Methoden bestimmt worden. Die vorliegende Übersicht zeigt eine deutliche Diskrepanz zwischen Daten aus indirekten Methoden (z.B. Potentiometrie und Extraktion mit Lösungsmitteln) und von spektroskopischer Techniken. Diese Diskrepanz geht weit über die experimentellen Unsicherheiten der zwei verschiedenen Arten von Methoden hinaus. Der Unterschied ist vielmehr auf allgemeine Problem zurückzuführen. Denn die indirekten Methoden könnten das chemische Gleichgewicht während der Messung stören und falsche Ergebnisse liefern. Darüber hinaus können indirekte Methoden nicht zwischen Innersphere- und Outersphere-Komplexe unterscheiden. Damit könnten Veränderungen der Aktivitätskoeffizienten als Änderungen der log β-Werte falsch interpretiert werden. Daher ist die Anwendung der spektroskopischen Methoden (z. B. TRLFS und UV/Vis) für die präzise Bestimmung von thermodyna-

mischen Daten von großer Bedeutung, um die verfügbaren Literatur-Daten zu validieren und um eine zuverlässige thermodynamische Datenbank für Actiniden unter natürlichen Bedingungen zu schaffen.

Für zukünftige Arbeiten auf dem Gebiet der Endlagersicherheit sind Untersuchungen bei erhöhten Temperaturen zwingend notwendig. Ein wichtiges Arbeitswerkzeug ist die pH-Messung, die normalerweise potentiometrisch mittels einer Glaselektrode gemessen wird. Diese ist aber nur bei Temperaturen bis 50 °C zuverlässig. Deswegen wurden erste Anstrengungen unternommen, den pH-Wert spektroskopisch mittels Indikatorfarbstoffe zu messen. Hierzu wurde eine Messzelle eingesetzt, die über Lichtleiter an ein Spektrometer gekoppelt wird und mit der bei Temperaturen bis 200 °C und Drücken bis 30 bar gearbeitet werden kann. Im ersten Schritt wurden die Säurekonstanten der Farbstoffe Bromocresol-Blau und –Grün als Funktion der Temperatur ermittelt für den Temperaturbereich 25 – 90 °C. Anschließend wurden beide Farbstoffe als pH-Indikatoren für die pH-Messung von Propionat- und Lactatlösungen verwendet, um die Temperaturabhängigkeit der Säurekonstanten zu ermitteln. Die erhaltenen Ergebnisse für die Propionsäure stimmen sehr gut mit Literaturwerten überein zwischen 25°C und 90°C. Für Lactat wurde die Temperaturabhängigkeit der Säurekonstante für den gleichen Temperaturenbereich neu bestimmt, da sie in der Literatur nicht verfügbar ist. Diese Arbeit zeigt, dass die Methode zur spektroskopischen Messung des pH-Wertes gut geeignet ist und in zukünftigen Experimenten bei höheren Temperaturen und Drücken eingesetzt werden kann.

Summary

The work within this project network dealt with the migration behaviour of actinides in the natural clay rock barriere. To this end, samples of natural clay rock (Opalinus clay and COx) were characterised with respect to properties that are relevant for the migration of actinides. The sorption properties of Opalinus clay and COx with respect to europium (Eu (III)), curium (Cm (III)), neptunium (Np(V)) and plutonium (Pu(V)) were studied in numerous experiments. Here, we could show for Eu (III), Cm (III) that the clay minerals in natural clay rocks are mainly responsible for the sorption of metal cations. The experimental sorption data could well be described by using a simple model that considers only the sorption on the clay minerals illite, montmorillonit representing all other clay minerals and calcite as the carbonate buffering compound. For this purpose the surface complexation model of [Bradbury and Bayens, 2002, 2005a, b] has been applied.
Using time-resolved laser fluorescence spectroscopy (TRLFS), it was possible to identify outer-sphere sorbed trivalent lanthanides and actinides onto different montmorillonites and illite. Furthermore, the quantification of Cm(III)/clay outer-sphere sorption in D_2O at different ionic strengths was shown. The results were confirmed by ion exchange model calculations.

In contrast to the trivalent Eu and Cm with their fixed oxidation state, the Np and Pu are redox-sensitive metal cations. Therefore, in sorption experiments the redox speciation of Np and Pu plays a important role. For this purpose, XANES, EXAFS, XPS were used for the speciation of actinides on the clay mineral surface and UV/Vis/NIR absorption spectroscopy, capillary electrophoresis (CE) and liquid-liquid extraction were performed to determine the redox speciation in the aqueous phase. If CE is coupled to an ICP-MS, this method is a promising method for future tasks, especially for the redox speciation at very low concentrations. Therefore further development work has been undertaken in collaboration with the University of Cologne to be able to use these methods in sorption experiments and other relevant solutions up to actinide concentrations of 10^{-9} mol/L and lower.

For the redox-sensitive actinide Np it was found that Np(V) is partially reduced in the OPA/pore water system to Np(IV) at a low metal concentration of 10^{-7} M. The relatively small K_d value of 33 ± 9 L/kg confrims that Np(V) must be still in the system. XAFS characterisation that had to be performed at higher metal concentrations of 10^{-4} M showed that no reduction occurs, even after 4 months reaction time. A significant difference between OPA and COx could not be found in case of Np. The reduction of Np (IV) is kinetically slow. However, the Np(IV) should be the stable oxidation state in an equilibrium stage according to thermodynamic equilibrium calculations based on the measured Eh values in solution.
Pentavalent plutonium (Pu(V)) was not stable from the beginning and was reduced to Pu (IV) within the first few weeks. On the surface of the clay tetravalent Pu was detected by XPS and XANES even at high metal concentration of 10^{-4}M. The result is consistent with thermodynamic

calculations based on the measured Eh values. As expected, a higher Kd value is measured up to 500 L/kg. However, the K_d value varies with the solid-to-solvent ratio from Kd = 43 to 517 L/kg. For experiments, where the Pu concentrations were near the solubility limit, the question arises whether a K_d value is a reasonable parameter to describe the sorption of tetravalent Pu. In these solutions the tetravalent dissolved Pu concentration is solubility controlled, meaning that not only sorption takes place, but mainly a surface precipitation has to be considered. Sorption experiments at lower Pu concentrations of 10^{-9} M yields in significantly higher K_d values, which increase within a year by an order of magnitude (log K_d (12 days) = ~ 4.0 (L/kg), log K_d (1 year) = ~ 5.3 (L/kg)). An explanation for this behaviour cannot be given, but clearly shows that the Pu sorption has to be investigated on pure clay minerals to be able to explain, which component is responsible for each single reaction – sorption and reduction – and to elucidate the complex behaviour in the natural system.

One further important mobilisation aspect was studied in this project: the influence of natural organic matter (NOM) on sorption of actinides on clay. Although, natural argillaceous rocks normally contain only small amounts of NOM, however, due to its sorption-related properties (high specific surface, high cation exchange capacity CEC, low pK value) and the relatively high complexation constants log β for the complex formation with actinides, NOM can be have a significant impact on the sorption. For this purpose, experiments were performed with synthetic mixtures of montmorillonite and humic acid (HA). In the presence of HA (10 mg / l) the Eu (III) sorption on montmorillonite decreased in the pH range 7 to 9, while in HA-free clay suspension the sorption remains unchanged strong. Under the experimental conditions used in this work HS was not released from the natural clay in significant concentrations. Model calculations of the HA impact with the NICA-Donnan model show that the experimental data for Ln(III)/An(III) could qualitatively reproduced but the model significantly overestimate the complexation with HA, particularly in the high pH range.

The diffusion of Pu and HTO in OPA was studied by means of a "through-diffusion" method. The obtained diffusion coefficients agree well with values from other "through-diffusion" experiments. However, experimental difficulties occured: 20-40% of Pu was sorbed on the surfaces of the diffusion cell. The non-sorbed and in the solution remaining Pu is present in the pentavalent oxidation state and can be regarded as mobile Pu content. The tetravalent Pu at or in the clay core shows no preferably transport path, and is concentrated in a few spots. Why the Pu is concentrated at these points could not be clarified; no correlation could be found between Pu and Fe(II) on the clay. However, it appears that a reliable post-mortem analysis is harder than expected. Therefore, we abdicated further post-mortem analysis, until we will developed a reliable technique. These couldn't unfortunately be implemented in this phase of the project. Out-of-diffusion experiments showed that the Pu is not desorbed into the aqueous phase and remains virtually irreversible sorbed in the clay. Thus, clay rock can be considered as very good retention barrier for plutonium under reducing conditions.

To better understand the behavior of actinides in natural argillaceous rocks, especially on the geological time scale, a uranium deposit in an Argillaceous -rich formation (Lodève Basin, France) was regarded as a natural analogue. The speciation of uranium with respect to the interaction with the existing and prevailing clay organic components as well as the clay minerals (chlorite, illite) was the focus of this investigation to draw conclusions on a retention mechanism. μ-XANES and μ-EXAFS results show that the uranium in the sediment exist in the tetravalent oxidation state. This U(IV) forms nano-crystalline UO2-like phases. From the element correlations using various techniques (μ-XRF, STXM and μ-FTIR), one can develop the following but preliminary hypothesis of an uranium immobilization. There is no correlation between Fe and U, and thus Fe-minerals can be excluded as sites the U (VI) can be reduced to U (IV). But uranium is correlated with potassium, an indicator element for Illite, from clay minerals. Simultaneously, the illite-type minerals are associated with organic components of the clay. This may suggest that U (VI) in the aqueous phase is reduced to sparingly insoluble U (IV) by clay organic compounds and subsequently immobilized by sorption or surface precipitation. However, this conclusion must be proven, because open issues against this hypothesis are still not answered (see Section 4.2.1).

A further work package was the basic research of the interaction of actinides with humic substances and clay organic components (COC). One polymeric organic component in the clay is kerogen, which can be extracted from the clay by groundwater with high pH produced in presence of concrete surfaces. Complexation experiments of kerogen extracted from natural clay and Cm (III) were performed. The results from TRLFS clearly show a complexation of Cm (III) by the kerogen extract. However, it could not be clarified whether this complexation is caused by the kerogen itself or by inorganic contaminants in the extract such as pyrite. Since it was impossible to extract a pure kerogen without altering the organic structure, because the calculation of a complexation constant would have no meaning and would only lead to false conclusions, we decided to abdicate on an extensive experimental program at this time.

A second study of actinide interactions with organic components focused on the complexation of tetravalent Np with fulvic acid (FA). As is generally known the tetravalent Np(IV) hydrolyses already at low pH values forming hydroxo complexes and colloids. Extended XAFS and XPS analysis should clarify whether they have to deal with mixed ternary complexes, or whether it is a simple binary complex. The investigations of the Np(IV) fulvate complexation between pH 1 and 3 showed, however, that by means of XAFS and XPS no clear distinction can be made between the ternary and the binary complex. There was no clear correlation between the results of the spectroscopic methods and the pH values, the reaction time, and the nature of the preparation of the Np(IV) fulvate. In some experiments, two Np-O distances were found (~ 2:22 Å and ~ 2:42 Å), in other experiments only one Np-O distance varying between 2:30 and 2:38 Å. In any case we can clearly conclude from the results that Np is bound to a carboxyl group (monodentate or bidentate) and that oligomers or colloids forming nanoparticles can be excluded. To estimate a complexation constant at pH 1 and 1.5 – conditions with minimised hydrolysis - we started from a pure NpFA(IV) complex, taking into account the so-called loading capacity or the deprotonation of the fulvic acid. The

conditional complexation constant for an ionic strength of 0.1 M NaCl was estimated to logβ = 7.0 or 7.6 at pH 1 and 1.5, respectively. The pH dependence cannot be explained by the present model, but the conditional complexation constant qualitatively matches with literature values of humic complexes of tetravalent actinides as a function of pH.

The replica of a natural clay system with pure components focused in this project on the polymerisation of low molecular weight organic molecules in the presence of pure swelling clay under clearly defined conditions. This approach to synthesise a pure kerogen consisting of only C, O, H and N atoms has the advantage that it avoids inorganic impurities - these could be from natural extracts never completely removed - and gaining important knowledge about the pathway, possible catalytic effects of the tonal phase and the influence of the composition of exchangeable cations. By means of a Maillard reaction of D-glucose, glycine or catechol in the presence of Na-/Ca-rich bentonite (IBECO) a brown polymeric organic-clay system has been produced after a one month reaction at 80 ° C and several drying and humidification cycles. The components were investigated using various analytical methods (pyrolysis-gas chromatography-mass spectrometry (Py-GC/MS), µFT-IR, XRD, TEM, STXM, NEXAFS). The pyrolysis was changed gradually due to the outcome of the analysis to adapt the final kerogen product in terms of organic H/C- and O/C ratio of kerogen from the Bure or Tournemire site. Our final kerogen product agreed well in the O/C ratio, but was too low regarding the H/C ratio and hence, resembles more a charcoal or soot product. In a new approach the pyrolysis must be further adapted to yield a kerogen that is very similar to a natural Kerogen from clay rock.

A literature study has been performed in order to get an overview about the complexation of actinides in different oxidation states with small organic ligands. Due to the availability of numerous studies and a broad set of data, only chosen ligand systems with systematic variations of their molecular structure are discussed to give a basic insight into the complexation mechanism. The comparison of the given stability constants showed, that the complex formation is influenced by a number of factors, like the alkalinity of the ligand and its molecular structure. In the case of aliphatic carboxylic acid ligands, functional groups in α-,β- or γ-position to the coordinating COOH group increase the stability constants of the complexes distinctively. This effect is attributed to an additional contribution of the additional functional group, resulting in a partial chelating effect. However, the available thermodynamic data is determined by various methods. The present overview shows a distinct discrepancy between literature data from indirect methods (e.g. potentiometry and solvent extraction) and spectroscopic techniques, which is far beyond experimental uncertainties of these two different types of methods. The difference is rather attributed to the general problem, that indirect methods disturb the chemical equilibrium during the measurement, which might provide biased results. Furthermore, indirect methods are unable to distinguish between inner- and outer-sphere complexes and thus changes in activity coefficients may be misinterpreted for changes in log β values. Hence, application of spectroscopic methods (e.g. TRLFS and UV/Vis) for the precise determination of thermodynamic data is of major importance to validate the available literature data and to establish a reliable thermodynamic database for actinides under natural conditions.

The last work package dealt with the aspect of experiments at elevated temperatures. For future work in the field of repository safety, studies at elevated temperatures are necessary. An important working tool is the measurement of pH that is normally measured potentiometrically using a glass electrode, but which is reliable only at temperatures up to 50 ° C. Therefore, initial efforts have been made to measure the pH value spectroscopically using dyes. For this purpose, a measuring cell was developed, which is coupled via fiber optics to a spectrometer and which can work at temperatures up to 200 ° C and pressures up to 30 bar. In the first step, the acid constants (pK_s) of the dyes Bromocresol Green and Blue were determined as a function of temperature in the temperature range 25-90 ° C. Subsequently, both dyes were used as pH indicator for determining the acidity constants of propionate and lactate as a function of temperature. The results obtained for the propionic acid agree very well with literature values between 25° C and 90° C and confirms the reliability of the method. The new acidity constants of Lactate, which doesn't exist above 25° C in the literature, were determined in the same temperature range. This work showed that the method of spectroscopic measurement of pH is suitable and can be used in future experiments at elevated temperatures and pressures.

Contents

1 Introduction

For the long-term safety assessment of a nuclear repository, the knowledge is crucial of the interaction and transport of long-lived radionuclides in the technical, geotechnical and geological barriers. The actinides play a very important role. Their migration in the potential host formation – foreseen for a repository - and their transportation behaviour after releasing into the aquifer have to be known to compare the suitability of possible potential host rocks (salt, clay, granite) to provide the required proof of safety. This is necessary in order to ultimately be able to elect a host formation for a repository. The aim of this joint project is to elucidate the geochemical behavior of actinides, especially under reducing conditions in the natural clay under the influence of organics (humic substances, organic clay components) and thereby collect the necessary data to apply them for the safety case of a host formation.

The influence of the chemical environment on the mobilization or immobilization of the actinides, including the kinetics of these processes is at the foregound of considerations. Against the background for the disposal of actinides in clay, in contrast to other host formations such as salt, diffusion processes are important. The parameter dependence of the different processes has to be elucidated. The transport behaviour of actinides depends again on the composition and the corresponding physical properties of the clay rocks, but also on various parameters of the aquatic-specific system, such as pH, Eh, ionic strength, CO_2 content, concentration and charge of the actinides, competing ions, the presence of complexing ligand and the concentration of colloids. Here, just the organic ingredients can play an important role, which has to be examined based on earlier studies of kaolinite as a model clay mineral. In the aquifer system, the propagation behavior of actinides is determined strongly by humic substances due their complexing, redox and colloidal properties, Therefore, they can have a significant influence on the retention or transport of actinides in the repository. Clay organic compounds like Kerogen might play also a strong role regarding migration processes.

In this work natural clay rock samples were characterised in terms of the migration of actinides relevant properties. To obtain a sufficient understanding of the process of actinide-clay interactions like sorption and redox reactions, the spatial distribution of the clay matrix and the bonding state of dissolved and sorbed actinides were investigated. This has been started in basic investigations of the sorption process on the clay rock, as well as on single pure clay minerals. Then diffusion experiments have been performed to get information of the transport properties of actinides as well as for the diffusion mechanism. In addition the complexation of actinides with humic substances and clay organic components like Kerogen has been probed in required basic studies. To understand the origin and properties of humic substances and clay organic compounds the natural clay rock system was attempted to reconstruct the natural system with pure clay and organic components. Such "synthetic systems" also allow specific studies of the influence of natural clay organic compounds on the actinide migration in a host rock.

2 Characterisation of relevant clay rock samples

2.1 Rock sample catalogue

The Opalinus clay samples from the Mont Terri site have been delivered from the Bundesanstalt für Geowissenschaften und Rohstoffe (BGR). The samples – drilling cores - were delivered in September and November 2006, and each drilling core was wrapped in air-tight aluminium foil bags filled with nitrogen. The samples from the Benken site came from borehole BEZ E24/2. The samples from the Bure site were taken from the borehole EST104 No. 490 at an approximate depth of 490 m from the topographic surface. All clay samples were stored in a metal container filled with argon gas to avoid further oxidation of redox sensitive clay components. On time to time from this clay material powder samples for sorption experiments and smaller cores for diffusion experiments were prepared.

Table 2-1: Samples from the Mont Terri site delivered by BGR and used fort he project.

No.	Borehole	Charge	Depth (m)	Comments
1	BHE 24	01	3.30 – 3.56	
2	BHE 24	02	3.56 – 3.89	
3	BHE 24	13	6.81 – 7.05	
4	BHE 25	1	2.98 – 3.16	Foil defect
5	BHE 25	10	6.27 – 6.45	
6	BHE 25	11	6.45 – 6.61	
7	BHE 25	12	6.61 – 6.81	Foil defect
8	BLT 11	01		2 small discs
9	BLT 12	01	1.58 – 2.00	Core broken
10	BLT 12	02		2 small discs
11	BLT 12	02	2.03 – 2.28	Vented
12	BLT 13	01	1.69 – 2.09	
13	BLT 13	02	2.09 – 2.49	
14	BLT 13	03	3.45 – 3.76	
15	BLT 14	01	0 – 0.25	
16	BLT 14	01	0.25 – 0.50	
17	BLT 14		0.50 – 0.90	
18	BLT 14		0.90 – 1.57	
19	BLT 14		1.57 – 2.12	
20	BLT 14		2.12 – 2.52	
21	BLT 14		2.52 – 2.97	

To minimise heterogeneity of the samples and to make the experiments of different project partners comparable, the powder and core samples prepared at KIT-INE were delivered to

each interested project partner. The name and the depth of the delivered samples from BGR are scheduled in Table 2-1. Furthermore, OPA clay from the municipality Benken, Switzerland, and Callovo-Oxfordian Clay from the Bure site, France, were used for the experiments: No. 22 and 23 in Table 2-1.

Table 2-2: OPA, COx, natural and synthetic clay minerals, and other materials used for sorption studies

Clay	Name	Location
OPA	BEZ E24 / 02 BEZ E24 / 03	Benken, Züricher Weinland (Switzerland), 113 m depth
COx	EST 104 / 490 EST 25691 PAC1001Dif1749	Bure, Meuse/Haute-Marne (France), 490 m depth
Natural Smectite, Montmorillnit Wyoming-Bentonite	SWy-1/SWy-2	Crook County, Wyoming (USA)
Natural Smectite, Montmorillonit Bentonite from Milos		Island Milos (Greece)
Texas-Montmorillonit		Gonzales County, Texas (USA)
Synthetic smectite	Beidellite	Prepared by KIT-INE
Synthetic smectite	Ca/Na-montmorillonite	Université de Haute Alsace, Mulhouse (France)
Illit du Puy	IdP-2	Le Puy en Valey, Massif Central (France)
γ-alumina	Aluminiumoxid C	Degussa
Calcite		Creel (Mexico)

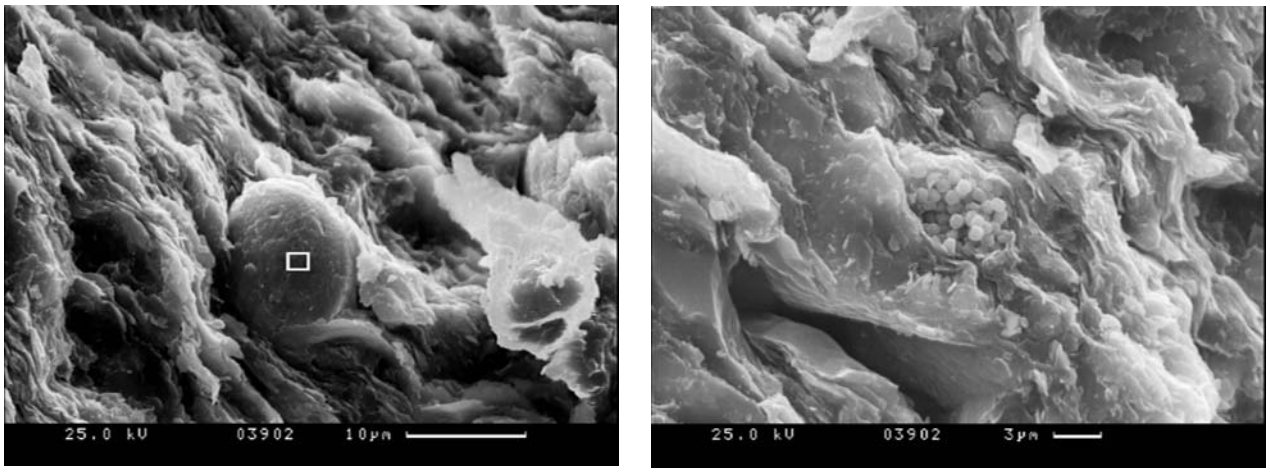

Figure 2-1: REM images of OPA clay. In the image on the left a round calcite crystal is surrounded by flaky clay minerals. In the right image a pyrite conglomerate can by seen reformed by diagenesis.

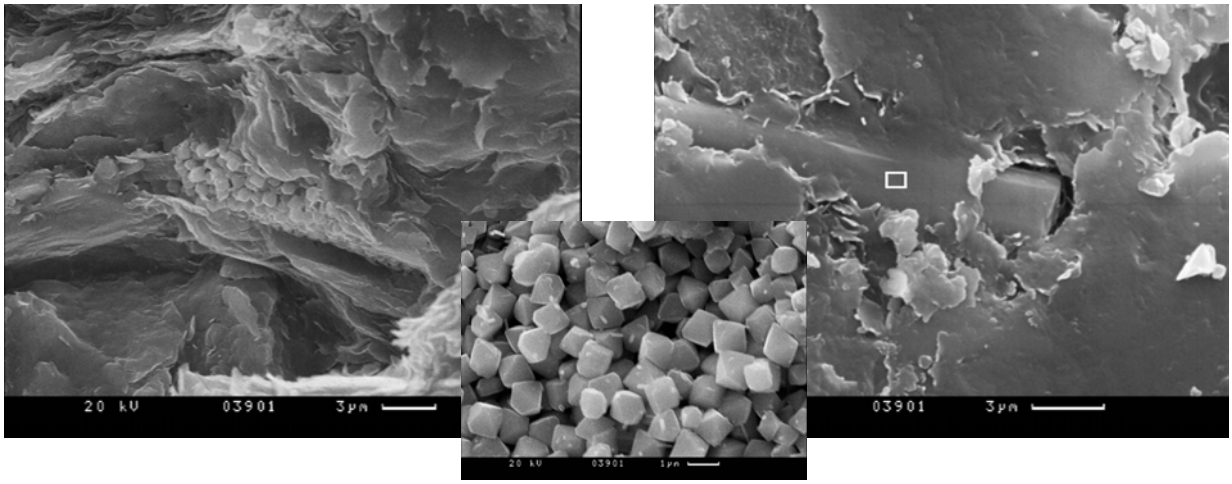

Figure 2-2: REM images of COx clay. In the left image a pyrite conglomerate surrounded by flaky clay minerals (small image: magnification of the cubical pyrite crystals), in the right image rutile crystals with their characteristic columnar habitus.

2.2 Mineral composition and physicochemical characteristics of clay rock

The OPA clay and the COx clay have been thoroughly characterised by Nagra and ANDRA using many samples. The average composition of both clay rocks are summarised in Table Table 2-3.

We assume that small variations of the mineralogy and physico-chemical properties from the average composition - Table 2-1 - have no significant influence on the conclusions from the experiments. Nevertheless, some own characterisations have been performed. Furthermore, the minerals zircon ($ZrSiO_4$), Hematite (Fe_2O_3), Sphalerite (ZnS), Rutile (TiO_2) and Apatite ($Ca_5[(PO_4)_3(OH, F, Cl)]$) were detected accessory minerals by raster electron microscopy (REM) for OPA. For COx anhydrite/gypsum, pyrite, zircon, rutile and coelestine have been found by REM as accessory minerals. The main mineral components from Table 2-1 were confirmed by x-ray diffractometry [Hartmann,2010]. The clay mineral fraction of OPA is composed mainly by kaolinite, Illite and Illite/Smectite mixed layers. In contrast to OPA, the COx contains only very small amounts of kaolinite and chlorite and the main clay minerals are Illit/Smectite mixed layers, Illite and Smectite. The amount of calcite with 17.3 wt.% is twice the amount in the OPA (8-10 wt.%).

Fe(II) has been detected by XPS with contents of 1.42 to 1.49 ± 0.3 atom-% for OPA and1.23 wt.% for COx. Unfortunately, the location of the Fe(II) could not be achieved, maybe due to very small and finely dispersed particles. According to [Nagra, 2002], the Fe(II) of OPA is found in the minerals siderite ($FeCO_3$), ankerite (café$(CO_3)_2$) and pyrite (FeS).

Table 2-3: Average mineralogical composition and physicochemical characteristics of OPA clay fromBenken/Schweiz [Nagra,2002] and Callovo-Oxfordian clay COx from Bure/France (clay particle size fraction (< 2 µm) and organic carbon: [Claret et al., 2002].

Minerals	**OPA**[b] (wt.-%)	**COx**[c] (wt.-%)	**SWy-2**[d] (wt.%)
Calcite	16,0 ± 10,0	20,0 ± 4,0	< 0.5
Dolomite/Ankerite	1,0 ± 0,4	4,0 ± 2,0	<0.5
Siderite/Fe-Minerals	4,0 ± 2,4	1,9 ± 0,8	3.85-4.3[e]
Quartz	20,0 ± 5,0	22,0 – 35,0	1
Albite	1,0 ± 0,3	1,0 ± 0,1	<1
Orthoclase	2,0 ± 1,0	2,0 ± 0,1	<1
Pyrite	1,1 ± 1,0	0,7 ± 0,2	
Illite	18,0 ± 6,0	8,0 ± 1,0	1
Smectite	<	6,0 ± 1,0	97-100
Illite/Smectite mixed layers	14,0 ± 4,0	28,0 ± 2,0	
Kaolinite	17,0 ± 6,0	≤ 1,0	<1
Chlorite	5,0 ± 2,0	0,4 ± 0,1	<1
Organic carbon	0,6 ± 0,3	1,31 ± 0,3	≤ 0.15
Total CEC meq kg^{-1}	106 ± 7	140[f]; 171-176[j], 250-400[g]	760[h] – 910[i]
Total surfaces EGME m^{2}g^{-1}	94 ± 13	n.s.	n.s.
BET external surfaces m^{2}g^{-1}	28 ± 9; 32[j], 39[j]	32[j]; 35 ±1.5, 36.7[j]	32-43[j]
pH porewater	7.25	7.3[k]	

<: below the detection limit; a: Opalinus Clay and Murchisonae layers; b: [Nagra, 2002]; c: clay fraction and organic carbon: [Claret et al. 2002]; residual mineral content: [Gaucher et al., 2004] and [Griffaut, 1999] (cited in [Motellier et al., 2003]); d: [Bradbury&Baeyens, 1995], [Rabung et al., 2005], stated for conditioned SWy-1; e: stated for total Fe as Fe2O3; f: [Bouchet et al., 1997], stated for sample at depth about 490m; g: [Claret et al., 2004]; h: [Rabung et al., 2005], stated for conditioned SWy-1; i: [Michot et al., 2004]; j: own measurements; k: [Jacquot, 2002] (cited in [Montes et al., 2005]); n.s. not specified.

The pH of clay pore water amounts to 7.25 for OPA [Nagra, 2002] and 7.30 for COx [Hartmann et al., 2008]. The Eh value was estimated to -185 to -156 mV [Jacquot, 2002; Luckscheiter et al., 2004].

Further details of the characterization of the natural clay material included cation exchange capacity (CEC) determination by the Cobalt hexamine (Cohex)- method and XRF analysis,

which is summarized in the following tables. The specific surface area determined by N_2-BET is 36.7 m^2/g for the Callovo- Oxfordian argillite (sample PAC1001Dif1749) and 39.0 m^2/g for Opalinus Clay (sample OPA/BHE-24-2). Concerning the CEC of the OPA sample summing up the exchangeable cations would lead to a considerable higher CEC of 17.1-17.6 meq/100g which can originate from an excess of Na due to the high concentration of NaCl in Mont-Terri OPA. Therefore the Cohex quantification determined by UV/VIS is documented here.

Table 2-4: X-Ray fluorescence analysis (XRF) of the Callovo- Oxfordian sample (PAC1001Dif1749) and the Opalinus Clay sample (OPA/BHE-24-2).

Element (wt. %)	PAC1001Dif1749	OPA/BHE-24-2
SiO_2	42.78	48.38
CaO	24.58	10.71
Al_2O_3	14.87	22.05
Fe_2O_3	7.185	8.499
K_2O	3.804	3.832
SO_3	2.93	1.95
MgO	2.09	2.25
TiO_2	1.07	1.22
P_2O_5	0.21	0.352
Na_2O	0.212	0.465
SrO	0.0683	0.0475
MnO	0.039	0.0722
ZrO_2	0.0301	0.0252
BaO	0.0268	0.0324
V_2O_5	0.023	0.021
Cr_2O_3	0.022	0.017
Rb_2O	0.0189	0.0186
ZnO	0.015	0.02
NiO	0.011	0.015
Y_2O_3	0.0046	0.0047
CoO	n.d.	0.011
Ga_2O_3	n.d.	0.004

n.d.: not detected

Table 2-5: Cation exchange capacity (CEC) as determined by the Cohex method for the Callovo- Oxfordian (COx) sample (PAC1001Dif1749) and the Opalinus Clay (OPA) sample (OPA/BHE-24-2).

	Na [meq/100g]	K [meq/100g]	Ca [meq/100g]	Sr [meq/100g]	Mg [meq/100g]	CEC (meq/100g)
COx	2.20-2.33	1.05-1.06	5.64-5.77	0.22-0.23	3.39- 3.48	11.95-12.09
OPA	6.49-6.65	1.23-1.24	5.72-5.86	0.11	3.58-3.77	12.91-12.96

2.3 Natural Trace element distribution

Other activities aimed on the role of mineral and organic reservoirs in trace metals solubility and mobility controls in clay rocks, namely Callovo-Oxfordian claystone. Two cases are explored in detail in collaborative work with BRGM to look on the natural distribution of nickel and iodine, which can determine the mobility of the radioisotopes in the formation.

In the case of nickel in deep details together with some insights from cobalt, zinc and lead behaviors were gathered and a manuscript has been submitted (Grangeon et al., 2011, in review). Most Ni-enriched phases, identified from a combination of physical and chemical methods are pyrite (~400 µg/g Ni), sphalerite (~300 µg/g Ni), chlorite (~300 µg/g), organic matter (~300 µg/g), muscovite (100- 200 µg/g) and carbonate (mainly calcite and minor dolomite, ~10 µg/g). Despite their high abundance in the formation (up to ~80% in the top of the formation), carbonates are a quantitatively minor nickel reservoir whereas most of Ni is beard by pyrite and chlorite, that are minor mineral phases. From in-situ survey of pore water composition within the formation, pyrite is shown to be a major source of solute Ni in oxidised conditions. From both laboratory kinetics experiments and in-situ pore water composition measurements, carbonate minerals appear as the main buffers of solute nickel concentration with Ni solubility range at ~0.2-1 µmol/L. Cobalt and nickel have similar distribution, whereas lead and zinc have partly different reservoirs (e.g. sphalerite, ZnS).

In the case of iodine a multidisciplinary approach was used to define iodine immobilization mechanisms by biocarbonates in the Callovo-Oxfordian formation (Lerouge et al., 2010). For this purpose, different techniques of observation (optical microscope, scanning electron microscope (SEM), cathodoluminescence (CL)) and of analyses (infrared spectrometry (IR), electron microprobe (EPMA), spatially resolved synchrotron-based X-ray fluorescence (µ-XRF) and X-ray diffraction (µ-XRD)) were performed on two entire and centimeter-sized carbonate shells. Combined (SEM, CL, IR and µ-XRD) data indicates that the biostructure of the Rhynchonella shell is relatively well-preserved but bio-aragonite slowly transforms into calcite, whereas the bivalve shell is entirely re-crystallized into diagenetic calcite and celestite. EPMA and µ-XRF data show bioaccumulation of iodine in carbonate shells, confirming previous work on present-day mollusks. EPMA analyses give evidence of iodine content up to 1200 ppm in the preserved Rhynchonella shell and up to 2000 ppm in recrystallized bivalve shell. µ-XRF elemental mapping shows that iodine is more homogeneously distributed in biocalcite of the Rhynchonella shell than in re-crystallized calcite of the bivalve shell, suggesting

a loss of iodine during re-crystallization processes, but not a total exclusion of iodine from the carbonate structure. Combined EPMA data and µ-XRF elemental maps do not give evidence of any correlation between the iodine location and the distribution of other elements.
The implication of these results for radio-iodine is that under undisturbed far-field conditions mt natural iodine would not be accessible for isotopic exchange with radio-iodine, reducing the effective K_d to negligible values.

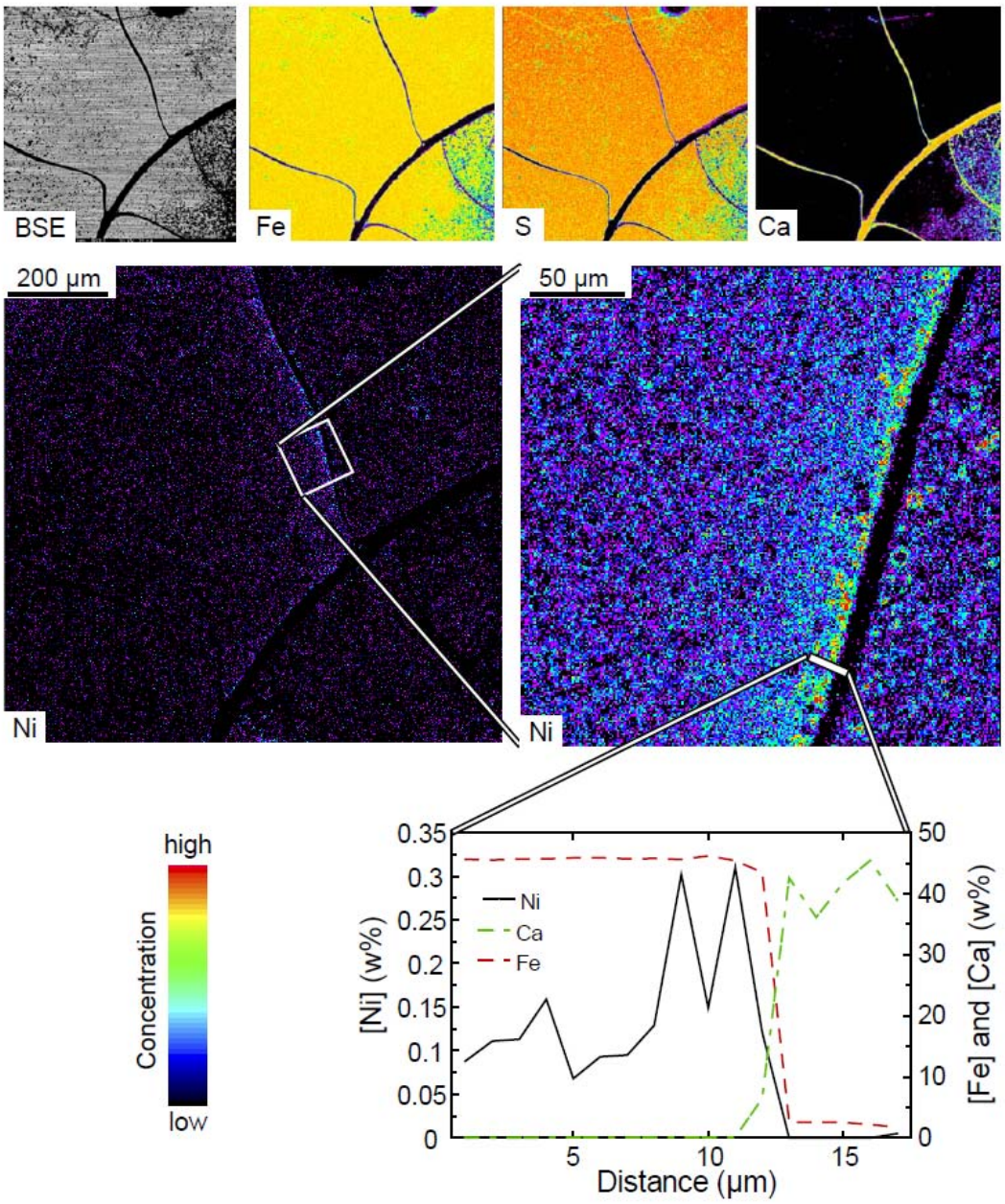

Figure 2-3: Top line, from left to right: back-scattered electron map of part of an ammonite (septae appear as dark lines and camerae as greyish zones), and corresponding Fe, S, and Ca chemical maps (microprobe experiments). Middle left: Ni chemical map. Same location, but increased in size. Enlarged view of the white square at middle right (different experiment). Bottom: Ni (solid line), Ca (dot-dashed line) and Fe (dashed line) quantitative analyses of the line materialized in white on the middle right figure. Figure taken from [Grangeon et al., 2011, in review].

2.4 Natural organic matter/ kerogen inventory

In the beginning of the project, work focused on the detailed characterization of the natural organic matter (NOM) present in the Callovo-Oxfordian clay formation and the Opalinus clay. Beside looking in detail on the nano- to microscale distribution of NOM (Schäfer and Denecke, 2010; Schäfer et al., 2009a; Schäfer et al., 2009b) another activity focused on the extraction of different hydrophilic and hydrophobic compounds from the natural claystone samples for later planned actinide complexation studies (Grasset et al., 2010).

Key findings of these activities, which are already published in peer reviewed journals were: Synchrotron based (C-, K-, Ca-, O- and Fe-edge XANES) scanning transmission X-ray microscopy (STXM) and FT-IR microspectroscopy was used to identify under high spatial resolution the distribution of clay-organic matter with different functionality using principal component and cluster analysis. The results show that in this old (Jurassic) geological formation, small parts of the organic inventory (1–5%) keeps the structure/functionality and can be mobilized as hydrophilic humic substance type material (HA and FA). HA and FA were extracted following the standard International Humic Substance Society (IHSS) isolation procedure. Target spectra analysis shows best correlation for isolated humic acids with organics found in smectite-rich regions, whereas the extractable FA has better spectral similarities with the illite mixed layer minerals (MLM) regions.

The major fraction (>95%) of the organic matter (OM) is associated with minerals. In order to understand the importance of OM on the chemistry of this formation, we have developed a protocol allowing extraction/fractionation of organic compounds in the rocks. The protocol is based on classical methods currently used for the isolation of humic substances from soils and for the separation of kerogen in ancient sediments using sequential extraction with solvents and water at different pH values. This allows us to the remove a large part of the minerals and to suspend almost all (>90%) of the OM (associated with residual recalcitrant minerals) in water. The OM can then be analyzed via spectroscopic methods, such as mass spectrometry (MS), Fourier transform infra-red spectroscopy (FTIR), or C (1s) near-edge X-ray absorption fine structure (NEXAFS) spectroscopy. The molecular composition of the solvent-soluble, directly-extractable part shows the OM to be thermally immature. The solvent-soluble fractions obtained after acid and alkaline treatments are mostly polar in nature and have a high degree of aliphaticity. C(1s) NEXAFS analysis of water soluble organic fractions indicates a progressive increase in aliphaticity and a decrease in carboxylic/carbonyl groups with consecutive extraction steps.

Another activity within the project focused on the isolation of kerogen from the Opalinus Clay whole rock based on a protocol established in the petroleum community [Vandenbroucke&Largeau, 2007]. The motivation of kerogen isolation was to investigate in a further step the complexation behavior of this kerogen with respect to radionuclides (i.e. trivalent actinides; Cm) in batch sorption and spectroscopic studies. This procedure consists of

several acid attacks under anoxic atmosphere at 60-70°C. Then, the removal of pyrite is realized by an additional chemical leaching procedure [Acholla&Orr, 1993]. As mentioned before, the organic content of these formations is low in comparison to potential petroleum reservoir rocks and this fact induces difficulties to extract pure organic products without residuals of inorganic phases (i.e. silicates, pyrite) present [Deniau et al., 2008]. In petroleum research, the presence of residual inorganic materials in the isolated fraction can be neglected as the chemical methods applied afterwards are not sensitive to these impurities (i.e. Rock Eval parameters). However, in order to elucidate the potential radionuclide complexation by kerogen, which is expected to have low amounts of complexation groups, these impurities have to be minimized. We succeeded to reduce the amount of inorganic mineral phases co-extracted with the kerogen-type material. SEM-EDX measurements (see Figure below) show that the inorganic phases as shown by the quantitative analysis are still present and sum up to a total amount of 18.3 wt% (Al, Si, Fe, S). Comparing these results to literature data [Deniau et al., 2008] who found between 19.6-37.7 wt% S and 14.3-30.1 wt% Fe in isolated kerogen samples (no Si and Al quantification documented), this clearly documents the improvements made in this study.

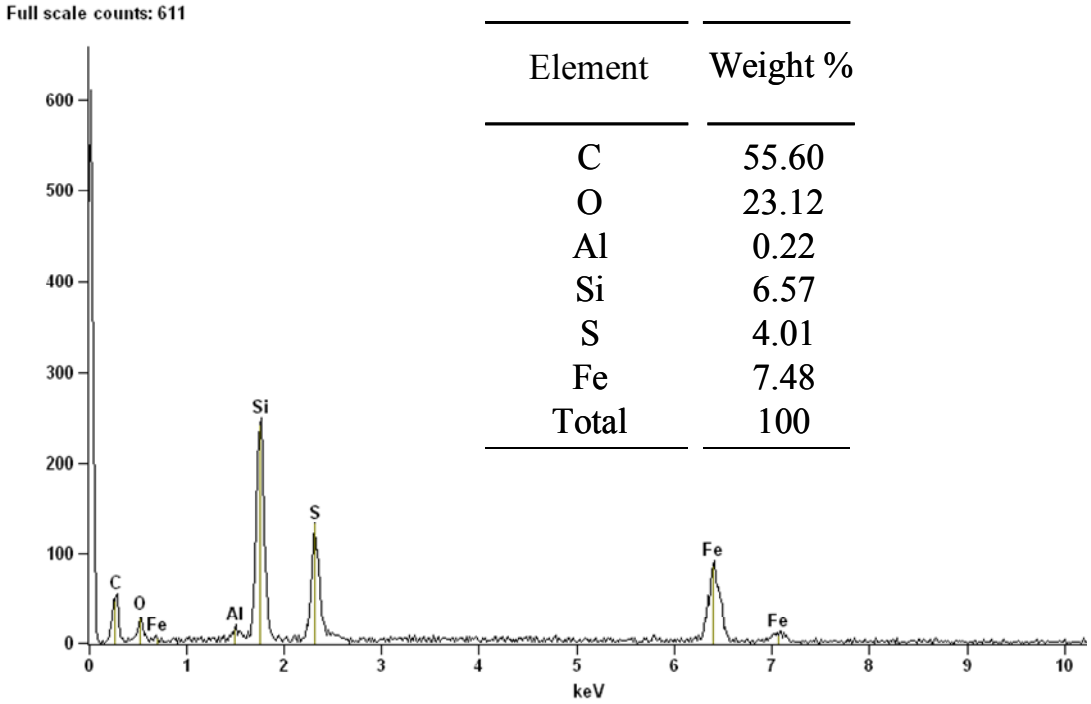

Element	Weight %
C	55.60
O	23.12
Al	0.22
Si	6.57
S	4.01
Fe	7.48
Total	100

Figure 2-4: SEM measurements and quantitative results on extracted products from Opalinus Clay

3 Studies of the sorption of actinides on clay rock

The identification of the relevant mineral phases in natural clay rock responsible for the sorption can be achieved by comparing data obtained from experiments with heterogeneous composed sediments and from experiments with pure mineral phases. In this project the purified Na-rich montmorillonite SWy-2 was used as a surrogate for clay minerals occurring in clay rock. Additionally, the influence of calcite as potential sorbent and humic acid as potential complexing compound on the sorption of radionuclides in the pure clay system was studied. Comparison of results from these batch experiments in the pure system, TRLFS studies and from model calculations one can identify the main clay mineral phases in natural clay rock responsible for the sorption of radionuclides. The assignability of available geochemical data on radionuclide speciation in heterogeneous natural systems can also be assessed from these results.

3.1 Sorption of trivalent actinides and lanthanides (Eu(III), Cm(III)) on OPA and COx.

3.1.1 Experimental

The sorption of Curium, Europium and hexavalent Uranium was studied in batch experiments and by spectroscopic methods like time-resolved laser fluorescence spectroscopy (TRLFS), EXAFS, and XPS. The europium was introduced as a surrogate metal ion for the trivalent actinides.

Batch experiments

In Table 3-1 the experimental conditions of all performed batch experiments is summarised. The pH dependence of the sorption on a heterogeneously composed natural clay rock experiments was studied in the experiment No. 1 to 14. The question about the relevance of outer-sphere complexation on clay minerals has been probed with the variation of the ionic strength and the samples were characterised by TRLFS. Sodiumperchlorate that shows non-complexing properties towards the trivalent and hexavalent cations was used as electrolyte in the solution. For experiment 14 – sorption on Ca-Montmorillonit - Calciumperchlorat was used to avoid ionic exchange as competition reaction between Na^+ and Ca^{2+}.
For the batch experiment a solid to liquid ratio (S/L) of 2 g/L was chosen. At this S/L the cations are mainly bound to the “strong sorption sites” of the clay. Only at lower S/L the cations start to sorb on the “weak sorption sites”. In the experiments 15 to 18 only 0.3 g clay per 1 L NaCl was mixed to get the same conditions as in the TRLFS experiments.

OPA / COx clay samples were crushed and dissolved in the electrolyte solutions. The clay-suspensions were homogenised by stirring over several hours. The metal cations were added to 10 to 20 ml of the suspension in polyethylene (HDPE, Zinsser Analytics, Frankfurt/M.). As metal cations Eu(III) (Europium plasma standard solution, suprapure®, 1000 µg/L Eu, 5 % HNO_3) and U(VI) (UO_2^{2+}, Alfa Uranium ICP standard solution, 1000 µg/L U, 5 % HNO_3) were chosen. The used metal concentration was 1-2x10^{-7} mol/L. These concentrations are low enough to avoid precipitation of hydrolysis products of the metal cations. The sorption on the vial surfaces are small compared to the sorption on the clay material.

The pH value has been adjusted with 0.01 and 0.1 M NaOH or HCl (Merck, Darmstadt, Germany) in a range between 2.7 and 11.9 intervals of 0.5 (pH-meter Schott CG810, pH electrode Orion 8103 Ross®, semi-micro combination). An alteration of the S/L was not expected because only very small amounts of acid or base were necessary to fix the pH value. Due to the high amount of carbonate in the natural clay rock of OPA and COx and the waiving of buffers a small shift of the pH was not avoidable. After adding the metal cations, the samples were slowly mixed in rotation machine for five to seven days. Then aliquots were taken for the analysis of the samples by ICP-AES and ICP-MS. Details of the experiments can also be found in [Hartmann, 2010; Hartmann et al. 2008].

The distribution ratio (Rd, L/kg) was taken for the representation of sorption data.

$$R_d = \frac{c_{initial} - c_{final}}{c_{final}} \cdot \frac{V}{m} \qquad (3\text{-}1)$$

where $C_{initial}$ (mol/L) is the initial nuclide activity/concentration, C_{final} (mol/L) the final (equilibrium) nuclide activity/ concentration, V (L) the liquid volume, and m (kg) the mass of the solid phase

Time-resolved laser fluorescence spectroscopy (TRLFS)

The set-up of the laser system is described elsewhere [Hartmann, 2010]. For the experiments a Nd:YAG pumped dye-laser (Continuum ND 6000, Powerlite 9030, 10 Hz) was used. As dye to get the appropriated wavelength for the excitation of the Cm(III) Exalite 398 was used. The excitation of the Cm(III) was performed at 396.6 nm and corresponds to the maximum in the Cm^{3+}(aq) absorption and excitation spectra.

Table 3-1: Overview of experimental conditions of all batch experiments performed for the sorption experiments of Cm(III) and U(VI) (at 298 K). The Cm(III) / clay mineral-Outersphere complexation were investigated in experiment 15 to 18

	Solid matter	**Condi-tions**	**Electro-lyte**	Ionic strengths [mol/l]	S:L [g/l]	**pH-value**	Eu(III)-Conc. [mol/l]	U(VI)-Conc. [mol/l]
1	OPA	aerobic	$NaClO_4$	0.1	2	2.7 – 11.1	$1 \cdot 10^{-7}$	-
2	COx	aerobic	$NaClO_4$	0.1	2	3.8 – 11.3	$1 \cdot 10^{-7}$	-
3	SWy-2	aerobic	$NaClO_4$	0.1	2	3.1 – 11.0	$1 \cdot 10^{-7}$	-
4	OPA	aerobic	$NaClO_4$	0.1	2	3.3 – 10.8	-	$1 \cdot 10^{-7}$
5	COx	aerobic	$NaClO_4$	0.1	2	5.8 – 10.8	-	$1 \cdot 10^{-7}$
6	SWy-2	aerobic	$NaClO_4$	0.1	2	2.9 – 10.7	-	$1 \cdot 10^{-7}$
7	SWy-2 + 10 ppm HS	aerobic	$NaClO_4$	0.1	2	3.9 – 11.5	$1 \cdot 10^{-7}$	-
8	SWy-2 + 10 ppm HS	aerobic	$NaClO_4$	0.1	2	4.1 – 11.6	-	$1 \cdot 10^{-7}$
9	SWy-2 (80 Gew.%) + 10 ppm HS + $CaCO_3$ (20 Gew.%)	aerobic	$NaClO_4$	0.1	2	2.7 – 11.7	$1 \cdot 10^{-7}$	-
10	SWy-2 (80 Gew.%) + 10 ppm HS + $CaCO_3$ (20 Gew.%)	aerobic	$NaClO_4$	0.1	2	5.3 – 11.0	-	$1 \cdot 10^{-7}$
11	SWy-2 (80 Gew.%) + $CaCO_3$ (20 Gew.%)	aerobic	$NaClO_4$	0.1	2	3.1 – 11.9	$1 \cdot 10^{-7}$	-
12	SWy-2 (80 Gew.%) + $CaCO_3$ (20 Gew.%)	aerobic	$NaClO_4$	0.1	2	3.9 – 11.8	-	$1 \cdot 10^{-7}$
13	Beidellit	aerobic	$NaClO_4$	0.1	2	2.7 – 7.0	$1 \cdot 10^{-7}$	-
14	synth. Ca-Montmo-rillonit	aerobic	$Ca(ClO_4)_2$	0.066	2	4.0 – 9.3	$1 \cdot 10^{-7}$	-
15	SWy-2	aerobic	NaCl	0.01 – 0.17	0.3	~4.0	$2 \cdot 10^{-7}$	-
16	IdP-2	aerobic	NaCl	0.01 – 0.17	0.3	~4.0	$2 \cdot 10^{-7}$	-
17	synth. Ca-Montmo-rillonit	aerobic	NaCl	0.01 – 0.17	0.3	~4.0	$2 \cdot 10^{-7}$	-
18	synth. Na-Montmo-rillonit	aerobic	NaCl	0.01 – 0.17	0.3	~4.0	$2 \cdot 10^{-7}$	-

All TRLFS measurements performed in the frame of this project are summarised in Table 3-2. The sorption of Cm(III) and Eu(III) was probed on the natural clay rock OPA and COx, the synthetic beidellite and mixture of SWy-2 and calcite in the ratio 80:20 wt.% (experiments No. 1 to 9). For that 0.3 g/L solid material in 0.1 M aqueous sodium perchlorate solution were used. This S/L was the best ratio where the loss of light due to scattered light was acceptable for the measurement. The final concentration of the trivalent cation was 1-2 x 10^{-7} M. After mixing all components the samples were left under shaking for at least two days to reach equilibrium.

In experiment 10 to 25 (Table 3-2) the outersphere sorption of Cm(III) was investigated with the natural montmorillonites SWy-1, Milos and STx-1, a synthetic montmorillonite in the Na form, the Illit IdP-2 and the γ-alumina. The S/L was 0.3 g/L each and the ionic strength was varied between 0.01 and 0.20 M NaCl in H_2O and D_2O. The Cm(III) concentrations amounts 2 x 10^{-7} M. After two days the pH or the pD value was checked. The fluorescence emission lifetime in H_2O was measured in 5 µs intervals at 1 ms exposure time, in D_2O in 50 µs intervals at 10 ms exposure time. For the quantification of the outer-sphere sorption the ionic strength was increased from 0.01 M with 3 M NaCl in H_2O and D_2O, respectively.

Concerning the uranyl sorption on clay the important question of the existence of the $Ca_2UO_2(CO_3)_3$ complex was investigated in experiment No. 26 to 29 at conditions described in Table 3-2. Table 2-1 The uranyl concentration was 2 x 10^{-5} M and the S/L 2 g/L in 0.1 M $NaClO_4$.

Table 3-2: Summary of the experimental conditions of the performed TRLFS measurements (1 to 29 at 298 K).

	Solid matter	**H_2O/ D_2O**	**Electrolyte**	**Ionic strength [mol/l]**	**S:L [g/l]**	**pH value**	**[Cm(III)]- [mol/l]**	**[Eu(III)] [mol/l]**	**[U(VI)] [mol/l]**
1	COx	H_2O	$NaClO_4$	0,1	0,3	7,45	$1 \cdot 10^{-7}$	-	-
2	OPA	H_2O	$NaClO_4$	0,1	0,3	7,16	$1 \cdot 10^{-7}$	-	-
3	COx (Tonfraktion)	H_2O	$NaClO_4$	0,1	0,3	4,95 7,41 9,96	$1 \cdot 10^{-7}$	-	-
4	COx	H_2O	$NaClO_4$	0,1	0,3	8,77 8,89	-	$2 \cdot 10^{-7}$	-
5	OPA	H_2O	$NaClO_4$	0,1	0,3	7,04 7,62	-	$2 \cdot 10^{-7}$	-
6	COx (Tonfraktion)	H_2O	$NaClO_4$	0,1	0,3	3,87 3,93	-	$2 \cdot 10^{-7}$	-
7	Beidellit	H_2O	$NaClO_4$	0,1	0,3	3,15 – 8,79	$1 \cdot 10^{-7}$	-	-
8	Beidellit	H_2O	$NaClO_4$	0,1	0,3	4,19 – 10,34	$2 \cdot 10^{-7}$	-	-
9	SWy-2/Calcit	H_2O	$NaClO_4$	0,1	0,3	4,43 – 12,02	$2 \cdot 10^{-7}$	-	-
10	SWy-1	H_2O	NaCl	0,01 – 0,20	0,3	~4,0	$2 \cdot 10^{-7}$	-	-
11	Milos	H_2O	NaCl	0,01	0,3	~4,0	$2 \cdot 10^{-7}$	-	-
12	STx	H_2O	NaCl	0,01	0,3	~4,0	$2 \cdot 10^{-7}$	-	-
13	γ-Al_2O_3	H_2O	NaCl	0,01	0,3	~4,0	$2 \cdot 10^{-7}$	-	-
14	SWy-1	D_2O	NaCl	0,01 – 0,07	0,3	~4,0	$2 \cdot 10^{-7}$	-	-
15	Milos	D_2O	NaCl	0,01	0,3	~4,0	$2 \cdot 10^{-7}$	-	-
16	STx	D_2O	NaCl	0,01	0,3	~4,0	$2 \cdot 10^{-7}$	-	-
17	synth. Na-Montmorillonit	D_2O	NaCl	0,01	0,3	~4,0	$2 \cdot 10^{-7}$	-	-
18	γ-Al_2O_3	D_2O	NaCl	0,01	0,3	~4,0	$2 \cdot 10^{-7}$	-	-
19	SWy-1	D_2O	NaCl	0,01 – 0,11	0,3	~4,0	$2 \cdot 10^{-7}$	-	-
20	Milos	D_2O	NaCl	0,01 – 0,12	0,3	~4,0	$2 \cdot 10^{-7}$	-	-
21	STx	D_2O	NaCl	0,01 – 0,11	0,3	~4,0	$2 \cdot 10^{-7}$	-	-
22	synth. Na-Montmorillonit	D_2O	NaCl	0,01 – 0,18	0,3	~4,0	$2 \cdot 10^{-7}$	-	-
23	SWy-1	H_2O	NaCl	0,001 – 0,18	0,3	~4,0	$2 \cdot 10^{-7}$	-	-
24	Milos	H_2O	NaCl	0,001 – 0,16	0,3	~4,0	$2 \cdot 10^{-7}$	-	-
25	IdP-2	H_2O	NaCl	0,01 – 0,20	0,3	~4,0	$2 \cdot 10^{-7}$	-	-
26	SWy-2/Calcit	H_2O	$NaClO_4$	0,1	2	7,43	-	-	$2 \cdot 10^{-5}$
27	SWy-2 mit $NaHCO_3$	H_2O	$NaClO_4$	0,1	2	7,62	-	-	$2 \cdot 10^{-5}$
28	(kein Feststoff)	H_2O	$NaClO_4$	0,1	2	3,65	-	-	$2 \cdot 10^{-5}$
29	COx	H_2O	$NaClO_4$	0,1	2	7,80	-	-	$2 \cdot 10^{-5}$

Measurement of the pD value

For the pD measurement a special gadget was made at KIT-INE. It consists of two micro half-cells: on glass electrode and one Ag/AgCl electrode as reference electrode (Kurt-Schwabe-Institut für Mess- und Sensortechnik e.V., Meinsberg; Figure 3-1) was put into a quartz cuvette with screw top. The electrodes were calibrated with solutions of known D^+ concentrations and constant ionic strength of 0.1 M NaCl/DCl [Freyer et al. 2009] and $-\log[D^+]$ of 2, 3, and 11. From plotting the potential of the electrodes against the $-\log[D^+]$, a straight line was gotten proving that the measurement was correct (Figure 3-2). The pD value was evaluated from the linear relationship by linear regression.

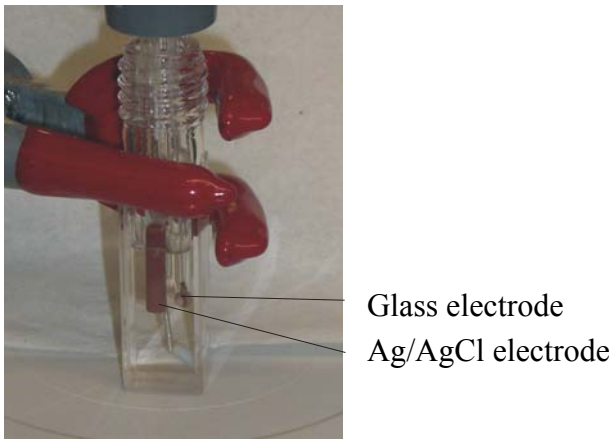

Figure 3-1: Gadget for pD measurement in a special quartz cuvette for TRLFS.

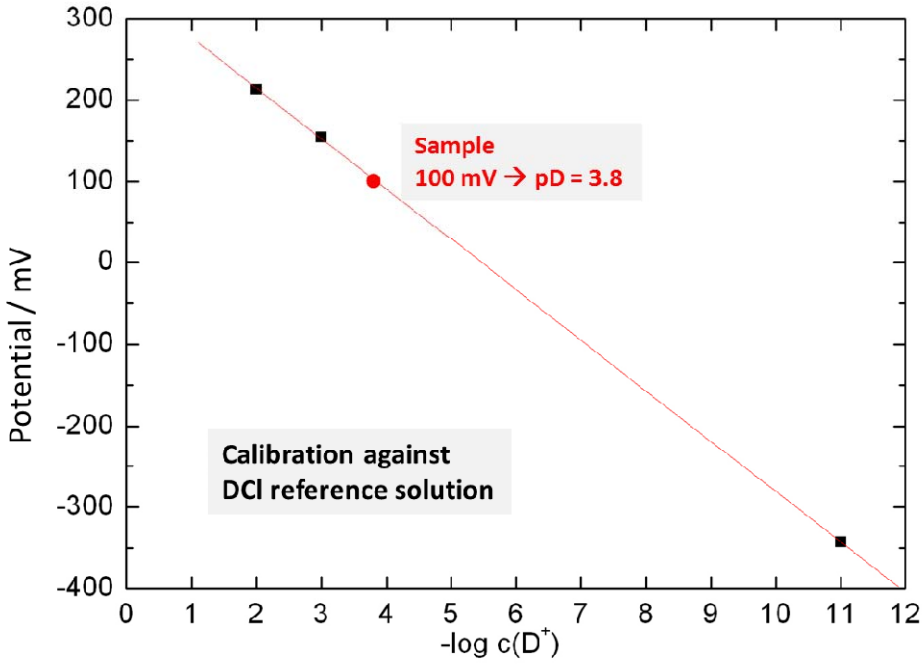

Figure 3-2: Calibration of the pD value with DCl reference solutions of known D+ concentration.

Modelling

The calculation of the species distribution has been performed with the program ECOSAT 4.8 (*Equilibrium Calculation Of Speciation And Transport* [Keizer and van Riemsdijk 1999]. For the modelling of the metal ion sorption on clay simplifications and estimates were required due to the huge number of potential interaction in reality and the large number of unreliable surface complexation formation constants found in literature; especially for the sorption on calcite and the formation of ternary surface complexes. It is assumed that the sorption of Eu(III) mainly takes place on the clay minerals. The solid content of the clay was fixed to the real concentration of clay minerals in the OPA (54 wt.%) and COx (42 wt.%), and for calcite (OPA: 6 wt.%; COx: 17.3 wt.%).
Only for the clay minerals smectite and illite site capacities for sorption, protolysis constants, selectivity constants for the ion exchange reaction and surface complexation formation constants exist in the literature. Therefore, the sorption of the other clay minerals of kaolinite, chlorite, illite-smectite mixed layers were equated with smectite and illite. Hence, the content of these clay minerals very added one half each to the content of smectite and illite. All parameter for the surface complexation and ion exchange reaction are summarised in Table 3-3. For the modelling of the Eu(III) sorption on synthetic Montmorillonite in the Ca form the surface complexation constants were depicted from [Bradbury et al. 2005].

For the calculations, carbonate concentrations were assumed to be in equilibrium with calcite in a closed system with no gas phase. For the natural clay rock experiments, we checked this assumption by analysing the inorganic carbon concentration (DIC) exemplary in some samples. Calculated and measured values were in fair agreement.
Competitive complexation reaction of other ligands like OH^-, CO_3^{2-}, and humic acid were considered in the modelling, whereas all other water constituents were neglected, because they are very weak complexing ligands or they be available at only very low concentrations. The stability constants of all regarded aqueous species are summarised in Table 3-4 for Eu(III). The formation constants of relevant solid compounds are given in Table 3-5. According to the modelling solid phases have not formed at Eu(III) concentrations used in the experiment. The adsorption model 2PNE SC/CE (*two site protlysis non electrostatic surface complexation and cation exchange*) from [Bradbury & Bayens, 1997, 1999, 2002, 2005b; Bradbury et al., 2005] was applied. Ion exchange reactions were treated by applying the Gaines–Thomas convention [Gaines&Thomas 1953].

The effect of humic acid on the sorption of Eu(III) on natural clay rock and SWy-2/Calcite mixture was modelled with the NICA-Donnan model and the parameter set of [Milne et al. 2003] (see Table 3-6). This model is implemented in the ECOSAT code and describes the complexation of metal cations with humic acid (HA). It takes into account the heterogeneity

of the functional groups that are responsible for proton and cation binding as well as the macro-molecular properties due to its molecular size. It is a combination between the Donnan model, which describes the non-specific electrostatic interactions between the surrounding solution and the negative charge of the polyelectrolyte – humic and fulvic acids – and the NICA model (Non Ideal Competitive Adsorption) that handles the specific cation binding. In the Donnan model the humic substances are considered as behaving like a gel and posses a homogeneous charge and potential distribution over the whole humic particle.
However, the sorption of HA on clay is not considered by this model. For the total sorption of Eu(III) the experimentally determined amount of HA was taken. It was assumed that sorption behaviour of the latter is equal to the sorption behaviour of Eu(III)-)-humate complexes. This amount of sorbed metal humate species and the modelled amount of sorbed species in the inorganic system was summed up to yield the modelled total sorption of Eu(III).

Table 3-3: Parameters for calculations of Eu(III)/U(VI) sorption onto the different solids. In all cases the Davies Equation was used for activity corrections [Davies, 1962].

				COx		**OPA**		
Background electrolyte				0.1 mol/l $NaClO_4$ (Ionic strength was appointed as variable value)				
Initial Eu(III)-/U(VI) concentration				$1 \cdot 10^{-7}$ mol/l				
Solid to liquid ratio (S/L)				2 g/l				
Solid	Mineral phase			42 wt.% clay minerals (20 wt.% montmorillonite, 22 wt.% illite,)		54 wt.% clay minerals (18 wt.% montmorillonite, 36 wt.% illite)		
				17,3 wt.% calcite (based on Ca^{2+}-analysis in solution)		6,0 wt.% calcite (based on Ca^{2+}-analysis in solution)		
				Na-montmorillonite		**Na-illite**		**Ca-montmor.**
				Eu(III)	**U(VI)**	**Eu(III)**	**U(VI)**	**Eu(III)**
	Cation exchange capacity[a]			$8.7 \cdot 10^{-1}$ eq/kg		$2.25 \cdot 10^{-1}$ eq/kg		
	Site capacity[a]	Typ of surface sites:	$\equiv X^S OH$	$2.0 \cdot 10^{-3}$ mol/kg		$2.0 \cdot 10^{-3}$ mol/kg		
			$\equiv X^{W1} OH$	$4.0 \cdot 10^{-2}$ mol/kg		$4.5 \cdot 10^{-2}$ mol/kg		
			$\equiv X^{W2} OH$	$4.0 \cdot 10^{-2}$ mol/kg		$4.5 \cdot 10^{-2}$ mol/kg		Look at Na-mont-morillon.
	Protolysis constants [log *K*][a]	$\equiv X^S OH + H^+ \Leftrightarrow \equiv X^S OH_2^+$		4.5		5.5		
		$\equiv X^S OH \Leftrightarrow \equiv X^S O^- + H^+$		-7.9		-6.2		
		$\equiv X^{W1} OH + H^+ \Leftrightarrow \equiv X^{W1} OH_2^+$		4.5		5.5		
		$\equiv X^{W1} OH \Leftrightarrow \equiv X^{W1} O^- + H^+$		-7.9		-6.2		
		$\equiv X^{W2} OH + H^+ \Leftrightarrow X^{W2} OH_2^+$		6.0		9.0		
		$\equiv X^{W2} OH \Leftrightarrow \equiv X^{W2} O^- + H^+$		-10.5		-10.5		
Cation exchange reaction K_c (I = 1)	$3Na\text{-mont} + Eu^{3+} \Leftrightarrow Eu\text{-mont} + 3Na^+$			30^b	-	-	-	-
	$3Na\text{-illit} + Eu^{3+} \Leftrightarrow Eu\text{-illit} + 3Na^+$			-	-	76^a	-	-
	$2Na\text{-mont} + UO_2^{2+} \Leftrightarrow UO_2\text{-mont} + 2Na^+$			-	1.4^c	-	-	-
	$2Na\text{-illit} + UO_2^{2+} \Leftrightarrow UO_2\text{-illit} + 2Na^+$			-	-	-	$4,5^d$	-
	$2Na\text{-Ton} + Ca^{2+} \Leftrightarrow Ca\text{-Ton} + 2Na^+$			4.1^b	4.1^b	11^d	11^d	-
	$3Ca\text{-Ton} + Eu^{3+} \Leftrightarrow Eu\text{-Ton} + 3Ca^{2+}$			-	-	-	-	13^a
Surface complexation constants for „*strong*“ and „*weak sites*“ [log K_{SC}][a, c, d]	$\equiv X^S OH + Eu^{3+} \Leftrightarrow \equiv X^S OEu^{2+} + H^+$			1.6	-	3.1	-	0.6
	$\equiv X^S OH + Eu^{3+} + H_2O \Leftrightarrow \equiv X^S OEuOH^+ + 2H^+$			-6.4	-	-4.4	-	-6.2
	$\equiv X^S OH + Eu^{3+} + 2H_2O \Leftrightarrow \equiv X^S OEu(OH)_2 + 3H^+$			-15.7	-	-12.7	-	-14.2
	$\equiv X^{W1} OH + Eu^{3+} \Leftrightarrow \equiv X^{W1} OEu^{2+} + H^+$			-0.5	-	0.3	-	-1.4
	$\equiv X^{W1} OH + Eu^{3+} + H_2O \Leftrightarrow \equiv X^{W1} OEuOH^+ + 2H^+$			-	-	-6.2	-	-
	$\equiv X^S OH + Eu^{3+} + CO_3^{2-} \Leftrightarrow \equiv X^S OEuCO_3^0 + H^+$			8.3	-	-	-	-
	dto. $+ H_2O \Leftrightarrow \equiv X^S OEuOHCO_3^- + 2H^+$			-0.25	-	-	-	-
	$\equiv X^S OH + UO_2^{2+} \Leftrightarrow \equiv X^S OUO_2^+ + H^+$			-	3.1	-	2.6	-
	$\equiv X^S OH + UO_2^{2+} + H_2O \Leftrightarrow \equiv X^S OUO_2OH + 2H^+$			-	-3.4	-	-3.6	-
	$\equiv X^S OH + UO_2^{2+} + 2H_2O \Leftrightarrow \equiv X^S OUO_2(OH)_2^- + 3H^+$			-	-11.0	-	-10.3	-
	$\equiv X^S OH + UO_2^{2+} + 3H_2O \Leftrightarrow \equiv X^S OUO_2(OH)_3^{2-} + 4H^+$			-	-20.5	-	-17.5	-
	$\equiv X^{W1} OH + UO_2^{2+} \Leftrightarrow \equiv X^{W1} OUO_2^+ + H^+$			-	0.7	-	0.1	-
	$\equiv X^{W1} OH + UO_2^{2+} + H_2O \Leftrightarrow \equiv X^{W1} OUO_2OH + 2H^+$			-	-5.7	-	-5.3	-
Carbonate				equilibrium with calcite, closed system (no gas phase)				

X: smectite and illit respectively ^{S}: *strong sites*, $^{W1}/^{W2}$: *weak sites,* a: [Bradbury at al., 2005], b: [Bradbury&Baeyens, 2002], c: [Bradbury&Baeyens, 2005a], d: [Bradbury&Baeyens, 2005b]

Table 3-4: Formation constants for aqueous Eu(III) species that were considered in the model calculation (β^0 constants were corrected to I = 0). Formation constants of Am(III) species from [Guillaumont et al., 2003] were taken as analogue values for Eu(III).

Eu(III) species and reaction of formation	log β^0	Reference
$Eu^{3+} + H_2O(l) \Leftrightarrow EuOH^{2+} + H^+$	-7.200	b
$Eu^{3+} + 2H_2O(l) \Leftrightarrow Eu(OH)_2^+ + 2H^+$	-15.100	b
$Eu^{3+} + 3H_2O(l) \Leftrightarrow Eu(OH)_3 + 3H^+$	-26.200	b
$Eu^{3+} + CO_3^{2-} \Leftrightarrow EuCO_3^+$	8.000	a
$Eu^{3+} + 2CO_3^{2-} \Leftrightarrow Eu(CO_3)_2^-$	12.900	a
$Eu^{3+} + 3CO_3^{2-} \Leftrightarrow Eu(CO_3)_3^{3-}$	15.000	a
$Eu^{3+} + HCO_3^- \Leftrightarrow EuHCO_3^{2+}$	3.100	a
$H^+ + CO_3^{2-} \Leftrightarrow HCO_3^-$	10.329	a
$2H^+ + CO_3^{2-} \Leftrightarrow H_2CO_3$	16.683	a

l: pure liquid; a: [Guillaumont et al., 2003]; b: [Brabury et al., 2005]

Table 3-5: Formation constants of Eu(III)-, U(VI)- and other minerals considered in the model calculation. Formation constants of Am(III) species from [Guillaumont et al., 2003] were taken as analogue values for Eu(III).

Mineral and reaction of formation	**log β^0**	**Reference**
$Ca^{2+} + CO_3^{2-} \Leftrightarrow CaCO_3$	8.410	a
$Ca^{2+} + 2H_2O \Leftrightarrow Ca(OH)_2 + 2H^+$	5.200	a
$Eu^{3+} + 3H_2O(l) \Leftrightarrow Eu(OH)_3(am) + 3H^+$	-16.900	b
$Eu^{3+} + CO_3^{2-} + OH^- \Leftrightarrow EuCO_3OH(am, hyd)$	20.200	b
$Eu^{3+} + 2CO_3^{2-} + 5H_2O(l) + Na^+ \Leftrightarrow NaEu(CO_3)_2 \cdot 5H_2O(cr)$	21.000	b
$UO_2^{2+} + CO_3^{2-} \Leftrightarrow UO_2CO_3(cr)$	14.760	b

am: amorphous , hyd: hydrated, cr: crystalline; a: [Lindsay, 1979]; b: [Guillaumont et al., 2003];

Table 3-6: Parameter for modelling of Eu(III) and U(VI) binding on humic acid (Milne et al., 2001; Milne et al., 2003). Qmax1/2: number of sites with low and high affinity, p1/2: heterogeneity parameter β1/2: formation constants of Eu(III) and U(VI) humate complexes, n1/2: non-ideality parameter.

NICA-Donnan-parameter	Q_{max1} **[mol/kg]**	p_1	Q_{max2} **[mol/kg]**	p_2
HS (suspension)	3.15	0.62	2.55	0.41
	log β_1	n_1	log β_2	n_2
$HS_{a/b}$-Eu	1.92	0.57	3.43	0.36
$HS_{a/b}$-UO_2	2.45	0.45	4.81	0.32

3.1.2 Results and discussions

In Figure 3-3 the sorption of Eu(III) on OPA, COx, and SWy-2 is shown as sorption edge in log R_d (a) and % sorbed Eu(III)(b) in the pH range between 3 and 11. The Eu(III) sorption increases with the pH below values smaller than 7. From pH 7 and higher the curve flattens to a plateau with log R_d values of 4 to 5 for OPA and around 5 for COx. This corresponds to a sorption of Eu(III) higher than 95 %. In contrast to OPA and COx, the Eu(III) sorption on SWy-2 furthermore increases with pH to reach a log R_d of about 6 at pH 10.5. Similar shapes of the sorption edges have also been found for trivalent lanthanide/actinide interaction with pure clay mineral phases [Rabung et al., 2005; Bradbury & Baeyens, 2002]. It was interpreted as cation exchange on pH independent permanently charged surface sites of the clay minerals at lower pH (< 4) and inner-sphere surface complexation reactions at amphoteric surface hydroxyl groups situated at clay platelet edges at higher pH. Experiments carried out under aerobic conditions and in an Ar atmosphere (exclusion of oxygen) did not yield significantly different data. The influence on metal ion sorption of oxidized Fe(III) oxide/hydroxides, possibly generated under aerobic conditions due to pyrite oxidation, is therefore expected to be of minor relevance. Bradbury and Baeyens studied the Eu(III) sorption onto OPA [Bradbury & Baeyens, 2003a] for porewater conditions and without pH variation. Their results are in good agreement with our findings; they are also plotted in Figure 3-3 at pH 6.3 and 7.8. No data for Eu(III) sorption (or its analogues) onto COx were found in the literature.

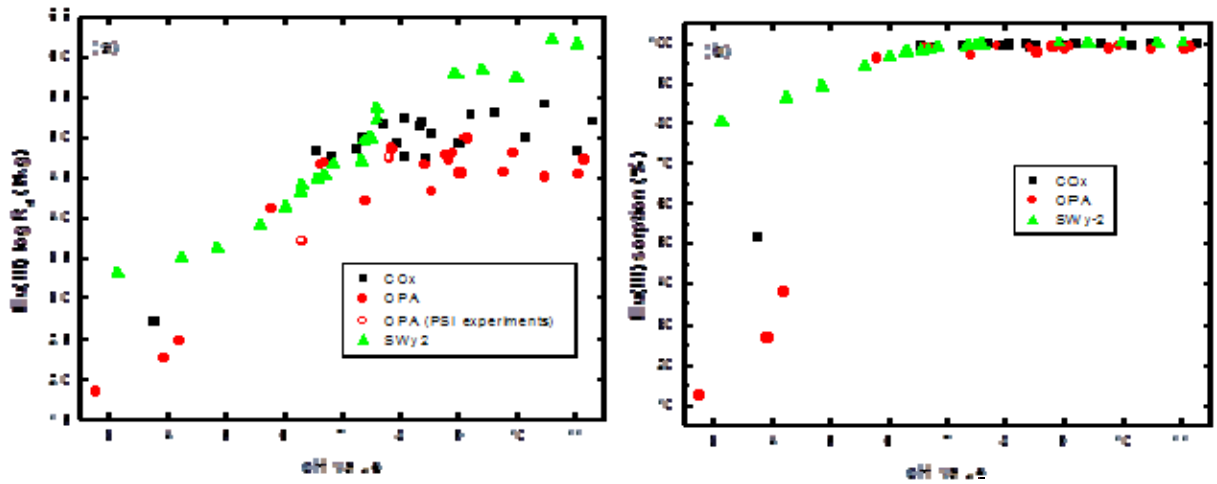

Figure 3-3: Eu(III) sorption on OPA, COx und SWy-2 in dependence of pH illustrated in log R_d (a) and % (b). Experimental conditions: [Eu(III)] = $1 \cdot 10^{-7}$ mol/l, solid to liquid ratio (S/L) = 2 g/l, I = 0,1 mol/l NaClO4.

The different developing of the sorption at pH < 7 of the three clay materials qualitatively corresponds to their different cation exchange capacity; OPA and COx (106-121 and 350-400 meq/kg) show lower sorption than SWy-2 (870 meq/kg). Additionally, the clay mineral fraction determining the sorption amounts for SWy-2 2 g/L, but it is only 1.08 and 0.84 g/L for OPA and COx respectively due to their heterogeneous mineral content.

The calculated speciation of Eu(III) in the presence of COx and OPA is plotted in Figure 3-4. In the calculations, the natural clay rocks are simulated by a mixture consisting of illite, montmorillonite, and calcite. Due to the fact that no literature data are available for the other minerals– mainly kaolinite, chlorite – their amounts were added to the amount of illite and montmorillonite, to half each. This results in 36 wt.% Illite, 18 wt.% montmorillonite, and 6 wt. calcite. The originally exact mineral ratios are specified in Table 2-3. The total calcite content was taken from the analysis Ca^{2+} of a sample with pH of 2.8 where the total calcite should be dissolved. It is assumed that the Ca^{2+} content in solution matches the calcium of the totally dissolved calcite. An sorption of Eu(III) on the calcite was not considered in the modelling. Calculations take into account sorption to clay minerals and complexation in solution by hydroxide and carbonate ions. Dissolution and precipitation of calcite along the considered pH range is considered and this controls the dissolved carbonate concentration. At pH values < 6, Eu(III) speciation is dominated by the free Eu(III) aquo ion and ion-exchange-bound Eu(III). The difference between model calculations and experimental data shows in terms of the calculated Eu(III) sorption a significant sorption reduction at 7–9.5. This is due to formation of aqueous $Eu(CO_3)_+$ and $Eu(CO_3)_{2-}$ complexes which are not considered as sorbing species in the model, but they are the dominant species in solution.

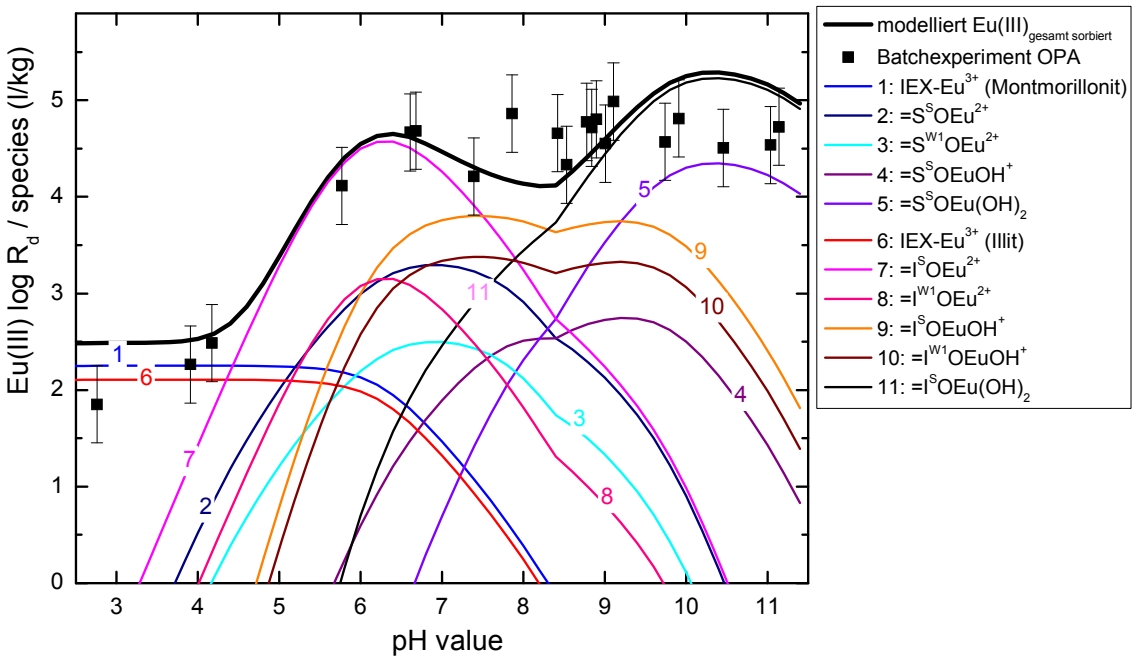

Figure 3-4: Eu(III) sorption on OPA and modelling as a function of pH. Experimental conditions: [Eu(III)] = $1 \cdot 10^{-7}$ mol/l, S/L = 2 g/l, I = 0,1 mol/l NaClO4. (IEX = Ionenexchange, I = Illite, S = Smectite, S = strong sites, W1 = weak sites).

In Figure 3-5 the modelling of the COx sorption data is shown. The clay mineral fraction of COx – in total 42 wt.%, mainly composed of illite/smectite mixed layers, illite, smectite, and a little kaolinite, chlorite – was simulated in the model with 22 wt.% illite, 20 wt.% mont-

morillonite, and 17.3 wt.% calcite. The total Eu(III) sorption is modelled quite well. However, there is a significant underestimation of the total Eu(III) sorption in the calculation between pH 6.5 and 9. The largest difference between modelled and experimental values is about $\Delta(\log R_d) \sim 1.5$ L/kg at about pH 7.5. The sorption data are well described by the used model in the pH range higher than 9.

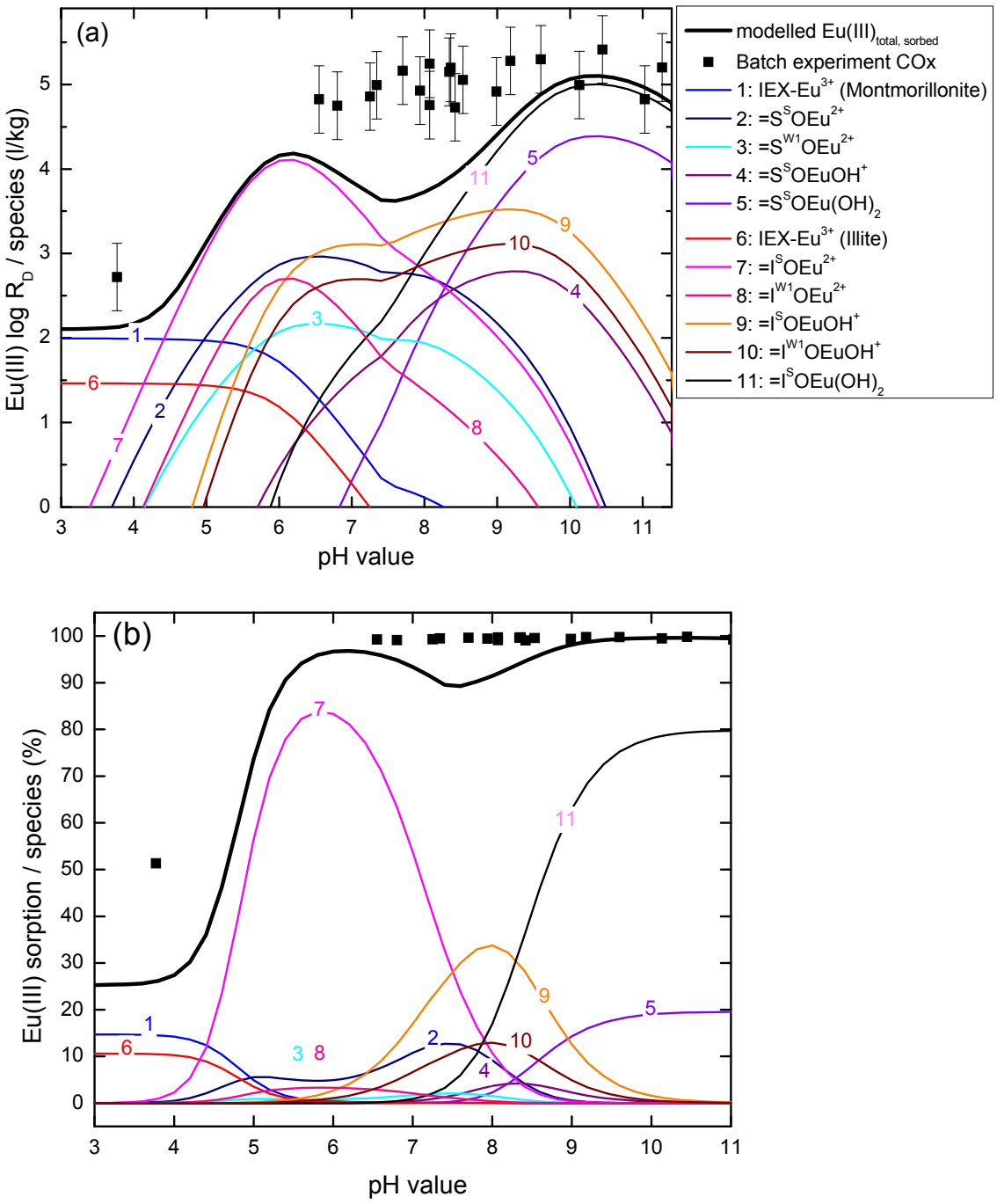

Figure 3-5: Eu(III) sorption on COx and numerical modelling in as a function of pH shown as log $\boldsymbol{R_d}$ (a) and in % (b). Experimental conditions: [Eu(III)] = $1 \cdot 10^{-7}$ mol/l, S/L = 2 g/l, I = 0,1 mol/l $NaClO_4$. (IEX = ion exchange, I = illite, S = smectite, S = ***strong sites***, W1 = ***weak sites***).

In Figure 3-6 the amount of the Eu(III) species sorbed on illite and montmorillonite was summed up and separately illustrated for OPA and COx. In the lower pH range (<4.3) where the sorption is governed by pH independent cation exchange (outer-sphere complexation), the montmorillonite dominates the sorption. The montmorillonite possess a four times higher cation exchange capacity than illite (870 as opposed to 225 meq/kg). At higher pH values (pH< 4.3) the inner-sphere complexation is the dominating mechanism and the sorption on illite predominates. Here, the Eu(III) surface complexes $\equiv I^{S}OEu^{2+}$, $\equiv I^{S}OEuOH^{+}$, and $\equiv I^{S}OEu(OH)_2$ mainly contribute to the Illite sorption. This is also expressed in the surface complexation constants of Illite-Eu(III) complexes (log K_{SC} = 3.1 / -4.4 / -12.7) that are manifold higher than the corresponding montmorillonite-Eu(III) complexes (log K_{SC} = 1.6 / -6.4 / -15.7). The sorption occurs on the strong sites rather than on the weak sites, even the amount of the latter one is higher in the clay rock. However, the strong sites forms more stable complexes that are occupied first by trace amounts of metal ions (1 x 10^{-7} M).

The calculation of the species distribution of Eu(III) in solution as a function of pH with thermodynamic data from Table 3-3, Table 3-4 and Table 3-5 shows that Eu^{3+} is the main species at pH values below 5, occurring as free Eu^{3+} in solution and as outer-sphere complex. The complex $EuHCO_3^{2+}$ plays no role. In the pH range 6 to 9 the complexes $EuCO_3^{+}$ and $Eu(CO_3)^{-}$ are stable and they occur in relevant concentrations causing a decrease of the modelled amount of europium sorbed to clay. The divergence in calculated and experimental data could point to the possible existence of ternary clay/Eu(III)/carbonate surface complexes, which are not considered as sorbing species in the model. Stumpf et al. reported the existence of ternary Eu(III) complexes in smectite and kaolinite suspensions under atmospheric conditions at pH ≤ 6.65 using TRLFS [Stumpf et al., 2002]. Marques et al. have studied the possible formation of clay / Eu(III) carbonat surface complexes on Na-rich Montmorillonite by batch experiments and modelling [Marques et al., 2008]. Their experiments could be described very well by comprising the sorption of Eu(III) carbonate and Eu(III) hydroxo carbonate complexes on strong sites forming $\equiv S^{S}OEuCO_3$ and $\equiv S^{S}OEuOHCO_3^{-}$ surface complexes. The surface complexation constants log K_{SC} have been estimated to

log K_{SC} = 8.3 for the reaction $\equiv S^{S}OH + Eu^{3+} + CO_3^{2-} = \equiv S^{S}OEuCO_3 + H^{+}$

log K_{SC} = -0.25 for the reaction $\equiv S^{S}OH + Eu^{3+} + CO_3^{2-} + H_2O = \equiv S^{S}OEuOHCO_3 + 2H^{+}$

With these data a new modelling of the COx experiments was performed with surface species on montmorillonite and illite. This is illustrated in Figure 3-7. The modelling curve does now match much better with the experimental data. Unfortunately, data for the ternary surface complexes on illite are not available from literature, but the existence of them is already proved in experiments [Marques, 2010]. According to the modelling the species $\equiv S^{S}OEuCO_3$ occurs in significant amounts between pH 6 and 10 and predominates at pH ~7.9 the surface

species. The surface species $\equiv S^{S}OEuOHCO_3$ can be neglected in contrast. Nevertheless, other reasons for the divergence of modelling curve and experimental data cannot be excluded, like the influence of other mineral phases in natural clay rock on Eu(III) sorption.

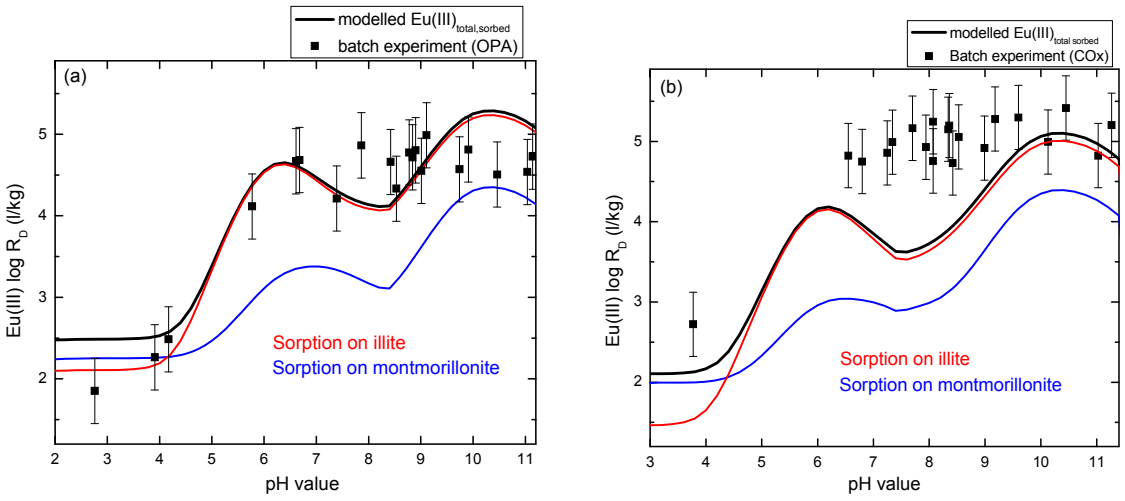

Figure 3-6: Eu(III) sorption on OPA (a) and COX (b) together with numerical modelling of the total Eu(III) sorption as well as sorption on illite and montmorillonite as function of pH. Experimental conditions: $[Eu(III)] = 1 \cdot 10^{-7}$ mol/l, S/L = 2 g/l, I = 0,1 mol/l $NaClO_4$.

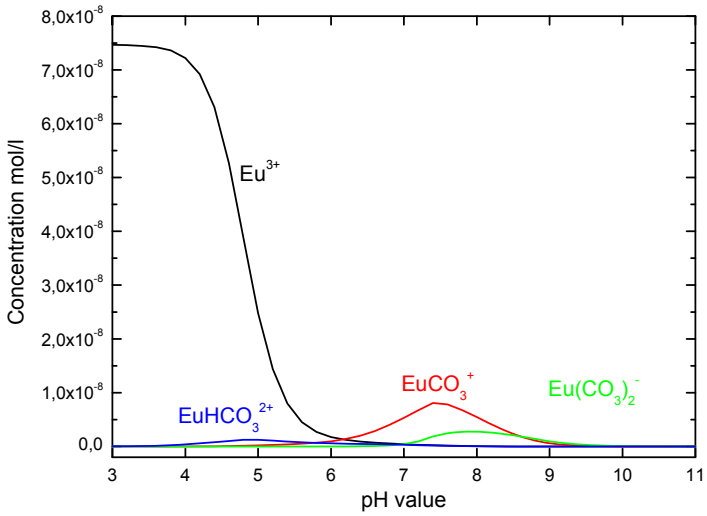

Figure 3-7: Numerical modelled aqueous Eu(III) speciation in COx suspension. Conditions: [Eu(III)] = 1·10-7 mol/l, S/L = 2 g/l, thereof 17.3 % calcite, I = 0.1 mol/l NaClO4.

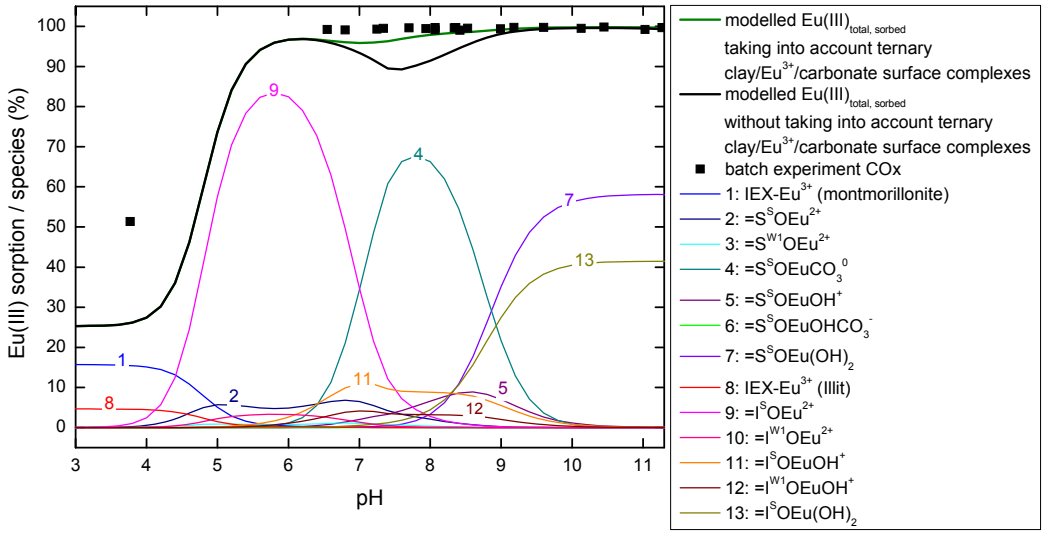

Figure 3-8: Eu(III) sorption on COx and modelling as a function of pH by regarding (dark green line) and disregarding (black line) ternary Clay/Eu^{3+}/carbonate surface complexes shown in %. Experimental conditions: [Eu(III)] = $1 \cdot 10^{-7}$ mol/l, S/L = 2 g/l, thereof 17.3 % calcite, I = 0.1 mol/l $NaClO_4$. (IEX = Ion exchange, I = illite, S = smectite, S = strong sites, W1 = weak sites).

Based on the high calcite or carbonate content of natural clay rocks – OPA contains 6 to 10 wt.% and COx 20 wt.% - the dissolved carbonate concentration is controlled by the solubility of calcite at pH > 8.5. The solubility of calcite ($CaCO_3$(cr)) is exceeded until pH ~7.5 and higher and limits the CO_3^{2-} concentration in solution to < $5x10^{-4}$ mol/L at pH ~ 9 (s. Figure 3-9). The OH^- concentration increases with the pH and at pH > 9 the Eu(III) dihydroxide surface species of Illite and Smectite preponderate.

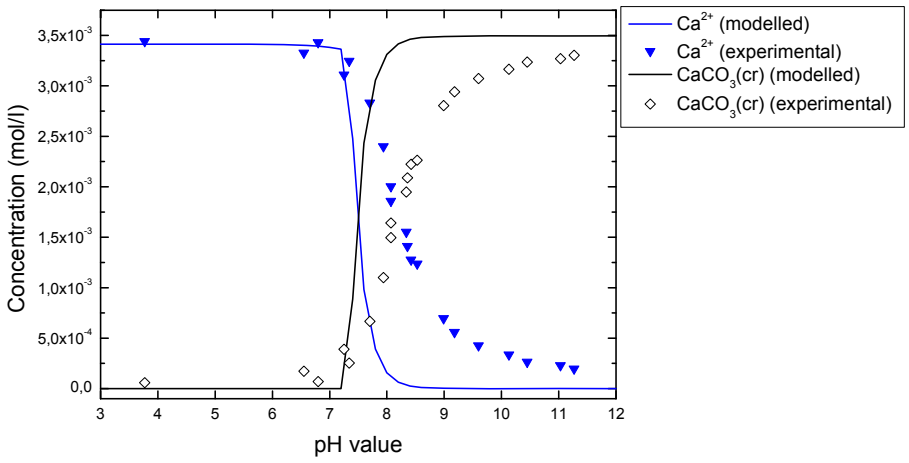

Figure 3-9: Experimentally determined Ca^{2+} concentration in the solution of the Eu(III) sorption experiments on COx and OPA as well as the modelled Ca^{2+} and $CaCO_3$(cr) concentration as a function of pH. The experimental $CaCO_3$(cr) data were extrapolated from the measured Ca^{2+} values.

3.2 Eu(III)/Cm(III) sorption on clay / calcite mixture

As already mentioned before, the OPA and COx clay consist of not only illite and montmorillonite but also of other mineral phases. One of these mineral phases at higher concentrations in the clay rock is calcite. To elucidate the role of calcite on the sorption of Eu(III) / Cm(III) some experiments have been performed with a mixture of Na-rich montmorillonite (SWy-2) and calcite in percentage of 80 : 20 wt.%. This approximately corresponds to a content of calcite in COx. The sorption of Eu(III) on this clay / calcite mixture is shown in Figure 3-10. The Eu(III) is almost totally sorbed at pH < 7, which is similar to the sorption on natural clay rock without calcite addition. The modelling result coincides quite well with the experimental data, but it underestimates again the Eu(III) sorption at pH values between 6.5 and 9. The used model specifies dissolved carbonate complexes of Eu^{3+} responsible for the inhibited sorption.

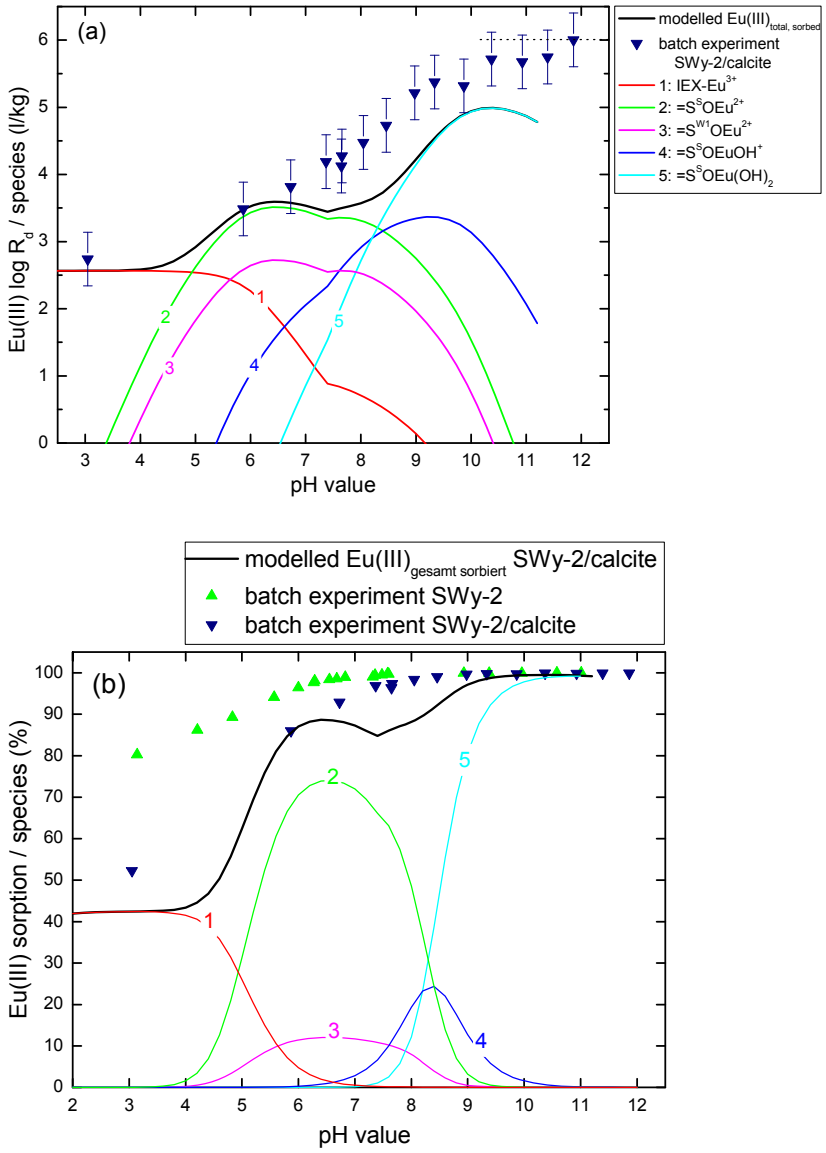

Figure 3-10: Eu(III)sorption on mixture of Na-rich montmorillonite (SWy-2) with calcite (80 : 20 wt.%) shown as (a) log R_d and (b) in Experimental conditions: [Eu(III)] = 1·10-7 mol/l, S/L = 2 g/l, I = 0,1 mol/l NaClO4. (IEX = ion exchange, S = smectite, S = ***strong sites***, W1 = ***weak sites***). The dotted line corresponds to the upper limit log R_d due to the detection limit of the ICP-MS for Eu(III analysis.

The lower sorption on SWy-2 / calcite compared to pure SWy-2 at pH< 6.5 comes from the lower content of the clay mineral and hence, a lower cation exchange capacity. Furthermore, the calcite is dissolved at lower pH and hence, the Ca^{2+} ions can compete with the Eu(III) for sorption sites. Because no other compounds than montmorillonite and calcite are present in the system and that the course of the sorption is similar to that of COx, one can conclude that other mineral phases as components of the natural clay rock have no significant contribution to the Eu(III) sorption. The model calculations by considering the ternary clay / Eu^{3+} / carbonate surface complexes moreover exhibit that the data of the batch experiments can be described much better in the near neutral pH range (s. Figure 3-11). The $\equiv S^{S}OEuCO_3$ surface complex emerges at pH ~5.5 and predominates from pH 6.5 to 8.5 over the surface species $\equiv S^{S}OEuOH^{+}$ that normally prevails in the absence of carbonate. At high pH values the surface complex $\equiv S^{S}OEu(OH)_2$ is the dominating species. The Eu(III) hydroxocarbonate complex is not relevant in this system over the whole pH range.

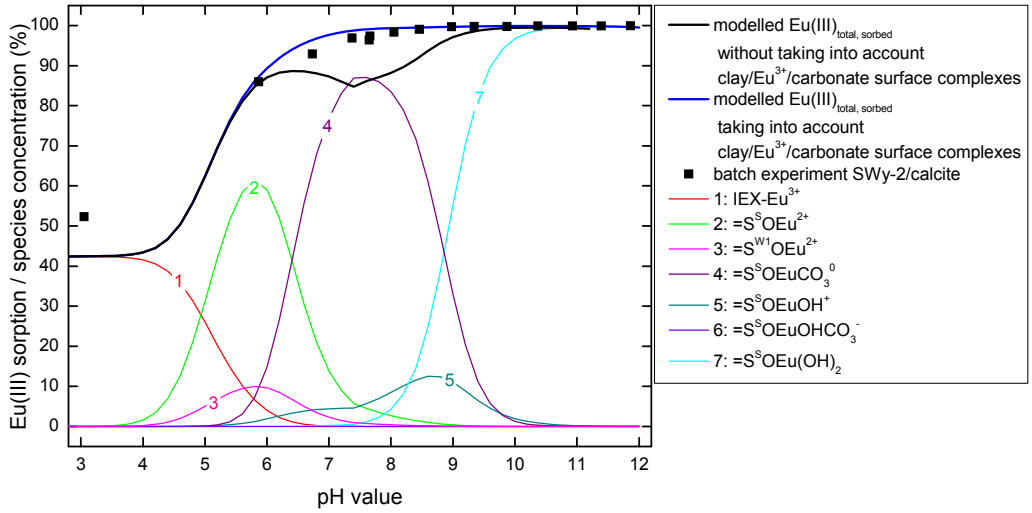

Figure 3-11: Eu(III)sorption on mixture of Na-rich montmorillonite (SWy-2) with calcite (80 : 20 wt.%) and modelling as a function of the pH value regarding (blue line) and disregarding (black line) ternary clay/Eu3+/carbonate surface complexes shown in %. Experimental conditions: [Eu(III)] = 1·10-7 mol/l, S/L = 2 g/l, I = 0,1 mol/l NaClO4. (IEX = ion exchange, S = smectite, S = ***strong sites***, W1 = ***weak sites***).

TRLFS studies of Cm(III) sorbed on clay / calcite mixture

To elucidate the sorption of trivalent actinides on a molecular level, TRLFS measurements were performed parallel to the batch experiments. Unfortunately, the Cm(III) and Eu(III) fluorescence emission spectra in OPA and COx suspension could not be evaluated, because either they were extreme noisy or the had very broad undifferentiated peaks. For that, spectroscopic studies have been made with Cm(III) in Na-SWy-2 / calcite suspension. The spectra of the Cm(III) in such suspensions show the typical red shift with increasing pH value (s. Figure 3-12).

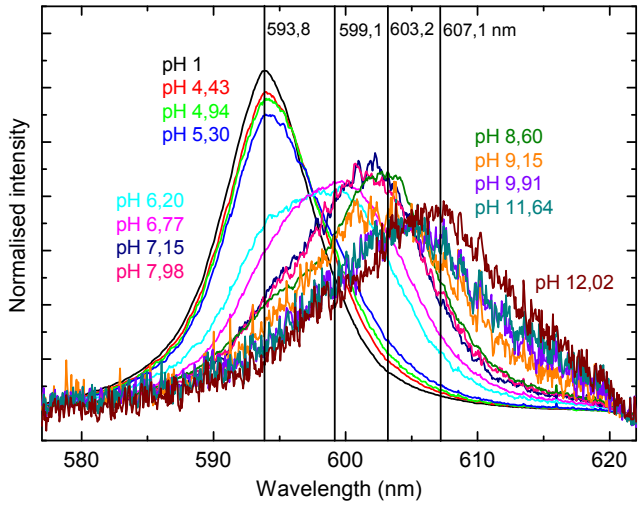

Figure 3-12: Cm(III) fluorescence emission spectra in suspension of Na-rich montmorillonite (SWy-2) and calcite mixtures (80 : 20 wt.-%) as a function of pH normalised to identical peak area. Experimental conditions: [Cm(III)] = 2·10-7 mol/l, S/L = 0,3 g/l, I = 0,1 mol/l NaClO4.

The spectra are identical with the pure spectra of the Cm(III) aquo ion with a peak maximum at 593.8 nm below pH values of 4. At this conditions only free Cm^{3+} or outer-sphere sorbed Cm(III) aquo ions occur. The peak maximum shifts towards higher wavelengths with increasing pH from 4 to 12. The same shift was observed in experiments of Cm(III) and smectites with peak maxima at 559.1, 603.2, 607.1 nm [Rabung et al., 2005] and 598.8 and 603.3 nm [Stumpf et al., 2001]. This could be a indication that Cm(III) sorption mainly takes place on the clay and that the calcite does not or only partially contribute to the sorption. The same hint is obtained from the fluorescence life-time of these peaks. However, the intensities of the signals are very low due to stray light effects and quench effects of the solid particles. These effects impede the evaluation of the fluorescence life-time. Nevertheless, the life-times were shorter than 200 µs in all measurements and this is similar to the life-times of species inner-spherically bound on the clay as surface complexes. The results from the measurement of Cm(III) sorption in the clay / calcite system significantly differ from measurements in the pure calcite system [Marques, 2006; Stumpf & Fanghänel, 2002]. In these experiments two peaks were found with peak maxima at 607.5 and 618.0 nm with life-times of 314±6 µs and 1302±75 µs, indicating that two sorption species occur. The shorter lifetime represents a inner-sphere surface complex of Cm(III), whereas the longer life-time is due to a emplacement of Cm(III) into the calcite crystal.

In Figure 3-13 the spectra of Cm(III) in the SWy-2/calcite suspension and pure calcite suspension (from [Stumpf & Fanghänel, 2002]) are faced at two different contact times (48 h, and 8 as well as 6 months). The spectra clearly show that the peak of the embedded Cm(III) species increases with time whereas the contribution of the inner-sphere surface complex is reduced. In the SWy-2/calcite suspension such a peak with maximum around 618 nm and a

very long fluorescence life-time was never observed even after very long contact times. From these results we conclude that the Cm(III) is mainly sorbed by the clay only. This is additionally proved by the higher fluorescence intensities in SWy-2/calcite suspension in contrast to the pure calcite suspension.

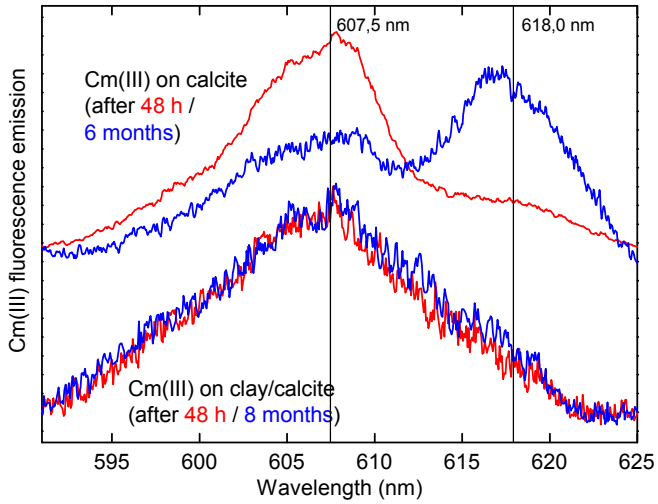

Figure 3-13: Cm(III) fluorescence emission spectra of $[Cm^{3+}] = 8.9 \cdot 10^{-8}$ mol/l in aqueous calcite suspension (pH ~8, S/L = 1 g/l, I = 0.1 mol/l NaClO4 according to (Stumpf and Fanghänel, 2002)) and of $[Cm^{3+}] = 2 \cdot 10^{-7}$ mol/l in clay / calcite suspension (pH 12.02, S/L = 0.3 g/l, I = 0.1 mol/l NaClO4; along the lines of the Cm(III) sorption complex 3 in (Rabung et al., 2005)) after contact times of 48 h and several months.

3.3 Conclusions from the sorption studies with trivalent actinides

All results from numerical modelling of the batch experiments as well as the spectroscopic measurements indicate that the sorption of Cm(III) and Eu(III) on the heterogeneous composed clay rocks OPA and COx is caused by the clay minerals alone. Other mineral phases in the OPA and COx like calcite or quartz are obviously not relevant under the conditions of the experiments. This is also the consequence of the low specific surface of the latter mineral-phases. SWy-2 has a specific surface of 43 m^2/g, whereas the calcite in the clay/calcite mixture possessed specific surface of only 0.77 m^2/g. This results in a very low number of bindings sites that corresponds to only 2.7 % of all binding sites available in the same mass of montmorillonite.

The distribution of surface species of Cm(III) and SWy-2/calcite based on the evaluation of TRLFS results are shown in Figure 3-14. There is a good agreement to the numerical modelling of the surface complexes considering ternary clay/Eu(III)/carbonate surface complexes exhibited in Figure 3-11. Cm(III) species 1 corresponds to the sum of $\equiv S^{S}OEu^{2+}$ and $\equiv S^{W1}OEu^{2+}$. Spezies 2 is equal to the sum of $\equiv S^{S}OEuOH^{+}$ and $\equiv S^{S}OEuCO_3$, which could not differentiated in the spectra due to bad quality of the spectra.

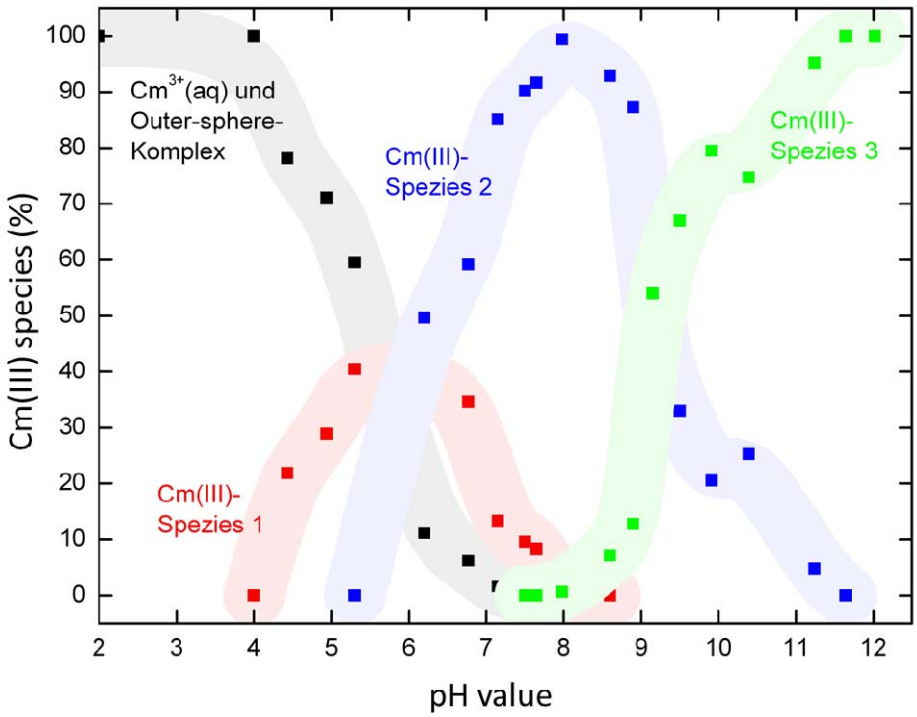

Figure 3-14: Distribution of surface species of Cm(III) on a mixture of Na-rich montmorillonite (SWy-2) and calcite (80 : 20 wt.-%). Experimental conditions: [Cm(III)] = 2·10-7 mol/l, S/L = 0.3 g/l, I = 0.1 mol/l NaClO4. (More details in Hartmann 2010).

The results of the batch experiments, numerical modelling and TRLFS studies show

- the dominance of clay minerals for the retention of trivalent lanthanides and actinides in natural clay rock,
- the transferability of available mechanistic sorption data to the description of Ln(III)/An(III) speciation in heterogeneous natural systems, and
- the relevance of ternary carbonate surface complexes for the retention of trivalent lanthanides/actinides. A reliable prediction in the frame of safety assessment of repositories by geochemical modelling has to regard such species.

3.4 Sorption of pentavalent neptunium and plutonium on OPA and COx

As mentioned in the former chapters, numerous studies have been performed clearly demonstrating that transport in these argillaceous rocks is controlled by molecular diffusion. However, only few studies have been performed on the sorption and redox behaviour of neptunium (Np), and plutonium (Pu) in natural clay rocks like OPA and COx. A few batch and diffusion experiments of Np(V) on OPA [Wu et al., 2009], Pu(IV) on COx [Latrille et al., 2006] has been performed. Furthermore, Wu et al. studied Np sorption in OPA clay rocks with a low solid to liquid ratio (S/L) and performed only short kinetic experiments.
The aim of this study is to characterize the retention of Np, Pu on the two selected clay rocks OPA and COx taking into consideration the redox processes. Since the distribution coefficients (K_d) for the sorption of actinide on the host rock of a nuclear waste repository are important parameters for diffusion and transport modelling. The K_d values for the sorption of actinides on OPA/COx are determined directly by batch experiments on crushed material. The objective at the end of the project is to compare this K_d value with the value derived from the in-diffusion experiments.

3.4.1 Materials and Methods

Actinides

For all sorption experiments, stock solutions of plutonium and neptunium in the pentavalent oxidation state are used. The pentavalent oxidation state of Pu(V) and Np(V)were obtained by potentiostatic electrolysis and its purity was verified by UV-Vis spectroscopy [Cohen, 1961]. The actinides concentration is determined by liquid scintillation counting (LSC).

Opalinus Clay (OPA)

For the batch type sorption studies Opalinius Clay mineral (OPA) is crushed, sieved (< 500 µm) and freeze dried under atmospheric conditions. The anaerobic OPA crushed powder is prepared under Ar atmosphere (inert glove box) from the OPA bore core BHE-24-2 (Mont Terri) [Wu et al., 2009; Van Loon et al., 2005]. The cation exchange capacity determined by the COHEX method is 12.93 ± 0.04 meq/100g.

Callovo Oxfordian Clay (COx)

The Callovo Oxfordian argillites come from boreholes (EST 25691) located on the site of the underground laboratory operated by Andra at Bure (Meuse/Haute Marne, France). A complete description of the core sample drilling and conditioning procedures is available elsewhere

[Gaucher et al., 2004]. The sample is grounded and sieved at <500 μm in the absence of oxygen, under Ar atmosphere, in order to prevent any oxidation of redox sensitive materials such as, for example, pyrite, organic matter, adsorbed Fe(II) and iodide. The cation exchange capacity determined by the COHEX method is 12.02 ± 0.10 meq/100g.

Batch experiments

All sorption experiments are conducted according to batch procedures described below at initial actinides concentrations in the range of 3.0×10^{-4} - 1.0×10^{-8} M. The batch experiments are carried out in Zinsser vials (20 mL, material: HDPE) over a period up to about 1 year at room temperature. The solid to liquid ratio (S/L) of 10, 20, 50, 200 g/L of clay rocks are chosen for the experiments, preconditioned with pore water in 0.1 M NaCl by shaking continuously the suspension for 10-15 days to achieve equilibrium pH of 7.2 for COx and 7.6 for OPA. After mixing Pu(V), Np(V) solutions with the preconditioned clay rocks suspension, the pH values were readjusted by adding 0.1 M HCl or 0.1 M NaOH. For characterisation of the suspension the solid and liquid phases were separated by ultrafiltration using 10 kD filters (5000 rpm for 1 h). The supernatants were analysed in order to determine the content of free actinides in the liquid phase by liquid scintillation counting (LSC). The sorbed amount of Np and Pu (dried clay rocks, solid phase) was also measured for some samples by XAFS and XPS. For all sorption experiments, about 10 % adsorption of RN on the Zinsser vials walls depending on S/L ratio of the clay rocks and radionuclide has been taken into consideration for evaluating the K_d values.

UV-Vis absorption spectroscopy (UV-Vis)

The oxidation states of Np(V), Pu(V) in the stock and sample solutions are confirmed by UV-Vis spectroscopy with a high-resolution UV-Vis/NIR spectrometer Cary 5 (Varian). The samples are measured in 1 cm inert-gas quartz cuvettes (Hellma) with tight screw tops, or in polystyrene semi-micro cuvettes (Brandt). UV-Vis/NIR spectra are taken from 800 nm to 1200 nm for Np, 400 nm to 900 nm for Pu.

X-ray photoelectron spectroscopy (XPS)

Clay suspensions and wet pastes were prepared for XPS analysis by drying small portions on an indium foil in an anoxic glove box. The samples were moved into the XP spectrometer (PHI model 5600ci) without air contact by means of a vacuum transfer vessel. Monochromatic Al K_α x-rays were used for excitation in conjunction with an electron flood gun for sample surface neutralization. Atomic concentrations were calculated from the areas of elemental lines of survey spectra. Narrow scans of elemental lines were recorded for determination of chemical shifts and spectral features.

X-ray absorption fine structure spectroscopy (XAFS)

For the XAFS measurements, filtrate solutions and suspension with clay were filled into 400 µl capped PE vials and mounted in a special air tight sample holder, which is connected to an Ar supply line at the experimental station to keep the samples under oxygen-free conditions during XAFS measurements. The measurements were performed at the INE beam line using a new inert gas sample cell design [Brendebach et al, 2009] for redox sensitive radionuclides. The spectra were calibrated against the first derivative X-ray absorption near edge structure (XANES) spectrum of a Zr foil, defining the energy of the first inflection point as E(Zr 1s) = 17998.0 eV. All Pu L3, Np L3 XAFS spectra are measured in standard fluorescence yield detection mode.

Capillary electrophoresis coupled with ICP-MS (CE-ICP-MS)

A commercial Beckman Coulter P/ACE MDQ capillary electrophoresis system (Fullerton, U.S.A.) was coupled to an inductively coupled plasma sector field mass spectrometer (Element XR, Thermo Fisher Scientific, Bremen, and Germany). Conventional fused silica capillaries (Beckman Coulter, Fullerton, U.S.A.) with an internal diameter of 50 µm and lengths of 74 cm were used for the separations. A commercial parallel path micro-nebulizer (Mira Mist CE, Burgener, Canada) with a borosilicate spray chamber (Mini glass chamber, Burgener, Canada) interfaces both apparatuses. To generate an aerosol a makeup liquid (2 % HNO_3, 10 % ethanol, 1 ppb Rh as internal standard) was introduced by a syringe pump at a nominal flow rate of 8 µL min^{-1}. For the measurement, separated supernatant solutions from clay suspension were taken in 1 mL glass vials under inert atmosphere. However the fast injection of the sample into the CE has been performed under air atmosphere. Therefore, the effect of air cannot be excluded from the experiments. Separations were performed at -20 kV and at a constant pressure of 0.8 psi (to avoid clogging) and they were completed within 15-18 min.

Liquid-liquid extraction

The oxidation state of Np and Pu at low concentration after the separation by centrifugation using 10 KD ultrafilter under anaerobic conditions and supernatant solution was analyzed by liquid-liquid extraction using 1-phenyl-3-methyl-4-benzoylpyrazolone-5 (PMBP) [Nitsche et al., 1994] and 2-thenoyltrifluoroacetone (TTA) (Merck, Germany) as extracting agents. A 0.6 mL portion of the supernatant filtrate solution was taken together with 0.2 mL 2 M HCl and 0.8 mL 0.025 M PMBP (in Xylene) and 0.5 M TTA (in Toluene) solutions and then vigorously shaken for 10 min. The phases were separated by centrifugation for 10 min (5000 rpm) and aliquots of each phase were taken for radiometric analysis.

Sorption modelling

Model calculations are performed using the computer program ECOSAT 4.8 (acronym for Equilibrium Calculation of Speciation and Transport [Keizer and van Riemsdijk, 1999]). Bradbury and Baeyens developed a 2-site Protolysis Non Electrostatic Surface Complexation

and Cation Exchange (2SPNE SC/CE) model for the description of surface complexation and cation exchange reactions [Bradbury&Bayens, 2005, 2009]. For the calculations, carbonate concentrations were assumed to be in equilibrium with calcite in a closed system with no gas phase.

3.4.2 Results and discussions

The fraction of actinides sorbed and the distribution coefficient were calculated by using the following equations:

$$Sorption = 1 - \frac{[An]_{eq}}{[An]_0} \times 100 \quad (\%) \qquad (1)$$

$$K_d = \frac{x}{m} \times \frac{1}{[An]_{eq}} \quad (\mathrm{mL/g}) \qquad (2),$$

where $[An]_{eq}$ and $[An]_0$ (moL/L) are the equilibrium and initial concentrations of actinides in solution, respectively; x (mol) is the amount of sorbate; m (g) is the mass of sorbent.
The batch experiments are conducted as a function of the solid-to-liquid ratio in the range of 10–200 g/L at 0.1 M NaCl under 1% CO_2 in a glove box (<1 ppm O_2).

Sorption of neptunium on clay rocks
The sorption of Np(V) increased proportionally to the solid-to-liquid ratio (see in Figure 3-15). The highest sorption is 87±6 % at 200 g/L. This increase in the sorption is directly correlated to an increase of the surface site concentration. The results agree favorably well with previous studies [Wu et al., 2009; Amayri et al., 2011; Fröhlich et al., 2011]. For a total Np(V) concentration of 3.0×10^{-7} M, the K_d values 36± 15 L/kg at pH 7.6 for OPA and 27± 8 L/kg at pH 7.2 for COx is obtained, which are more or less independent of the solid-to-liquid ratios from 10–200 g/L (see in Table 3-7 and Table 3-8). However, the amount of sorbed Np at S/L = 10 is significant smaller after 6 weeks interaction time compared to 4 months interaction time. This can be a hint that a limited number of various sites on the clay surface occurs that a) differently bound Np(V) on the surface and mirror different kinetic modes, or b) a fast kinetic of the Np(V) sorption is superimposed by a slow kinetic of a reduction reaction from Np(V) to Np(IV). This limit of sites is compensated not before 50 g/L of clay, as always, the mechanism looks like.

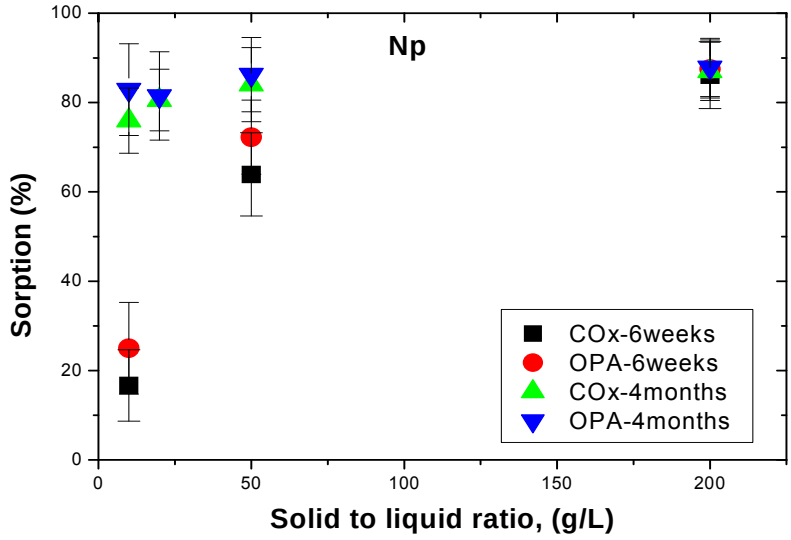

Figure 3-15: Sorption of neptunium on OPA/COx in pore water as a function of solid to liquid ratio (S/L), I = 0.1 M NaCl, [Np(V)] = $3x10^{-7}$ M, contact time= 6 weeks and 4 months.

Table 3-7: Kd values and percentage sorption of Np and Pu on OPA (pH 7.6) in Pore water at $3x10^{-7}$ M.

Solid to liquid ratio, [g/L]	**Kd [L/kg] & sorption [%] of Np**	**Kd [L/kg] & sorption [%] of Pu**
10	33.0/25±3	517/84±3
20	52.0/36±6	303/86±6
50	30.0/70±7	146/88±5
200	32.0/87±5	42.6/89±6

Table 3-8: Kd values and percentage sorption of Np and Pu on COx (pH 7.2) in pore water at $3x10^{-7}$ M.

Solid to liquid ratio, [g/L]	**Kd [L/kg] & sorption [%] of Np**	**Kd [L/kg] & sorption [%] of Pu**
10	20.0/17±4	242/71±6
20	35.0/33±5	367/88±3
50	32.0/64±8	166/89±4
200	30.0/86±4	68.0/93±5

The sorption of Np onto clay rocks (COx, OPA) has also been investigated as a function of metal concentration in the concentration range between 3.10^{-8} mol/L and 3.10^{-7} mol/L. As can be seen in Figure 3-16 for Np(V), there is almost constant K_d values in this concentration

range. The lowest sorption of Np is about 17 % at S/L ratio of 10; where as 87 %, the highest Np sorption has been found at S/L ratio of 200 g/L after 6 weeks contact time. There is a linear dependency between the total sorption and the liquid to surface area ratio (S/L range from 10-200 g/L) under these conditions showing the effect of available sorption sites.

Table 3-7 and Table 3-8 show the K_d values and the percentage of Np sorbed on COx and OPA in pore water at different S/L and at reaction time of 6 weeks. The influence of the contact time on the sorption of Pu/Np has been investigated for the solutions with the different concentrations, under inert atmosphere. A strong influence has been found between the sorption rates between 1 week and 4 months after the contact of clay rocks with both actinides (10 to 40 % of higher sorption after 4 months depending on the actinides).

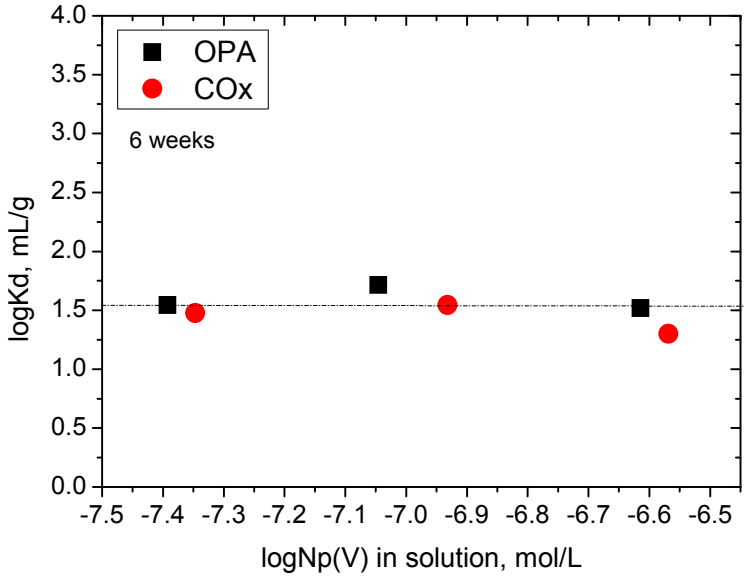

Figure 3-16: Distribution coefficient (Kd) for the sorption of Np on OPA/COx in pore water as a function of neptunium concentration, I= 0.1 M NaCl, [Np(V)] = $3x10^{-7}$ mol/L, contact time= 6 weeks.

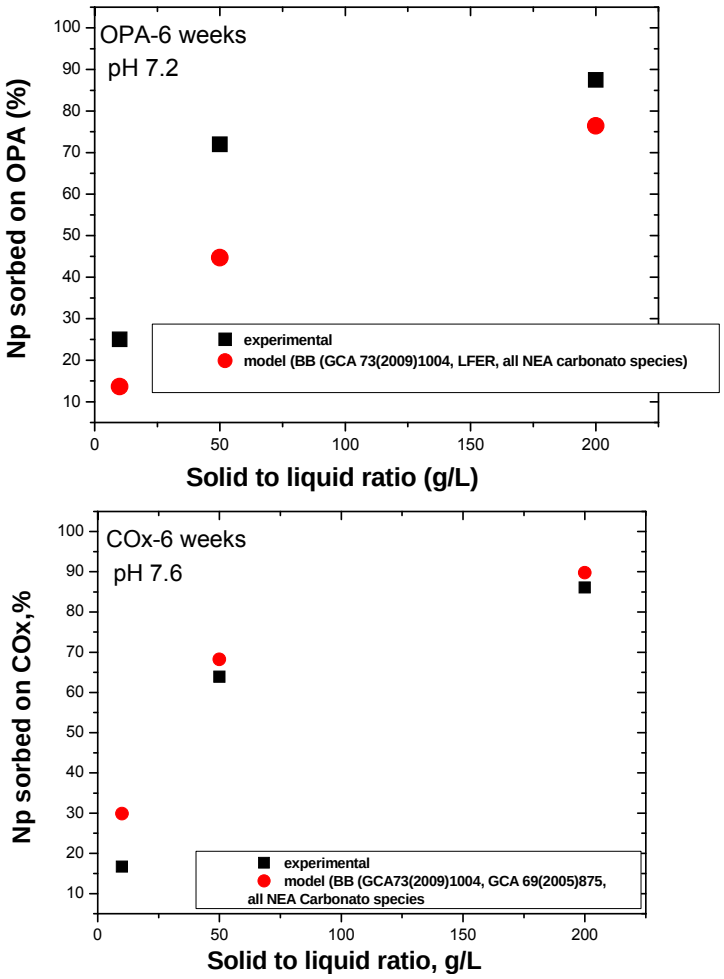

Figure 3-17: Comparison of experimental and modelling sorption studies of Np on OPA (top) and COx (bottom) clay minerals as a function of solid to liquid ratio (S/L), pH 7.6 and 7,2, .I= 0.1 M NaCl, [Np(V)] = $3x10^{-7}$ mol/L, contact time= 6 weeks.

Sorption modelling

The experimental data of Np sorption on clay has been model by the 2 site protolysis non-electrostatic surface complexation and cation exchange (2SPNE SC/CE) sorption model from [Bradbury&Baeyens, 2009]. For the species in aqueous solution – mainly hydrolysis and carbonate species - the NEA data have been taken. As solid phase the clay mineral illite has been taken. The following constants for the surface complexation of strong sites on the illite have been chosen to be

$\log K_{SC} = -2.0^{a}$ and -1.48^{b}: $\equiv S_SOH + NpO_2^+ = \equiv S_SONpO_2 + H^+$

$\log K_{SC} = -10.3^{a}$ and -11.68^{b}: $\equiv S_SOH + NpO_2^+ = \equiv S_SONpO_2OH + 2H^+$

a: value directly depicted from [Bradbury&Baeyens, 2009]; b: calculated by linear free relationship (LFER) for illite in [Bradbury&Baeyens, 2009]

The sorption model calculations for Np with clay rocks OPA/COx are comparable with batch experimental data in pore water system (Figure 3-17). For the OPA the deviation is higher than for the COx. The deviation might be explained by the uncertainty in the redox behaviour of Np(V) on the surface. In the modelling 100% Np(V) is assumed, but after 6 weeks some Np(IV) has already been formed. On the other hand, if we regard the Np(IV)/Np(V) couple and pure sorption, the results are underestimated; if we include surface precipitation, the experimental data are overestimated. However, the results are due to the high uncertainties not so bad, but the modelling needs further detailed treatment.

Sorption of plutonium on clay rocks

The interaction of pentavalent plutonium with COx and OPA clay has been studied and shows that more than 85 % of the plutonium is retained on both clay mineral surfaces after 6 weeks contact time (see Figure 3-18). From spectroscopic characterisations we know that the Pu(V) is quickly reduced to Pu(IV). About 80-90% of the Pu is retained on OPA at S/L ratios from 20 to 200. However, the amount of sorbed Pu on COx at S/L ratio of 10 is with 72% lower than for OPA. At higher S/L ratios the sorbed amount of 88-93% on COx is similar to the values of OPA for a 6 weeks contact time.
A strong sorption of Pu(IV) on Callovo oxfordian was also observed by [Latrille et al., 2006] and their K_d values are comparable with our results (see Table 3-10), although their values are a little larger. The interactions between the Pu and mineral surfaces are complex because of its redox behavior. The sorption behaviour of PuO_2^+ is significantly influenced by redox conditions occurring in solution and on the mineral surfaces. PuO_2^+ can easily be reduced in contact with mineral surfaces and sorbed on mineral surfaces as in the form of Pu(IV) [Keeney-Kennicutt & Morse, 1984, 1985]. If it is really a sorption is unclear, because the Pu(IV) concentration is controlled by its solubility in solution at concentrations used for the experiments. A surface precipitation of Pu(IV) as a hydroxide or hydrated oxide cannot be excluded in our experiment, because the total concentration of Pu slightly exceeds the solubility of Pu(IV). It has to be emphasised, that the K_d concept might be not valid for tetravalent Pu experiments and should better be described by regarding its solubility. Although the K_d concept might not be valid for Pu(IV), here, anyhow the K_d values are given in this work to render results comparable with literature values. The experiment in [Latrille et al., 2006] has been performed below the solubility limit and the authors have proved that no surface precipitation occurred. So their K_d values are valid in the sense of the K_d concept. This might be the reason for their slightly higher sorption data compared to our values.

Table 3-9: logKd values for plutonium on Callovo–Oxfordian clay rock

Experimental conditions	logKd [mL/g] This work	logKd [mL/g] [Latrille et al, 2006]
[^{242}Pu(V)] = 3x10^{-7} mol/L, S/L=10-200 g/L, pore water, pH 7.2. Reaction period: 42 days	1.85-2.45	
[^{238}Pu(IV)] = 3x10^{-10} mol/L and 3x10^{-11} mol/L, S/L=20 g/L, Reference water, pH 7.0-7.8, Reaction period: 72 days		2.50-3.50

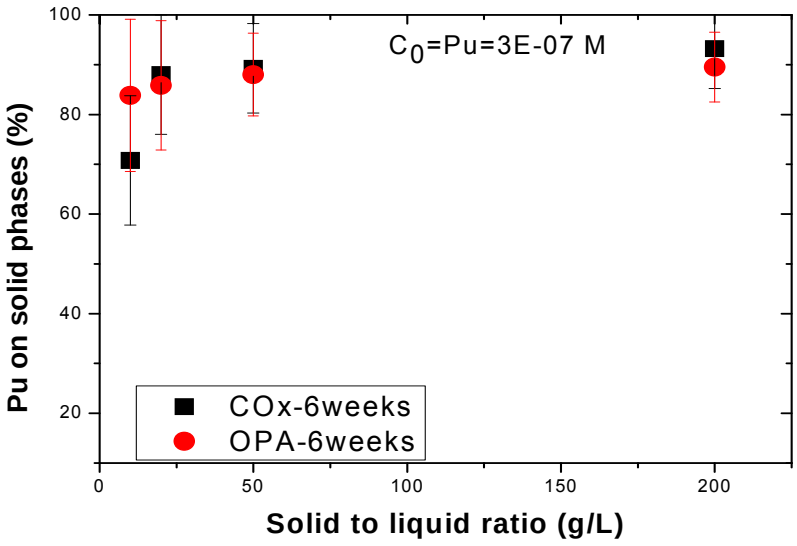

Figure 3-18: Interaction of plutonium with OPA and COx in pore water as a function of solid to liquid ratio (S/L), I= 0.1 M NaCl, [Pu(V)] = 3E-07 M, contact time= 6 weeks

To check if the Pu sorption experiments are influenced by the solubility of Pu(IV) we performed a one at Pu concentrations of about 5x10^{-9} M ^{238}Pu. The Pu sorption pH edge was measured at 20°C in OPA porewater. All experiments were performed in a glove box under argon atmosphere. The pH was adjusted by adding analytical grade KOH or HCI. The experiments were performed in high density polyethylene (HDPE) 20 ml Zinsser bottles (Zinsser Analytics, FrankfurtlM.) with a solid/solution ratio of 2 g/L. At the end of the experiment the solid was separated from solution by centrifugation (10 min at 16000 rpm). 5 ml of the supernatant were acidified (2% HN03) and analyzed for Pu by LSC. Concentrations of AI, Si, Mg and K were measured on a Plasma 400 ICP-AES (Perkin-Elmer).

We monitored the concentration of Pu in solution in batch experiments in pH range from 4.75 to 10.23 over one year. Above pH 6 a “steady state concentration” was reached after 12 hours.

As a function of time no further evolution of the Pu concentration was observed. In seven batches we observed a significant drop of the Pu concentration already after one hour of reaction. The post-mortem XRD analysis of these clays with help of Rietfeld refinement method revealed in these samples an unusual high amount of pyrite (~ 40 %) compared to the other samples (~ 1 %). In the "normal samples" the Eh decreased from the initial value of ~ 350 mV to values of around ~ 200 - 150 mV after 12 hours and in the samples rich in pyrite down to a value of ~ 70 mV after one hour. Starting from pH 4.75 the Pu concentration in solution decreases with increasing pH and reaches a sorption maximum at pH 7.2 (Figure 3-19). At pH values > 7.2 the Pu concentration in solution increases again. According to the results of the batch sorption data a strong Pu sorption under the experimental conditions of the diffusion experiments is expected. Some samples were kept in the glove box and resampled after one year. The Pu concentrations for the samples at pH > 7.2 after one year were close to the detection limit of Pu in our system (detection limit in our experimental set-up 1 x 10^{-11} mol/L). The pH showed only slight changes and the Eh remained within the error of the measurement (± 50 mV).

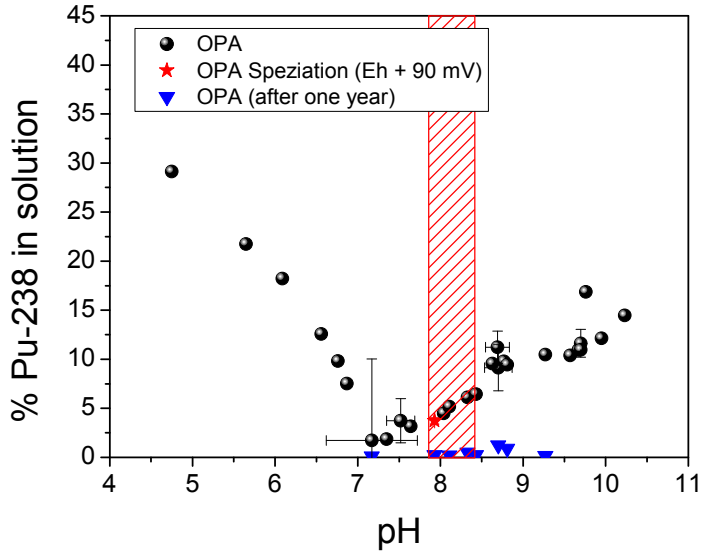

Figure 3-19: Sorption experiments of Pu-238 on Opalinus Clay. The filled pattern indicates the pH region of the diffusion experiments.

We measured the evolution of the Pu speciation as a function reaction time in the OPA supernatant porewater and on the solids at pH ~ 8. In the supernatant solution the Pu is to 87 % Pu(V/VI) and 13 % Pu(IV). To determine the oxidation state of the Pu sorbed on the clay sample we washed clay with concentrated HNO3. The Pu removed from the clay after 24 hours consists of Pu(IV) 80 % and Pu(V/VI) 20 %. After one year all the Pu was sorbed on the clay and the oxidation state was found to be IV.

Figure 3-20 illustrates the changes of the logK_d values with the contact time in comparison to literature values from [Latrille et al., 2006], [Lujaniene et al., 2007], and [Zuo et al., 2010].

The figure demonstrates again that the K_d value for the Pu(IV) increases of about one order of magnitude during a reaction time of one year. The initial Pu concentrations of all experiments shown in the graph were below the solubility and precipitation of Pu is not expected: this work [Pu] = $5x10^{-9}$ M; [Latrille et al., 2006] [Pu] = $3x10^{-10}$ M; [Lujaniene et al., 2007] [Pu] = $1x10^{-9}$ M; [Zuo et al., 2010] [Pu] = $1x10^{-11}$ M. However, the log K_d values varies over two order of magnitudes demonstrating that the sorption experiments of Pu cannot easily be interpreted. The experiments demonstrate the need of experiments with pure clay minerals to elucidate first the question, which component of the natural clay is responsible for the sorption. If this question was clarified, then reliable K_d values, or better surface complexation constants for the surface complexation model, can be determined in the pure system and then compared with the natural system.

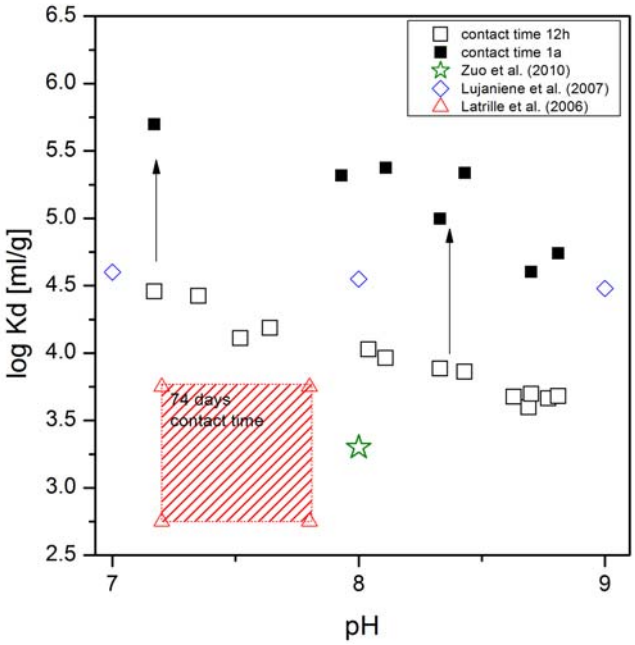

Figure 3-20: Batch sorption data of Pu(IV) sorption on Opalinus clay after 12h contact time and one year contact time showing the increase in Kd values observed. For comparison data on the Callovo-Oxfordian argillite after 74 days contact time [Latrille et al., 2006], on Triassic clay from Šaltiškiai and Chinese shale rock are inserted.

Desorption

Desorption experiments are carried out at pH values 7.2 and 7.6 under the same experimental conditions used in the sorption experiments. The Np and Pu sorbed onto both clay rocks is desorbed in fresh pore water and buffered at the appropriate pH value and shaken continuously. Almost no desorption from both clay rocks is found after contact time of 1 month.

This indicates that the Np, supposable Np(IV), and Pu(IV) ions are strongly bound onto clay rocks and shows chemisorption rather than physisorption. Therefore, the sorption is might be irreversible process. Further, it can be concluded that the inner sphere complexes of Np/Pu on both clay rocks have been expected.

3.5 Influence of humic acid on the An(III) sorption

It could be shown in some studies that organic compounds can be extracted from pore water aor ground water with high pH values [Claret et al., 2002, 2003]. Such high pH values can be generated by contact of ground water with concrete, which is part of the repository´s constructions. In this organic fraction compounds occur which can resemble fulvic and humic acids. Because it is well known that humic acids in solution complex the trivalent actinides very strong, an influence on the sorption, and hence, a mobilisation can not be excluded. Organic compounds fixed in the clay rock play no role concerning the sorption process. To investigate the influence of organic compounds in solution on the Eu(III) sorption on clay rock, batch experiments were performed with Eu(III) and Na-monmorillonit SWy-2 and Aldrich humic acid (AHA), as well as in the system SWy-2 / AHA / Calcite. The results of these studies are compared with results of the Eu(III) sorption investigations without humic acid. In the binary system of mineral phases and humic acid or ternary system mineral phase / humic acid / metal ion the humic acid sorption on the mineral phase depends among other parameters on the pH value of the solution [Křepelová, 2007].

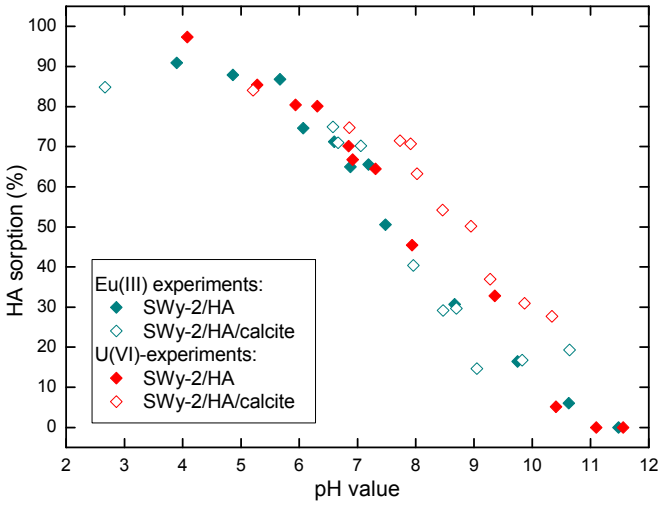

Figure 3-21: Sorption of AHA on SWy-2 as a function of pH in the sorption experiments of Eu(III) and U(VI) (not shown in this report) with AHA (2 g/l SWy-2, 10 mg/l AHA) and with AHA and calcite (1,6 g/l SWy-2, 0,4 g/l calcite, 10 mg/l AHA). [Eu(III)] bzw. [U(VI)] = 1x10-7 mol/L, I = 0,1 mol/L NaClO4.

Figure 3-21 shows the experimental results of the sorption of AHA on clay from various batch sorption experiments.concentration of AHA in solution was determined by measurement of the organic carbon and by UV-Vis spectroscopy. The amount of AHA on the clay decreases with increasing pH value for both systems. This behaviour was also observed in sorption studies with kaolinite [Křepelová, 2007]. This behaviour is based on electrostatic effects, because with increasing pH value the negative surface charge of the clay as well as

the negative charge of AHA increases too. Therefore, the AHA is repelled by the clay surface and the sorption decreases. Nevertheless, part of th AHA is sorbed despite the negative charge and hence, other sorption mechanism must occur.

This could be (i) surface complexation, (ii) ion exchange between OH_2^+ or OH^- groups of the clay surface and anionic groups of the AHA according to the following reaction:

$\equiv OH_2^+ + {}^-OOC\text{-}HA = \equiv OOC\text{-}HA + H_2O$

or

$\equiv OH^- + {}^-OOC\text{-}HA = \equiv OOC\text{-}HA + OH^-$.

Also formation of bridges by metal cations (Al^{3+}, Ca^{2+}, Mg^{2+}, Fe^{2+}) between the negative charge of the clay and the AHA are possible [Schmeide et al., 2000].

The sorption of Eu(III) in presence of HA on Na-montmorillonite is shown in Figure 3-22. Additionally, the sorption of Eu(III) on the pure SWy-2 and SWy-2/calcite mixture including the corresponding numerical modelling are illustrated. In presence of AHA the sorption of Eu(III) is smaller in comparison to the pure SWy-2 at pH > 6, reaches a minimum with about 70 % at pH ~8.7 and finally increases at higher pH values. The sorption on clay/AHA reaches a maximum of 92 % at high pH values that is somewhat lower than on clay/AHA/calcite. At pH<6 the Eu(III) sorption is higher on clay/HS than on the pure clay mineral.

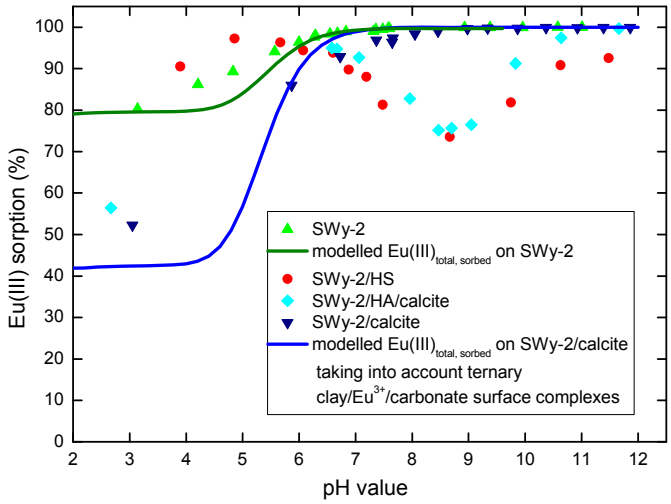

Figure 3-22: Eu(III) sorption on Na-rich montmorillonit (SWy-2) without and with Aldrich humic acid (AHA, 10 mg/l) and/or calcite (Clay : calcite = 80 : 20 wt-%) and numerical modelling of the sorption on SWy-2 (dark green) and SWy-2/calcite by considering ternary clay/Eu3+ carbonate surface complexes (blue) in %. [Eu(III)] = 1x10-7 mol/L, S/L = 2 g/L, I = 0,1 mol/L NaClO4.

The sorption of Eu(III) is strongly influenced even in small amounts of AHA. [Rabung, 1997] has experimentally proved in the system Eu(III)/hematite/HA that the humic acid (HA) bound on the mineral is the species that governs the sorption properties of the material. The HA is

mainly sorbed on the strong sites of the hematite surface [Rabung, 1997; Rabung et al., 1998]. Photo electron spectroscopy (XPS) of Uranyl on kaolinite exhibits that the HA is not sorbed on the mineral as a homogeneous layer, but occurs between the single kaolinite particles [Křepelová, 2007]. Therefore, on the surface of the mineral in the system metal ion/clay/HA many binding sites are still available for the sorption of the metal cation that are not occupied by the HA. Because the sorbed HA provides itself binding sites for the metal ion by forming humate complexes on the surface, the sorption of Eu(III) at lower pH values is higher than in the humic acid-free system.

The decreasing sorption of Eu(III) in presence of AHA in the pH range between 6 and 9 is attibuted by the pH-dependent Desorption of AHA from the mineral surface (s. Figure 3-21). Here, the formation of Eu(III) humate complexes competes between $HA_{surface}$ and $HA_{solution}$. [Fairhurst&Warwick, 1998]. According to Sakuragi et al. (2005), the interaction between the HA and the metal ions is not altered, regardless of sorbing the metal ion on HA in solution or HA sorbed on the mineral surface.

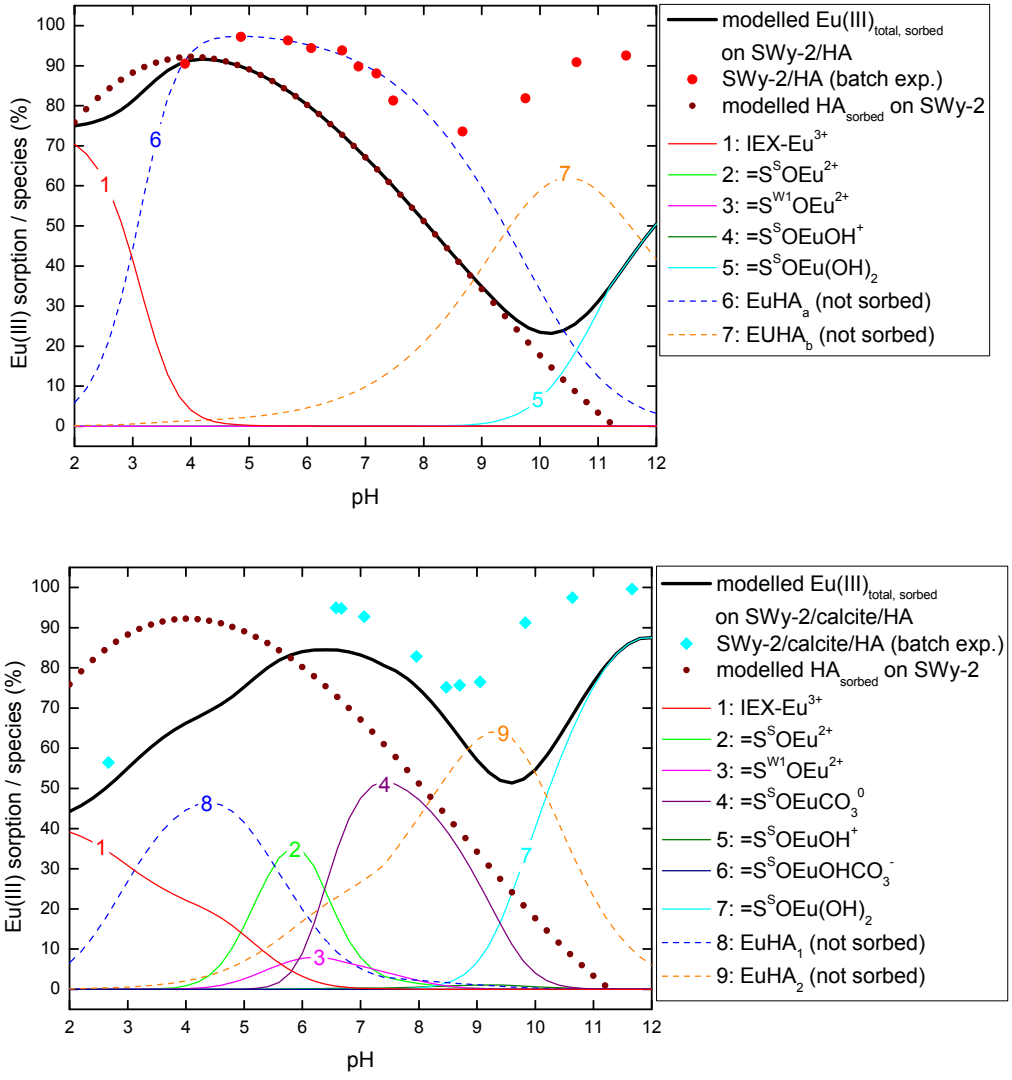

Figure 3-23: Eu(III) sorption on Na-rich Montmorillonite (SWy-2) with humic acid (10 mg/l) and (b) on Na-rich Montmorillonite (SWy-2) with humic acid (10 mg/l) and calcite (clay : calcite = 80 : 20 wt.%) as well as model-

ling as a function of pH value and taking into account ternary clay/Eu^{3+}/carbonate surface complexes plotted in %. The graph includes the experimental data of the HA sorption on SWy-2. Species 1 bis 5 (a) and 7 (b) are Eu(III) surface complexes; species 8 and 9 are the Eu(III) humate complexes in solution. Experimental conditions: [Eu(III)] = 1·10-7 mol/l, S/L = 2 g/l, I = 0,1 mol/l $NaClO_4$. (IEX = Ion exchange; (= CAC), S = Smectite, S = ***strong sites***, W1 = ***weak sites***).

The Eu(III) sorption in the SWy-2/HA system without (a) and in presence of calcite (b) and the HA sorption on SWy-2 as well as numerical meodelling based on the NICA-Donnan model are presented in Figure 3-23. It must be emphasised that the sorption of the HA is not regarded by the model. Therefore, the experimentell derived HA sorption on clay (Figure 3-21) is equilised to the sorption of Eu(III) humate complexes on clay in both systems, clay/HA and clay/HA/calcite. The total Eu(III) sorption results from the sum of calculated sorption of inorganic Eu(III) species on clay and the experimentically derived sorption of Eu(III) humate complexes.

In both systems the Eu(III) fraction sorbed by ion exchange dominates at pH < 4. The numerical modelling exhibits that a sorbed Eu(III) humate complex governs the sorption between 4 < pH < 8.5 and suppresses other complexation reactions. In the clay/HA/calcite system significant fractions of surface complexes on clay (outer-sphere species, $\equiv S^{S/W1}OEu^{2+}$, $\equiv S^{S}OEuCO_3$, and $\equiv S^{S}OEu(OH)_2$) occur beside the Eu(III) humate surface species and other solution species.

The minimum of the pH course can be modelled in principle, but it is shifted to higher pH values of around 10. The sorption is under-estimated by the modelling over the total pH range, especially at pH 8.5 and higher (in the clay/HA system upt to 60 %, in the clay/HA/calcite system up to 40 %). At higher pH values the increasing sorption is caused by the species $\equiv S^{S}OEu(OH)_2$, which is also undervalued. Anyhow, the diffence between sorption of Eu(III) in presence of HA and in the free-HA system is rather small (at pH12 ~8% lower, Figure 3-22). One can assume that the present HA affects the sorption Eu(III) only weak at higher pH values. The numerical modelling overestimates the fraction of the $EuHA_b$ complex in solution (Figure 3-23).

From other studies concerning the modelling of humate complexation by the NICA-Donnan model with parameters from Milne et al, (2001, 2003) it is known that the humate complexes are significantly overestimated [Geckeis, 2010]. This is obvious in numerical modelling of Cm(III)/Am(III) in Gorleben groundwater, where only the humate complexe are predicted at higher pH values. Instead of that, in experimental characterisation of these groundwaters the carbonate complexes are the dominating species. Anyway, the humate complexes can reduce the retention of trivalent actinide in the clay system. The available set of parameter in the NICA-Donnan model have to be revised for Ln(III) and An(III) cations.

However, the relevance of humic acid-type organic compounds occurring in porewater have to be checked, especially the question whether actinide organic complexes can be a mobile species by diffusing through the clay matrix.

3.6 Outersphere complexation of trivalent actinides

The permanent negative charge of most of the clay mineral, resulting from isomorphic substitution of higher chaged to lower charged cations in the crystal lattice, is compensated by cations from the surrounding solution, which are absorbed predominantly by electrostatic attraction to the basal planes of clay minerals and they form so-called outer-sphere complexes. In the outer-sphere complexation of the cation the hydration sphere remains fully intact. Electrostatically bound cations can exchange with other cations in the supernatant solution. This happens through reactions that occur rapidly, stoichiometrically and reversibly (Bolt et al., 1976; Grim, 1953; van Olphen, 1963). In general, the sorption as a result of such cation exchange reactions is independent of the pH-value, except when, for example, competing cations are released by dissolution of the clay minerals due to changes in the pH. The cation exchange processes dominate the interactions between cations and clay minerals at low pH values (<5) and low ionic strengths.

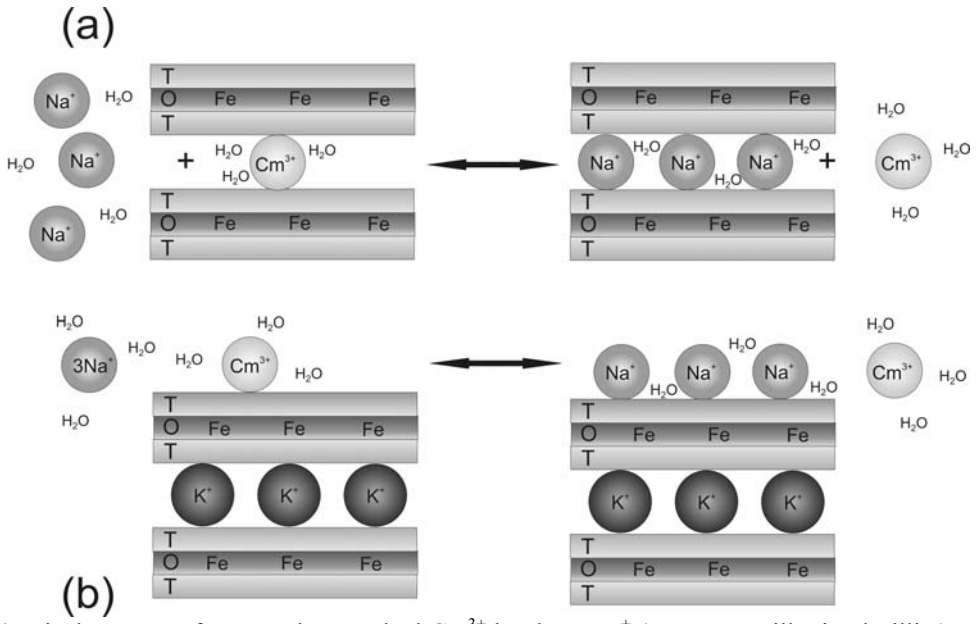

Figure 3-24: Displacement of outer-sphere sorbed Cm^{3+} by three Na^{+} (a: montmorillonite, b: illite) at increasing ionic strengths resulting in increased Cm3+ ion concentrations in solution.

At low ionic strengths (NaCl) the cation with the higher charge (Cm^{3+}) is preverentially sorbed on the clay. The curium is released into the solution with increasing ionic strength due to ion exchange reaction between Cm^{3+} and three Na^{+} ions at the outersphere sorption sites. (Figure 3-24). The cation exchange reaction takes place in case of montmorillonite not only on the surface, but also in the clay interlayer space (Figure 3-24(a)),, whereas in case of illite only the cation exchange on the surface is possible due to the irreversibly bound K^{+} ions in the interlayer space (Figure 3-24(b)).

Cm^{3+} and Sm^{3+}, chosen for the TRLFS- and EXAFS investigations, keep as outer-sphere complex nine water molecules in the first hydration shell. Consequently, the peak maximum in TRLFS spectra does not change for a Cm^{3+}/Sm^{3+} outer-sphere complexes and the lifetime

remains constant compared to the uncomplexed aquo ion. So far, therefore, a distinction was not possible between aquo ions and outer-sphere sorbed cations by using spectroscopic methods and the outer-sphere complex formation couldn't be quantified, since these were based only on changes in the ligand field of the fluorescent cation.
The TRLFS studies presented below show the Cm (III) outer-sphere complex formation in various clay suspensions at pH ~ 4. Here, the quenching effect of iron on the Cm (III) fluorescence emission was taken to help. Iron, which was built by displacement of an Al^{3+} in the crystal structure of clay minerals, causes, in addition to H_2O, an additional diminution of Cm(III) fluorescence emission by dynamic quenching, when it comes to a collision between fluorophore and quencher and the excited molecule makes an energy exchange with the quencher transfering back into its the ground state. The higher the Fe content in the crystal lattice of clay minerals, the shorter the average distance and therefore the shorter is the lifetime of the fluorescence emission of sorbed Cm (III) species. Cm (III) ions bound as outer-sphere complex can be distinguished from non-sorbed aquo ion based on their shorter fluorescence lifetime, because the distances of aquo ions are too large for an interaction with the iron. The lifetimes should correlate with the corresponding iron content of the clays used.

Table 3-10: Physico-chemical properties of γ-Alumina (Al_2O_3), purified Na-montmorillonites (SWy-1, Milos und STx-1) and the synthetic Na-montmorillonit ($NaMont_s$) as well as Na-illite (IdP-2).

	Al_2O_3	**Na-$Mont_s$**	**Na-STx-1**	**Na-Milos**	**Na-SWy-1**	**IdP-2**
Fe^{3+} [Gew.-%]	0	0,002	0,62	1,3	2,97	5,32
CEC [meq/kg]	0	630	912	937	881	225
N_2-BET [m²/g]	119	98	84	28	35	138

CEC: cationic exchange capacity

In Table 3-10 the different Fe-contents of the sorbents and clays used in the experiments are listed. Since the cation exchange capacity and specific surface area for the outer-sphere complex formation play an important role, these are also listed. The origin, properties and preparation of materials and clays and other details are described in [Hartmann, 2010; Hartmann et al., 2008a].

The quantification of the outer-sphere complex formation are carried out by means of the TRLFS. This was done by gradually increasing the ionic strength (NaCl) and thereby increasing the exchange of outer-sphere sorbed Cm^{3+} by Na^+.

The TRLFS measurements were performed for clays with high Fe contents in H_2O and D_2O. For clays with low Fe contents the Cm (III) outer-sphere complex formation was quantified only in D_2O. In H_2O the fluorescence emission lifetime of the Cm(III) is about at 65-68 microseconds due to quenching effect of the water molecules in the first coordination sphere,

if not even more quenching effects, such as by iron, manganese or organic ligands are present. Unlike for H_2O, the quenching effect of D_2O molecules on the Cm (III) fluorescence emission lifetime is low. The lifetime of the Curium in D_2O is ~ 1250 ± 180 microseconds [Wimmer, 1992; Kimura&Choppin, 1994]. The difference between the fluorescence emission lifetime of the non-sorbed aquo ions and the outer-sphere sorbed Cm^{3+} quenched by the Fe is much greater and the difference between the quenching rates is much more pronounced than in H2O. Consequently, TRLFS measurements in D_2O are more sensitive and they can also provide information about the outer-sphere sorbed fraction of Cm (III) ions sorbed on clays with very low Fe contents.

3.6.1 Identification of the An(III)/clay outer-sphere complexation

In Figure 76 (a) and (b) all measured fluorescence emission spectra are represented of Cm (III) in clay suspensions and Al_2O_3 in 0.01 mol / l NaCl at pH ~ 4 in H_2O and D_2O. The spectra are identical with the spectrum of the Cm-Aquoions concerning the peak position and width and they show a peak maximum at 593.8 nm. Under the given conditions the Cm^{3+} ion retains its hydration shell and is either completely dissolved as Cm (III) aquo ion or occurs as an outer-sphere complex [Edelstein et al., 2006].

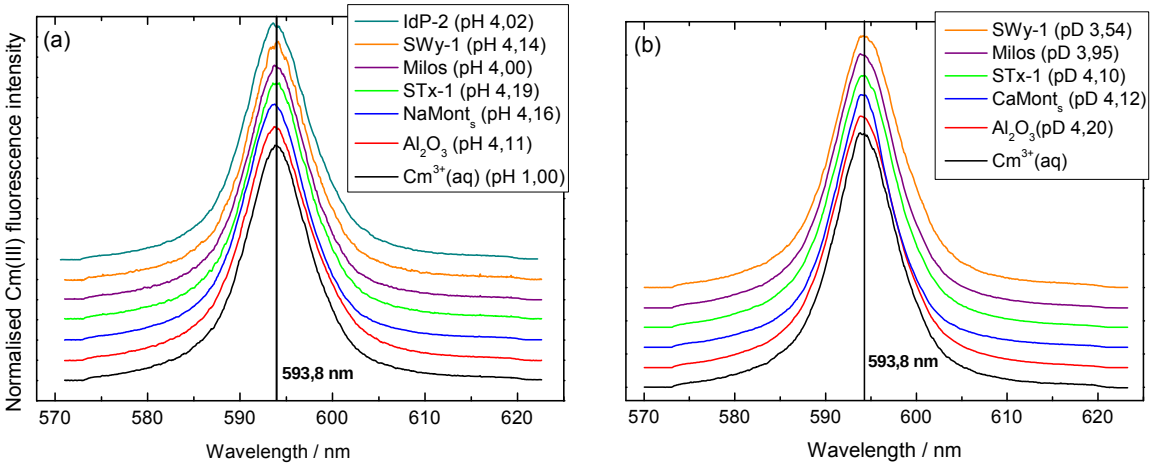

Figure 3-25: Cm(III) fluorescence emission spectra of various clay and Al_2O_3 suspensions (a) in H_2O ($2 \cdot 10^{-7}$ mol/L Cm(III), 0.3 g/L, 0.01 mol/L NaCl) at pH 4 to 4.19. The spectra for Cm^{3+}(aq) was measured in $HClO_4$ at pH 1. (b) in D_2O ($2 \cdot 10^{-7}$ mol/l Cm(III), 0.3 g/l, 0.01 mol/l NaCl) at pD 3.54 bis 4.2. The spectra for Cm^{3+}(aq) was measured in 0.01 mol/l NaCl in D_2O at pD 3.75.

In Figure 3-26, the Cm (III) fluorescence emission lifetimes in H_2O are shown, which were measured in all montmorillonite suspensions and in Al_2O_3. γ-alumina has been studied as a reference mineral with no permanent charge and without iron in the crystal structure. The

lifetimes vary for the different clay suspensions and correlate with the corresponding Fe content of the clay used (Figure 80 (a)).
The shortest life time was determined to be $\tau = 32 \pm 2$ microseconds for Cm (III) in SWy-1 suspension with the highest Fe content of 2.97 wt -% (and 4.25 wt -% Fe_2O_3) of all montmorillonites, which therefore corresponds to the most quenched fluorescence emission. For Cm (III) sorbed to Milos (1.30 wt -% Fe) and STx-1 (0.62 wt -% Fe) $\tau = 49 \pm 3$ microseconds or $\tau = 57 \pm 3$ microseconds were determined accordingly to their different Fe levels. For comparison, the Cm (III) aquo ion in $HClO_4$ measured at pH 1 showed a lifetime of $\tau = 68 \pm 4$ microseconds. This value agree very well with values in the literature between $\tau = 65$ and 68 microseconds [Fanghänel et al., 1995; Beitz&Hessler, 1981; Beitz et al., 1988].
The measured lifetime of Cm (III) in γ-alumina suspension of $\tau = 65 \pm 4$ ms coincides with that in the Cm (III) aquo ion in $HClO_4$. In suspension of the synthetic montmorillonite Na-$Mont_s$, which has a very low Fe content of only 0.002 wt%, the outer-sphere complexation is indicated by a low quenched fluorescence emission lifetime of $\tau = 62 \pm 4$.

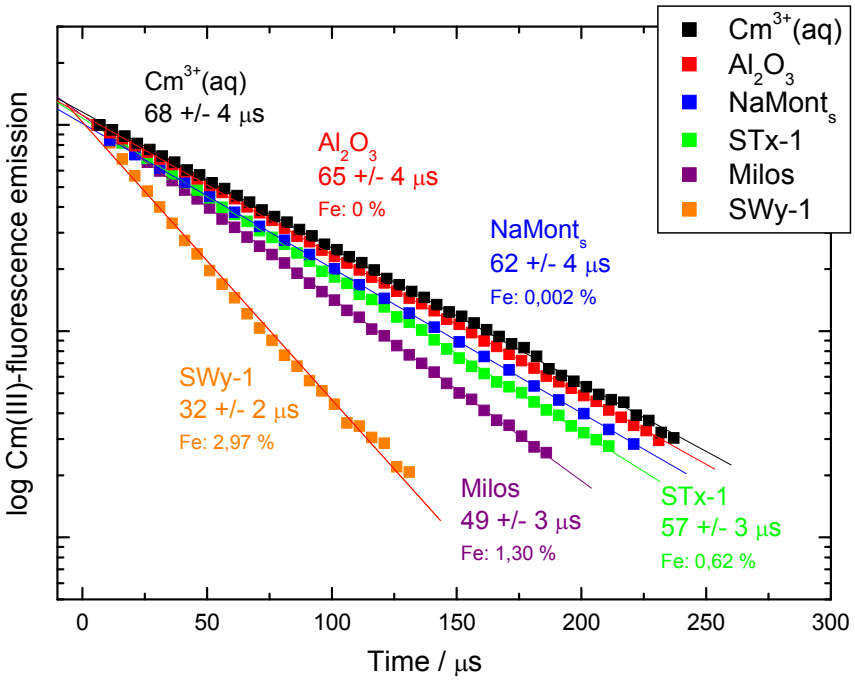

Figure 3-26: Cm(III) fluorescence emission lifetimes of various clay and Al_2O_3 suspensions in H_2O ($2 \cdot 10^{-7}$ mol/L Cm(III), 0.3 g/L, 0.01 mol/L NaCl) at pH 4 to 4.19. The lifetime for Cm^{3+}(aq) was measured in $HClO_4$ at pH 1. The lifetime of the montmorillonites show a mono-exponential decay.

In the literature, no information could be found for fluorescence emission lifetimes measured by TRLFS of Cm(III) sorbed as outer-sphere complex on clays with different iron concentrations. However, studies exist with trivalent europium sorbed on montmorillonites with different Fe contents at low pH values [Takahashi et al., 2006; Kowal-Fouchard et al., 2004; Tertre et al., 2006]. The Cm(III) fluorescence emission lifetimes for the measured montmorillonite suspensions in H_2O all show a mono-exponential curve (Figure 3-27),

because at low ionic strengths (<0.01 mol / l) and at pH ~ 4, the Cm(III) ions on the montmorillonite are present predominantly as outer-sphere complex (> 95%). The small proportion of non-sorbed Cm(III) aquo ion in H_2O is not evident from the decay curves. By comparison, in γ-alumina suspension only Cm(III) aquo ions occur due to the lack of layer charges that makes any outer-sphere complexes difficult. As expected, the measured fluorescence emission lifetime is also mono-exponential similar to that of the Cm^{3+}(aq) in $HClO_4$ at pH 1.

The life times belonging to the the Cm-fluorescence emission spectra in D_2O from Figure 3-25(b) are shown in Figure 3-27. They show a bi-exponential pattern except for the γ-alumina. The long lifetime of 1250 ± 180 microseconds is due to the excitation of non-sorbed Cm(III) aquo ion. The short life time varies for the different clays and is correlated with the respective iron content of the clay minerals (Figure 3-29(b)).

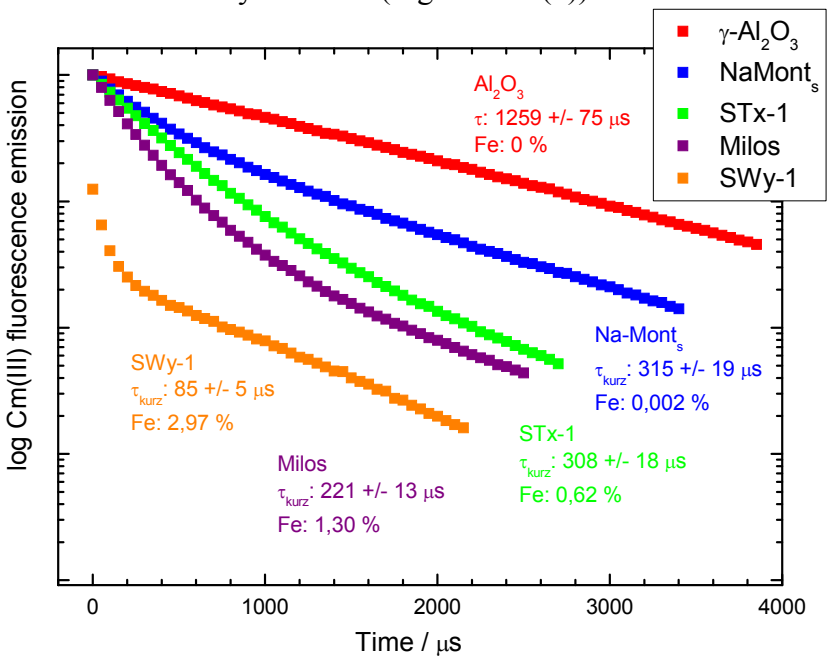

Figure 3-27: Cm(III) fluorescence emission spectra of various clay and Al_2O_3 suspensions in D_2O ($2 \cdot 10^{-7}$ mol/l Cm(III), 0.3 g/l, 0.01 mol/l NaCl) at pD 3.54 bis 4.2. The lifetime for Cm^{3+}(aq) was measured in 0.01 mol/l NaCl in D_2O at pD 3.75.

The short lifetime is assigned to the Cm(III) outer-sphere complex that is quenched due to the low Fe-Cm distance. It amonunts in the SWy-1-clay suspension 85 ± 5 microseconds and increases according to the decreasing iron content from Milos (221 ± 13 microseconds), STx-1 (308 ± 18 microseconds), to the synthetic Na-rich montmorillonite with the lowest Fe concentration (463 ± 28 microseconds). In the suspension with γ-alumina, which contains no iron and which forms no outer-sphere complexes due to lack of permanent charge, only one lifetime of 1259 ± 75 microseconds was measured. This is consistent with those reported in the literature values for the Cm(III) aquo ion in D_2O [Wimmer, 1992; Kimura&Choppin, 1994]. All lifetimes in the clay suspensions show a bi-exponential decay. Therefore one can assume a slow exchange between non-sorbed Cm(III) aquo ion and an outer-sphere complex

in comparison to the fluorescence lifetime of the excited state, which is much more long-lived in D_2O than in H_2O.

The long lifetime of the Cm (III) aquo ion in STx-1 suspension with ~ 661 microseconds is much shorter than 1250 ± 180 microseconds. This becomes apparent in Figure 3-27 where the decay curve at the end is much steeper then the decay curve of all other clays that are parallel to the branch measured in Al_2O_3 suspension. Possibly the STx-1 suspension was slightly contaminated with H_2O or protons during the preparation, so that the lifespan shortens. The quenching rates ($1/\tau$) itself is only slightly affected. The much larger τ_0/τ_1 ration in D_2O increases the sensitivity of the spectroscopic quantification of outer-sphere bound curium.

A bi-exponential decay of emission was observed in the H_2O suspension of Na-illite-rich IdP-2, which has the highest Fe content (5.32 wt -%) of all examined clays (Figure 3-28).

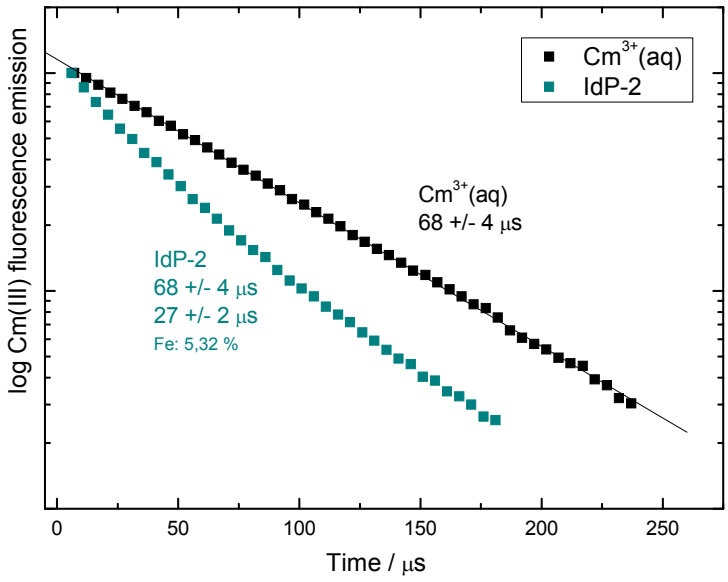

Figure 3-28: Bi-exponentiell decay of the fluorescence emission lifetime of Cm(III) in IdP-2 suspension in H_2O ($2 \cdot 10^{-7}$ mol/l Cm(III), 0.3 g/l, 0.01 mol/l NaCl) at pH 4.02. For comparison the mono-exponential decay of the $Cm^{3+}(aq)$ lifetime in $HClO_4$ at pH 1 was shown.

Illite has only a low cation exchange capacity (CEC) of 225 mEq / kg, while the montmorillonite exhibit a three-to fourfold higher CEC (Table 25). The permanent negative layer charge is compensated mainly by illite with K + ions in the interlayer, which in general are not interchangeable [Bradbury&Baeyens, 2005b]. Only the cations on the external surfaces are interchangeable. Therefore, the CEC of illite is strikingly lower than that of montmorillonite, although the extent of isomorphous substitution is higher [Van Olphen, 1963]. For this reason, non-sorbed aquo ions in higher concentration occur simultaneously together with outer-sphere sorbed Cm(III) cations at low ionic strengths. The long life time of 68 ± 4 microseconds corresponds to the Cm(III) aquo ions and the short one of 27 ± 2 microseconds to the outer-sphere complex.

The fluorescence emission lifetime of Cm(III) sorbed as outer-sphere complex of illite, which is shorter than for montmorillonite, thus correlates again in good agreement with the iron concentration (Figure 80 (a)), which is the highest compared to the montmorillonite.
The efficiency of quenching depends on the distance between Cm(III) as fluorophore and Fe(III) as a quencher. Thereby the efficiency E decreases with increasing distance r according to Equation 3-1.

Equation 3-1 $$E = \frac{R_0^6}{R_0^6 + r^6}$$

R_0 corresponds to the Förster radius [Stryer, 1978], the distance between quencher Fe (III) and the fluorophore Cm (III) with a quenching efficency of 50%. This means that half of all excited Cm(III) atoms relax via dynamic quenching processes into the ground state. At this radius, the measured fluorescence emission lifetime is reduced by half. The influence of dissolved Fe(III) on the quench behavior of the Cm(III) fluorescence emission was studied bei [Stumpf et al., 2004] with TRLFS in H_2O.
A Förster radius of 4.5 Å was calculated by the correlation between the Cm(III) fluorescence emission lifetimes and the concentration of Fe(III) [Stumpf, 2004], while the graphical analysis yielded a distance of 9 Å. The average distance between Fe and Cm in SWy-1 should therefore be between 4.5 and 9 Å, since the measured lifetime is reduced by about one half, while the average distance should be greater for the montmorillonite and correspondingly lower for the illite.

The different distribution of the Fe atoms embeded into the octahedral layers of the clays studied here seems to have no influence on the measurement results. According to [Vantelon et al., 2003] the individual Fe atoms are distributed homogeneously and isolated from each other in the Wyoming montmorillonite SWy-1. The octahedral layer of STx-1, however, has a heterogeneous distribution with local accumulations of iron, while the clay of Milos shall represent an intermediate stage between the two. The Fe content of each individual clay, however, correlates well with the measured lifetimes. A possible reduction in efficiency by iron accumulation as obtained for the STx-1, could not be observed.

The exchange between Cm(III) aquo ions and outer-sphere complex on illite must be very slow compared to the lifetime of the excited state of curium of about 6.8 10^{-5}, since the fluorescence emission lifetime shows a bi-exponential decay . The slow exchange between aquo ion and outer-sphere complex is underlined by the TRLFS measurements in D_2O. Here, the measured Cm(III) fluorescence emission lifetime for all the clay suspensions showed a bi-exponential pattern. In contrast, we assume that a fast exchange takes place among the outer-sphere sorbed Cm(III) ions, because the fluorescence lifetimes was mono-exponential for Cm in different montmorillonite suspensions with >95% outer-sphere complexation.

The spatial arrangement of the outer-sphere complexes in the area of the hexagonal cavities determined by EXAFS (Section 5.3) reveals that they must take up different distances from

the clay mineral surface to Fe incorporated into the crystal structure. These different distances would be expressed in case of a slow exchange between the outer-sphere sorbed Cm(III) ions present in multi-exponential decay curves. Since the course is clearly mono-exponential, the exchange must be relatively fast compared to the excited state. The measured lifetime is an averaged value, which is composed of various quenching effects of various Cm-Fe distances.

In Figure 80 the ratio of long and short Cm(III) fluorescence lifetimes in H_2O and D_2O are plotted as a function of the iron content of the clays as a Stern-Volmer graph. The strength of the quenching (reduced lifetime) correlates strongly with the Fe content of the clays. Thereby, the data obtained in D_2O cannot be described by a simple linear function. This is due to the fact that the distance r between Cm and Fe as a quencher acts with the sixth power in the quenching efficiency E (Equation 58).
If the data points in Figure 80 are interpolated, the curve does not achieved $\tau 0/\tau 1 = 1$ at an iron content of 0 wt -%. Here, an intercept of ~1.05 and ~3 is obtained for H_2O and D_2O, respectively. This observation could be interpreted as evidence for a further quenching mechanism (see Section 5.1.1 and 4.3.1).

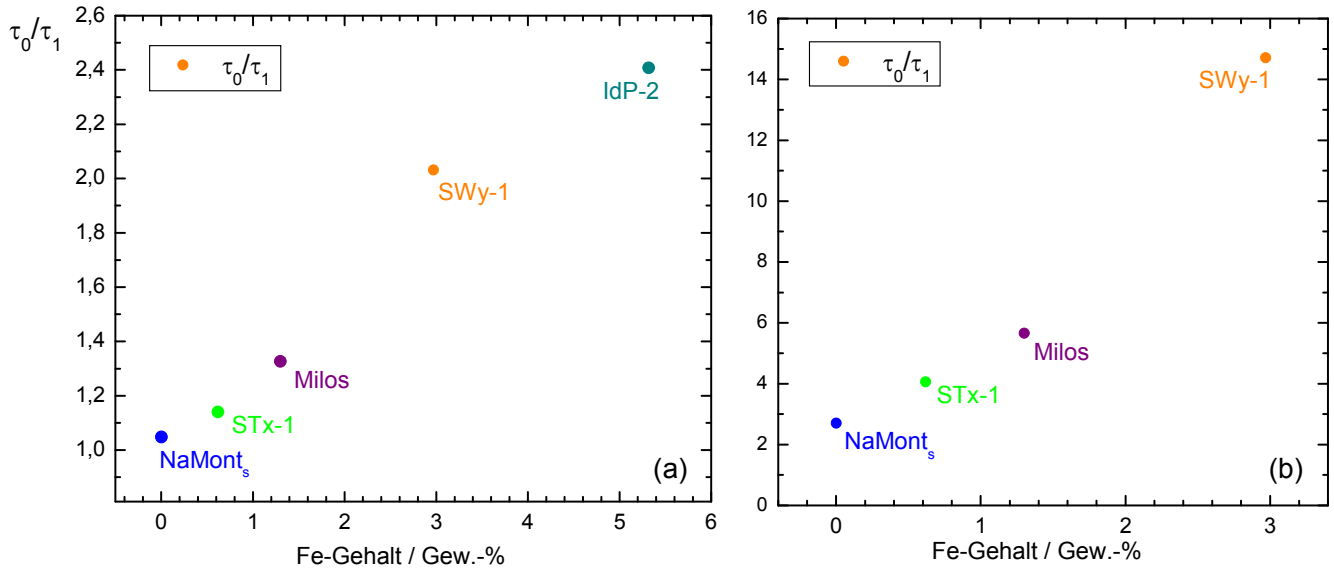

Figure 3-29: Plot of the Cm(III) fluorescence emission lifetime as a function of Fe content of the various used clays as Stern-Volmer-Plot (jeweils $2 \cdot 10^{-7}$ mol/l Cm(III), 0.3 g/l, 0.01 mol/l NaCl). Measurements (a) in various montmorillonite and illite suspensions in H_2O (pH values see Figure 3-25(a) and (b) in D_2O (pH values see Figure 3-25(b)).

Comparison of the quenching rates in H_2O und D_2O

To compare the results of the TRLFS measurements in H_2O with those from the D_2O system the quenching rates of both systems were faced. The quenchings rate K_{obs} is calculated from the reciprocal of the Cm(III) fluorescence emission lifetime τ (Equation 3-2). In H_2O τ is 68

microseconds in accordance with [Fanghänel et al., 1995] and hence, the quenching rate of Cm(III) in pure H_2O is calculated to 14.7 ms^{-1}.

Equation 3-2 $$K_{obs} = \frac{1}{\tau[ms]}$$

Quenching rates from measurements of Cm(III) clay suspensions in H_2O are the sum of quenching rates $K_{Cm_{Fe}}$ of the energy transfer to iron incorporated in the crystal structure of the clay minerals and the rate of H_2O $K_{Cm_{H_2O}}$ (Equation 3-3) and can be calculated using Equation 3-4. They correspond to the reciprocal value of the measured short lifetime in the H_2O system.

Equation 3-3 $$K_{H_2O} = K_{Cm_{Fe}} + K_{Cm_{H_2O}}$$

Equation 3-4 $$K_{H_2O} = K_{Cm_{Fe}} + \frac{1}{0{,}068ms} = \frac{1}{\tau_{kurz_{H_2O}}}$$

In the D_2O system, the quenching rate is analogous to that in H_2O.

Equation 3-5 $$K_{D_2O} = K_{Cm_{Fe}} + K_{Cm_{D_2O}}$$

Equation 3-6 $$K_{D_2O} = \frac{1}{\tau_{kurz_{D_2O}}} + 0$$

K_{D_2O} corresponds to the quenching rate of iron and thus to the reciprocal value of the measured short lifetime in D_2O, as the quenching effect of D_2O ($K_{Cm_{D_2O}} = \frac{1}{1{,}3ms} = 0{,}7\ ms^{-1}$) is negligible and can be set to zero for simplification (Equation 3-6). In Table 3-11, the quenching rates are listed for the H_2O impact, estimated from the available literature values, as well as the influence of iron, which correspond to the reciprocal value of the short lifetimes measured in D_2O.

Table 3-11. Quenching rates by energy transfer to iron that corresponds to the reciprocal value of the short lifetime in D_2O and the H_2O influence for comparison of quenching rates in the D_2O- and H_2O system.

Clay	**Quenching rate Fe (in D_2O)**	**Quenching rate H_2O**	**Quenching rate H_2O + Fe**		**Fe wt.-%**
	$K_{Cm_{Fe}} = \frac{1}{\tau_{kurz_{D_2O}}[ms]}$	$K_{Cm_{H_2O}} = \frac{1}{0{,}068ms}$	$K_{H_2O} = K_{Cm_{Fe}} + K_{Cm_{H_2O}}$ [ms^{-1}]	$\frac{1}{\tau_{kurz_{H_2O}}[ms]}$	
SWy-1	14,5	14,7	29,2	31,3	2,97
Milos	5,3	14,7	20,0	20,4	1,3
STx-1	3,9	14,7	18,6	17,5	0,62
Na-Mont$_s$	3,6	14,7	18,3	16,1	0,002

The quenching rates of Cm(III) fluorescence emission by H_2O and Fe determined by different ways agree very well, so that the measurement results in H_2O and D_2O system are well comparable. The TRLFS is thus suitable as a spectroscopic method for the characterization and quantification of Cm(III) / clay outer-sphere complex formation. The difference in the quenching rates is the higherst for the synthetic Na-montmorillonite with 2.2 ms^{-1}. It is also striking that the quenching rates of STx-1 and Na-Monts in D_2O with 3.9 and 3.6 ms^{-1} differ very little, although the Fe content varies by more than two orders of magnitude.

Perhaps this could be seen as an indication of additional quenching mechanisms, such as crystal lattice defects acting as energy acceptors that can occur more frequently in synthetic clay minerals due to low time for cristallisation compared to natural clays. Using the higher sensitivity of TRLFS this effect could become noticeable in D_2O especially for $Na\text{-}Mont_s$ as the clay with the lowest Fe content, even it is of little relevance for outer-sphere complexes compared to the energy transfer to iron.

The investigations to the An(III) / clay outer-sphere sorption presented here show that iron seemingly has the highest quenching efficiency on the fluorescence emission compared to other quenching metals such as Cu^{2+}, Pb^{2+}, Cd^{2+}, Co^{2+}, Ni^{2+}, Mn^{2+} , Cr^{3+} and others (Section 2.4.2.3). The quenching effect of other metals is apparently negligible in the outer-sphere complex formation and the Fe content, which correlates well with the quenched fluorescence emission lifetimes and intensities can be used to quantify the outer-sphere sorbed actinide ions. The results shown in the present study, however, point to the presence of other quenchers, such as an energy transfer to crystal defects which are caused for example by the incorporation of iron and other elements in the octahedral or as well tetrahedral layer of clay minerals. This certainly appears to have only little or no relevance in the outer-sphere sorption compared to structurally bound iron. Other elements like Mg^{2+}, Mn^{2+}, Ti^{2+} or the Fe^{2+} have often larger ionic radii than Fe^{3+} and generate much larger deformations. Even the substitution of Si^{4+} by Al^{3+} or even the much less frequent exchange of Fe^{3+} and Ti^{4+} in the tetrahedral layer cause extensive defects, since the exchanged elements are significantly larger than Si^{4+}. A correlation between the levels of these elements and the measured fluorescence lifetimes and intensities could not be established so far.

Table 3-12. Ionic radii of cations that might occur in tetrahedal or octahedral layers of clay minerals.

Elements	**Al^{3+}**	**Fe^{3+}**	**Mg^{2+}**	**Mn^{2+}**	**Ti^{2+}**	**Fe^{2+}**	**Si^{4+}**	**Ti^{4+}**
Ionic radius [Å]	0.57	0.67	0.78	0.91	0.80	0.82	0.26	0.61

In the inner-sphere complex formation the fluorescence emission intensities are quenched to below 10% irrespective of of iron content or the content of other elements. This quenching of fluorescence emission could be caused by crystal defects.

3.6.2 Quantification of the An(III)/clay outer-sphere complex

The Cm(III) clay outer-sphere complex formation was quantified by using the fluorescence emission decay of Cm (III) as a function of ionic strength in different clays suspensions in H_2O and D_2O. For a quantification of the outer-sphere complex formation in H2O the montmorillonites were selected with the highest concentrations of Fe (SWy-1 and Milos). Due to the high Fe content and the resulting quenching effect the difference between the fluorescence emission lifetime of the Cm(III) aquo ion and the outer-sphere sorbed Cm(III) ion for the SWY-1 is the largest from all montmorillonite systems. In addition, the quantification of the outer-sphere complex formation was also performed with the Na-rich illite IdP-2 with an almost twice as high Fe content, but with much lower CEC than the SWy-1. Firstly, TRLFS measurements in D_2O should check, whether the measurements confirm the results in H_2O. On the other hand, the proportion of outer-sphere sorbed Cm (III) to $NaMont_s$ that has only a small percentage of structurally bound Fe (0.002 wt -%), should be quantified with the help of the higher sensitivity of TRLFS in D_2O. This was not possible in H_2O due to the small difference between the lifetime of the aquo ions (65 microseconds) and the very low quenched outer-sphere complex (62 microseconds). In Figure 3-30 (a) the different Cm(III) fluorescence emission spectra for the SWY-1 suspension in H_2O is presented at varying ionic strengths.

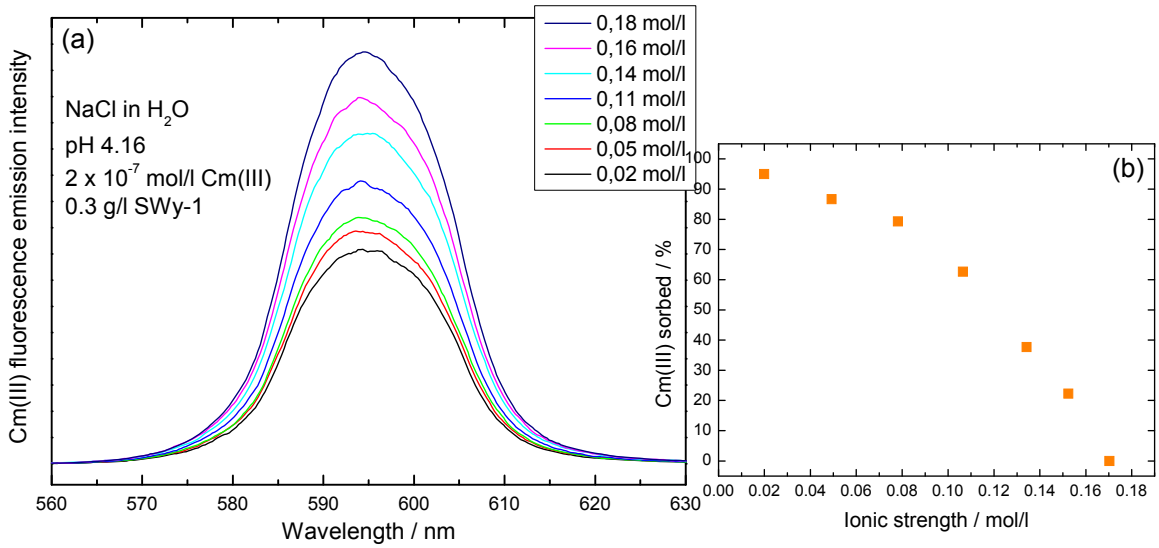

Figure 3-30: (a) Intensities of fluorescence emission of $2 \cdot 10^{-7}$ mol/l Cm(III) in aqueous SWy-1suspensions (0.3 g/l) at pH 4.16 and different ionic strengths. The fluorescence emission spectra were taken from lifetime measurements (1 µs delay, grating 300 lines/mm). In (b) the amounts of SWY-1 sorbed Cm(III) are shown calculated from differences in fluorescence emission intensities of emission spectra recorded at different ionic strengths.

The spectra shown are from the lifetime measurements after 1 ms time delay with a 300 lines per mm grating. By using this grating higher intensities can be achieved for the necessary

long measurement periods. The spectra are much broader than usual for fluorescence emission measurements with a grating of 1200 lines/mm, resulting in a higher resolution. With increasing ionic strength and increasing proportion of Cm (III) aquo ion in the solution and thus also a greater distance between Cm and Fe, the quenching effect of iron decreases, and hence, the fluorescence emission intensities increase. The ionic strength-dependent outer-sphere complex formation can therefore clearly be quantified by measuring the Cm(III) fluorescence emission intensities.

The amounts of Cm(III) sorbed on SWy-1 calculated from the differences of the fluorescence emission intensities in the emission spectra recorded at different ionic strengths (each at 1 ms delay) are shown in Figure 3-30 (b).

For the calculation of the sorbed amounts we assumed that approximately 95% of the curium is absorbed at an ionic strength of 0.02 mol/l. This corresponds to the amount that was quantified using the lifetimes in SWy-1 suspension (Figure 3-31). The concentration of the Cm(III) outer-sphere species quantified by fluorescence emission intensities decreases with increasing ionic strength. The decrease in fluorescence intensity with decreasing lifetime coincides with the classical Stern-Volmer theory. The validity of the relationship is illustrated by means of the fluorescence emission intensities in Figure 3-30 (a). The intensity of F_1 of the outer-sphere sorbed Cm(III) on SWy-1 is half of F_0, which also corresponds to the ratio of lifetimes (65 µs/32 µs = τ_0/τ_1). From this result one can conclude that the assumption of an active dynamic quenching process is correct. F_0 was measured at a concentration of $NaClO_4$ of 0.2 mol/l where the Cm(III) is exclusively present as dissolved aquo ion. In Figure 3-31, the Cm(III) fluorescence emission lifetimes for the SWy-1 suspension that corresponds to the fluorescence emission spectra in Figure 3-30 (a)) are shown at varying ionic strength. The decreasing quenching effect of Fe(III) on the fluorescence emission due to the exchange reaction of Cm^{3+} by Na^+ with increasing ionic strength is documented by the increasing fluorescence lifetimes. At an ionic strength of 0.01 mol/l a lifetime quenched by H_2O and Fe(III) of only 32 microseconds was measured in the SWy-1 suspension, while the lifetime is τ = 65 microseconds at 0.20 mol/l. This time period corresponds to the fluorescence emission lifetime of the non-sorbed Cm III) aquo ion.

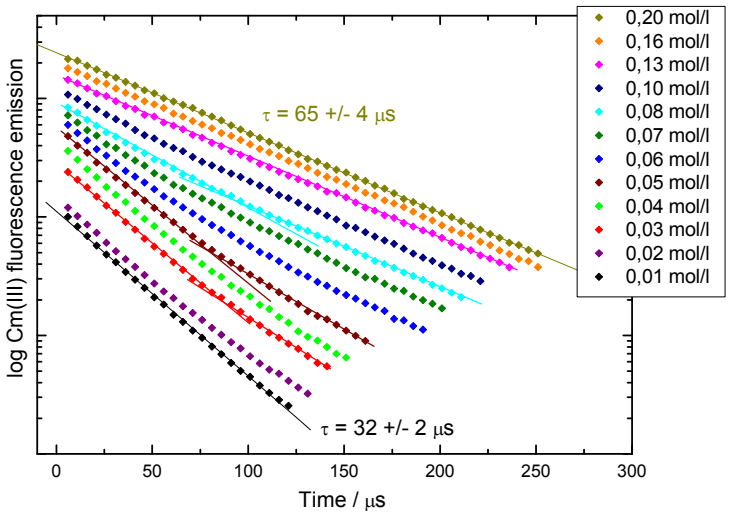

Figure 3-31: Cm (III) lifetimes in aqeous SWy-1 suspension ($2 \cdot 10^{-7}$ mol/L Cm (III), 0.3 g/l) at pH 4.16 and various ionic strengths (plotted arbitrarily for clarity). The time dependence of the fluorescence emission shows a mono-exponential decay at low and high ionic strength and a bi-exponential decay at intermediate ionic strengths.

Using the measured fluorescence emission intensities or lifetimes the outer-sphere complex formation between Cm (III) and SWy-1 could be quantified by considering the different fluorescence yields for the outer-sphere sorbed species and the aquo ion in the bulk solution. The fractions (F_0 and F_1) for aquo ion and outer-sphere complex can be obtained by bi-exponential fitting of the fluorescence decay measured at different ionic strengths. The lifetimes were fixed at 65 microseconds (Cm^{3+} aquo ion) and 32 microseconds (outer-sphere sorbed Cm^{3+}). For the outer-sphere complex the quenched lifetime determined at an ionic strength of 0.01 mol/l was used. The decrease in fluorescence with time follows a bi-exponential rate law:

Equation 3-7

$$F(x) = F_0 \cdot e^{-\frac{x}{\tau_0}} + F_1 \cdot e^{-\frac{x}{\tau_1}}$$

$F(x)$: Total fluorescence emission intensity at time x

τ_0 und τ_1: Fluorescence emission lifetimes of Cm(III) aquo ions or outer-sphere complex

F_0 und F_1: Total fluorescence emission intensity at time $x = 0$ of Cm(III) aquo ions or outer-sphere complex

The following applies:

Equation 3-8

$$F_0 + F_1 = 100\ \%$$

However, the quantum yield generally decreases slightly with decreasing fluorescence emission lifetime, ie Equation 3-8 only conditionally applies. The lower quantum yield for the quenched lifetime of the outer-sphere complex was considered mathematically by calculating the real outer-sphere fraction from the resulting percentage for the outer-sphere complex multiplied by τ_0/τ_1 and from the sum of the result and the percentage of the real aquo ion. The Rd values were converted into [% sorbed] according to Equation 3-9. The experiments were carried out at a solution to solid ratio of 0.3 g / liter.

Equation 3-9

$$\%sorbed = 100 \cdot \left(\frac{R_d}{R_d + \frac{V}{m}} \right)$$

V: volume of bulk solution [l]; m: mass of the clay [kg]

In Figure 3-32 the fractions of the Cm(III) outer-sphere sorbed to SWy-1 determined by using the fluorescence emission lifetimes are shown as a function of the ionic strength. At low ionic strengths (<0.01 mol/l) more than 98% of Cm (III) are sorbed as outer-sphere complex on the SWy-1 surface. With increasing ionic strength the fraction of sorbed Cm^{3+} decreases. At an ionic strength of about 0.19 mol/l more than 99% of the Cm ions are in solution and the Cm(III) outer-sphere complexation on the clay mineral is less than 1%.
Also, the outer-sphere complex formation of Cm^{3+} on the Na-rich montmorillonite Milos was quantified by TRLFS (Figure 3-32) by utilising the ionic strength effect. The lifetimes were fixed each at 65 microseconds (Cm^{3+} aquo ion) and 49 microseconds (outer-sphere sorbed Cm^{3+}). The quenched lifetime of Cm (III) outer-sphere complex was determined at an ionic strength of 0.01 mol/l (Figure 3-26). At ionic strengths <0.01 mol/l over 97% of the Cm (III) is sorbed as outer-sphere complex. The sorption again decreases with increasing ionic strengths. Furthermore, the fraction of the outer-sphere complex of Cm (III) on illite IdP-2 is displayed in Figure 3-32 as a function of the ionic strength. To quantify the outer-sphere complex formation, each lifetimes were fixed at 65 microseconds (Cm^{3+} aquo ion) and 27 microseconds (outer-sphere sorbed Cm^{3+}). The quenched lifetime of Cm (III) outer-sphere complex of 27 microseconds was determined again at an ionic strength of 0.01 mol/l (Figure 3-28), in which only ~ 85% of the Cm (III) is sorbed on illite. With increasing ionic strength the Cm^{3+} is released more easily into the solution than in montmorillonites. The reasons for the decreased sorption on illite at low ionic strengths compared to the montmorillonite are explained in more detail in Section 5.2.1.

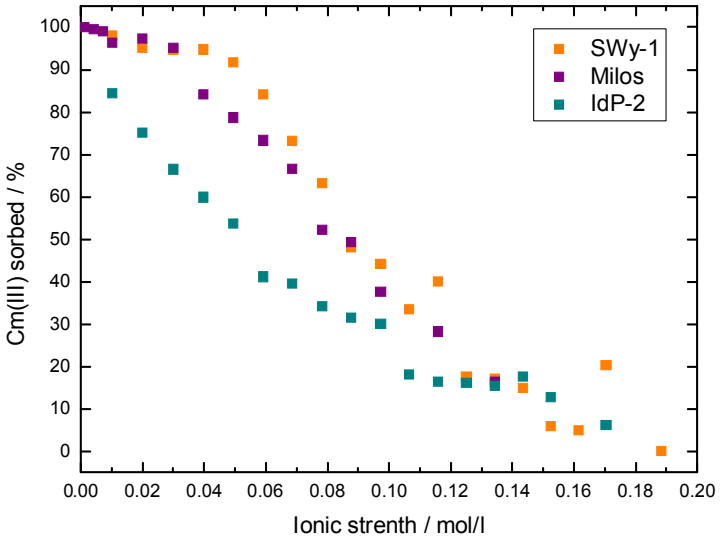

Figure 3-32: Cm(III) outer-sphere complexation in H_2O on SWy-1 at pH 4.16, Milos at pH 3.97 and IdP-2 at pH 4.02 as a function of ionic strength ($2 \cdot 10^{-7}$ mol/l Cm(III), 0.3 g/l).

In Figure 3-33, the Cm (III) fluorescence emission lifetimes for Na-Mont$_s$ in D_2O are shown at varying ionic strength. By bi-exponential curve fitting of the fluorescence decay the fraction of sorption of Cm^{3+} via outer-sphere complex formation can be quantified analog to the experiment in H_2O. The each long life was fixed at 1250 microseconds (Cm^{3+} aquo ion). For the outer-sphere complex, the short lifetime at an ionic strength of 0.01 mol/l was taken. These are shown in Figure 3-27.

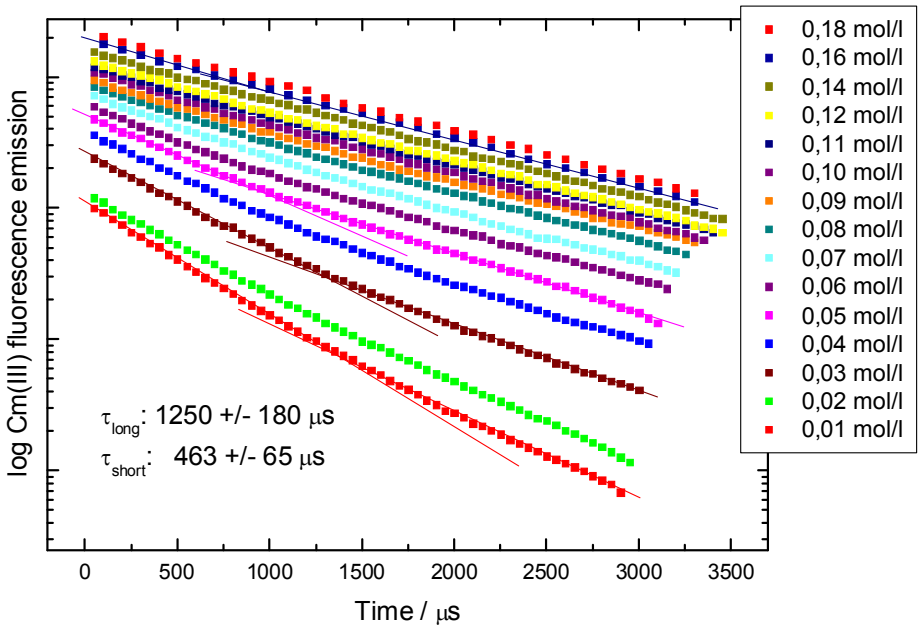

Figure 3-33: Cm(III) life time in clay suspensions of synthetic Na-montmorillonite NaMont$_s$ in D_2O ($2 \cdot 10^{-7}$ mol/l Cm(III), 0.3 g/l) at pD 4.12 and various ionic strengths (plotted arbitrarily for clarity). The fluorescence emission shows a bi-exponential decay (τ_{long} = Cm(III) aquo ion , τ_{short} = Cm(III) outer-sphere complex).

Even slight contamination in solution, which can not be excluded from the the sample preparation, can cause quenching. But their effect on quenching rates ($1/\tau$) can be neglected. The values for τ_{long} are not the same for all experiments and are usually somewhat lower than

the theoretical value for the aquo complex in D_2O. It is therefore assumed that traces of H_2O as a contaminant are present in the D_2O solution.

In Figure 3-34 the results of the quantification of the outer-sphere complexation of Cm (III) on various clays in D_2O are plotted. The sorption curves are in good agreement within the error limits and are consistent with the calculated values of the outer-sphere complex formation in H_2O (Figure 3-32).

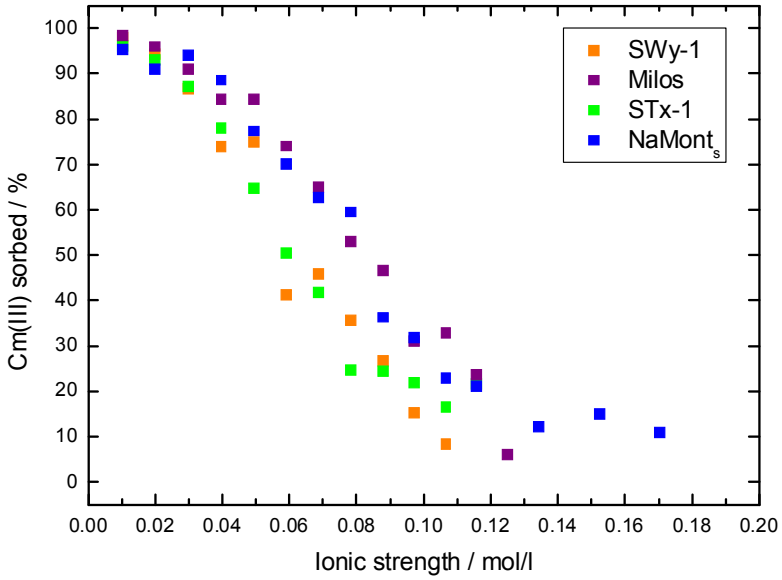

Figure 3-34: Cm(III) outer-sphere complexation in D_2O on SWy-1 at pD 3.99, Milos at pD 3.76 and NaMont$_s$ at pD 4.12 as a function of ionic strength ($2 \cdot 10^{-7}$ mol/l Cm(III), 0.3 g/l)

Modelling of the Cm (III) / clay outer-sphere complex formation

The experimenatl quantification of the outer-sphere complex formation between Cm (III) and clay were additionally described by model calulations. Cation exchange reactions, forming outer-sphere complexes on clay minerals can be expressed with a selectivity coefficient. This is obtained by applying the mass action Act. The model calculations of the cation exchange experimentally investigated by TRLFS were performed for Na^+-background concentrations between 0.01 and 0.2 mol/l. A selectivity coefficient of 30 (I = 0) was applied for the Cm-Na exchange reactions. This value was deduced from Eu-Na exchange experiments on montmorillonite (SWy-1) [Bradbury&Baeyens, 2005a]. For the model calculations 881 meq / kg and 937 meq / kg for SWy-1 and Milos, respectively, were applied as CEC (Table 25). All other parameters used in the calculations, such as protolysis, types and capacities of sorption sites are listed in Chapter 3.3 (Table 19). In Figure 3-35 the experimental and modeled data of the sorption of Cm^{3+} by outer-sphere complex formation on Na-rich montmorillonite and SWy-1 in H_2O, are shown as a function of ionic strength. The modeled results are in good

agreement with experimental data within the uncertainties of the analytical methods and the values for the selectivity coefficients and within the experimental error.

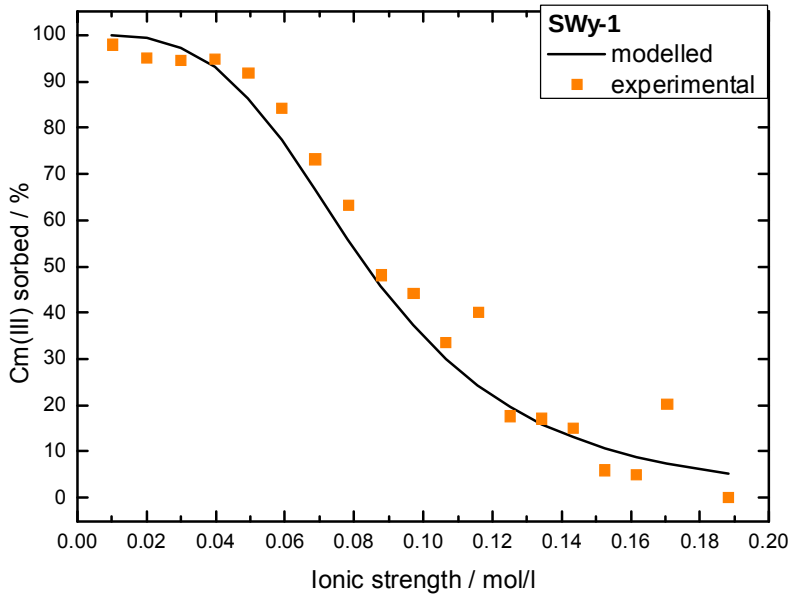

Figure 3-35: Comparison of modelled and experimental results for Cm (III) outer-sphere complex formation on SWy-1 in H_2O by TRLFS at pH 4.16 (experiment A) or pH 4.07 (experiment B) as a function of ion strength ($2 \cdot 10^{-7}$ mol/l Cm(III), 0,3 g/l).

The experimental and the modelled data of the outer-sphere complex formation of Cm^{3+} on the Na-rich montmorillonite Milos in H_2O are shown in Figure 3-36. Milos-montmorillonite has a higher cation exchange capacity (937 meq / kg) than SWy-1 (881 meq / kg). Hence, the Cm(III) sorption decreases less rapidly for Milos than for the SWy-1 at ionic strengths > 0.01 mol/l. The experimentally determined values agree very well with those from the model calculation.

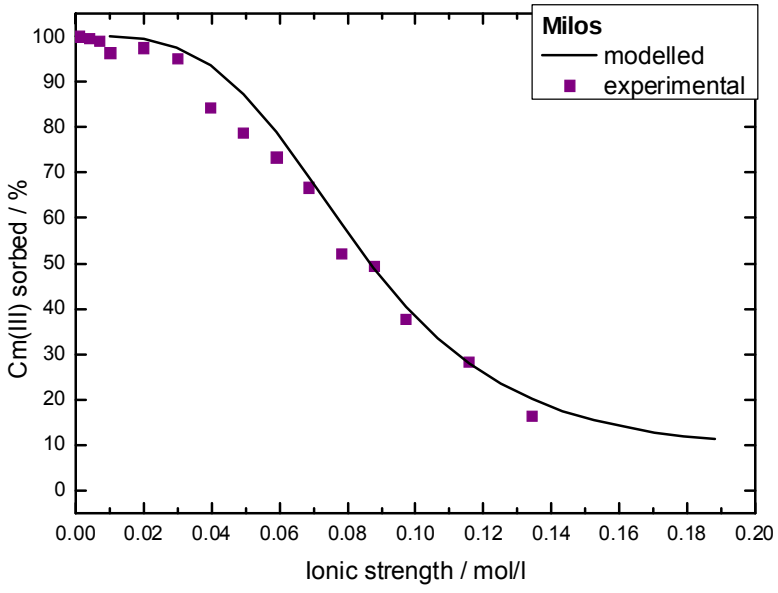

Figure 3-36 Comparison of modelled and experimental results for Cm (III) outer-sphere complex formation on Milos montmorillonite in H_2O at pH 3.97 as a function of ion strength ($2 \cdot 10^{-7}$ mol/l Cm(III), 0,3 g/l).

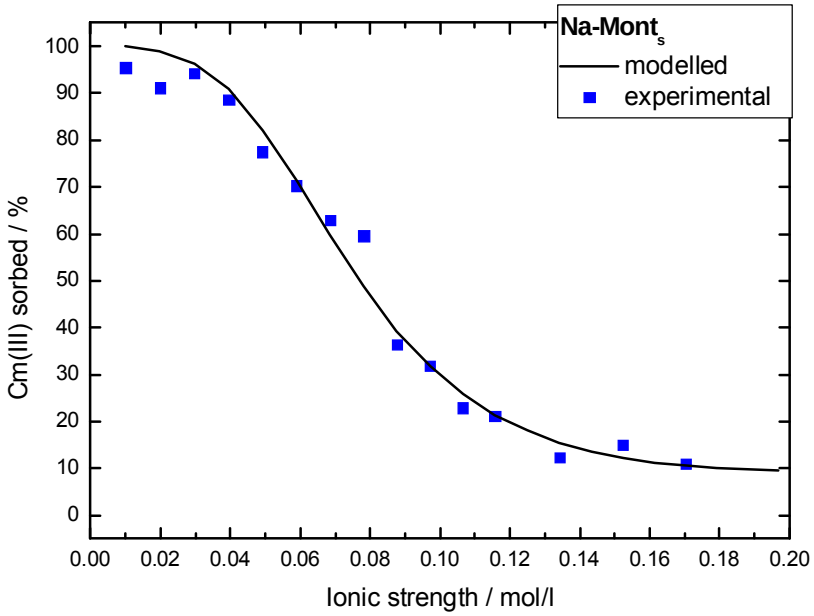

Figure 3-37 Comparison of modelled and experimental results for Cm (III) outer-sphere complex formation on synthetischem Na-montmorillonite $NaMont_s$ in D_2O at pD 4.12 as a function of ion strength ($2 \cdot 10^{-7}$ mol/l Cm(III), 0,3 g/l). Assumptions for modelling see in the text.

In Figure 3-37 the modelled and experimental results of Cm(III) sorbed on synthetic Na-montmorillonite (CEC = 630 meq / kg) in D_2O are shown. Again, experimental and modelled data match very well. A quantification of the outer-sphere complexation can only be carried out in D_2O because of the higher sensitivity TRLFS in this medium. The much higher sensitivity makes on one hand sorption studies of clays with very low Fe content possible. On the other hand broad applications are offered to investigate spectroscopically sorption processes with other minerals containing iron at trace concentrations.

The experimental results of outer-sphere sorption experiments with Milos and STx-1 – both clays with very similar CEC – are shown in Figure 3-38. It is obvious that the calculated values deviate significantly from the experimental results for the STx-1, whereas the values match for Milos. The reason of the discrepancy might be due to a contamination of the STx – D_2O suspension with small amounts of H_2O (see also Figure 3-27). The long lifetime, which is used to quantify the Cm (III) outer-sphere sorption, is quenched to ~ 661 microseconds.

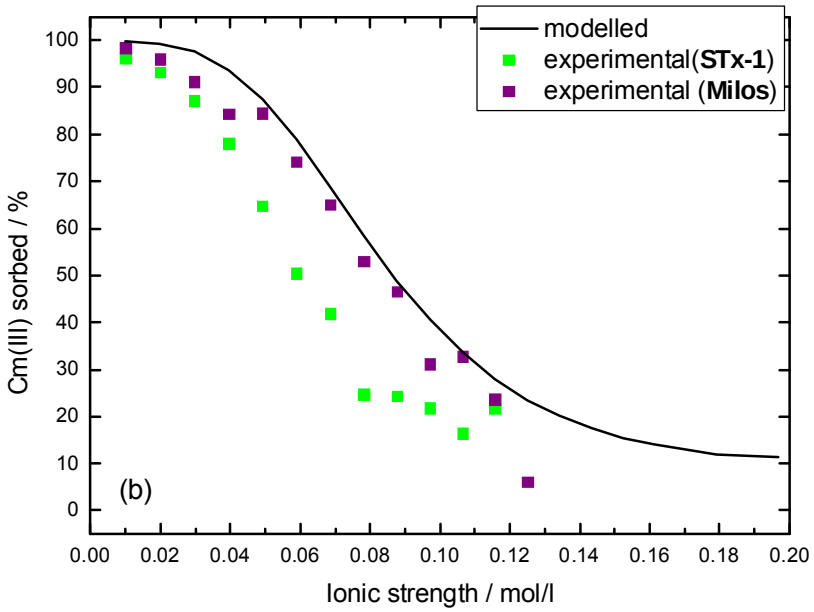

Figure 3-38: Comparison of modelled and experimental results for Cm (III) outer-sphere complex formation on Milos and STx-1 at pD 3.76 and pD 4.01 in D_2O as a function of ion strength ($2 \cdot 10^{-7}$ mol/l Cm(III), 0,3 g/l). Assumptions for modelling see in the text.

In Figure 3-39, the TRLFS results for Cm (III) sorption on IdP-2 in H_2O are compared with the modeled values. It was used by a selectivity coefficient of ${}^{Cm}_{Na}K_c = 76$, which was deduced from studies of the sorption of Eu (III) on illite du Puy (IdP-1 and IdP-2 [Bradbury & Baeyens, 2005b]. The modelled curve overestimates significantly the Cm(III) sorption (black curve in Figure 3-39) at low ionic strengths. Again, a partial dissolution of the clay at pH ~ 4 is assumed. During the reaction period particular aluminum and divalent cations such as Ca^{2+} and Mg^{2+} were released in relevant concentrations from the crystal structure of clay minerals into the solution (s. Table 3-13). These cations and Cm^{3+} compete for the available binding sites on the clay primarily at low ionic strengths. With increasing ionic strengths the competing cations are exchanged by Na^+ from solution. Die Al^{3+} concentration is censoriously compared to Ca^{2+} or Mg^{2+} due to its higher charge and tendency for sorption. [Bradbury & Baeyens, 2005b] have measured the cation concentration as a function of ionic strength in their sorption experiments with Illit du Puy and found about 10^{-5} mol/l for Al^{3+}, and about 10^{-4} mol/l for Ca^{2+}/Mg^{2+}. The model calculation in Figure 3-39 was performed by regarding the competing of these cations in solution of our own Eu(III) batch experiments at various ionic strengths. For the modelling the highest concentration found in the experiment were taken: $Al^{3+} = 6{,}09 \cdot 10^{-5}$ mol/l, $Ca^{2+}/Mg^{2+} = 2{,}49 \cdot 10^{-5}$ mol/l. Other cations like Ti^{4+} and Mn^{2+} had much lower concentration that are relevant and they were neglected. The applied selectivity coefficient of ${}^{Al}_{Na}K_c = 10$ and ${}^{Me^{2+}}_{Na}K_c = 11$ ($Me^{2+} = Ca^{2+}$, Mg^{2+}) were depicted from [Bradbury & Baeyens, 2005b].

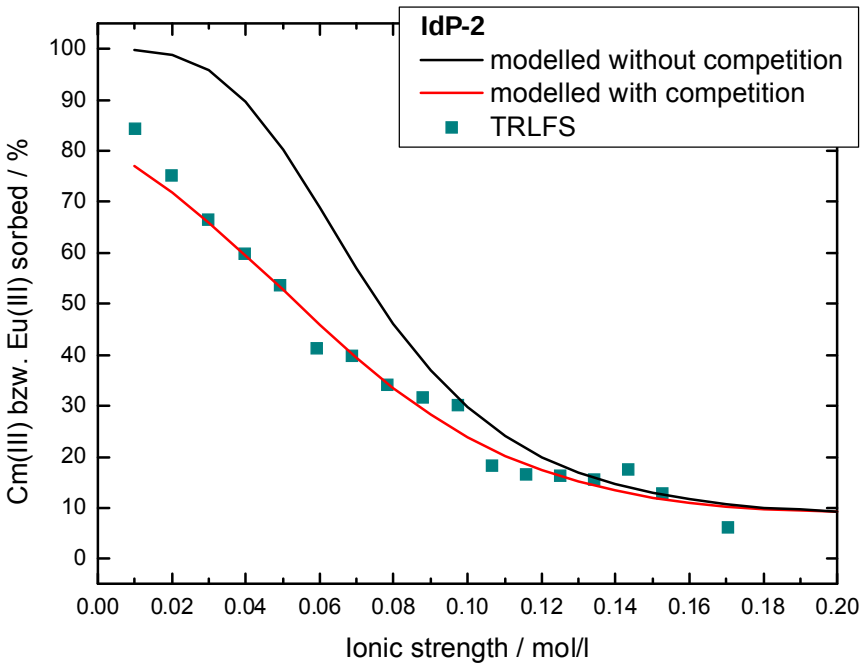

Figure 3-39: Comparison of modelled (with and without considering other competing cations) and experimental results for Cm (III) outer-sphere complex formation on IdP-2 in H_2O by TRLFS at pH 4.02 as a function of ion strength ($2 \cdot 10^{-7}$ mol/l Cm(III), 0,3 g/l). Competing cations: $6.09 \cdot 10^{-5}$ mol/l, Al^{3+} and $2.49 \cdot 10^{-5}$ mol/l Ca^{2+}/Mg^{2+}.

The modelled curve by regarding the competing cations agrees now very well with the experimental data measured by TRLFS. Additional calculation showed that at ionic strengths > 0,1 mol/l less than 10% of the total Al^{3+} in solution is sorbed on the clay. The percentage of Al^{3+} sorption increases very strongly with decreasing of the ionic strength below 0.1 M ionic strenght. Therefore, the competing effect has only small or no effect on the Cm^{3+} sorption at ionic strengths above 0.1 M.

IdP-2 possesses a significant lower CEC as montmorillonite. Therefore, competing effects due to ions released from the clay at tracer concentrations plays a minor role for montmorillonite.

Table 3-13: Concentrations of cations Al^{3+}, Ca^{2+} und Mg^{2+} in aqeous clay suspension due to partial dissolution of the respective clay at pH ~4. Black: elements of batch experiments; blue: elements of the TRLFS experiments.

Clay suspension Sample		Al^{3+} [mol/l]			Ca^{2+} [mol/l]			Mg^{2+} [mol/l]		
		lowest	∅	largest	lowest	∅	largest	lowest	∅	largest
IdP-2	**Batch**	1.76E-05	3.57 E-05	6.09E-05	8.40E-06	8.81 E-06	1.27E-05	3.94E-06	7.48E-06	1.22E-05
SWy-1	**TRLFS**		2.93E-06			1.73E-05			2.96E-06	
	Batch	1.47E-05	3.81E-05	1.04E-04	1.14E-05	1.23E-05	1.39E-05	2.70E-06	9.56E-06	1.73E-05
Milos	**TRLFS**		<5.56E-07			1.45E-05			3.00E-06	
STx-1	**TRLFS**		<5.56E-07			2.01E-05			2.57E-06	
Na-Mont$_s$	**TRLFS**		2.94E-06			2.32E-05			1.78E-05	
	Batch	1,34E-05	3,44E-05	6,81E-05	1,44E-05	2,24E-05	3,50E-05	1,20E-05	1,74E-05	3,06E-05

Batch experiment on Eu(III)/clay outer-sphere complexation

In Figure 3-40 the results of batch experiments with Eu(III) and IdP-2, SWy-1 and the synthetic Na-montmorillonite are compared with each of the modeled values. Here too, experiment and calculation agree quite well within the uncertainties. Deviations are particularly recognizable at higher ionic strengths. An explanation for this behaviour can not be given at the moment.

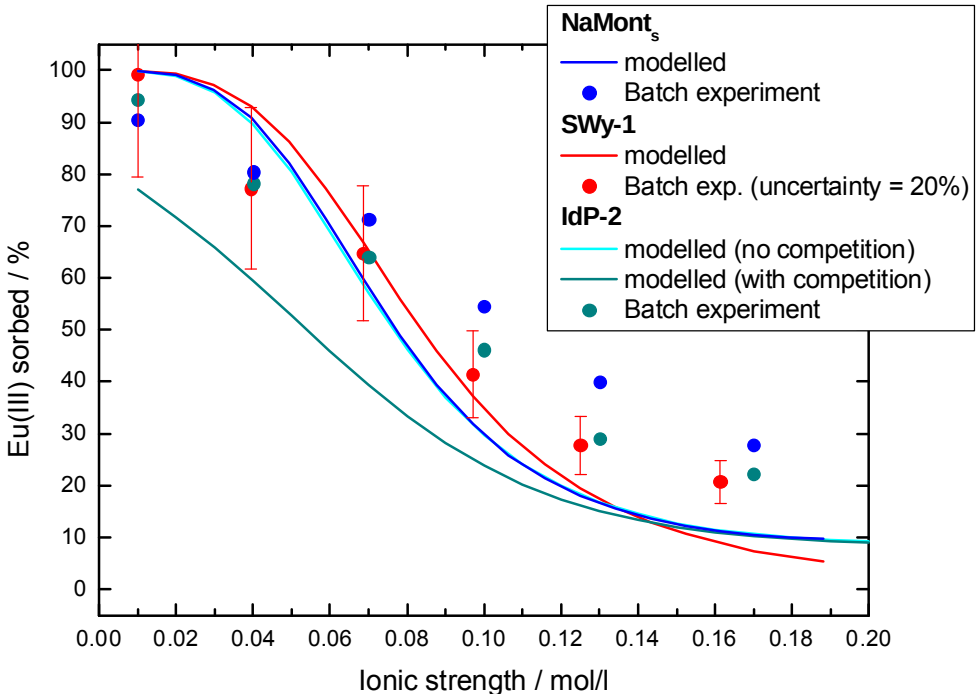

Figure 3-40: Comparison of modelled and experimental results of batch experiments on Eu(III) outer-sphere complex formation on NaMont$_s$, SWy-1 and IdP-2 in H_2O at pH 3.88 to 4.02 as a function of ionic strength ($2 \cdot 10^{-7}$ mol/l Eu(III), 0.3 g/l). The uncertainty of the method is estimated to be 20 %.

4 Studies of the diffusion of actinides and analoga

Owing to its small hydraulic conductivity (10^{-14}-10^{-13}), it is expected that transport of solutes will be dominated by diffusion. The objective of this work is to understand actinide diffusion in clay mineral-rich geological formations in order to provide support for improved representation of these processes in performance assessment and to enhance safety case credibility. This study addresses the diffusion of tritiated water (HTO) and ^{238}Pu. The samples were collected in the Mont Terri underground laboratory where the OPA is situated -200 to -300 m below the surface. Therefore a sample cell -autoclave system (SCAS) was required for carrying out actinide diffusion experiments in clay stones under their natural, confining pressure.
In our experiments we used ^{238}Plutonium. ^{238}Pu is a radioactive isotope of plutonium with a half-life of 87.7 years and is an alpha emitter. Because of its alpha activity (6.3 10^{11} Bq/g), it can be measured by a-spectrometry down to very low concentrations (detection limit in our experimental set-up 1 10^{-11} mol/L). This is important because of the low solubility of Pu in natural waters (Coppin, 2003).

4.1 Diffusion of Pu in OPA clay rock

4.1.1 Experimental set-up

The design of the INE diffusioll cell/autoclave system (SCAS)

To counteract the swelling of clay in contact with groundwater, to avoid disaggregation and to simulate the confining stress within the geological formation, a specifically adapted experimental set-up was developed. The heart of the diffusion cell is a thin-walled stainless steel cell (Figure 4-1) which holds the clay sample (0 20 mm, length 10 mm). All parts of the diffusion cell which are in contact with solution are coated with PEEK. The thickness of the wall of the stainless steel is 2/10 mm. After the positioning of the sample, two PEEK distribution plates are placed on each side of the sample and the autoclave is sealed with screws. This cell is then placed in an autoclave. This autoclave has a volume of 300 ml and is filled with 250 ml of water. With help of a stainless steel pump we pressurized the autoclave with pressures between 0-100 kbars.

Due to the construction of the cell, the confining pressure acts isotropically onto the clay sample. The tubing for tracers and sampling are constructed in such a way that they are kept under ambient pressure and tracer injection and sampling can be performed in closed circulation loops

The solutions are circularly pumped from 100 mL PE storage containers in split cycles with a 2-channel peristaltic pump (IPC, Ismatec, 1dex, USA). The Opalinus Clay samples were re-

saturated by circulating these solutions in contact with the respective end of the sample for 5 weeks. This time was found to be sufficient to reach re¬saturation (Van Loon et al., 2003). Subsequently, the solutions were replaced by fresh ones and the solution in one container was spiked with the desired tracer.

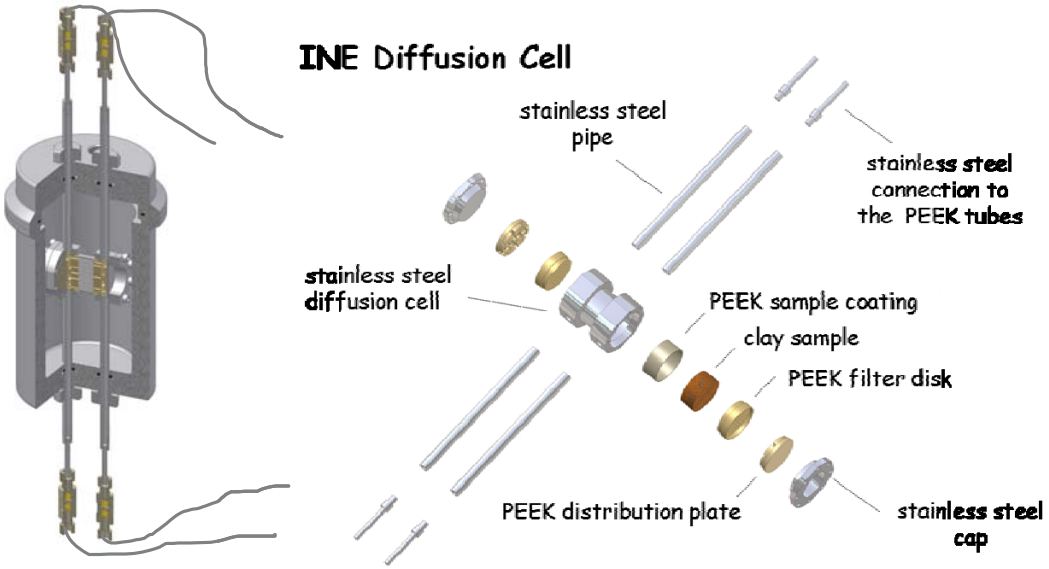

Figure 4-1: Shematic presentation of the INE diffusion cell/autoclave system (SeAS). On the left side the autoclave with the core holder an the feeding system (two pipes connected via tubes with the perestaltic pumps) is shown. On the right side the diffusion cell is illustrated.

Sample preparation and characterisation

The Opalinus (OPA) clay stone sample used for our experiments was provided by NAGRA from the Mont Terri underground research laboratory (URL). All preparation steps were performed under anaerobic conditions in a glovebox. The bore core (BEZ A24/3) With a diameter of 100 mm was sliced into 2-cm-thick pieces using a diamond saw (no lubricating fluid was used). Each slice was cut in two parts. A 20 mm diameter core was drilled out of tile inner part of each slice to avoid tile use of artificially oxidized clay rock material. All samples were drilled perpendicular to tile bedding plane.

The residue of the core was ground in a glove box and the mineralogy of the samples was determined using X-ray diffraction. Quantitative analysis was performed using the Rietfeld method (TOPAS, Bruker AXS). The mineralogical composition is comparable to the one published in (NAGRA, 2002). The porosity of the sample measured by mercury porosimetry was 10 %. The total organic matter (TOC) in tile starting material was measured to be 0.5-1.3 wt % using a LECO-125 CIS analyser. The chemical composition of the sample was determined by XRF.

After completion of the diffusion experiments the samples were pushed out of the diffusion cell and embedded in epoxy-resin (Struers, Fellbach, Germany) to avoid drying out of the

sample. These samples were cut perpendicular to the bedding in two pieces using a diamond saw in the glove box (no lubricating fluid was used) after the epoxy-resin had hardened. The intersection was cleaned with Tesafilm (Beiersdorf, Hamburg) to remove remaining sawdust.

One half of the sample was used for autoradiography. As detector the phosphor storage screen technology was used (Cyclone, Storage Phosphor System, Packard Instrument Company, USA). The measurement period was between 1 h and 7 days. Radiation is stored in reusable phosphor screens of $BaFBrEu^{2+}$ crystals as defect energy. For reading out, the screens are scanned with a red laser and the emission of blue light stored in crystal defects is detected. The main advantages compared to film techniques are the higher sensitivity and the enhanced linear dynamic range. The lateral resolution is 600 dpi equal to about 40 Ilm. The a-activity of the Pu in the diffusion sample was determined against a 500 ppm NIST standard of natural ^{238}U.

In the other half of the sample, the diffusive Pu profile in the rock was determined using the high-resolution abrasive peeling method [Van Loon and Eikenberg, 2005]. Therefore, the sample was mounted on a sample holder and 46 grinding steps using a P220 abrasive paper and 32 grinding steps using a P80 abrasive paper were performed. The grinding paper was manufactured by Struers (Fellbach, Germany). The grinded samples were acidified (HN03, HF and HCI) and shaken for 24 hours. Parts of the grinded samples were used to determine the mineralogy by X-ray diffraction. Therefore a few mg were diluted in ethanol and placed on a silicon wafer (cut in the 711 direction) sealed airtight with a XX dome.

Artifical porewater

The recipe for the artificial pore water used in the diffusion experiments is given in [Van Loon et al., 2003]. Analytical grade chemicals were used to prepare the artificial pore water. The pH was adjusted to the desired values using NaOH and HCI. All the solutions were prepared with deionized water Milli-Q Reagent Water System from Millipore with a resistivity of> 18 MΩ cm^{-1}. The solution pH was measured using an Orion 525A with a Ross electrode calibrated using 4 standard buffers (pH 3, 5, 7 and 9, Merck). Redox potenials were measured with a Orion 525A using a METROHM InLab®Redox Ag redox electrode. Commercial redox-buffers (220mv and 640 mY, Schott instruments) are used for calibration. The measured potential was converted into Eh versus standard hydrogen electrode (SHE) by correction for the potential of the Ag/AgCI reference electrode. The evolution of the Eh was in one experiment continuously in-line measured using an IONODE SI30 gel redox-electrode. The initial and final pH and Eh of the OPA porewater is given in Table 4-1.

Table 4-1: Experimental details of the Pu diffusion experiments. De is the effective diffusion coefficient.

Run number	Run time (days)	D_e HTO OPA (⊥) to bedding (m^2s^{-1})	Initial/final ^{238}Pu conc. (nmol/L)	Initial pH / Eh (V)	Final pH/Eh (V)
HTO test	100	1.53×10^{-11} $6.6 \pm 0.5 \times 10^{-12}$	-	7.8 / 0.360	7.9 / 0.370
OPA1-SCAS1	150*	1.55×10^{-11}	7.64 / 0.028	7.8 / 0.360	8.4 / 0.030
OPA1-SCAS2	280	1.60×10^{-11}	5.63 / 0.287	8.4 / 0.400	8.5 / 0.390
OPA2-SCAS3	93	1.45×10^{-11}	5.38 / 0.312	7.9 / 0.380	8.2 / 0.370

** 120 days in and 30 days out diffusion*

Activity measurements

The activity of the Pu and HTO in solution was measured by liquid scintillation counting (LSC). For Pu 100 III of the sample was acidified with 20 III of 65 % HN03. Then 20 III was placed in a 20-ml polyethylene (PE) counting vial and 10-ml scintillation cocktail was added (Ultima Gold XR, Canberra-Packard). For HTO 20 III of the sample was placed in a 20-ml polyethylene (PE) counting vial and IO-ml scintillation cocktail was added (Ultima Gold XR, Canberra-Packard). The samples were vigorously shaken and placed in a liquid scintillation counter (Quantulus, WALLAC).

The counting efficiency for each tracer was measured using artificial pore water with known amounts of activities. Background measurements were performed in a similar way using artificial pore water without radiotracers. The detection limit of the LSC for Pu in the OPA porewater is about 2×10^{-11} mol/L.

HTO and Pu diffusion in OPA

To test our experimental set-up (e. g. excluding boundary flow effects) and to compare our diffusion cell with other diffusion cells used in literature we performed HTO experiments according to [Van Loon et al., 2003].

The ^{238}Pu diffusion experiments were performed at four different run times and different initial pH values (see Table 4-1). All 3 samples were made out of a drill core from Mont Terri provided by NAGRA.

Pu oxidation states in solution

The Pu oxidation states (Figure 4-2) as a function of time in the Opalinus porewater were determined by PMBP-extraction [Nitsche et al., 1994]. In the stock Pu solution we used in our experiments 15 % Pu(IV) and 85 % Pu(VI) were initially determined in solution.

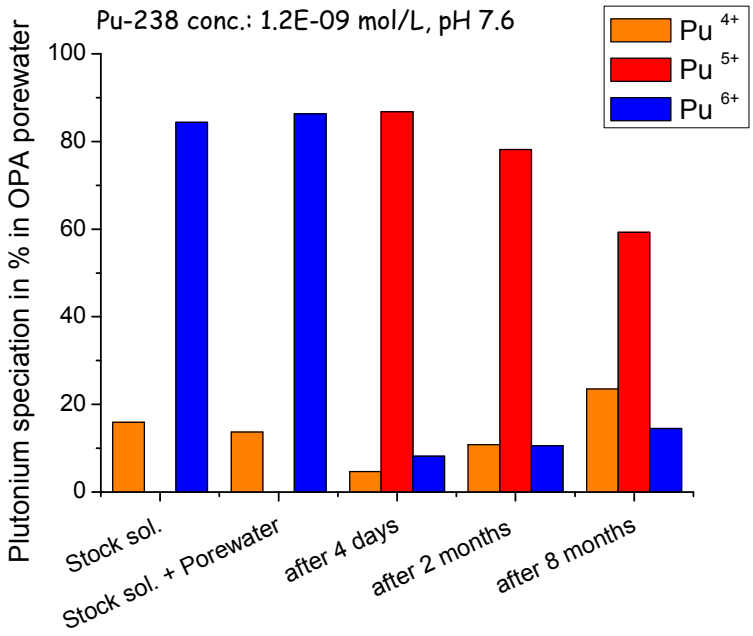

Figure 4-2: Evolution of the Pu speciation in the OPA porewater. The sorbed Pu(IV) from the container walls was added to the Pu(lV) in solution

4.1.2 Results

HTO diffusion in OPA

With four different OPA samples we measured the effective diffusion coefficient (De) perpendicular to the bedding for HTO. We used HTO to verify if our diffusion cells show any preferential pathways. All values are given in Table 1. The average De was found to be $1.53 \cdot 10^{-11}$ m2/s. All obtained results are within a variation range of 10 % of the average value. In one experiment (HTO Test) we cut the diffusion core at the end of the HTO experiment into a half to verify by autoradiography if the HTO diffusion was homogeneous within the core (Figure 4-3). The HTO distribution in the OPA is homogenous. No preferential pathway or any enrichment of the HTO within the sample was detected.

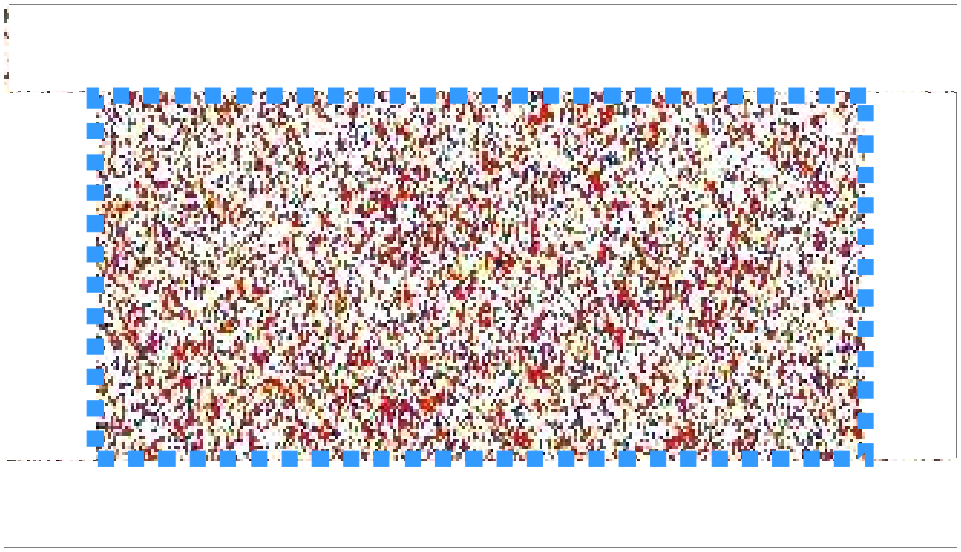

Figure 4-3: HTO diffusion in the OPA visualized by autoradiography. The blue rectangle represents the OPA core. Red indicates high HTO activity. The cooler the color gets the lower the HTO concentration. It can be seen that the HTO is distributed homogeneously within the OPA core.

Evolution of the Pu oxidation states in the OPA porewater

The Pu oxidation states (Figure 4-2) as a function of time in the Opalinus porewater, in which was no reducing component, were determined by PMBP-extraction [Nitsche et al., 1994] for a period of one year. In the Opalinus porewater the pH was adjusted in the beginning to pH 8.2 and the Eh was ~380 mV. No change in pH and Eh was observed during the experiment. Whereas in the stock solution 85 % Pu(VI) and 15 % Pu(IV) were observed, the Pu oxidation state changed predominantly to Pu(V/VI) (72 %) after 4 days equilibration time in the OPA porewater. The evolution of the Pu-238 concentration in solution indicates with increasing run time a continuous but steady decrease of the Pu concentration. After one year, only 26 % of the initial Pu was found in solution. After washing the container with HNO_3 at the end of the experiment the Pu were found to be sorbed on the container walls. This Pu was found to be nearly 100 % Pu(IV). Adding the sorbed Pu from the container walls to the Pu in solution (Figure 4-2) the Pu oxidation states changed to 83 % Pu(IV) and 17 % of Pu(V/VI) in the OPA. In the experiments with clay minerals present no sorption on the container wall was detected.

Results of the Pu diffusion in OPA

Three different diffusion experiments are presented, two behave equally and one is different (Figure 4-4). For OPAl-SCASl we observed a first strong and fast decrease in the Pu reaching a "steady state" concentration of $2.7 \cdot 10^{-11}$ mol/L after seven days. During the experimental run time of 150 days the pH shifted from 7.83 to 8.43 and the Eh dropped from 430 to 30 mY. In the two other experiments the pH and the Eh of the OPA porewater remained unchanged throughout the experiment. The Pu concentrations dropped in OPAI-SCAS2 by one order of magnitude of $\sim 6 \cdot 10^{-10}$ mol/L after 16 days. In the OPA2-SCAS3 experiments the decrease in

the Pu solution concentration appeared faster. After 70 days the Pu concentrations for both systems converged and reached a "steady state" concentration of~$3 \cdot 10^{-10}$ mol/L.

At the end of the experiment OPA2-SCAS3 (93 days) the Pu oxidation state in the solution was determined. Like in the OPA porewater in contact with the Opalinus clay, we found as the dominant oxidation state Pu(V/VI) whereas on the OPA Pu(IV) was dominant.

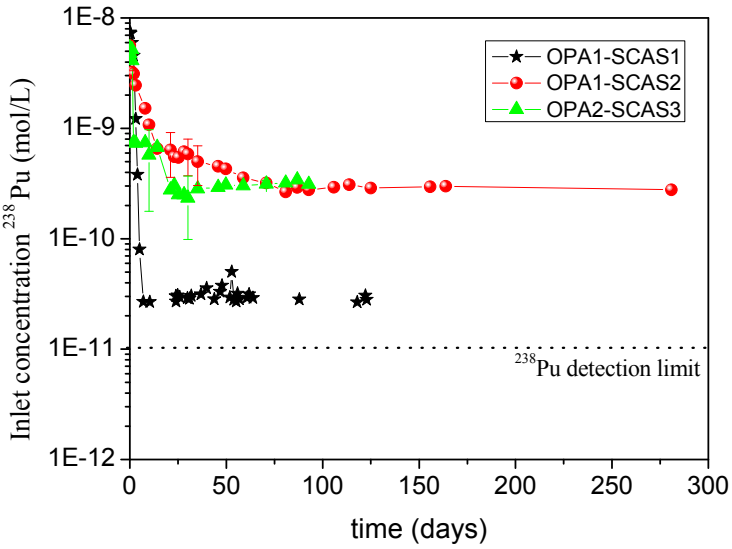

Figure 4-4: Evolution of the solution ^{238}Pu concentration in the diffusion experiment as a function of time

On the blank concentration side of the all 3 experiments the first a-activity was measured after 30 days experimental duration. A selective Pu extraction indicated that the detected a-activity was not due to through-diffusion of ^{238}Pu, but came from ^{228}Th released to the solution from the Opalinus clay sample.

At the end of the experiments the autoclave system and connected tubings were washed for two hours with 65 % HNO_3 to check sorption to the experimental set-up. This test showed that around 20-40 % of the initial ^{238}Pu concentration was sorbed on the container walls and the tubings ofthe diffusion experiment.

Out diffusion experiments

After 120 days of experimental run time we replaced the Pu spiked OPA porewater of the OPAl-SCASl experiment against fresh OPA porewater. No Pu out diffusion was observed during 30 days. Similar out diffusion experiment over 40 days have been performed after the in diffusion of Pu into Bure clay with the same result that no Pu was released from the clay into the solution. The in and out diffusion is illustrated in Figure 4-5.

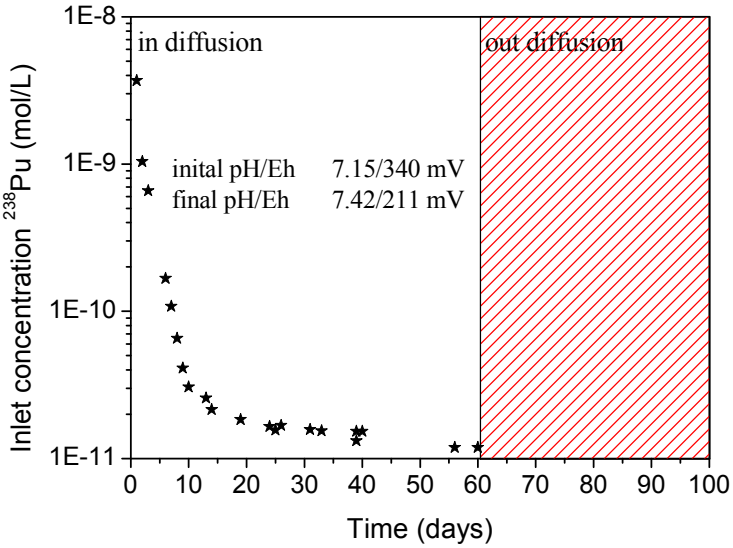

Figure 4-5: In and out diffusion experiment with ^{238}Pu in a Bure clay (PAC 1002/K70; 13.47 – 13.61 m depth). The initial concentration of Pu in the porewater was $7.8x10^{-9}$ mol/L.

Analysis of the cores

Traces of saw dust contaminated the embedding medium (epoxy-resin), therefore the interface between embedding medium and the clay sample was difficult to determine by autoradiography in the first samples (Figure 4-6). By putting a silver foil to create a sharp contrast on the sample we solved the problem (Sample OPAl-SCASl). All 3 cores show clearly that no preferential pathways for the migration of Pu exist.

It is evident that the Pu diffusion within the OPA is not homogenous. The Pu is always concentrated in distinct areas which are distributed differently within the core. In Figure 4-6 the Pu concentration is indicated by colours. Red means areas of Pu concentrationand the lighter the colour, the lower the concentration. The highest punctual concentration of Pu measured was 200 ppm in the crosscut through the clay core of OPA2-SCAS3 we found 2 distinct areas on the left side where the Pu is concentrated. SEM-EDAX analysis showed no specific elemental concentration or any specific mineral phase in this area. By measuring the activity of the Pu sorbed on clay particles sticking on the distribution plate we were able to show that the solution really covered the whole sample. The measured profiles are subsequently different for the two sides of the sample. Whereas profile I shows the diffusion of the Pu of - 5 mm at the end of the experiment (93 days) the diffusion in profile 2 is much more restricted (- I mm). A similar observation was made for OPA2-SCAS2. In OPAI-SCASI we found some pyrite in the areas of high Pu concentration but also Pu enrichments in areas with no specific elemental concentration. In this core the Pu activity was concentrated at the surface of the core.

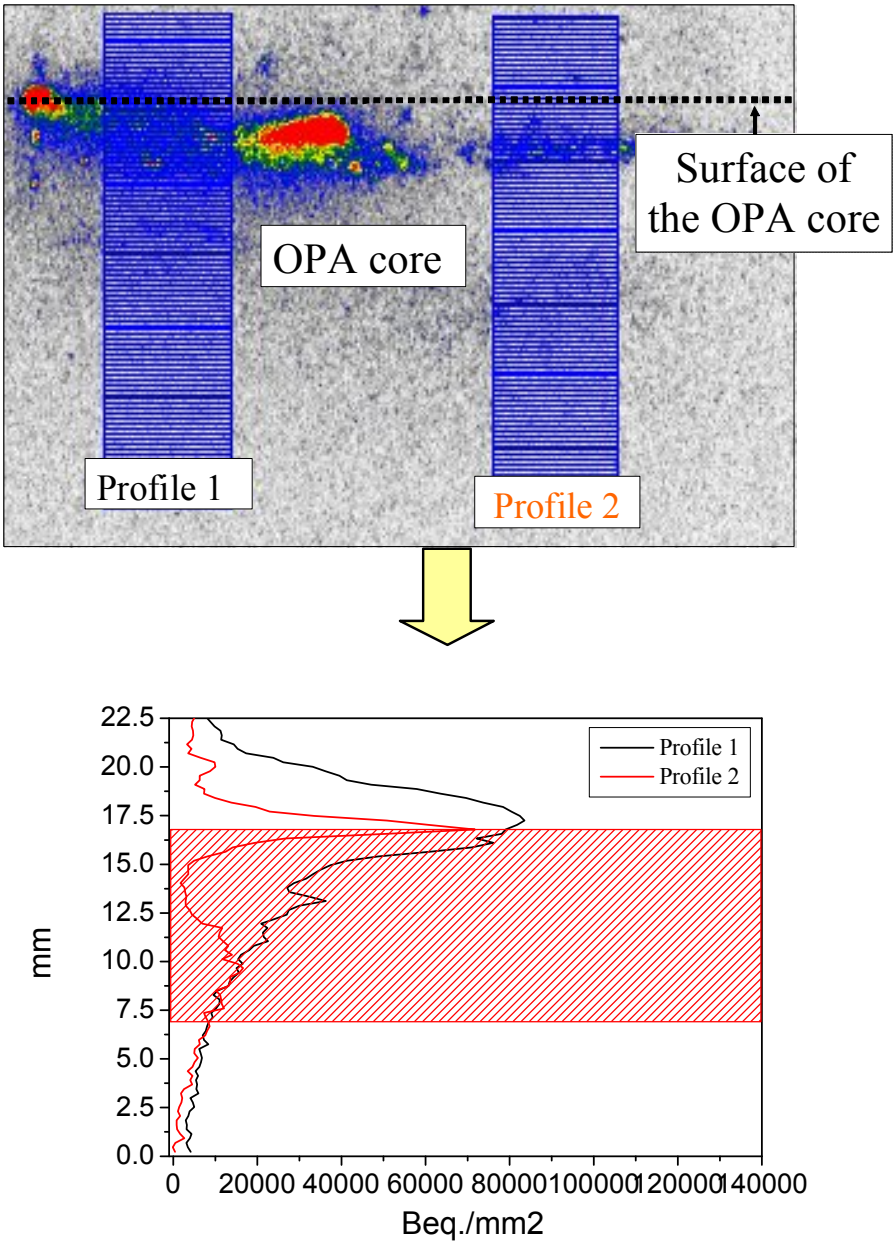

Figure 4-6: Two different diffusion profiles measured for OPA2-SCAS3 with autoradiography. The filled pattern indicates the clay sample. The dotted line indicates the background radiation from the Opalinus clay. The different colors represent different concentrations. Red indicates the highest and the grey color the lowest concentration.

HTO diffusion in OPA

The effective diffusion coefficient perpendicular to the bedding was found to be 1.53 x 10^{-11} m^2/s. This value is in good in agreement with the data of [Van Loon et al., 2003]. The results from the autoradiography demonstrated that the HTO diffusion within the core is homogenous. No preferential pathways exist for the diffusion of HTO and so Pu.

Pu in the OPA pore water

To investigate the stability of Pu in the OPA porewater the Pu concentration, oxidation state distribution, pH and redox potentials were monitored as a function of time. At first the Pu(VI)

is partly reduced in the OPA porewater to Pu(V). Because of the initial low Pu concentration no change in the Eh can be observed. In the sample the Pu(VI) is nearly completely reduced to Pu(V) and further to Pu(IV). This observation is in agreement with the observation made by [Neck et al., 2007]. Because of the reduction of the Pu(V) to Pu(IV) we might exceed the equilibrium concentration and consequently precipitate colloidal Pu(IV) which sorbs on the container walls. With a concentration of 1 x 10^{-10} moI/L we are at the solubility limit of Pu(IV) in the given system [(Neck et al., 2007)].

Pu concentrations in the diffusion and sorption experiments

Two trends for the Pu concentration can be observed in the diffusion experiments. In OPA1-SCAS1 the Eh dropped from 430 to 30 mV during the experiment. After only seven days Pu concentration reached a steady state of ~3x10^{-11} moI/L. In the other two experiments the Eh remained unchanged and the Pu concentration decreased slowly and finally remains one order of magnitude higher than in the OPA1-SCAS1. A post mortem Rietfeld refinement method of the upper layer of the OPA1-SCAS1 diffusion core, where we observed a drop in Eh, indicates a high amount of pyrite (-45%) in the uppermost layer of the core. A similar observation was made for the sorption experiments. In some samples, enriched from the beginning in pyrite, Pu was nearly completely sorbed within one hour of contact time accompanied by a decrease in Eh. At least two different possibilities exist concerning the fate of the initial Pu(VI) in solution.

- The Pu(V/VI) was reduced in solution with electrons from the OPA porewater to Pu(lV) [Neck et al., 2007]. The resulting Pu(lV), possibly present in colloidal form, is sorbed on the surface of the minerals at preferential sites or precipitates after exceeding the solubility limit as PuO_2(hyd, am). The Pu activity in this case was concentrated on certain spots on the surface of the diffusion core.
- The other possibility is that Pu(VI) was first sorbed and finally reduced on the mineral surfaces as it was described for pyrite by [Eglizaud et al., 2006] or [Wersin et al., 1994] for U(VI).

Because of the very low concentrations used in the experiments we have no direct possibility to verify the different possibilities so far and further experiments are needed.

4.1.3 Conclusions

Diffusion of Pu and HTO in the OPA was studied by the through-diffusion method. The diffusion coefficients for HTO from our experiments were in excellent agreement with those determined in through-diffusion experiments in other laboratories. The experiments show that (i) about 20-40 % of Pu is sorbed on components of the experimental set-up, (ii) there is considerable impact of the samples natural alpha¬emitting inventory, (iii) the mobile Pu inventory is dominated by Pu(V), (iii) there is no preferential transport pathway for Pu in the clay sample and that Pu is concentrated within the clay core at certain sites. The Pu sorbed on the

samples was reduced to Pu(IV). Futher experiments are needed to determine the reducing and subsequent sorbing phase. Traces of oxygen in the system will lead to the formation of iron oxides/hydroxide which will sorb the Pu directly out of solution.
Trustworthy determination of the diffusion behaviour of actinide ions in clay requires carefully designed experimental set-ups and development and application of a series of analytical techniques. Careful cross-checking is required in order to verify that the samples are not subject to undue disturbances, especially those resulting in preferential artificial transport pathways. Furthermore, delineation of natural activity inventory from the studied ions and identification of inventory lost in the equipment is a precondition for adequate interpretation of the experimental results.
Trustworthy interpretation of transport experiments also requires batch sorption data and 3D distribution of along the diffusion samples. The present work shows that all these objectives have been demonstrated for an in-house built diffusion experiment system and development and application of the required associated analytical techniques. These ongoing investigations will provide the necessary basis for credible description of sorbing radionuclide mobility in clay for the nuclear waste disposal safety case.

4.2 Analogue study on the uranium speciation in argillites from the Lodéve Basin (France)

Another objective was the comparison of natural organic matter clay association found in potential host rock formations (COx and OPA) with those found in uranium deposits of comparable mineralogy (i.e. argillite). Argillaceous clay-rich formations with organic matter and radionuclide (uranium) present in the Lodève Basin (France) was considered as potential analogue based on the geological history of the basin and the presence of the three main components, i.e. radionuclides (U), clays and natural organic matter, subject of our project (Marignac and Cuney, 1999; Schlepp et al., 2001). Main objective was a better understanding of the association between clay minerals (chlorite and illite), uranium and organic matter found in this sedimentary basin under the form of coal; a key question with regard to the understanding of U immobilization in nature considering geological time-scale.
Results of spatially resolved X-ray fluorescence and X-ray absorption fine structure investigations with a micrometer-scale resolution (μ-XRF and μ-XAFS, comprised of the near ionization threshold energy region, XANES, and the extended energy region, EXAFS) on two uranium-rich clay samples originating from Autunian shales in the Permian Lodève Basin (France), provided by CREGU (Centre de Recherche sur la Géologie des Matières Premières Minerals et Energétiques) are reported here. This argillaceous formation is a natural U deposit (or mineralization) associated with organic matter (bitumen) (Marignac and Cuney, 1999; Mathis et al., 1990). The goal of this study is to determine the U oxidation state in the sample and to ascertain if any correlation between the U distribution and that of other elements present in the organic-rich fine-grained pelites exists, which might give us insight into the

mechanism of U immobilization through either adsorption/co-precipitation with iron hydroxides and/or clay minerals.
Autoradiographic images and photographs of the samples are shown in Figure 4-7. Uranium-rich areas of the sample or hot spots are visible as dark spots in the autoradiographic images. Quantification of the hot spots shows that they contain ~2 mg 238-U/g material (sample marked P31) and ~25 mg 238-U/g material (sample P15).

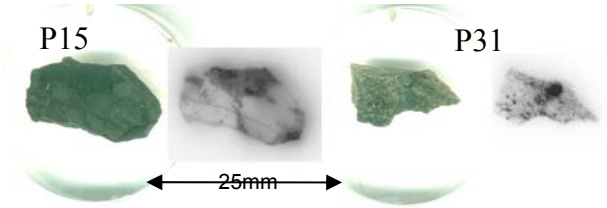

Figure 4-7: Photographs of the samples studied embedded in acrylic (designated P15 and P31) and their corresponding radiographic images.

µ-XRF and µ-XANES measurements are recorded at Beamline L at the Hamburger Synchrotron Labor (HASYLAB). A confocal irradiation-detection geometry is used, providing added depth information and allowing probing sample volumes below the surface, thereby avoiding any surface oxidation artifacts caused by cutting and polishing the clay sample. Elemental distribution maps are obtained by means of scanning µ-XRF and plotting recorded relative fluorescence intensities for each pixel and scaling them with a linear color code, with dark pixels corresponding to high count rates. By scanning arbitrary sample areas (xy scans) at different depths (z) using the confocal setup, stacks of tomographic cross sections can be easily recorded (Denecke et al., 2005a; Janssens et al., 2004). Polycapillary half lenses are used for both focusing and collimating optics. The focal spot diameter is approximately 16 µm. µ-XRF measurements are recorded using a band pass of wavelengths with an average weighted energy of 17.6 keV delivered by a Mo/Si multilayer pair (AXO Dresden GmbH, Germany) and a Si drift detector (Vortex, SII NanoTechnology USA Inc., Northridge, CA). U L3 µ-XANES are recorded using monochromatic X-rays at selected sample volumes of high U concentration identified in the µ-XRF maps at Beamline L. Both XANES and EXAFS are measured at positions of high U concentration identified by line scans of windowed U Lα counts registered with a high purity Ge detector (Canberra) at the INE-Beamline at the Ångströmquelle Karlsruhe, ANKA (Denecke et al., 2005b). The measured beamspot at the INE-Beamline is 300µm. Si(111) and Ge(422) crystals are used in the double crystal monochromator at HASYLAB and ANKA, respectively, and the energy is calibrated relative to the first inflection point in the K XANES of a Y foil (defined as 17.038 keV).
The measured distributions for K, Ca, Ti, Fe, Zr, and U in the area with the highest radioactivity at the top of sample designated P15 are shown in Figure 4-8 and Figure 4-9.

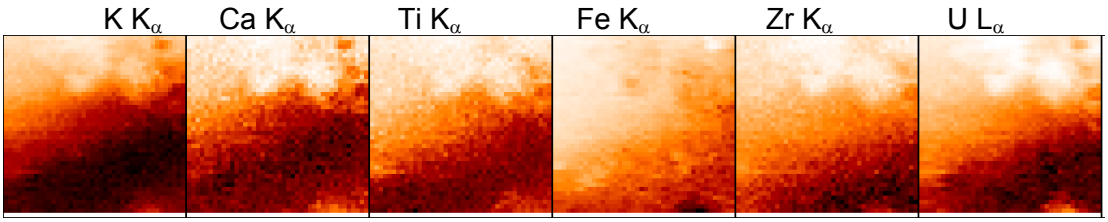

Figure 4-8: Distribution maps for the elements indicated in a 800 x 760 µm2 section (20 × 20 µm2 step size), recorded near the surface of sample P15.

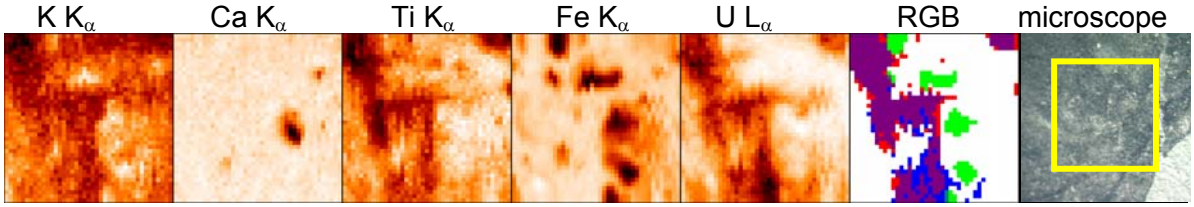

Figure 4-9: Distribution maps for K, Ca, Ti, Fe, and U in a 400 µm x 400 µm section (10 x 10 µm step size, 1s counting time), recorded under the surface of the sample 31 area marked in the microscope image at far right. RGB overlay image for regions of highest Ti, Fe, and U concentrations is shown.

These distributions demonstrate three general observations from this sample: 1) distinct patterns of element distributions are observed, despite the sample's general heterogeneous optical appearance 2) the U distribution is often correlated with the distributions of lighter weight elements K, Ca, and Ti (especially notable in the round features in the upper right corner of the maps) and 3) the U distribution is generally inversely correlated to areas of high Fe content.

In order to determine the valence state of the U in the pelites, U L3 µ-XANES (Figure 4-10 and Figure 4-11) and µ-EXAFS (Figure 4-12) are recorded at volumes and areas with high U Lα intensity. The energy position of the most prominent absorption peak in the XANES (the white line, WL) measured for different sample regions at two different beamlines (INE-Beamline Figure 4-10 and Beamline L and Figure 4-11) all lie within less than 1 eV of that for the U(IV) reference. The XANES features themselves also provide further evidence that the U hot spots contain U(IV). No evidence for the presence of any U(VI), which would be indicated by a decreased WL intensity and multiple scattering feature around 10 eV above the WL (Denecke, 2006), was found. We conclude that U is likely present in the sample in the tetravalent state.

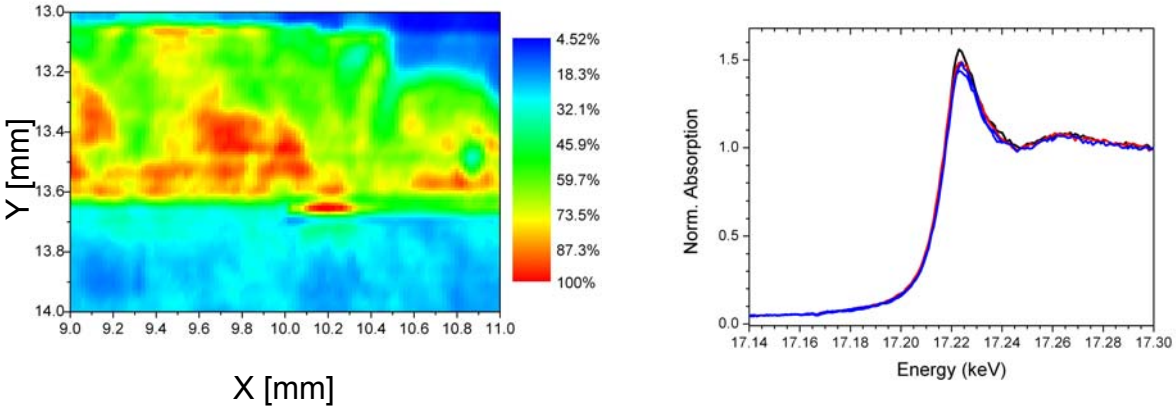

Figure 4-10: Left: U distribution for a 2000 x 1000 µm2 section (30 x 30 µm2 step size) recorded at the INE-Beamline at the surface of sample 15. The normalized U Lα intensity scale bar is indicated. Right: U L3 µ-XANES recorded at four independent areas with high U Lα intensity.

This interpretation is corroborated by the U L3 EXAFS spectrum (Figure 4-12). No short U-O distance expected for the U(VI) uranyl moiety is found in the EXAFS spectrum (Denecke, 2006). The data is well fitted beginning with a structural model similar to uraninite, UO_2 (Rundle et al., 1948). Best fit results are obtained with 4-5 O atoms at 2.29 Å with σ^2 = 0.013 Å^2 and 2-3 U atoms at 3.78 Å with σ^2= 0.008 Å^2. The distances are 2-3% smaller than expected for UO_2 and the intensities lead to a much smaller coordination number than expected (N(O)=8; N(U)=12). This may indicate that the UO_2-like phase is present as a nanoparticulate material with large surface area having relaxed (shortened) distances at the surface.

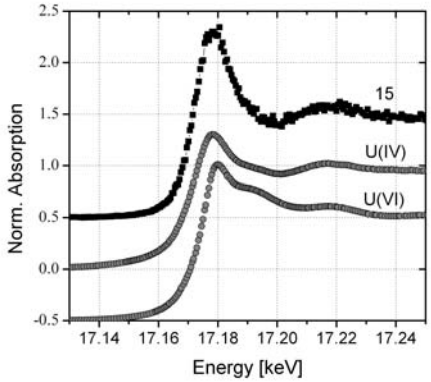

Figure 4-11: U L3 µ-XANES recorded at U hot spots of sample 15 at Beamline L (symbols) and compared to two U(IV) and U(VI) reference spectra (bottom)

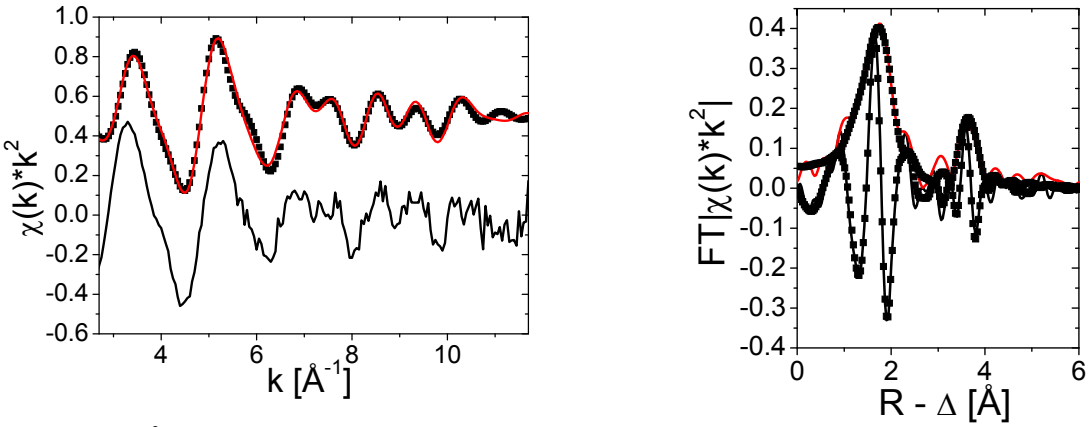

Figure 4-12: U L3 k^2-weighted EXAFS (χ(k); left bottom), Fourier-filtered data and best fit results (left top) and corresponding k^2-weighted Fourier transform (FT) data (right) plotted with best fit results. Experimental data = lines. Fit curves = symbols.

STXM results

The STXM data of sample 15 and results of PCA and cluster analysis are depicted in Figure 4-13. We observe a homogeneous distribution of organic carbon, with the exception of one strip (grey area, upper right in Figure 4-13), where no absorption at the carbon K-edge is detected. The yellow and red areas found in cluster analysis differ in their optical density (OD) and K content. The red areas exhibit a significantly higher OD below the carbon K-edge (OD ~0.8; see Figure 4-14) and significant absorption bands at potassium $L_{2,3}$-edge energies. This indicates that this organic material is associated with clay minerals possibly of illite-type. The relatively large edge jump (ΔOD ~0.4) of these regions shows that a rather large amount of organic material is associated with these clay minerals. The yellow areas indicated in the Figure 4-12 are additional organic material, which is not directly associated to these mineral phases. The low OD (<0.1) below the carbon edge found for this material might indicate that it is of almost pure organic nature. The average cluster C(1s)-edge spectra extracted from both regions (Figure 4-13) are not very different, except for the yellow areas appearing to have a higher aromatic content (absorption at 285 eV) and the illite-clay associated organics show higher absorption in the 287 eV region that suggest a higher aliphatic character or metal complexation (Plaschke et al., 2005).

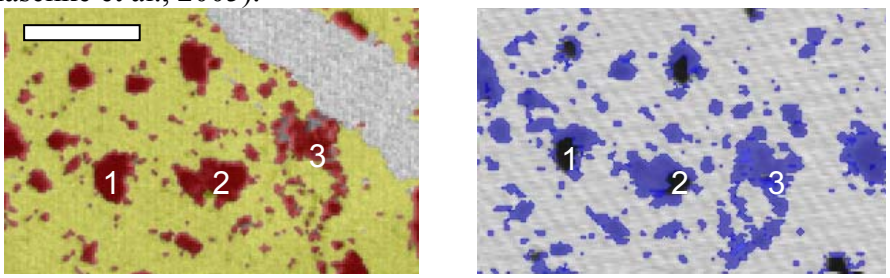

Figure 4-13: STXM PCA and cluster analysis of sample 15. (left) Distribution of organic functionality with two distinguishable clusters found using PCA and cluster analysis. (right) distribution of iron absorption. The scale bar is 10µm. As the Fe L-edge region is slightly rotated counter-clockwise numbers are inserted for orientation.

Three distinct regions in the iron L-edge image of sample 15 are identified. The grey cluster shows no OD; the cluster marked with black color does not show any iron $L_{2,3}$-edge features but a generally high OD (see Figure 4-14); the blue region is characterized by absorption features at the Fe L-edge. The areas are nearly coincident with areas exhibiting potassium absorption peaks and highest organic absorption. Spectral feature changes within particles in the blue cluster region (not shown separately) appear to indicate that the core part of these particles either exhibit no iron content or a higher absorption in the Fe(II) energy region, whereas in the rim region of these particles have a higher Fe(III) content.

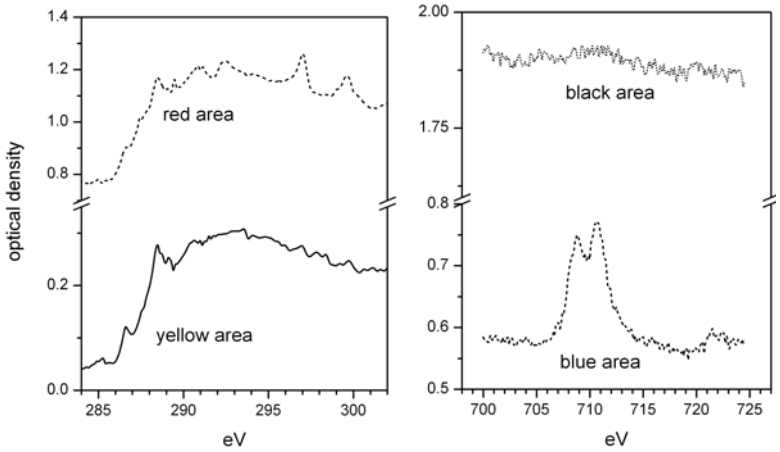

Figure 4-14: (left) Average C(1s) XANES of sample 15 of the yellow and red areas indicated in Figure 8and (right) average Fe L-edge spectra marked in blue and black.

In the fault breccia sample 31 STXM results, PCA and cluster analysis reveal two distinct regions of organic matter. The fracture network infill region (Figure 11) is characterized by organic material with a high content of oxygen containing functional groups (i.e. carboxyl-type groups absorbing around 288.6eV) and a clear π^* peak near 290.2eV, indicative of carbonate. The second region of generally higher OD is associated with clear absorption bands at 297 and 300eV, indicative of the potassium L-edges. This organic material is apparently associated with K-containing minerals. Interestingly, both carbon spectra show no C_{arom} absorption (~285eV), but the mineral associated organics have a significant higher aliphatic content (~287.4eV absorption). Some but not all K-rich regions coincide with Fe regions in Figure 4-15. The iron L_3-edge shows there is a high content of Fe(II) phases, which is visualized in the comparison with a hematite reference spectrum in Figure 4-16.

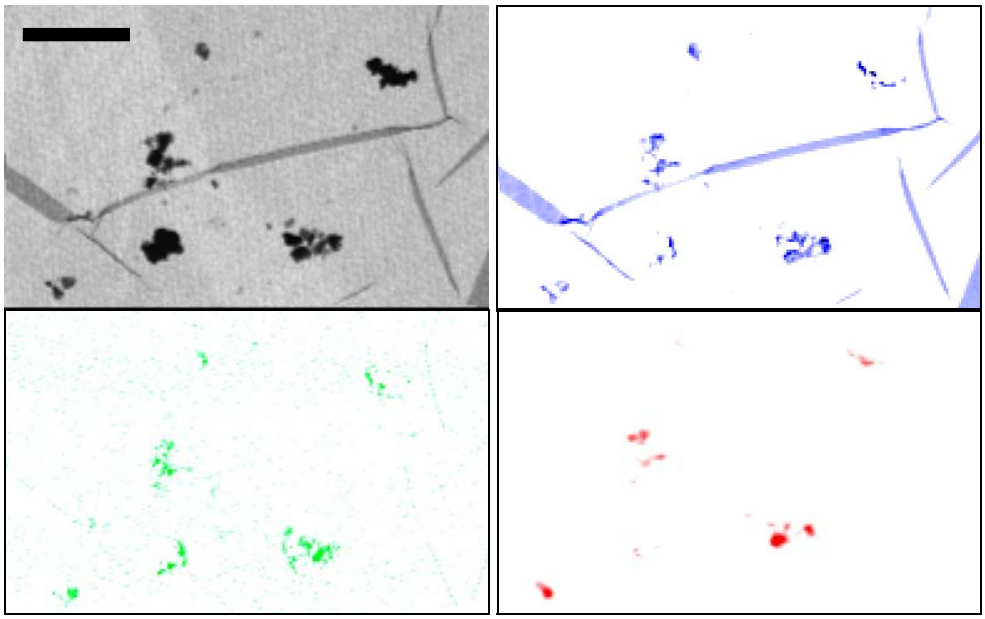

Figure 4-15: (upper row from left to right) STXM absorption image at 290eV and carbon distribution map; (lower row from left to right) potassium and iron distribution maps taken from XANES ratio images (sample 31). High color intensity indicates high content of selected element. The scale bar represents 10µm.

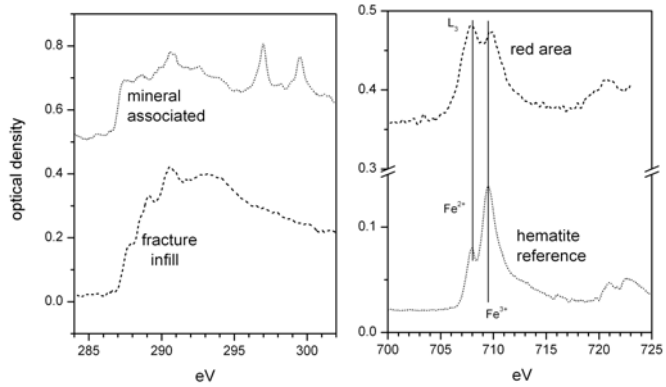

Figure 4-16: (left) Average C(1s) XANES of sample 31 fracture infill and the mineral associated organics. The mineral associated organics are clearly linked to potassium containing phases as indicated by the L-edges at 297 and 300eV. (right) Average Fe L-edge spectra from areas marked in red in Figure 11.

µ-FTIR results

Spectral maps imaging the spatial distribution of functional groups in the sample including aliphatics (ν_{CHali} ; 3000-2800 cm^{-1}), aromatics ($\nu_{C=C}$; 1750-1500 cm^{-1}), alcohols (ν_{OH} ; 3600-3100 cm^{-1}) or OH vibrations of clay minerals ('OH' 3720-3680 cm^{-1}) are extracted from scanning µ-FTIR data. An example of the maps is illustrated in Figure 4-17. Inspection of the functional group distributions reveals a correlation between the clay mineral vibration bands ('OH') and the organic matter functionalities (ν_{CHali}, $\nu_{C=C}$, ν_{OH}). This observation confirms the potassium (i.e. illite-type clay mineral) – organic matter correlation observed in the STXM investigations.

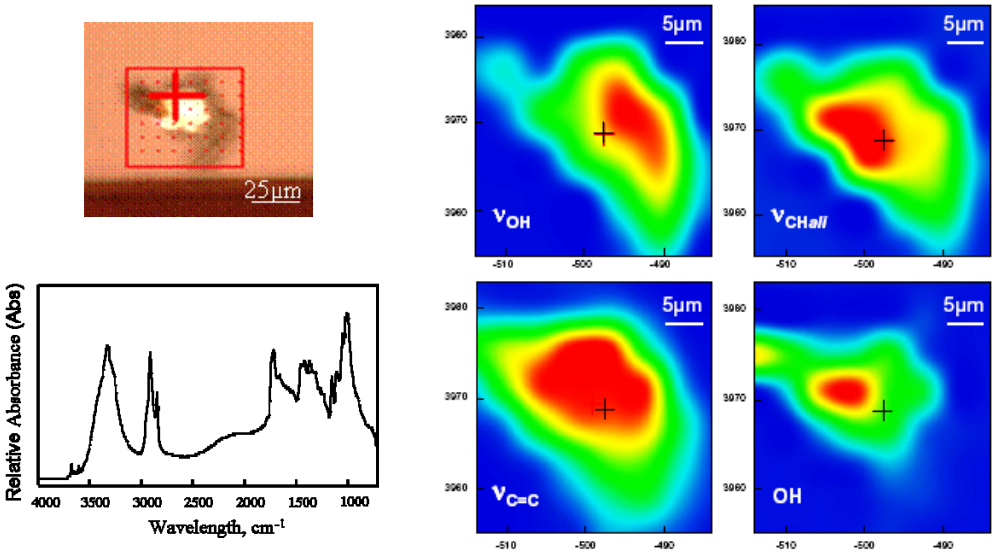

Figure 4-17: (upper left) Visible light microscope (VLM) image of the microtome sample 15 studied and (lower left) µ-FTIR spectrum of the spot marked by the cross line in the VLM image. (right) Maps of organic functional group distributions extracted from µ-FTIR data: alcohols (□OH; 3600-3100 cm-1), aliphatics (□CHali; 3000-2800 cm-1) and aromatics (□C=C; 1750-1500 cm-1), as well as OH vibrations of clay minerals ('OH' 3720-3680 cm-1).

4.2.1 Conclusions

In summary, application of various spatially resolved spectroscopic methods have been successful in characterizing the uranium speciation in sediment samples from the Lodève Basin and in evaluating if organic matter or Fe^{2+}, Mn^{2+}, S^{2-} mineral phases were responsible for uranium immobilization/enrichment in the sediment. µ-XANES and µ-EXAFS results show that uranium in both sediment samples studies is found in the tetravalent state, most probably in the form of nano-crystalline UO_2-like phase. The correlations between elements obtained by means of different techniques (µ-XRF, STXM and µ-FTIR) allow us to conclude the following. The uranium distribution in sample 15, originating from the contact zone adjacent to the fault zone, is positively correlated to the distribution of lighter weight elements (Ca, K, Ti). We deduce a correlation between clay minerals of illite- type and organic matter in the sample based on the observation that potassium (as indicator element) is found associated with both organic carbon and Fe and the observed spatial coincidence between µ-FTIR clay OH vibrations and various vibrations of organic functional groups.

Sample 31, originating from the breccia facies within the Lodève Basin fault zone, also exhibits a positive correlation between uranium and the elements K, Ti and a negative or anti-correlation between the distribution of uranium and those of Ca and iron. In sample volumes of highest potassium content, no Fe Kα signal is observed. Two distinguishable clusters of organic material in sample 31 are identified. The first type is associated with fracture infill and lacks K and Fe signatures, but displays a detectable carbonate peak in its C(1s) XANES. The second cluster type of organic material is associated with discrete mineral aggregates, exhibiting a spatial coincidence between carbon absorption and Fe and K absorption. Because

an anti-correlation between uranium and Ca/Fe exists and because carbonates (likely Ca-containing) are associated with organics in the fracture infill we conclude that the fracture infill in this sample is not associated with uranium.

From these observations we attempt to put forward a tentative hypothesis for the mechanism of uranium immoblization. Due to the lack of the correlation between uranium and Fe, we exclude Fe-minerals as dominant reductant during immobilization of U(VI) to U(IV). Combining the knowledge that uranium is found associated with potassium and that clay minerals of illite-type are associated with organic matter we conclude that organic material associated with clay minerals might have played a role as reductant thereby reducing incoming groundwater dissolved U(VI) to less soluble U(IV). This hypothesis remains speculative; numerous unanswered questions remain. For example, what role did the clay play? Did it act as a catalyst (Giaquinta et al., 1997) or was it merely an anchor for the organic material? In addition, how do we explain the apparent discrepancy between the spatial relationship between potassium and iron distributions observed in the μ-XRF maps with that from STXM results? To help refine our understanding of the redox partner involved in the reduction of U(VI) in this sediments combined μ-XRD/μ-XRF studies are planned.

We note a critical aspect of the comparison of μ-XRF and STXM results made in this study: the sample region actually analyzed. Disregarding the depth resolution used in the confocal setup (providing volume information), the estimated area probed with μ-XRF is 608,000 μm^2 for sample 15 and 160,000 μm^2 for sample 31. The STXM measurements are limited to an area of 1,600 μm^2 for both samples. The STXM area investigated in this study represents only 1‰ (sample 31) and 2.6‰ of the μ-XRF region probed. Expressed in another way, STXM results stem from an area equivalent to only 16 data points of all the data points plotted in the Figures 4 and 7 combined. This points to the imminent difficulty of nano-focused techniques, namely to which extent selected sample regions studied are representative of the macro-scale system of interest. With this in mind, the correlations made in this study are surprisingly consistent with one another.

5 Speciation of actinides in the clay system

The redox speciation of Np(V), Pu(V) in OPA and COx suspensions were investigated by X-ray absorption fine structure (EXAFS), UV-Vis/NIR absorption, and liquid-liquid extraction. The redox speciation of plutonium and neptunium on the solid clay was performed by EXAFS and x-ray photoelectron spectroscopy (XPS). Because of the strong sorption of some radionuclides, the concentrations in solutions are very low and reach the detection limit of radiometric measurements combined with the extraction methods. As a speciation method at such low concentrations and below, capillary electrophoresis (CE) coupled to ICP-MS was introduced and tested on the neptunium samples.

5.1 Speciation in solution

5.1.1 UV-Vis/NIR spectroscopy of Np(V)

One of the key questions is in what redox state each radionuclide occurs during the sorption process. For that the solution of each sample was measured by UV-Vis absorption spectroscopy.

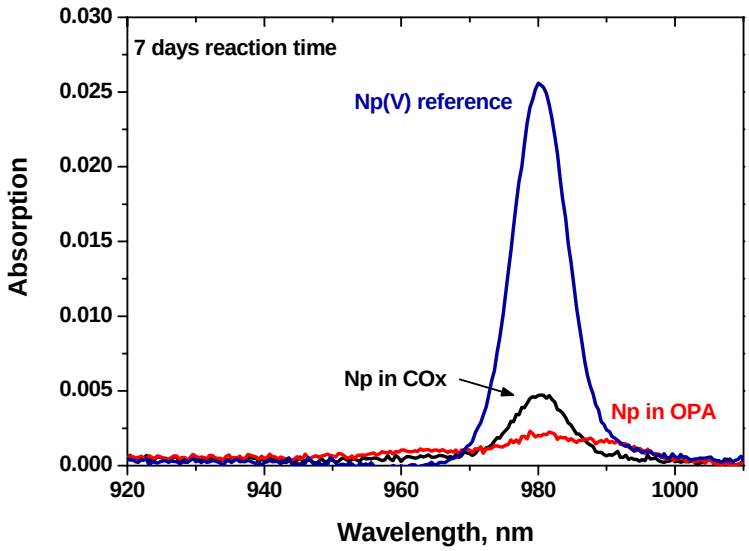

Figure 5-1: Absorption spectra of Np in supernatant solution after ultrafiltration from suspension solution of clay rocks, contact time = 1 week, S/L = 50, NaCl = 0.1 M.

In the following sections we only focus on the neptunium, because it shows a characteristic absorption band for the aquo NpO_2^+ ion at 981 nm with extinction coefficient high enough for the characterisation of Np in concentrations down to 10^{-6} mol/L. This cannot be achieved for Pu(IV,V). Figure 5-1 represents the UV-Vis spectra of the Np(V) reference solution and the supernatant solution of Np in OPA and COx clay minerals. Due to the similarity of spectral

features for both the Np samples and the Np(V) reference spectra, we conclude that the neptunium remaining in solution occurs in the pentavalent oxidation state. The amount of Np in solution calculated from the absorption coefficient is similar to the result from the radiometric measurement with in the range of about 13% uncertainties.

5.1.2 Eh Measurements

The sorption of Pu, Np increases with time supposing that they are slowly reduced to the tetravalent oxidation state. This can be confirmed by a steadily decrease of the Eh to values between -100 mV (Pu), and + 50 mV (Np) after 4 months without reaching a constant value. Looking in detail on the Pu/Np redox speciation diagram under the Eh/pH conditions for (OPA) pore water shows that the reduction to tetravalent Pu/Np is thermodynamically feasible (see Figure 5-9 and Figure 5-10).

5.1.3 CE-ICP-MS

Online-coupled capillary electrophoresis (CE) with inductively coupled plasma mass spectrometry (ICP-MS) has been successfully applied for the speciation of actinide ions at such low concentration [Kuczewski et al., 2003]. Therefore, CE-ICP-MS has been chosen as a speciation method for the characterization of Np species at low concentrations. Due to the speciation limitation of the absorption spectroscopy and the radiometric measurement we have performed Np speciation by CE-ICP-MS.

A commercial Beckman Coulter P/ACE MDQ capillary electrophoresis system (Fullerton, U.S.A.) equipped with an inductively coupled plasma sector field mass spectrometer Sector-field-ICP-MS (Element XR, Thermo Fisher Scientific, Bremen, and Germany). Conventional fused silica capillaries (Beckman Coulter, Fullerton, U.S.A.) with an internal diameter of 50 µm and lengths of 74 cm are used for the separations. A commercial parallel path micronebulizer (Mira Mist CE, Burgener, Canada) that operates with a makeup liquid (2 % HNO_3, 10 % ethanol, 1 ppb Rh as internal standard) interfaces both apparatuses. The makeup liquid is introduced to a syringe pump at a nominal flow rate of 8 µL min^{-1}. The nebulizer is connected to a borosilicate spray chamber (Mini glass chamber, Burgener, Canada).

For the measurement, separated supernatant solutions from clay suspension are taken in 1 mL glass vials under inert atmosphere. However the measurement has been performed under air atmosphere. The concentrations of Np in clay sample are between 1.0×10^{-7} and 1.0×10^{-9} M. Before each separation, the capillary is washed with BGE during 10 min at 20 psi. Separations are completed within 15-18 min. Sample injections are hydrodynamically carried out at 5 psi during 6 s. Separations are performed at -20 kV and at a constant pressure of 0.8 psi (to avoid clogging).

The first test should show how significant the impact of air on the Np(IV) is by using our commercial injection system. For that we injected a reference solution of 100% Np(IV) at concentration of $3x10^{-7}$ M in 0.01 M $HClO_4$ into the capillary and made a separation at a potential of 20 kV in an acetic acid buffer system. Figure 5-2 shows, that the Np(IV) was partly oxidized (~ 30 %) to Np(V), but that it should be possible to qualitatively detect Np(IV). Several mixtures of Np(V) and Np(IV) with different ratios are tested, to ensure the reliability of this separation and the migration time for our system.

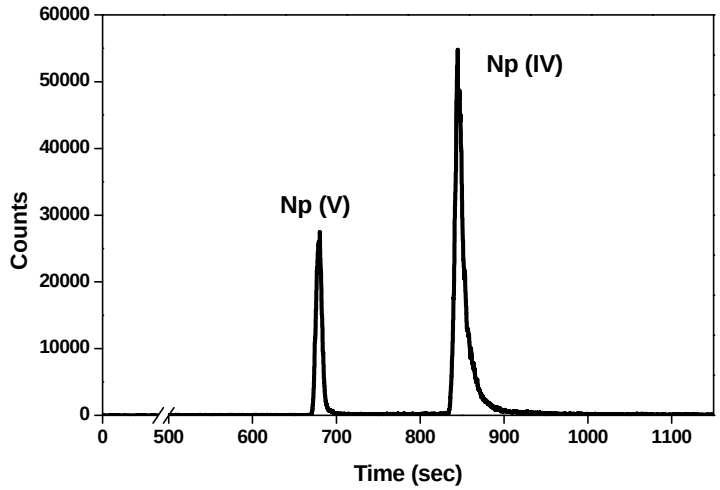

Figure 5-2: Electropherogram of an 30% Np(V) / 70% Np(IV) reference solution characterized by CE-ICP-MS, [Np]= $3x10^{-7}$ M, 0.01 M HClO4, separation in 1 M acetate buffer system, at a potential of 20 kV.

For the speciation of Np in clay solutions, filtrate (10 kD) supernatant solution was taken in small vials under Ar atmosphere and then injected under air into the CE. Figure 5-3 demonstrates that only Np(V) was found in supernatant solution with a concentration of about $2x10^{-8}$ M and this confirms the spectroscopic result at higher concentrations.

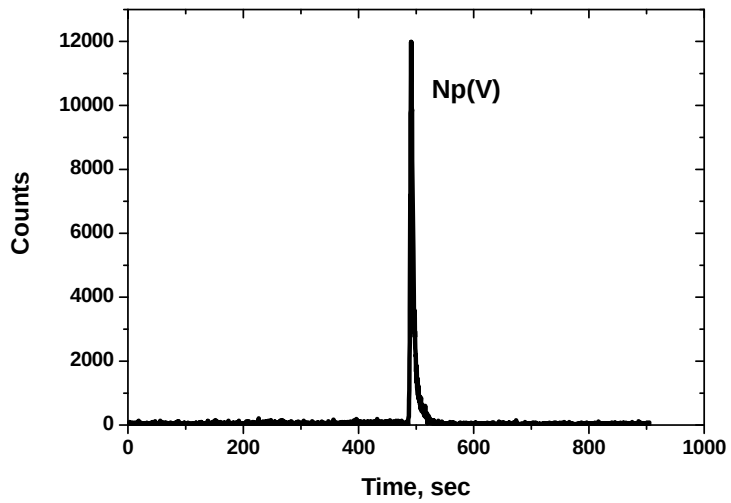

Figure 5-3: Electropherogram of Np-COx clay filtrate (aliquot) solution, [Np]initial = 2x10-8 M, 0.1 M NaCl, S/L = 20, contact time=7 months, CE separation with 1 M acetate buffer system at 30 kV.

5.2 Speciation of neptunium and plutonium on clay solid phases

XANES and XPS are two well appropriate methods to characterise oxidation states of metal ions on the surfaces. Both methods has successfully been used for determining Pu oxidation states in humate and fulvate complexes [Marquardt et al., 2004]. Both methods were used to characterise the Np and Pu on the clay surface as well as in solution.

5.2.1 XANES

For the XAFS measurements, filtrate solutions and suspension solids of radionuclides-clay rocks are filled into 400 µl capped PE vials and mounted in a special air tight sample holder, which is connected to an Ar supply line at the experimental station to keep the samples under <inert, near oxygen-free conditions during XAFS measurements. The measurements are performed at the INE-Beamline using this new inert gas sample cell design [Brendebach et al., 2009] for redox sensitive radionuclides. The spectra are calibrated against the first derivative X-ray absorption near edge structure (XANES) spectrum of a Zr foil, defining the energy of the first inflection point as E(Zr 1s) = 17998.0 eV. All Pu L3, Np L3 XAFS spectra are measured in standard fluorescence yield detection mode.

The results of the XANES of Np, Pu are shown in Table 5-1. In all samples the Np was detected as Np(V) (NpO_2^+, 'neptunyl') with the characteristic XANES features (low white line intensity, multiple scattering shoulder ~10 eV above white line). Note that the energy positions of Np(IV) and Np(V) almost coincide. This anomaly is explained for actinyl cations by charge transfer from the double-bound axial oxygen anions to the metal cation. The XANES spectrum of the Np(V) reference sample (Np(V)ref), neptunium sorbed on OPA (Np-OPA) and COx (Np-COx) are shown in Figure 5-4.

As expected, the white line maxima of the XANES of Pu in the OPA and COx samples are clearly located at the white line position of the Pu(IV) at 18067.8 eV (see Table 5-1). The XANES spectrum of Np(V)ref, Np-OPA, Np-COx are shown in Figure 5-5. The XANES spectra exhibit no multiple scattering resonance as expected for Pu(V) and Pu(VI) 'plutonyl' moieties and a strong white line intensity - the energy positions are in accordance with the Pu(IV) aquo ion. Hence, we can conclude that plutonium on the clay is in the tetravalent oxidation state and that the initial Pu(V) has to be reduced to Pu(IV) for all sorption samples.

Table 5-1: Energy positions of the XANES first inflection point and white line maximum positions for reference species and sorption samples. All values are given in eV (estimated calibration error ΔE ±0.5-1 eV).

Sample description (contact time 1 week)	first inflection point	white line maximum
Pu(IV)ref, solution	18062.4	18067.6
Pu(V)ref, solution	18059.8	18064.3
Pu-OPA, solid	18062.1	18067.9
Pu-COx, solid	18063.0	18067.8
Np(IV)ref, solution	17609.6	17614.7
Np(V)ref, solution	17609.0	17614.0
Np-OPA, solid	17608.4	17613.0
Np-COx, solid	17607.7	17612.5

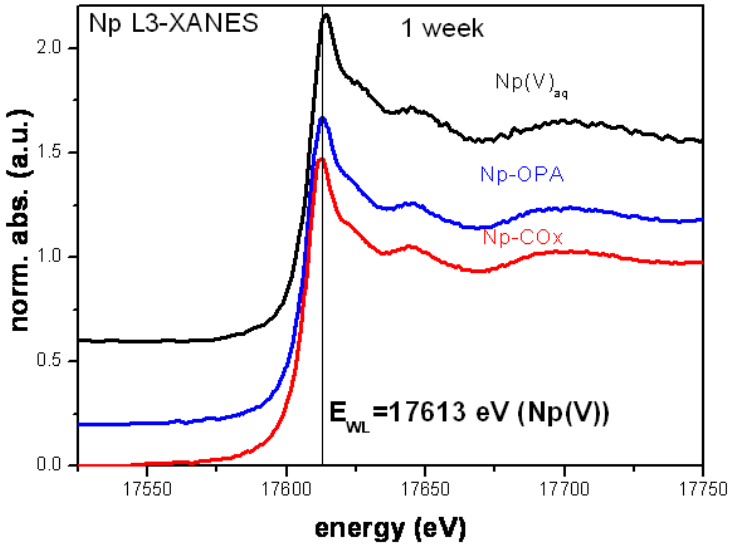

Figure 5-4: Np L3-XANES spectra of Np speciation in clay rocks (OPA, COx), [Np] =3E-04 M, 0.1 M NaCl, S/L = 50 , kinetic = 1 week, sample= filtrate suspension.

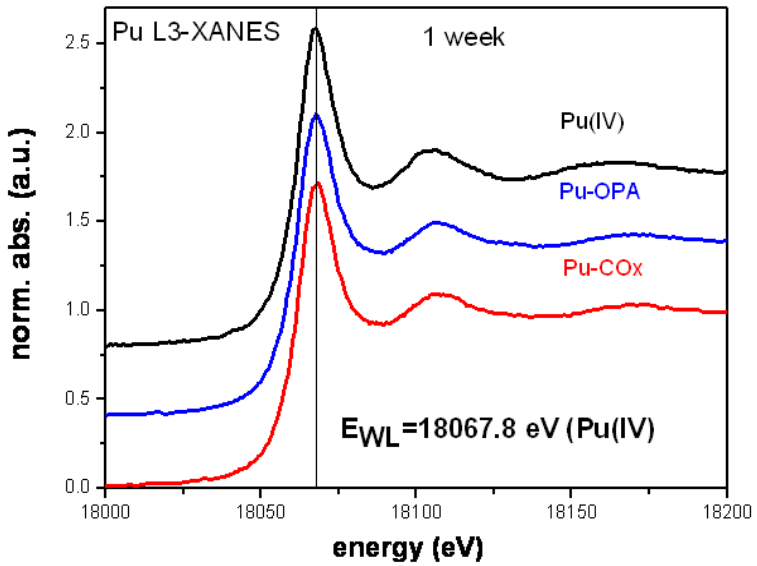

Figure 5-5: Pu L3-XANES spectra of Pu speciation in clay rocks (OPA, COx), [Pu] =3E-04 M, 0.1 M NaCl, S/L = 50, kinetic = 1 week, sample= filtrate suspension.

Table 5-2: Energy positions of the Np L3-XANES first inflection point and white line maximum positions for references and samples from campaign August 2011. All values are given in eV (estimated calibration error ΔE ±0.5 eV).

Sample description (4 and 8 months)	**contact time (months)**	**first inflection point**	**white line maximum**
Np(V)ref, aq [1]		17609.0	17614.0
Np(V)-OPA (august 2011)	8	17608.6	17612.0
Np(V)-OPA (Nov 2011)	4	17608.9	17613.3
Np(V)-OPA-Fe (august 2011)	8	17609.2	17612.7
Np(V)-OPA-Fe (Nov 2011)	4	17608.3	17613.3
Np(V)-COX (august 2011)	8	Nd	nd
Np(V)-COX (Nov 2011)	4	17608.6	17613.2
Np(V)-COX-Fe (august 2011)	8	17609.9	17613.2
Np(V)-COX-HQ (august 2011)	8	17609.7	17613.9
Np(IV)ref, aq [1]	-	*17609.6*	*17614.7*
Np(VI)ref, aq [2]	-	*17611.7*	*17616.0*

5.2.2 EXAFS

The XAFS technique is particularly useful speciation method and applied for the understanding the speciation of actinides on mineral surfaces. Atomic distances between the adsorbed actinide ions and sorbent atoms can be obtained by XAFS analysis and the interface reaction mechanisms can be inferred from the sorbate-sorbent polyhedral linkage. XAFS has proven to be valuable in discerning sorption mechanisms such as inner-sphere surface complexation, outer-sphere surface complexation, coprecipitation/structural incorporation and redox reactions.

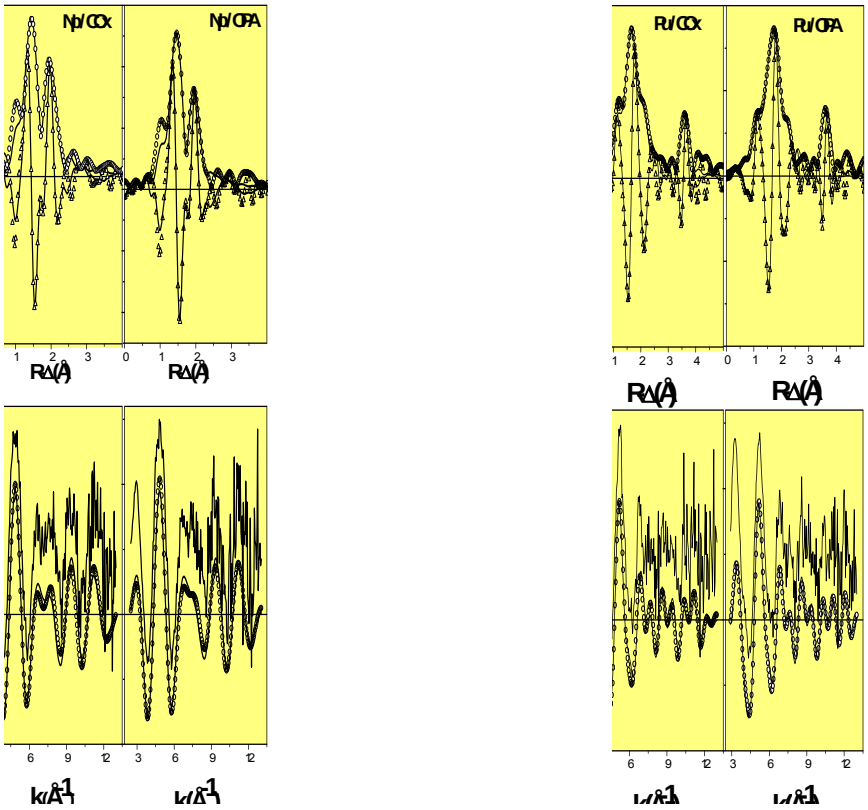

Figure 5-6: Pu/Np LIII-edge k3-weighted of EXAFS spectra and corresponding Fourier transforms (upper: Pu/Cox and Pu/OPA sample, lower: Np/Cox and Np/OPA sample), contact time: 1 week.

The Np LIII and Pu LIII EXAFS spectra and their corresponding FT's for Np(V)/Pu(V) sorbed on COx and OPA with 1 week contact time are shown in Figure 5-6. In all FT spectra one peak dominates, which can be attributed to an average Np/Pu–O coordination shell composed of oxygen atoms from both water molecules and oxygen atoms binding the meal ion to the clay mineral surface. The EXAFS parameters obtained by fitting the spectra of Np sorbed onto the clay surfaces are also listed in Table 5-3. Figure 5-6 shows the LIII-edge *k*3-weighted EXAFS spectra and corresponding FT's of Np(V) sorbed onto COx and OPA clay mineral surface at pH 7.2 and 7.6. (Solid line – experiment; dotted line – theoretical fit results from fits to $\chi(k)$). No indication of Np−Np bond distance in the spectra, which leads to no formation of Np precipitation on clay surfaces.

There are also no further distant FT peaks, which might be attributed to an Np−Al or Np−Si distance (Al and Si cannot be distinguished by EXAFS). Observation of an Np−Al/Si peak would be direct evidence for the sorbate-substrate interaction. With no evidence for an Np−Al/Si distance we are not able to distinguish between an outer-sphere and an inner-sphere complex nor can we identify monodentate or bidentate binding to the surface in the case of inner-sphere complexation of the Np(V) species onto the clay mineral. However, a monodentate ligated silanol or aluminol group would be expected to have a relatively long Np−Si/Al distance. The length of an Np(V)−OH bond is expected to be shorter than the Np(V)−O distances associated with those of coordinated water molecules and the oxygen atoms of surface

binding sites. By comparison to a reported hydroxyl An−O bond length for Np(V) and scaling to ionic radii, we expect R(Np−O) for a hydroxo ligand to be about 2.45 Å.

Table 5-3: Metric parameter from R-space fits to Np L3 edge. EXAFS fit parameters: EXAFS fit parameters: O1 axial oxygen backscatterer, O2 equatorial oxygen backscatterer, (f) indicates fixed parameter, S02 fixed at 1.0

Sample	***k-range ($Å^{-1}$) fit-range (Å)***	***Shell***	***N***	***R (Å)***	***ΔE_0 (eV)***	***σ^2 ($Å^2$)***	***r-factor***
Np (V)aq[a]		O1	2.5	1.82			
		O2	4.8±1	2.45			
Np (IV) aq[b]		O2	9±1	2.37			
Np / COX	2.5-13.0	O1	2.0	1.86(1)	3.55	0.0011	0.028
	0-2.39	O2	3.1	2.49(2)	9.29	0.0022	
Np / OPA	2.5-13.05	O1	2.0[f]	1.87(1)	4.77	0.0001	0.025
	0-2.39	O2	2.9	2.47(2)	6.83	0.0027	
Np / OPA magnetite	2.55-13.0	O1	2.0[f]	1.86(1)	2.14	0.0004	0.011
	0-2.39	O2	3.3	2.48(2)	7.91	0.0036	

a: [Heberlin et al. 2008]; b: [Antonio et al., 2001]

Therefore, we suggest that the apparent decrease in N for Np(V) in the samples might be an indication to the formation of a ternary OH−/Np/clay surface species. In this species, the Np coordination sphere is expected to be highly asymmetric and diminish of its EXAFS amplitude is expected.

The structure parameters of the NpO_2^+ aquo ion are analyzed using EXAFS (Np−Oax distance 1.82 Å; coordination number 2.5; Np−Oex distance 2.45 Å; coordination number 4–5). EXAFS data shows differences in the Np(V)-Oax bond distance of 1.86 ± 0.01 Å for the sorbed Np on both clay rocks, and 1.82 ± 0.01 Å for the Np(V)aq ion. Batch experiments and the EXAFS results leads to the conclusion that in Np(V) is bound to equatorial about three oxygen neighbors at 2.47~2.49 Å and its remaining first coordination sphere is completed with water molecules. The coordination number of sorbed Np(V) an apparent decrease, which may be indicate the formation of ternary OH−/Np/clay mineral surface species.

Table 5-4: Metric parameter from R-space fits to Pu L3 edge. EXAFS fit parameters: O1 1st oxygen backscatterer (bridging and terminal hydroxyl groups), O2 2nd oxygen backscatterer (terminal water), (g) indicates global parameter for both oxygen shells, S02 fixed at 1.0

Sample **(1 week)**	k-range ($Å^{-1}$) fit-range (Å)	shell	N	R (Å)	ΔE_0 (eV)	σ^2 ($Å^2$)	r-factor
Pu(IV)aq[a]		Oex	8-9	2.39			
Pu(V)aq[b]		Oax	2	1.82	4.92	0.0003	0.002
($HClO_4$ pH 1.6)		Oeq	4.5	2.47	-3.99	0.0049	
Pu(VI)aq(1 M $HClO_4$) [conradson 2001]		Oax	2	1.75			
		Oeq	5-6	2.41			
Pu / COX	2.85-13.0	O1	4.0	2.24(1)	-2.47[g]	0.0020	
	0-3.90	O2	3.2	2.41(1)	-2.47[g]	0.0016	0.026
		Pu	4.4	3.73(2)	-7.20	0.0074	
Pu / OPA	2.90-13.0	O1	4.1	2.26(1)	-1.61[g]	0.0022[g]	
	0-3.96	O2	2.8	2.41(1)	-1.61[g]	0.0022[g]	
		Pu	3.7	3.75(2)	-6.83	0.0059	

a: [Conradson et al., 2004]; b: [Rothe et al., 2011]

To obtain molecular-level information on the interaction of Pu with OPA and COx clay rocks, Pu L3-edge EXAFS spectra of the plutonium treated with both clay rocks are shown in Figure 5-6 together with the corresponding Fourier transforms (FT's) representing radial distribution functions of the atoms surrounding the Pu atom. In Table 5-4 shows the Pu-L_3 EXAFS structural parameters which are obtained. The average Pu-O1 (hydroxide) distance for sample Pu-OPA, Pu-COx are in the range of 2.22 – 2.26 Å, indicating that the Pu in all samples is sorbed at the clay surfaces as Pu(IV). A Pu-Pu interaction at ~3.75 Å with two Pu atoms is observed in all spectra, indicating the presence of polynuclear Pu(IV) species or Pu(IV) colloids at the clay surfaces. Finally it can be concluded that either a Pu surface precipitation occurs or an inner-sphere sorption of the polynuclear Pu(IV) species might be expected on both surfaces.

5.2.3 XPS

To investigate the redox state of sorbed radionuclides on the clay particles, surface sensitive XPS (x-ray photoelectron spectroscopy) is applied. Besides photoelectron spectroscopy of the radionuclides, analyses of the chemical states of iron and sulphur of the clay suspension indicate which of these elements may be available for reduction of the radionuclides to a less soluble state.

Actinide clay suspensions and wet pastes are prepared for XPS analysis by drying small portions on an indium foil in an anoxic glove box. The samples are conveyed into the XP spectrometer, PHI model 5600ci, without air contact by means of a vacuum transfer vessel. Monochromatic Al K_α x-rays are used for excitation in conjunction with an electron flood gun for sample surface neutralization. Atomic concentrations are calculated from the areas of elemental lines of survey spectra. Narrow scans of elemental lines are recorded for determination of chemical shifts and spectral features.

Actinides (Pu, Np) are doped into the clay suspensions at low concentrations, thus only the actinide 4f main lines are detected with low intensity. Fortunately, no complete spectral superpositions with elemental lines from the constituents of the clays are present. Only Pu $4f_{5/2}$ is superposed by the intense Ca 2s elemental line, while Pu $4f_{7/2}$ is not superposed. Np $4f_{7/2}$, $4f_{5/2}$, elemental lines can thoroughly be detected if present. However, Tc was not detected at the clay surfaces after a contact time of 7 days in suspension.

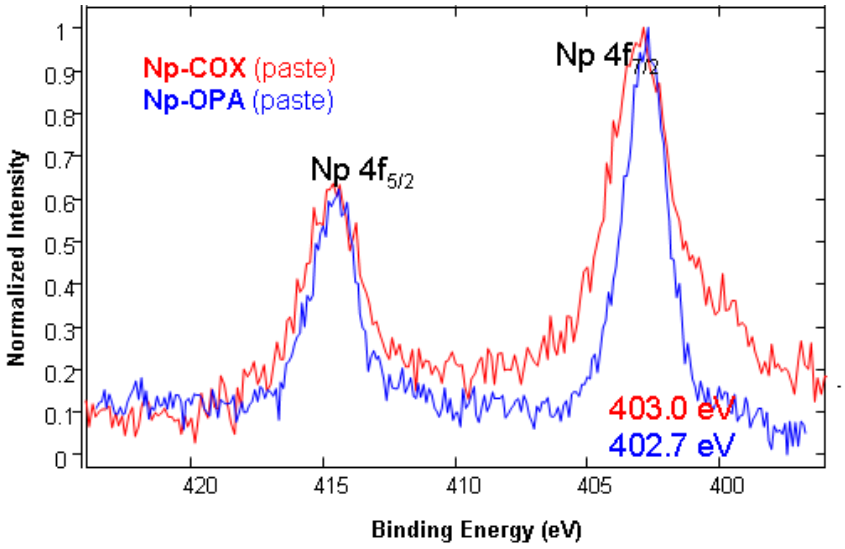

Figure 5-7: Np 4f7/2 spectrum, Al Kα mono x-ray excitation, charges referenced C1s (CxHy): 284.8 eV. Wet Paste: Opalinus and COx clay, Np(V) 4x10-4 M, 7 days contact time.

In case of Np-OPA, the Np $4f_{7/2}$ elemental line has a binding energy of 402.9 eV (Figure 5-7). However, Np(V) and Np(IV) have similar binding energies of the 4f elemental lines and conclusions concerning the valence state of Np are solely derived from the positions of 4f satellites if present. A satellite at about 6.5 eV higher binding energy is not detected indicating absence of Np(IV)oxide or Np(IV) eigencolloids. However, a distinction between sorbed Np(V) and ideal Np(IV) sorption of single, non-interacting Np atoms cannot be performed.

The Pu $4f_{7/2}$ elemental line at Pu-OPA samples has a binding energy of 426.0 eV typical for the tetravalent state (Figure 5-8). In addition, a satellite at about 6.5 eV higher binding energy is detected indicating a Pu(IV) oxide hydrate, presumably due to Pu eigencolloids.

The S2p spectra indicate solely the presence of sulfate and no sulfur in a reduced state like sulfide. The Fe $2p_{3/2}$ spectra has two components assigned to Fe(III) and Fe(II). No satellite typical for the Fe^{3+} ion was observed. No clear conclusions could be drawn about the bonding of the iron. The spectra are similar to reference spectra of Fe_3O_4 and iron silicates (iron bound in the clays).

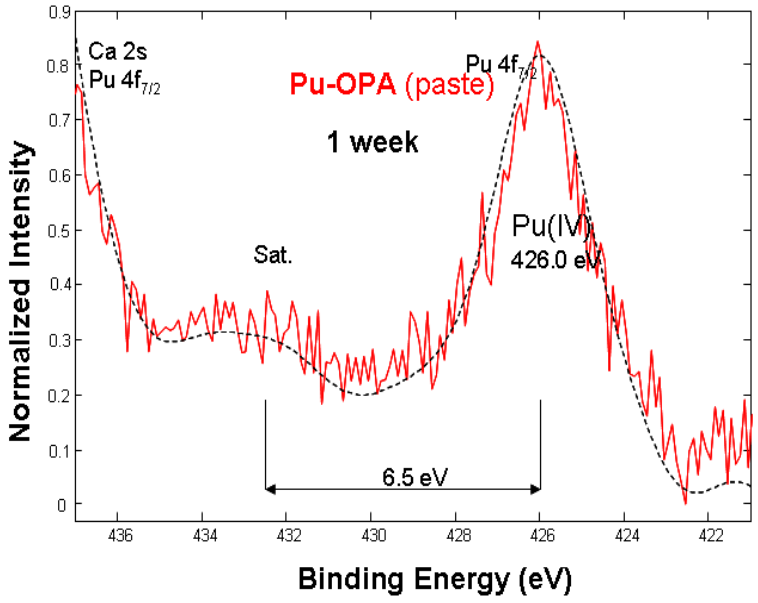

Figure 5-8: Pu 4f7/2 spectrum, Al Kα mono x-ray excitation, charges referenced C1s (CxHy): 284.8 eV. Wet Paste: Opalinus clay + Pu(V) 3x10-4 M, 7d contact time.

The relative portion of Fe(II) in the COx sample is less than in the OPA clay. The absolute Fe concentrations within OPA and COx clays are comparable. A change of the Fe 2p spectra upon Np and Pu interaction is not detected as may be expected by redox-reaction which is explained by the low metal concentration.
COx and OPA clays both contain Fe(II) which may be available for redox reaction with added radionuclides while sulphur is oxidized to sulfate and thus is not involved in redox reactions.

5.3 Redox speciation of plutonium and neptunium in clay/ porewater system

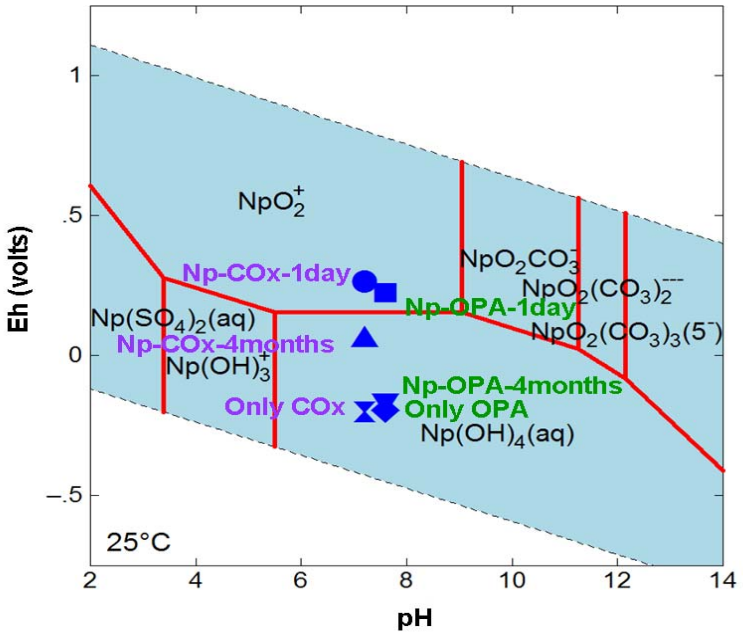

Figure 5-9: Eh-pH Diagram of neptunium OPA/COx system in pore water and speciation calculation are performed using Geochemist Workbench, thermochemical database, [Np]total = 1 x 10-8 M, I= 0.1 NaCl, T= 25 0C

Neptunium and plutonium geochemical behaviour are considerably significantly governed by their redox chemistry. Np can exist in solution as +3, +4, +5, +6, and +7 oxidation states, but only Np(IV) and Np(V) are most stable in natural environments. Neptunium's geochemical behaviour is highly influenced by its redox speciation. As seen in the Eh-pH diagram below (Figure 5-9), Np is commonly found as mobile Np(V), in the form of the dioxocation, NpO_2^+ under neutral, oxidizing conditions, and as at higher pH range the most predominant species are $Np^{(V)}O_2(CO_3)^-$ and $Np^{(V)}O_2(CO_3)_2^{---}$. However, in reducing conditions, only $Np^{(IV)}(OH)_4$ becomes the dominant species. This Np(IV) species is the least immobile because its low solubility and a strong sorption capacity to mineral surfaces [Silva et al., 1995]. Furthermore, the Np redox speciation with clay rocks system in pore water is complicated and not yet well studied. The opalinus clay and Callovo-oxfordian clay rocks are mixture of different clay minerals (like illite, Monmorilitite, kaolinite, calcite, smectite etc.) and containing trace amount redox active elements (e.g., Fe^{2+}/Fe^{3+}, sulphur, Al^{3+} etc) which might significantly influenced for the redox speciation in solution. On the contrary to redox sensitive cation, anions like sulphate plays also a role in pore water for the Np redox speciation. In Figure 5-9 the Eh-pH diagram for Np redox speciation in pore water modelled with with Geochemical Workbench is shown. Solid phases of Np are suppressed by the calculation and only dissolved

species are shown. As comparison the experimental pH and Eh values measured for the Np in clay rock suspensions - mixture of synthetic pore water and clay rocks - at varying contact time are plotted in the same graph. The measured Eh values slowly decrease with contact time between the pore water and the clay rock indicating that reaching redox equilibrium is a slow process. Obviously, the quilibrium state was not reached in our experiments, also caused by oxygen intrusion into the glove box during the experiment. However, the Eh values are located in the stability field of the tetravalent neptunium after 4 month. Hence, the Np(V) was can be reduced to Np(IV). The reduction mechanism – whether the reduction takes place in solution or on the clay surface - is unclear so far.

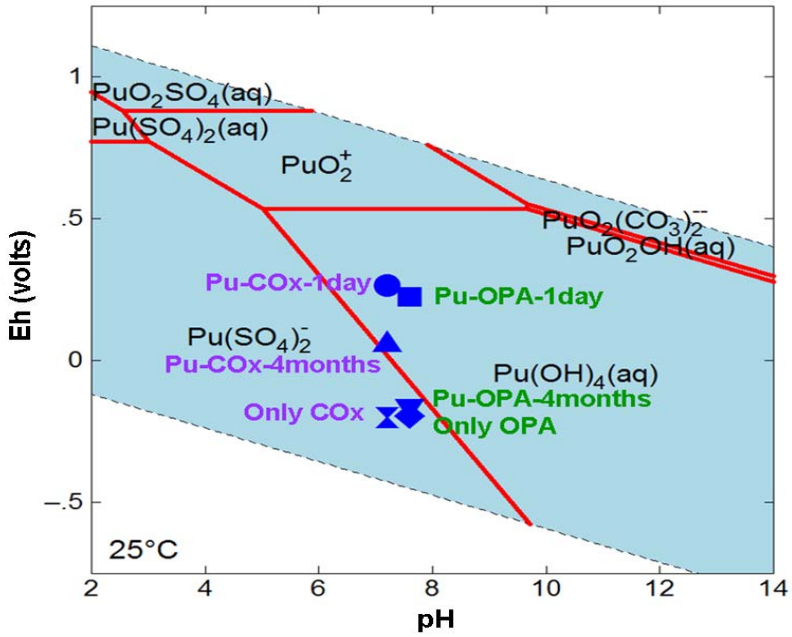

Figure 5-10: Eh-pH Diagram of plutonim OPA/COx system in pore water and speciation calculation are performed using Geochemist Workbench, thermochemical database, [Pu]total = 1 x 10-8 M, I= 0.1 NaCl, T= 25 0C

Plutonium redox speciation and its geochemical behaviour is also strongly governed by the redox conditions. In aqueous solutions, Pu can coexist in the trivalent, tetravalent, pentavalent, and hexavalent oxidation state, each shows distinct chemical behaviour. The Eh-pH diagram for Pu redox speciation in pore water is shown in Figure 5-10. Solid phases of Pu are suppressed by the calculation and only dissolved species are shown. Again for comparison reasons, the experimental pH and Eh values measured for the Pu in clay rock suspensions at varying contact time are plotted in the same graph. As in the Np experiments the Eh values slowly decrease with contact time between pore water and clay rock. In contrast to Np, already at the beginning the experimental Eh values are located in the stability field of the tetravalent Pu. At neutral and basic pH values the $Pu^{(IV)}(OH)_4$ is the relevant Pu species. The sorption of Pu on the clay rock was also much faster than for Np indicating a faster reduction of Pu(V) to Pu(IV). From the very low solubility limit of $Pu(OH)_4(am)$ in solution – this is con-

firmed by the very low Pu concentrations at the detection limit of the liquid scintillation counting - we assume that the Pu precipitates on the surface of the clay.

5.4 Basic developments on the capillary electrophoresis coupled to ICP-MS

For the speciation of actinides in solution spectrometric methods are limited to only relative high metal concentrations and they fail at tracer concentrations below 10^{-6} mol/L. For that capillary electrophoresis combined with ICP-MS (CE-ICP-MS) is a very sensitive analytic system that can have speciation limits down to 10^{-9} mol/L and lower, depending on the metal ion and composition of the solution. The CE-ICP-MS is a rather young method applied for metal speciation and therefore, development of the system, apparatus and separation system, are needed to improve reliability of the method as well as ist applicability on complex composed solutions. In this work package basic developments have been made that are outlined in the following chapters. The work has be done in a collaboration with the University of Cologne (Dr. B. Kuczweski, Abteilung Nuklearchemie).

5.4.1 Development of an optimised sample introduction into the ICP-MS for the use with the CE-ICP-MS

Conventional nebulisers which are used for the CE-ICP-MS coupling like the GE Micromist offer transfer rates of 10-25%. It should be possible to increase this transfer rate due to the low sample uptake of 100 µL/min by heating the spray chamber and the transfer line. Figure 5-11 shows the experimental setup.
From 50°C on the transfer rate is nearly 100% of the sample uptake. To prevent the condensation in the ICP-MS torch higher temperatures are required. However with higher aerosol temperature the rate of undesired oxides and double charged ions increases significantly. Therefore the optimum temperature of the spray chamber is between 50 and 55°C. Unresolved is the heating of the transfer line. This development was superseded with a new nebuliser provided by burgener. This parallel path nebuliser offers the transfer of a dry aerosol with a sample uptake of 2-10 µl/min which is controlled by a syringe pump.

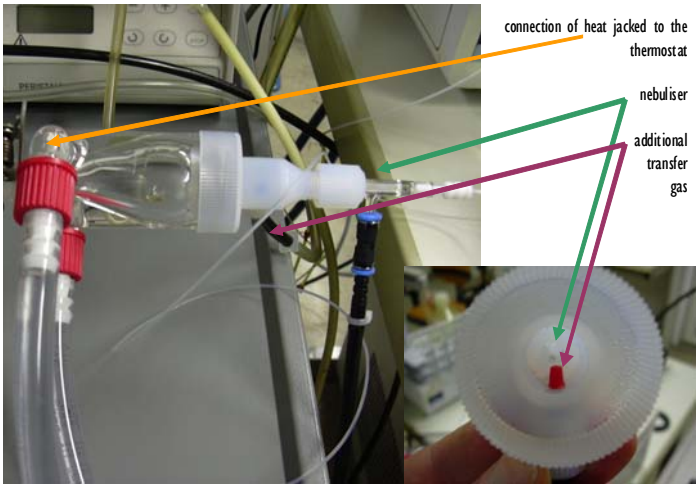

Figure 5-11: Experimental setup for the optimisation of the sample transfer of CE-ICP-MS.

5.4.2 Method development of a CE-DAD-ICP-MS for the simultaneous detection of humic substances (DAD) and metal ions (ICP-MS)

In cooperation with Johannes Gutenberg Universität Mainz the CE-ICP-MS detection unit was extended with a diode array detector. Figure 5-12 shows the scheme of the coupling.
Holmium and Aldrich humic acid (AHA) were used to test the principle. Humic acid was marked with iodine to determine the humic acid as well in the ICP-MS as with the DAD. Figure 5-13 illustrates the successful and simultaneous detection of Ho and AHA in form of an electropherogram. The left graph shows the data from the diode array where one can see the UV/VIS Spectra of humic acid and free iodine which is released from the humic acid. The right graph shows the merged data from the DAD at two wavelengths with the ICP-MS data at the masses of iodine and holmium. The first peak at 135 s ICP-MS / 112.5 s DAD can be identified as iodine by the DAD-spectrum. The second one at 185 s ICP-MS / 145 s DAD can be assigned as holmium humate complex. At 240 s ICP-MS / 185 s DAD the electroosmotic flow EOF was determined. The Ho signal with the maximum at 280 s ICP-MS is free Ho that was not complexed and therefore separated fast. The Ho between 240 s und 280 s is partly released from the complex. Strong and weak binding sites for metal ions at the humic acid are the reason for this phenomenon. The weak binding sites release the Ho during the separation continuously. This cause a continuos signal of Ho between the signal of free Ho and the Ho-humate complex.
In principle the methods works well and substances with a strong UV/VIS sorption can be identified easily. Only the limit of detection of the DAD (20 pbb for humic acid) should be improved by better optical focussing into the capillary.

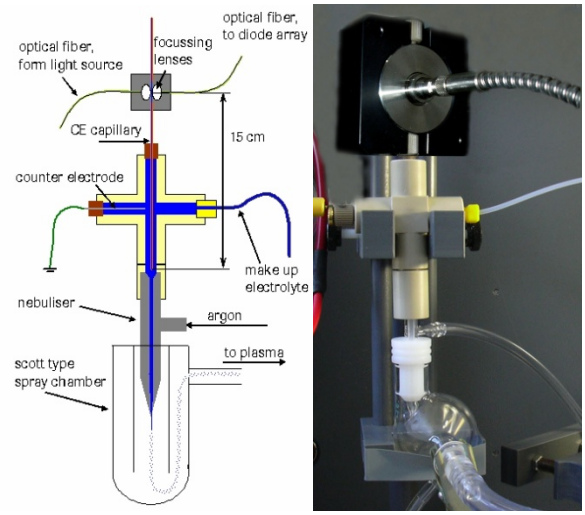

Figure 5-12: Sketch and photo of the CE-DAD-ICP-MS.

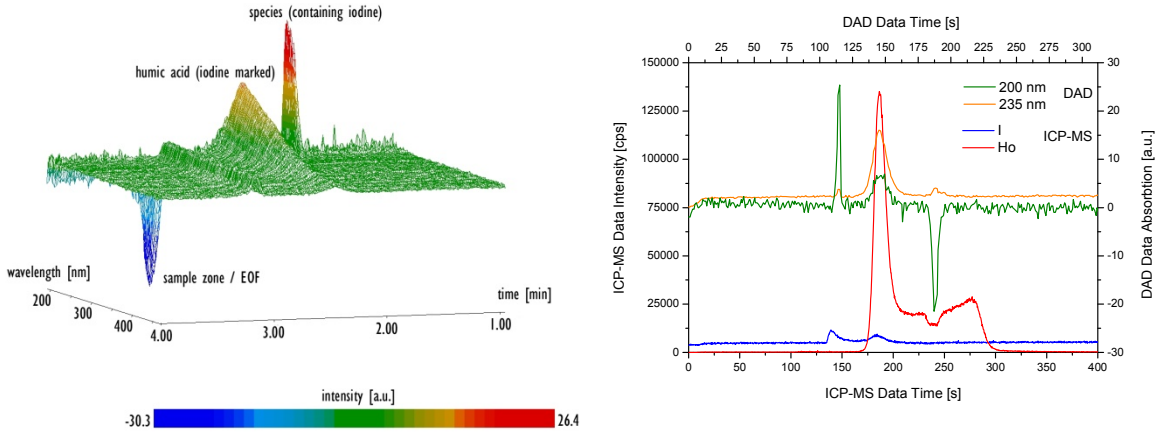

Figure 5-13: Separation of free Ho, free humic acid and Ho humate complexes by the CE-DAD-ICP-MS coupling (250 mg/L humic acid, 0,75 mg/L Ho, electrolyte 1 M AcOH, -25 kV, 250 mbar, FS capillary length 80(63) cm, 50 µm ID).

5.4.3 Development of separation parameters for the speciation of uranium with CE-ICP-MS

The separation of plutonium and neptunium species by CE-ICP-MS is a well established method with a acetate buffer electrolyte system, but uranium could not be separated with same conditions. It was necessary to apply a stronger complexing agent than acetic acid. EDTA proved to be the best additive. Table 1 gives the separation conditions. The solution of the two oxidation states was prepared by electrolysis. The content was measured by UV/VIS spectroscopy (as reference) and with the CE-DAD-ICP-MS. The solution was not stored under special conditions, therefore a fast oxidation was expected, but the complexing agents stabilise the oxidation states well. 10 and 80 minutes after the preparation and mixing with the

electrolyte the uranium speciation measurement gives within the errors the expected values. Figure 4 shows an electropherogram of Cs (as marker), U(VI) and U(IV).

Table 5-5: Separation conditions for uranium species with CE-ICP-MS.

Electrolyte	100 mM AcOH; 10 mM Na_2EDTA
Sample	in 8 M HCl electrolysed solution, mixed 1:1 with electrolyte after end of electrolysis
Voltage	+ 25 kV
Pressure	150 mbar
Capillary	fused silica, length: 65 cm, diameter: 363 µm / 50 µm

Table 5-6: Validation of the uranium species separation.

	U(IV)	U(VI)
expected (UV/VIS)	83 %	17 %
measured 10 min	81 %	19 %
measured 80 min	80 %	20 %

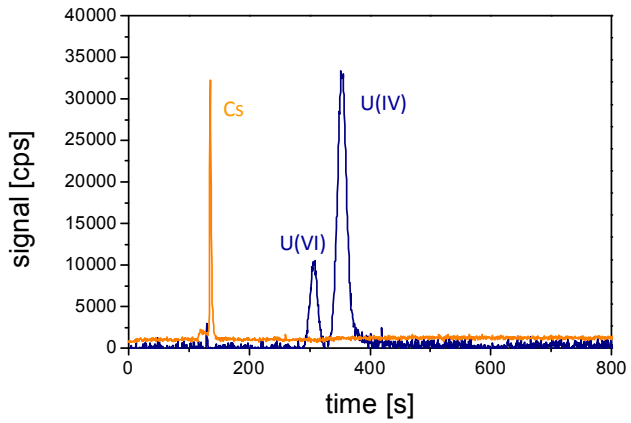

Figure 5-14: Separation of uranium species by CE-ICP-MS. (separation conditions see **Table 5-5**).

5.4.4 Modelling of the CE-separations for selected problematic separations

By support of the Charles University in Prague the model calculations of the used electrophoretic separation have been done. The software Simul allows understanding the processes, pro-

ceeding during the separation. For example the peak form differs strongly from the medium, in which the sample is injected. If plutonium standard solutions are injected into the capillary in diluted nitric acid, the peaks are broad and have a low intensity. After dilution with the electrolyte (1 M acetic acid) 1:1 the signals are small and have a higher intensity. Due to this this effect the limit of detection increases in spite of dilution. By the use of Simul it was possible to give an explanation of this phenomenon. A strong change in the electric conductivity causes that the Pu ions can leave the injection zone just slowly and cannot form sharp peaks. It was found by the theoretic calculation, that a dilution of the sample 1:1 with the electrophoretic buffer is a suitable remedy. The calculated electropherograms are shown in Figure 5-15.

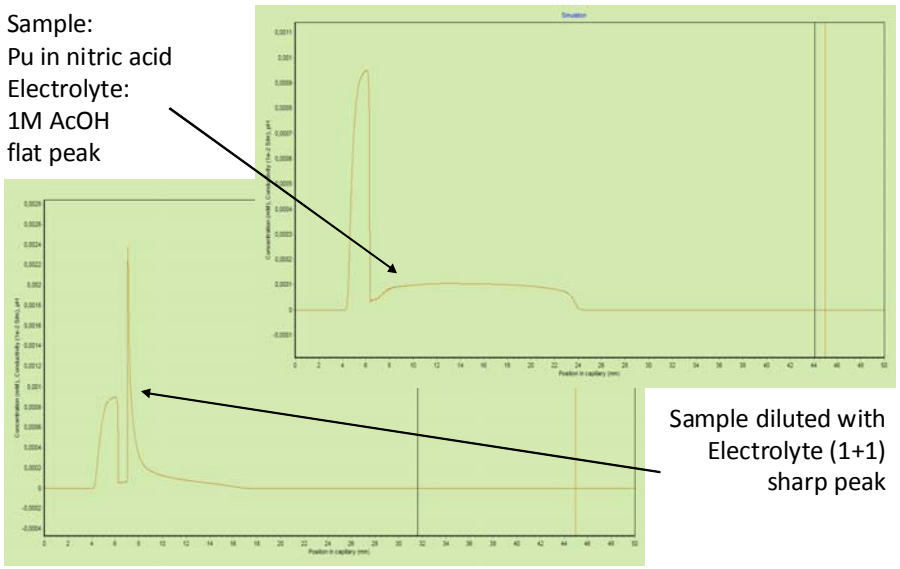

Figure 5-15: Simulation of concentration and conductivity vs. position in capillary. Right graph: Pu in nitric acid electrolyte: 1 M AcOH, left graph Pu in nitric acid 1:1 diluted with electrolyte. In each graph left signal: injection zone, right signal: resulting peak in electrophrogram.

6 Basic investigations of the actinide complexation with clay organic components and humic substances

6.1 Interaction of Cm(III) with Kerogen extracted from clay rock

Kerogen is a polymeric organic material in sedimentary rocks, which can be extracted by aqueous solutions at certain conditions, e.g. high pH values (s. also Chapter 2.4). The role of Kerogen regarding the mobilisation of radionuclides in clay systems is unclear so far. For that, we started experiments to study the complexation of the trivalent actinide Cm(III) with Kerogen extracted from the OPA clay. However, we have to admit that the remaining amount of inorganic phases in the kerogen are a major problem for complexation studies and the complexation behaviour observed so far is unfortunately driven by these impurities. The impurities are mainly $Fe^{2+/3+}$ and reduced/oxidised sulphur containing mineral residues (s. Figure 6-1 and Table 6-1). The content of Fe and S amount to be about 4 and 7 wt%, respectively. It should be mentioned that Kerogen from COx and OPA is very similar concerning the spectroscopic characteristics of the Fe L-edge & S K-edge.

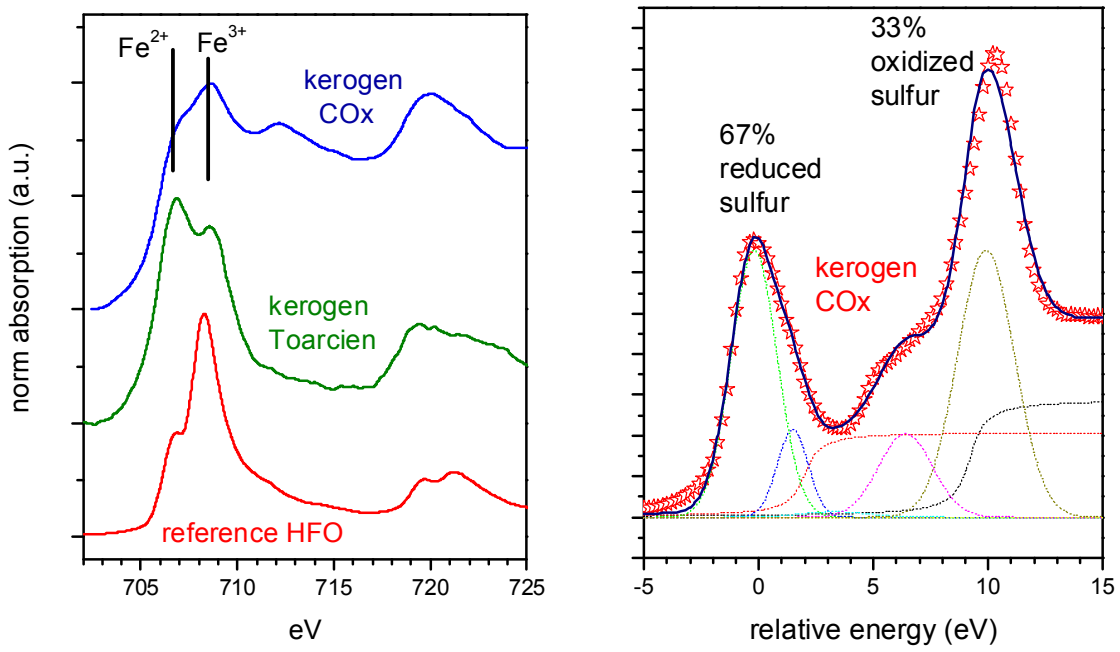

Figure 6-1: Characterisation of kerogen extracted from natural clay rock.

Table 6-1: Elemental composition of kerogen extracted from OPA. More than 78 wt.% are organic matter, but a high content of inorganic iron and sulfur compounds remain in the fraction.

Element	Weight %
C	55.60
O	23.12
Al	0.22
Si	6.57
S	4.01
Fe	7.48
Total	100

TRLFS spectra of Cm(III) in Kerogen solutions show a second peak indicating a interaction of Cm(III) with compounds in the Kerogen extract (s. Figure 6-2). Comparable drawbacks have been seen and are documented in investigations from Belgian groups where isolated kerogen from the Boom clay formation has been used. Due to this fact it was abdicated performing further Kerogen complexation experiments until the impurities can be removed without altering the structur of the Kerogen.

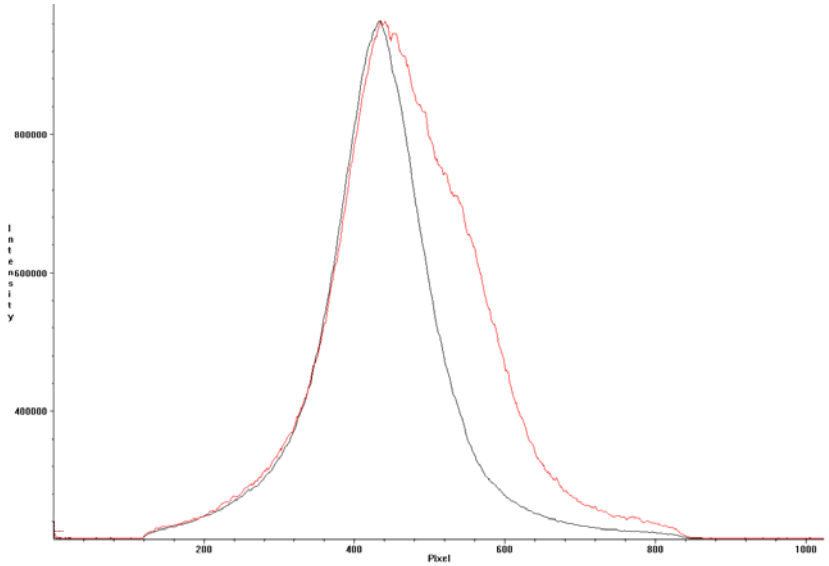

Figure 6-2: TRLFS of Cm(III) interaction with kerogen extracted from OPA.

The supposable importance of clay organic matter was shown in experiments from [Courdouan et al., 2008] with support from KIT-INE. They found a significant Cm complexation by DOM for OPA pore water, and a little complexation by DOM detected in the OPA and COx extracts under exclusion of CO_2. However, carbonates largely controlled Eu speciation under in situ conditions (pore water) of europium in OPA and COx pore water. For OPA the carbonate species $EuCO_3^+$ was calculated to be 54% and the second most important species the Eu-DOM complexes were calculated to be 29% of total dissolved Eu in the pore water. Despite the fact that carbonates are dominating the DOM in the OPA pore water may enhance

the Eu solubility by 5×10^{-8}M, representing about 1/3 of total dissolvable Eu. Which organic compound of the DOM in the pore water is responsible for this enhancement is unclear so far.

6.2 Basic investigations of the Np(IV) fulvate complexation

Humic substances (HS), a mixture of organic macromolecules, are ubiquitous distributed in the ecosphere. It can be not excluded that humic or fulvic-like organic compounds are contained in organic clay material. Therefore, in the context of disposal of radionuclides in clay rock formation as well as in other geological formation data are needed about the interaction of actinides and these organic compounds. Under reducing conditions that occur in deep geological formations neptunium is stable in the tetravalent oxidation state.

Experimental data related to the interaction of tetravalent actinides are limited and mainly focused on Th(IV) which is less hydrolysable tetravalent ion and for which the complexation starts at a reasonable pH values. But data for the complexation of Np(IV) with humic substances are very scarce. The mechanism of tetravalent actinide complexation with humic or fulvic acids (HA or FA) is not well clarified, because of manifold experimental difficulties such as interfering eigen-colloid formation, strong sorption behaviour and redox reactions. Reiller et al., 2008, emphasized in their review that more sound experimental data on the complexation of tetravalent actinides by humic or fulvic acids are needed. Therefore, we have initiated studies on the Np(IV) fulvate complexation with the goal to elucidate the complexation mechanism by minimizing eigen-colloid generation of Np(IV).
Furthermore most of Np(IV) complexation studies with HS have been performed at low pH 1 and 1.5 by UV-VIS/NIR absorption spectroscopy [Marquardt et al., 2000, Pirlet, 2003], XANES and EXAFS [Denecke et al., 2002, 2005; Schmeide et al., 2005]. However, the understanding of Np(IV) speciation in containing humic substances is not satisfactory due to their formation of colloids, the various Np(IV) hydrolysis species and their mixed hydroxo fulvate complex species.

In this work we started a further approach by preparing tetravalent Np(IV) fulvate by three distinct methods, characterised the Np(IV) fulvates by UV-Vis, XANES, EXAFS, and XPS and faced all results to get more insight into the mechanism of the complexation.

6.2.1 Materials and Methods

Neptunium-237

The neptunium solution was evaporated to dryness and dissolved in 8 M HCl. The solution was purified via anion exchange (BIO RAD® AG 1-X8). After a washing step with several millilitres of 8 M HCl, plutonium contaminations were removed with a fresh solution of 150

mg NH_4I in 5 mL 8 M HCl. Subsequently, neptunium was eluted from the ion exchanger with 4 M HCl/ 0.05 M HF and evaporated to dryness in a PTFE beaker. To obtain a solution containing only Np(V), the solution was fumed two times with 1 M $HClO_4$ and the residue was dissolved in deionized water. This stock solution could be stored at a pH value of 3 for several days. Neptunium (IV) was prepared using a zinc-amalgam treatment and potentiometric electrolysis.

Gorleben fulvic acid

The natural humic acid and fulvic acid from ground water of the deep borehole Gohy-573 in the Gorleben site (lower Saxony, Germany) were isolated, purified and characterized according to [Wolf et al., 2004]. Elemental composition (C, H, N, O and S) of Gohy-573 HA and FA are shown in Table 6-2. Preparations of Gohy-573 HA and FA solution were carried out according to the procedure described above. The Proton Exchange Capacity (PEC) value of Gohy-573 FA was determined to 6.82×10^{-3} eq/g.

Table 6-2: Elemental composition of the new prepared Gohy-573 FA and HA. Summarized are the mean values of triplicate analysis, carried out by Analytische Laboratorien, Lindlar, Germany, together with the standard deviation. For comparison, also the elemental compositions of the former charges are shown (Gohy-573 FA (one analysis) and the mean value for Gohy-573 HA I and II (see, Buckau 1991)). The data are normalized to a total CHNOS content of 100 %.

Humic substance GoHy-573	C (wt.%)	H (wt.%)	O (wt.%)	N (wt.%)	S (wt.%)
FA	54.1 ± 0.1	4.23 ± 0.08	38.94 ± 0.04	1.38 ± 0.02	1.32 ± 0.01
HA	59.3 ± 0.1	4.57 ± 0.02	32.1 ± 0.1	2.01 ± 0.06	2.02 ± 0.09
FA (old batch)	57.18*	4.85	35.38	1.14	1.44
HA (old batch)	56.79	4.64	35.76	1.73	1.73**

* new calculated value; ** only the value of separate pre-batch (HA I) is given.

Different preparation paths for Np(IV)-FA compelxation experiments

To minimise Np(IV) colloids formation, three different preparation paths for Np(IV) fulvate complexation have been performed. 1) Np(IV) is formed in strong acidic solution (pH<1) by electrolytic reduction of Np(V). Afterwards aliquots of the solution were mixed with fulvic acid solution to form the Np(IV) fulvate complex (preparation I). 2) Trivalent Np is mixed with fulvic acid solutions and slowly oxidised by oxygen impurities in the glove box atmosphere to form the corresponding Np(IV) fulvate complex (preparation II). Because of the slow oxidation process and the strong interaction of Np(IV) with the fulvic acid, the uncomplexed Np(IV) concentration might be kept below its solubility limit. Thus, this method will avoid colloid formation of tetravalent neptunium even at higher metal concentrations. 3) A pentavalent Np fulvate complex is prepared at pH 9. Then the Np(V) is reduced by dithionate forming the Np(IV) fulvate complex (preparation III) Then, the Np(V)FA was reduced to tetravalent

neptunium complex (Np(IV)FA) with Na-dithionite resulting in a pH of about 3, 4.5, and 5. It is assumed that the Np(IV) occurs in HA as unhydrolysed Np^{4+} ion directly after the reduction reaction, but slowly becomes hydrolysed and forms colloidal species with time.
All solutions were characterised by UV-Vis spectroscopy, x-ray photoelectron spectroscopy (XPS), and XAFS. The Np(IV) concentration was in the range of 10^{-5} to 10^{-4} M, the fulvic acid concentration was 30 - 1000 mg/L the pH of the solutions was varied between 1 and 4.5 and the ionic strength was 0.1 M NaCl. All experiments were performed in a glove box with argon atmosphere.

UV-Vis/NIR absorption spectroscopy (UV-Vis/NIR)

The oxidation states of Np(IV) in the stock and sample solutions are confirmed by UV-Vis/NIR spectroscopy with a high-resolution UV-Vis/NIR spectrometer Cary 5 (Varian). The samples are measured in 1 cm inert-gas quartz cuvettes (Hellma) with tight screw tops, or in polystyrene semi-micro cuvettes (Brandt). UV-Vis/NIR spectra are taken from 400 nm to 1100 nm. The spectra are analysed using Grams/A1 (7.02 version) software. All complexation experiments are conducted according to titration procedures with initial Np concentration in the range of $5.0.10^{-5}$ $-2.0.10^{-4}$ M. Multiple titration's with different concentrations of fulvic acid and Np has been performed. In each titration, appropriate aliquots of the titrant (fulvic acid) are added to the Np and mixed thoroughly with stirrer (for 1-2 min) before the spectrum has been collected.

XAFS Measurements

XAS investigations were performed at the INE-Beamline for actinide research [Rothe et al., 2006] at ANKA, Karlsruhe, Germany. A double crystal monochromator (DCM) is used, equipped with a pair of Ge(422) crystals (2d = 2.310 Å), and higher harmonic radiation suppressed by detuning the parallel alignment of the DCM crystals to 70% of photon flux peak intensity at the beginning of each scan. The incident photon flux, measured with an Ar filled ionization chamber, is held constant using a MOSTAB feedback system. The spectra presented are measured in fluorescence yield detection geometry using a five pixel Canberra LEGe detector; 8 to 10 scans are averaged to reduce the noise level. Spectra are calibrated against the first inflection point in the XANES spectrum of a Zr foil for Np L_3-edge measurements. The energy of the inflection point is defined as the first derivative maximum set to E(Zr1s) = 17998 eV and E(Y1s) = 17038 eV. XAS spectra are measured with a step width of 5 eV before the edge, 0.7 eV steps in a region of -30 eV to 30 eV relative to the edge position, and equidistant steps in wave number k of 0.03 $Å^{-1}$ thereafter. XANES spectra are isolated from XAS scans following subtraction of the pre-edge background absorption and normalization of the edge jump to unity. The energy position of the XANES spectrum serves as a cross-check of the redox stability of the samples after repeated EXAFS scans. EXAFS data analysis is based on standard data reduction and least squares fit techniques using the ATHENA [Ravel and Newville, 2005] and the UWXAFS [Stern et al., 1995] program packages, respec-

tively. Metric parameters (coordination numbers N, distance to neighbor atoms r, and EXAFS Debye-Waller factors σ^2) are determined using backscattering amplitude and phase shift functions for single scattering paths obtained from FEFF7 [Rehr et al., 1992]. The energy scale is transferred into wave numbers by setting the maximum of the most pronounced feature in the spectra, the so-called white line, to k = 0 $Å^{-1}$. A k range of 2.5 - 9.5 $Å^{-1}$ is Fourier-transformed using a Hanning window with 0.1 Å sills, and fits are performed in R space from 1.5 - 2.5 Å for each sample. The amplitude reduction factor S_0^2 is held constant at 1.0 [Brendebach et al., 2009].

X-ray photoelectron spectroscopy (XPS)

The XPS spectrometer used is a PHI model 5600 (7×10-8 Pa base pressure) with a multi channel detector. XPS spectra were acquired by use of monochromatic Al Kα (1486.6 eV) X-ray excitation, spot size around 1 mm^2. A neutralizer, i.e., a source of low energy electrons, is applied to compensate surface charging. The binding energy scale of the spectrometer was calibrated by making use of the well-known binding energies of Cu $2p_{3/2}$, Ag $3d_{5/2}$ and Au $4f_{7/2}$ lines of sputter cleaned pure metal foils [Schild&Marquardt, 2000]. High-resolution scans of elemental lines were recorded at 11.75 eV pass energy of the hemispherical capacitor analyzer which yields a full-width-at-half-maximum. The elemental lines of samples are charge referenced to the C 1s line of adventitious hydrocarbon or to the C 1s line assigned to hydrocarbon bonding in the case of organic compounds at a binding energy (BE) of 284.8 eV. Curve fitting was performed using nonlinear least-squares optimization of Gaussian–Lorentzian sum functions [Schild&Marquardt, 2000].

6.2.2 Results and discussion

a) Characterisation of Np(IV)-fulvate by UV/Vis/NIR spectroscopy

Fig. 1 shows the absorption spectrum in the wavelength range between 920 and 1020 nm of Np(IV) fulvate solution prepared at pH 1, 1.5 and 3 and fulvic acid concentrations between 100 and 1000 mg/L and with different preparation approaches. Three absorption bands at 960, 968 and around 978 nm dominates the spectra depending on the pH value and the fulvic acid concentrations. At pH 1 and low fulvic acid concentrations (100 mg/L) mainly the peak of Np(IV)free at 960 nm is observed. With pH increase the peaks at 968 and 978 nm evolve, corresponding to two Np(IV) fulvate species. They are denoted in the following as Np(V)-$FA^{(I)}$ and Np(IV)$FA^{(II)}$.

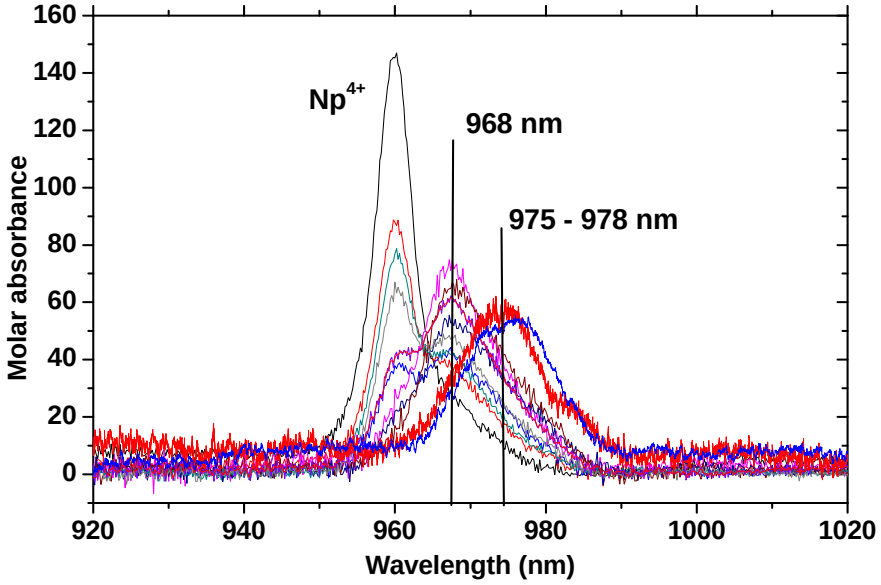

Figure 6-3: UV/Vis absorption spectra of Np(IV)-FA complexation between pH 1 and 3 and [Np(IV)] = 5E-05 M, [FA]= 100-1000 mg/L

At pH 1 and 1000 mg/L FA, mainly the absorption band at 968 nm was observed after 20 h of equilibration time and after 40 h a small new peak at 968 and 978 nm arises. By decreasing the FA concentration to 600 mg/L, 3 peaks were observed at 960 nm for the uncomplexed Np(IV) and at 968 and 978 nm for the fulvate species.

At pH 3 and 1000 mg/L FA, the peak at 978 nm besides a small one at 968 nm dominates the spectrum. No free Np(IV) was detected at 960 nm. By increasing the Np(IV) concentration, a new band near 984 nm appeared. However, only one isobestic point is found by plotting the spectra in the molar absorption scale indicating that only two species are directly correlated, the $Np(IV)_{free}$ and the $Np(IV)FA^{(I)}$. The evolution and the nature of the $Np(IV)FA^{(II)}$ species is so far unclear. Earlier studies by [Pirlet, 2003] showed also a dominating absorption band at 978 nm, by starting with the pentavalent Np(V) fulvate complex and reduction with dithionite (preparation III) but at higher pH values of about 7 than we have done (pH 3 - 5). We conclude from the pH independence of the peak maximum of the absorption band at 978 nm in the range between pH 3 and 7 that mainly one Np(IV) fulvate species prevails.

The FA concentration effect the Np(IV) fulvate complexation by varying the FA concentration from zero to 500 mg/L at constant Np(IV) concentration and pH value of 1 is illustrated in Figure 6-4. Again, one isobestic point can be found in the molar absorption scale indicating two species, the $Np(IV)_{free}$ and the $Np(IV)FA^{(I)}$. With increasing fulvate concentration the absorption at wavelengths larger than 980 nm steadily increases without evolving a new separated absorption band. In a first approach the relative weak absorption at longer wavelengths are neglected and the spectra a evaluated by only two species, $Np(IV)_{free}$ and $Np(IV)FA^{(I)}$.

The deconvulation is performed by the Program GRAMS (Galactic Co.), assuming the absorption peak area contrived by a mixed Gaussian-Lorentzian function. As shown in Figure 6-5, after subtracting the two deconvulated peak areas from the total composite absorption area, the residual part appears statistically zero in the investigated 920 nm to 1020 nm. For the absorption peaks of Np(IV) free ion and its fulvate complex with maxima at 960 and 968 nm absorption coefficients are calculated to be 150±10 L. $mol^{-1}.cm^{-1}$ and 65±15 L. $mol^{-1}.cm^{-1}$ respectively.

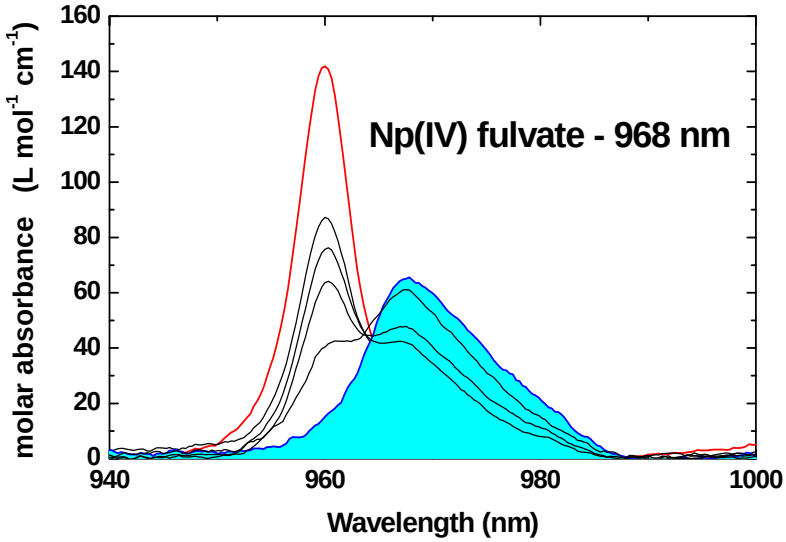

Figure 6-4: UV-Vis absorption spectra of Np(IV)-fulvate complex at 968 nm with varying FA concentration and constant Np(IV) concentration. [Np(IV)] = 3E-05 M, [FA]= 0-500 mg/L.

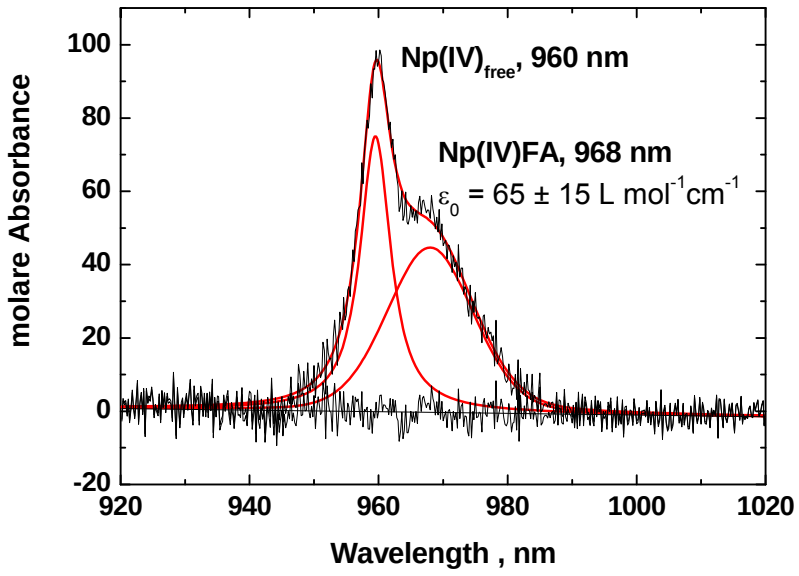

Figure 6-5: Illustration of the deconvulation spectra of the total absorption spectrum in to two single absorption bands for the free Np(IV) and Np(IV)FA(I). The peak maximums are found at 960 and 968 nm.

b) Np(IV)-fulvate by XAFS spectroscopy

XAFS measurements are performed repeatedly on various Np(IV) fulavte complexes to demonstrate that our specially designed sample cell is suitable to keep redox sensitive samples stable in an inert gas atmosphere long enough to measure good quality XAFS data.

XANES results

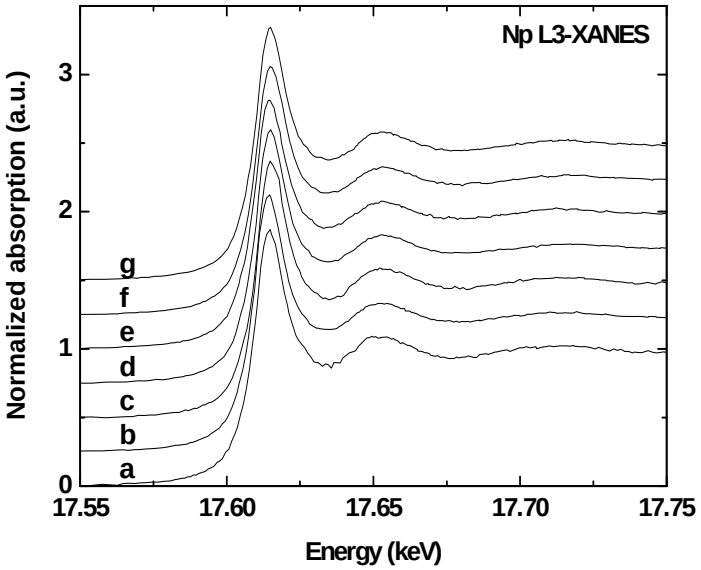

Figure 6-6: XANES of Np(IV) fulvate samples prepared in various ways (a, b: preparation (II); c, d: preparation (I); e, f, g: preparation (III). Spectra b, d, g: pH 1.0; Spectra a, c, f: pH 3.0; Spectra e: pH 4.5. A detail about the preparation is given in the text on page 110.

XANES spectra of Np(IV)FA complexes in H/NaCl solutions prepared by different approaches (method I to III, Page 110) are shown in Figure 6-6. The XANES spectrum of Np(IV)-FA shows the characteristic near-edge features of tetravalent Np compounds [Allen et al, 1997; Denecke et al, 2002, 2005; Schmeide et al, 2005**;** Brendebach et al, 2009]. All spectra are very similar irrespective of the preparation and the final pH value of 1.0 or 3.0. For all samples, the white line maximum are found at 17614.7±0.1 eV and the errors are estimated to lie in the order of one monochromator step of 0.7 eV. The absolute values might differ from those published in previous studies [Brendebach et al, 2009; Denecke et al, 2002, 2005; Schmeide et al, 2005], which is most likely caused by different energy calibrations of the X-ray monochromator or different monochromator crystals used in these experiments. However, the edge energy of the Np(IV) and Np(V) samples, determined as the inflection point of the edge, is nearly identical. Thus, the edge shift should be less suitable to distinguish between the tetra- and pentavalent oxidation states of actinides due to the combination of structural and electronic changes. Although the intensity of the white line in the XANES of Np(IV) samples is only slightly greater than that for the Np(V) sample [Brendebach et al, 2009], together with

evaluation of the EXAFS, we conclude that we can reliable distinguish between Np(IV) and Np(V) [Denecke et al., 2005].

EXAFS results

EXAFS measurements are performed to retrieve structural information of the first hydration shell surrounding the actinide ions. The Np LIII k3-weighted EXAFS spectra and the corresponding Fourier transforms are shown in Figure 6-7 for representative Np(IV)FA samples at pH 1, 3, and 4.5. The EXAFS spectra are very similar in the range up to 6 $Å^{-1}$, but show some difference at higher values. However, the scattering in the spectra in this k range makes evaluation somewhat difficult. The Fourier transform (FT) data in all cases show one dominant peak at approximately 1.9 Å (not phase shift corrected) that results from scattering on oxygen atoms of the coordinated water molecules.

Table 6-3 summarizes the structural parameters obtained from fits of the data according to the EXAFS equation. For five samples only one oxygen shell is observed with a variation in the distance between 2.24 and 2.38 Å. The Np(IV) atom is surrounded by about 6-8 oxygen atoms. There is no correlation among the preparation method and the distance as well as the coordination number of the oxygen atoms. Two samples are different from the other ones; they show two oxygen shells, one at a distance of 2.20-2.24 Å and one at 2.40 and 2.44 Å. This observation is in line with earlier results from [Denecke et al., 2002, 2005]. They found distances of 2.24 – 2.27 Å and 2.41 – 2.44 Å. However, the coordination number of 2 and 3 for each shell is rather low compared to [Denecke et al, 2005] with numbers between 3 and 4 and 5 – 7.

Table 6-3: Results from the fit EXAFS structural parameters of Np(IV) complexes with fulvic acid

Preparation of Np(IV)FA	fit range (Å)	N1 oxygen N2 oxygen	R1 (Å) R2 (Å)	σ2 (Å2)	ΔE0 (eV)	r-factor
a) pH 3 (preparation II)	1.23-2.36	6.2	2.36	0.0096	0.92	0.0021
b) pH 1 (preparation II)	1.29-2.30	8.6	2.24	0.0096	-5.98	0.0005
c) pH 3 (preparation I)	1.20-2.30	7.5	2.28	0.0097	-3.32	0.0004
d) pH 1 (preparation I)	1.17-2.36	7.4	2.32	0.0151	-1.03	0.0052
e) pH 4.5 (preparation III)	0.98-2.36	2.3 3.1	2.20 2.40	0.0073*	-2.29*	0.0012
f) pH 3) (preparation III)	1.07-2.42	2.4 2.7	2.23 2.44	0.0069*	0.26*	0.0037
g) pH 1 (preparation III)	1.23-2.36	6.7	2.38	0.0107	1.87	0.0013

The O shells of Np-O at distances of 2.20-2.24 Å is ascribed to a bonding between Np and hydroxyl ions, the longer Np-O distances at 2.40-2.44 Å is the average distance between coordinating water molecules and carboxyl groups. However, some samples showed only one average Np-O distance of 2.24 – 2.38 Å, which cannot be explained with respect to the preparation method at the moment. For the interpretation it is important that no Np-Np interaction with distances around 3.8 Å could be found in any sample. This observation is corroborate by the fact that we have not seen any dampening of the white line like it would be caused by polynuclear species. It can be concluded that the carboxylic groups of the fulvic acids are predominantly responsible for binding Np(IV) ions under the experimental conditions applied.

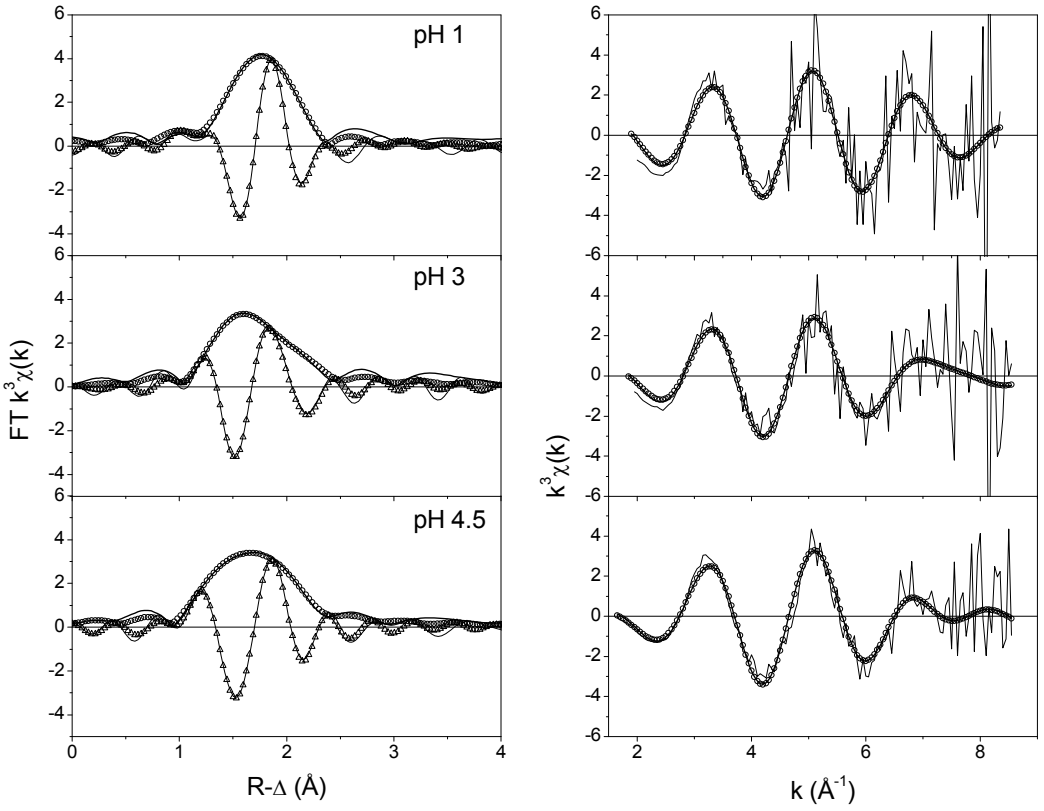

Figure 6-7: Np LIII- k3-weighted EXAFS spectra of Np(IV)-FA complex and corresponding Fourier transforms (upper: pH 1, middle: pH 3, lower: pH 4; preparation (III))

With our results from the XANES and EXAFS and results from other organic compounds characterised by [Bonin et al, 2009; Jeason et al, 2009, 2010] we can now suggest the following picture about the Np(IV) fulvate complexation that is illustrated in Figure 6-8.

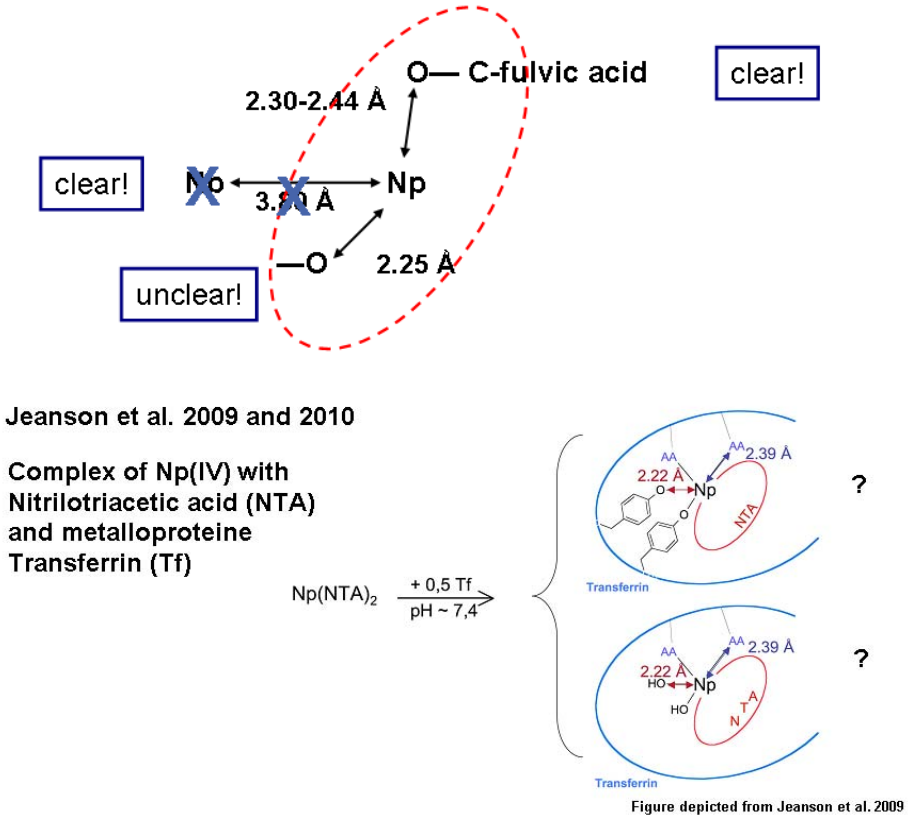

Figure depicted from Jeanson et al. 2009

Figure 6-8: Schematic representation of the Np(IV)-FA complex coordination structure according to EXAFS data. Explanation is found in the text!

[Jeanson et al., 2010] made some experiments with Np(IV) and two organic compounds Nitrilotriacetic acid (NTA) and Transferrin (Tf). They observed in the EXAFS two O shells, one at 2.22 – 2.23 Å and the other at 2.39 Å, for the system Np(IV) / NTA / Tf at pH > 7. Even they had a long range contribution between 3 to 4 Å for the ternary system and the binary Np(IV)/NTA system, the short range contribution lacks for the binary system! Attempts to fit the spectra with Np-Np contributions lead to a significant improvement of some spectra, but not to the global R factor of the fit. UV/Vis/NIR and microfiltration demonstrates that hydrolysed products remain negligible. Therefore they conclude that the short distance around 2.22 Å must be the result of the ternary complex! The long range distance is explained by a combination of triple scattering paths of NTA, multiple scattering contributions by Tf and only minor contribution from hydrolysed Np(IV). Two possible structures may be considered: (i) two tyrosine residues from Tf (2.22 Å), two Tf-sites and two NTA-sites (both between 2.34 and 2.39 Å); (ii) two OH instead of the tyrosine residues, two Tf-sites and two NTA-sites. If we consider FA as a heterogeneous compound with a high variation of binding sites, ternary complexes like the Np(IV)/NTA/Tf can be assumed: Np(IV)/FA(site1)/FA(site2) with tyro-

sine like sites or hydroxide groups. However, both assumption has to be proofed in future experiments. It is clear that the distance at 2.30 – 2.38 Å corresponds to monodentate bound carboxylate, and that we have no polynuclear species in solution. However, the distance at 2.40 – 2.44 Å could also be a bidentate carboxylate complex. The nature of the short distance at around 2.22 Å is unclear so far.

We also performed a separate experiments to observe the kinetic effect of Np(IV)-FA compelxation with varying contact time. The samples are prepared at pH 1 and 3 with 200 mg/L FA according to the complexation preparation II (see on Page 110). The contact time was 14 days and 3 months.

Table 6-4: Results from the fit EXAFS structural parameters of Np(IV) –FA with varying contact times

Sample	N	R (Å)	σ^2 (Å^2)	ΔE_0 (eV)	r-factor
200 mg/l FA, pH1, 14 days	9.5(1.2)	2.33(1)	0.018(2)	3.1(1.1)	0.0048
200 mg/l FA, pH3, 14 days	7.5(2.6)	2.32(2)	0.012(6)	-0.4(3.0)	0.0152
200 mg/l FA, pH1, 3 months	8.6(2.6)	2.34(3)	0.016(6)	3.7(2.6)	0.0015
200 mg/l FA, pH3, 3 months	8.6(1.3)	2.32(1)	0.018(3)	-0.3(1.3)	0.0026

Table 6-4 shows the fitted EXAFS structural parameters of Np(IV) –FA at both contact times (14 days and 3 months). The Np−O bond distance (R = 2*32*±0.02 Å) are determined for all Np(IV)-fulvate samples and the Np(IV) atom is surrounded by about 8-9 oxygen atoms. Despite the long contact time of three months no Np-Np bonds were found from the EXAFS. This experiment shows that no pH effect of the Np(IV)-FA complex and no aging of complex are obtained. However, either these changes in the complex with time cannot be measured by EXAFS or the changes are very small or do not exist in the experimental pH range.

c) Np(IV)-fulvate by XPS spectroscopy

The same samples prepared for the XAFS investigations were characterised by XPS. A typical XPS spectrum of Np(IV) fulvate, as illustrated in Figure 6-9, contains two Np 4f main lines, Np 4f5/2 at 415.5 eV and Np 4f7/2 at 403.5 eV, and two weak lines at 422.0 eV and 408.0 eV, which are shake-up lines (satellites) of the main lines. The spectra of each sample are very similar. The small differences in binding energies (6.8 eV) of the Np 4 f7/2 lines and in the satellite spacing's of the Np(IV)-fulvates are presumably caused by different pH during preparation. From the resemblance of the spectra we conclude that only one main Np(IV)-FA species occurs at pH 3 irrespective of the preparation method.

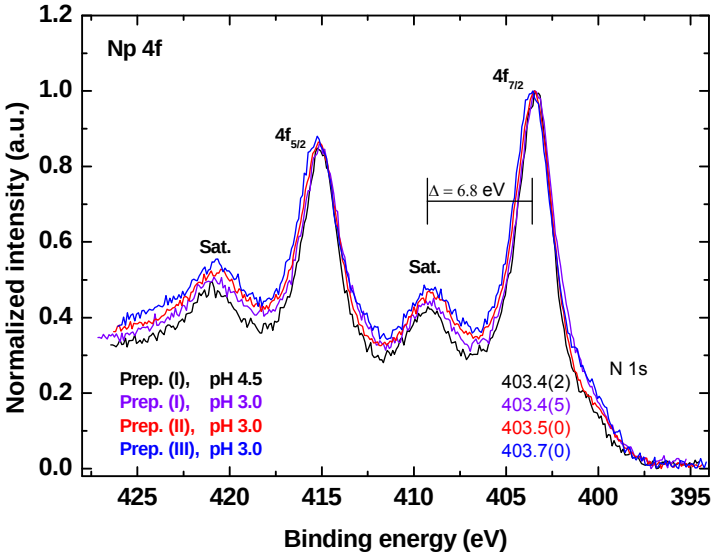

Figure 6-9: XPS spectra of Np(IV) fulvate samples prepared in various ways. Description of the preparation (I), (II), and (III) is given in the text. Np(IV) fulvate was measured as wet paste (precipitate + residual solution).

The peak separation between the main lines and shake-up satellites is indicated by (Δ). (Narrow scans of Np 4f spectra, Al Kα mono; X-ray excitation, charge reference: C 1s (C_xH_y) 284.8 eV) For the kinetic experiments with 14 days and 3 months contact time, the samples reacted 3 months show higher peak intensities, and hence, higher Np concentration than the 14 days Np-FA sample at pH 1-3 (Figure 6-10).

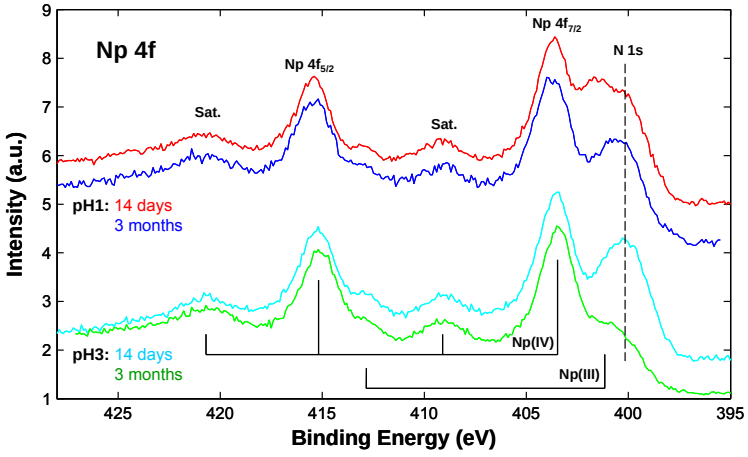

Figure 6-10: Np 4f lines and their satellites of Np(IV)-fulvates and XPS measurement performed after a reaction time of 1 days (red color line) and after 3 months of reaction (blue color line) at pH 1 and a reaction time of 14 days (olive color line) and after 3 months of reaction (green color line) at pH 3, acquired using monochromatic Al Kα X-rays.

An influence of pH (1, 3, and 4.5) on the XPS spectra of the Np-FA complexes has not been found after a reaction time of 3 months. However, the same conclusion can be made as for the

XAFS measurements, either these changes in the complex with time cannot be measured by XPS or the changes are very small or do not exist in the experimental pH range.

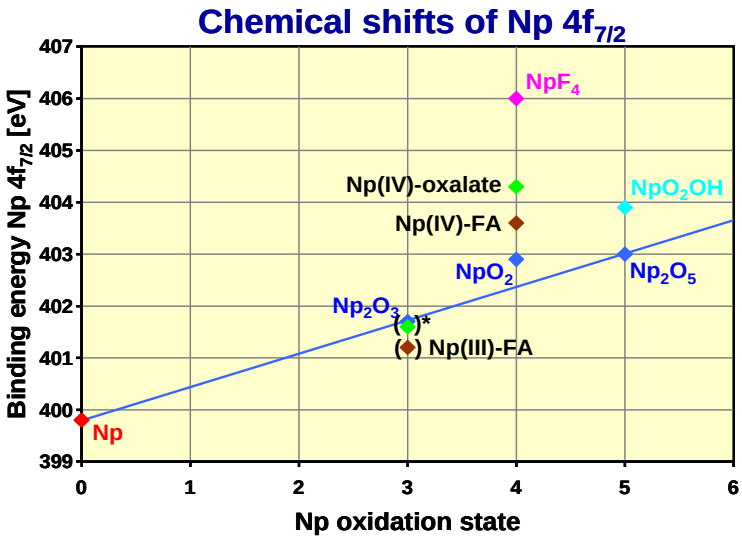

Figure 6-11: The chemical shifts of Np $4f_{7/2}$ spectra for the Np(III), Np(IV) and Np(V) complexes.

To get an indiciation how the Np $4f_{7/2/}$ line is altered by the chemical surrounding area of the Np atom, several Np compounds were measured by XPS. Figure 6-11 presents the binding energy (BE) of Np $4f_{7/2}$ spectra of Np^{4+}-fuvate, Np^{4+}-oxalate, Np(IV) hydroxide (amp), Np^{3+}-oxide, Np(III)-FA, NpO_2^+-hydroxide, NpO_2^+-oxide complexes. The electron density at the neptunium site is expected to be higher (decreased BE of Np $4f_{7/2}$ line) in the case of Np−O/OH and Np−O−C bonding than in the case of neptunium ions bound to carboxylic groups (increased BE of Np $4f_{7/2}$). So, if bonds other than to carboxylates are present at Np*(*IV*)*-fulvates, caused by hydrolyzed neptunium species, larger differences in BE between the $4f_{7/2}$ line and the satellite are expected ($\Delta BE > 6.8$ eV, s. in Figure 6-9). Similar results are also obtained for Th(IV)-humates [Schild et al., 2000]. Np $4f_{7/2}$ chemical shift of Np(IV)-HS is comparable with the data of Pu(IV)-HS and Th(IV)-HS.

2) Complexation constant

As mentioned above the XAFS and XPS cannt give a definite picture of the fulvate complexation and hereby the question whether a pure NpFA(IV) or a mixed ternary complex remains unsolved. To minimse the effects of mixed complexes on the thermodynamic complexatio constant, only data showing only two well separated peaks in the absortion spectra have been chosen for the evaluation. In the pH range 1 – 1.5, mainly one Np(IV) fulvate complex between Np^{4+} and the carboxylic groups of the FA (FA-COOH) is assumed forming the NpFA(IV) complex. Unfortunately, the hydrolysed species of the Np(IV), $Np(OH)^{3+}$, $Np(OH)_2^{2+}$, $Np(OH)_3^+$, and $Np(OH)_4$(aq) cannot be differentiated by absorption

spectroscopy. The total uncomplexed tetravalent Np(IV), including all hydrolysed species, can be measured. Hence, we have to calculate the amount of Np^{4+} and this has been done by the side reaction coefficient α. α is defined by the follwing reaction, deduced from the law of mass action of all hydrolysed species:

$$\left.\begin{aligned}[An]_{total} &= [An^{4+}]_f \left(1 + \sum_{n=1}^{4} \frac{{}^*\beta_n}{[H^+]}\right) \\ [An]_{total} &= [An^{4+}]_f \left(1 + \sum_{n=1}^{4} \beta_n [OH^-]^n\right)\end{aligned}\right\}$$

$$[An]_{total} = [An^{4+}]_f \alpha_{An(IV)}$$

Another problem that is needed for the estimation of the complexation constant is the deprotonation of the FA at such low pH values. The degree of deprotonation α_H can be measured by direct acid-base titration not lower than around pH 3.5. Therefore, an linear interpolation to pH 1 was made from the plot α_H as a function of pH value. This α_H has to be regarded as a rough estimate, only. By this way for pH 1 and 1.5 a degree of deprotonation of 1% and 8%, respectively, were obtained. Another way to correct the pH-dependence of FA is the introduction of the loading capacity LC of FA for the maximum Np concentration that can be bound at a certain pH value, here, pH 1 and 1.5. In Figure 6-12 the deduction of LC from experimental data is illustrated. The fitting of the lines yield in LC for pH 1 and 1.5 of (7 ± 1)% and (17 ± 1)%, respectively.

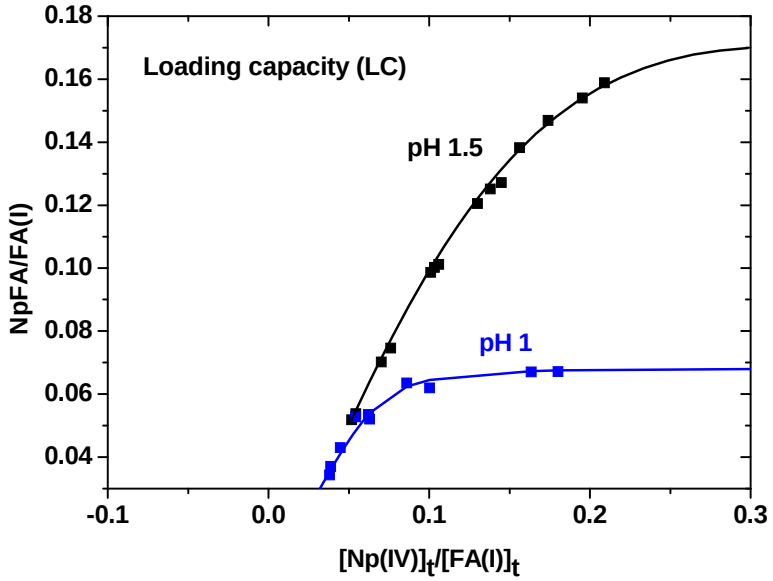

Figure 6-12: Determination of the loading capacity (LC) of fulvic acid for Np(IV) complexation at pH 1.0 and 1.5 from the experimental data according to the following expression:

$$\frac{[Np-bound]}{[FA(I)]_t} = 0.5 \cdot \left\{ \left(A \cdot \frac{[Np(IV)_t]}{[FA(I)]_t} + LC^* \right) - \left(\left(A \cdot \frac{[Np(IV)_t]}{[FA(I)]_t} + LC^* \right)^2 - 4 \cdot LC^* \cdot \frac{[Np(IV)]_t}{[FA(I)]_t} \right)^{0.5} \right\}$$

With all the needed parameter a complexation constant logβ of the NpFA(IV) complex formation was calculated, which is summarised in Table 6-5. Although the α_H and the LC are different, the logβs at the same pH value are very similar. The effect of the deprotonation parameters is not significant and estimate values can be used as a first approach for the determination of the complexation constant. However, the complexation constant logβ is not pH independent for the tetravalent neptunium.

pH	α_H (%)	LC (%)	log$\beta(\alpha_H)$	logβ(LC)
1.0	1	7 ± 1	7.0 ± 0.5	6.9 ± 0.2
1.5	8	17 ± 1	7.5 ± 0.4	7.7 ± 0.2

Table 6-5: Complexation constant of the NpFA(IV) complex at pH 1 and 1.5 and ionic strength of 0.1 M NaCl including the parameter degree of deprotonation α_H and the loading capacity LC.

If we compare the complexation constant with values deduced in the same way from experimental data of U(IV), Th(IV), Np(IV), and Pu(IV) humate complexation from [Reiller et al., 2008], the pH dependence of logβ is confirmed. Figure 6-13 illustrates that the present complexation constants fits well in a qualitative line that expresses the logβ as a function of pH.

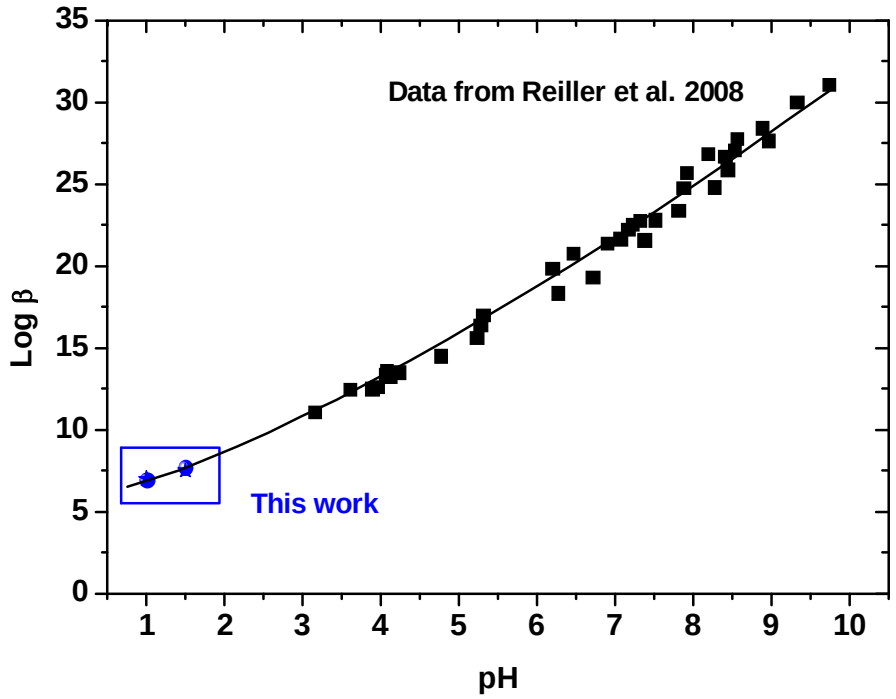

Figure 6-13: Complexation constant (Logß) for the tetravalent actinide (Th(IV), U(IV), Np(IV), and Pu(IV)) and humic substances with varying pH values.

7 Reproduction of a natural clay system from pure components

The reproduction of the natural clay system from pure components focused since the beginning of the project on the polymerization of low molecular weight compounds as natural organic matter building block under well-defined conditions and presence of swelling clay. The approach to synthesis kerogen from low molecular weight compounds containing solely the elements C, O, H and N has the advantage to avoid the problems of inorganic impurities inherent in the kerogen even after isolation and furthermore is a route to gain knowledge on the reaction pathway, possible catalytic effects of mineral phases (i.e. smectite) and influence of exchangeable cation composition. Until now several model humic substances have been synthesized (Arfaioli et al., 1997; Bosetto et al., 2002; Bosetto et al., 1997; Jung et al., 2005; Pompe et al., 2000) and most of them have been obtained via the Maillard reaction (Jokic et al., 2004; Maillard, 1912a; Maillard, 1912b) which consist in an amino-acids reduction step (melanoidin, glycine, melodoin) via sugars and is considered to be an important pathway in natural humification processes.

In our case, condensations of low molecular weight compounds have been realized by taking as initial components: (1) 0.05 $mol \cdot L^{-1}$ and 0.5 $mol \cdot L^{-1}$ of D-glucose ($C_6H_{12}O_6$) and glycine ($C_2H_5NO_2$), or (2) 0.05 $mol \cdot L^{-1}$ and 0.5 $mol \cdot L^{-1}$ of catechol ($C_6H_6O_2$). Each solution was kept in contact with the <2µm purified fraction of Na- or Ca-exchanged bentonite (Ibeco) during 1 months in an oven at 80°C under wetting/drying cycles. Elevated temperature and wetting/drying cycles have been shown to activate the formation of the dark brown polymer condensate (Benzing-Purdie et al., 1985; Bosetto et al., 2002; Bosetto et al., 1997). In order to study the potential smectite catalysis of the reaction and the influence of the exchangeable cations (Na, Ca) a characterization of the organic matter polymerized by several analytical techniques have been evaluated. An evaluation of the molecular composition of solid products has been conducted by the use of pyrolysis-gas chromatography-mass spectrometric (py-GC/MS; (Gadel and Bruchet, 1987)).

An exemplary GC/MS fractogram is shown in Figure 7-1. In the case of the D-glucose- glycine and Ca-smectite, compounds generated in the solid fractions are mainly cyclic organic compounds like alkyl-benzene or alky-phenol but also contains N-functions (pyridine, pyrrole, indole). Polymerization of catechol with Ca-smectite leads to the formation of aliphatic compounds (alkanes, and unsaturated alkenes) and few aromatics like alky-benzene.

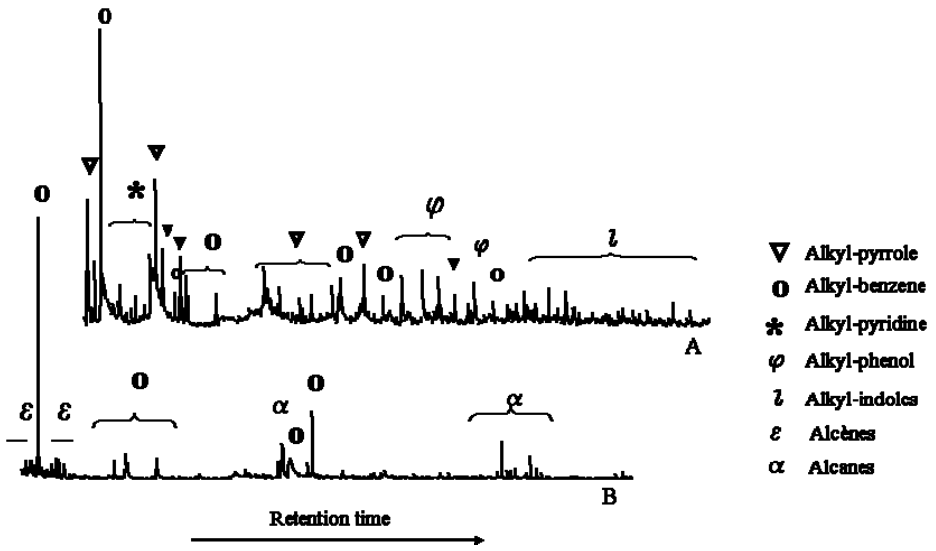

Figure 7-1: Py-GC-MS chromatograms obtained on the polymerisation products after 1 month at 80°C under wet/drying cycles.(A) Ca-smectite (smectite), Glucose (0.05mol.L-1) + Glycine (0.05mol.L-1) ; (B) Ca-smectite (Ibeco), catchol (0.05mol.L-1)

Unfortunately, the py-GC/MS experimental set-up used in GREGU (Nancy) is optimized for pure organic samples and the polymerized organic matter (OM) clay associates used in this study produced only weak signals. Precise analysis on the molecular composition of the clay mineral associated OM where therefore not possible by py-GC/MS.

However, the functionality of the OM was successfully determined by mean of μFT-IR analyses in collaboration with GREGU (Nancy, France) (Bosetto et al., 1997) and thus it will be possible to clearly identify a potential catalytic effect of clay minerals on organic matter polymerization. This data is planned to be published soon.
The reactivity of the clay fraction and potential changes in swelling properties have been investigated by XRD and TEM measurements in collaboration with the French Museum on Natural History and GREGU (Nancy). The investigations conducted on all initial samples and interstage products showed polymerized organic material in the smectite interlayers in the case of "Glucose + glycine" samples. The polymerization process and delaminating of the smectite layers (see Figure 7-2) was hereby a function of the initial organic matter to clay mineral fraction ratio. On the contrary, polymerization of catechol doesn't affect the swelling properties of the Ibeco smectite and no organic matter in the interlayer could be found at all OM/clay ratios investigated. These findings give possible insides in the contradicting results found in the literature on the availability of clay mineral interlayer space for organic matter preservation.

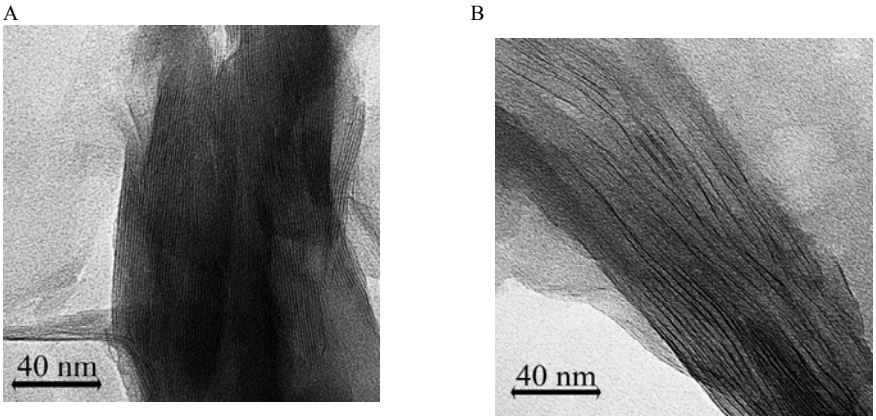

Figure 7-2: TEM images obtained on the polymerisation products after 1 month at 80°C under wet/drying cycles. (A) Ca-smectite (<2µm smectite of Ibeco bentonite), (B) Ca-smectite (<2µm of Ibeco bentonite), glucose + glycine (0.05mol.L-1)

The reactivity of the clay fraction and potential changes in swelling properties has to be considered as well. In addition, synchrotron based C1s-STXM measurements (NSLS, beamline X1A, Brookhaven National Laboratory, USA) have been realized on polymerized samples. The results (see as an example Figure 7-3 and Figure 7-4) show that the organic material synthesized still contains a higher amount of oxygen containing functional groups (phenol-type groups ~286.6eV; carboxyl-type groups ~288.4eV) and cannot be directly compared to smectite associated organic material found in the Callovo-Oxfordian formation (Schäfer et al., 2005b).

Looking in detail on the via Maillard reaction clay associated organic matter in comparison to the synthetic humic substances M42 from HZDR and the isolated fulvic acid GoHy711 revealed very comparable C1s- NEXAFS spectra (Schäfer et al., 2005a; Vilas et al., 2010).

In order to overcome the problem of humic substance synthesis a series of confined pyrolysis test was conducted on the "*GG -Ca-smectite*" polymerized products with the aim of reaching a kerogen-type material, taking into account the O/C and H/C atomic ratios published for the Toarcian and Callovo-Oxfordian formations of the Paris Basin (Deniau et al., 2008; Vandenbroucke and Largeau, 2007). Time-temperature parameters of pyrolysis were chosen to be 160°, 180°, 200° and 250°C during 24 hours in agreement with previous works published on Callovo-Oxfordian formation, see schematic figure below (Elie and Landais, 1997).

Elemental composition of the pyrolysis products are ploted in a conventional Van Krevelen diagram in the Figure 7-5 where characteristics of Toarcian and Callovo-Oxfordian kerogen are added as references. As it is visible on the Figure 7-5, the O/C values obtained are comparable with kerogen values from the Boom Clay formation (Belgium), whereas the H/C ratios fall within the range expected for black carbon (BC) or soot. Therefore, the experimental parameters of confined pyrolysis have to be adjusted and Rock Eval analysis will be performed to confirm the elemental compositions.

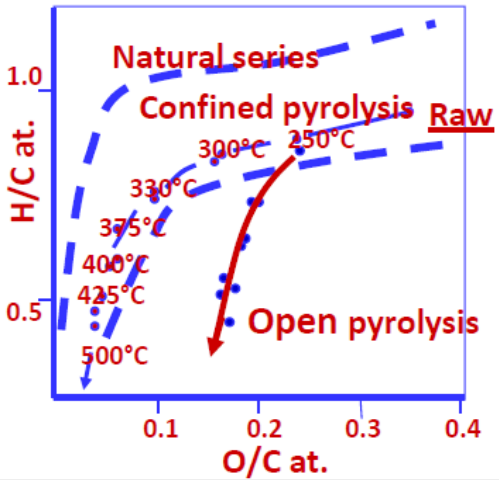

Figure 7-3: Schematic Van Krevelen diagram of the O/C vs. H/C trend observed in the natural system in comparison to the one obtained by different temperature adjustments in confined and open pyrolysis (Elie and Landais, 1997).

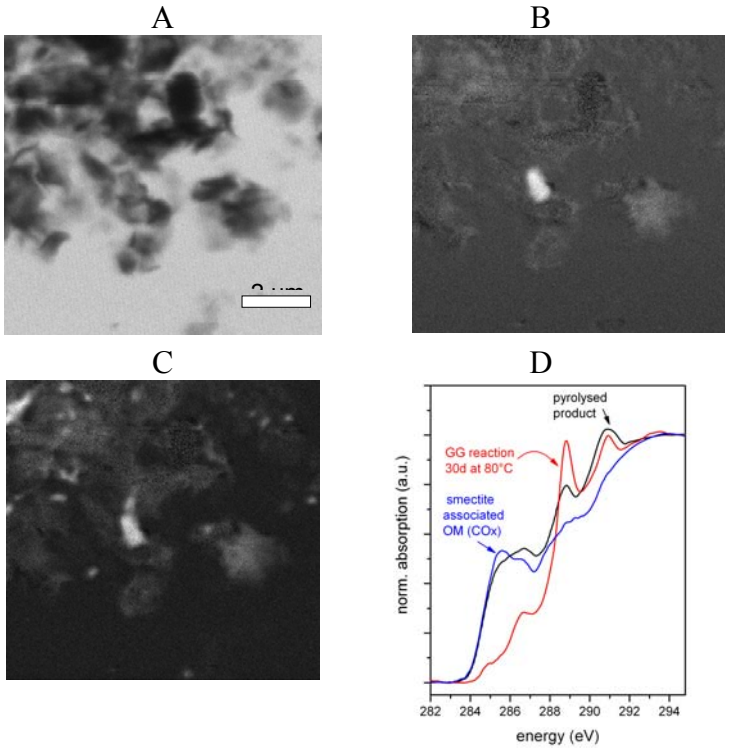

Figure 7-4: Carbon edge STXM investigations of Ca-exchanged bentonite reacted with glycose+glycine (GG) for 30 days at 70°C including wetting/drying cycles and treated with confined pyrolysis at 250°C for 24 hours. A: Absorption image at 280 eV below the carbon edge; B: Ratio image (light grey values indicate high concentration) showing the distribution of C=C functionality; C: Ratio image showing the distribution of carboxyl-type groups; D: Comparison of spectra obtained for the smectite associated natural organic matter (OM) in the Callovo-Oxfordian formation, the reaction products of GG polymerization and the polymerized samples after pyrolysis.

Taking the C1s STXM measurements of the pyrolysed products (see Figure 7-4) the polymerized organic material found shows a higher amount of oxygen containing functional groups (especially in the range of carboxyl-type groups; ~288.4 eV) confirming the elemental analysis results presented above. Interestingly, the absorption in the aromatics region (~285.2 eV) is quite comparable to the smectite associated organics found in the Callovo-Oxfordian formation and represents therefore a better analogue. However, the pyrolyzed products fall within the van Krevelen diagram more within the of char/soot or black carbon (BC) and are with respect to their H/C atomic ratio depleted, which shows that the pyrolysis parameters have to be adjusted for the Maillard reaction derived humic substances to reach the kerogen maturity of the COx organic matter.

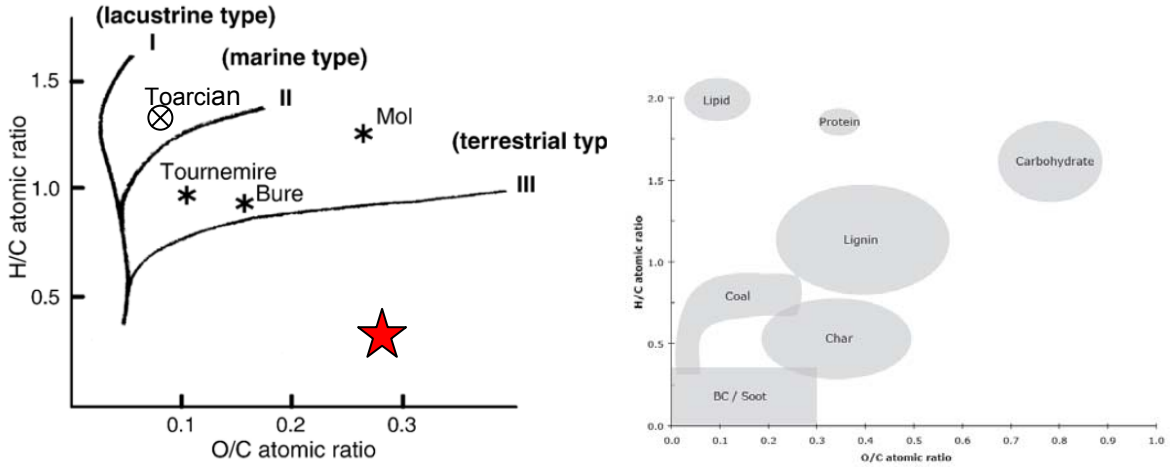

Figure 7-5: Van Krevelen diagram for natural kerogen samples (Deniau et al., 2008), additional inserted is the Toarcien kerogen (Vandenbroucke and Largeau, 2007Vandenbroucke and Largeau, 2007). The O/C and H/C atomic ratios of the series of "D-glucose, glycine and Ca Ibecco bentonite after confined pyrolysis at 160, 180, 200 and 250°C are represented by the red star. For comparison, a figure of showing different organic materials is added (Preston and Schmidt, 2006).

8 The role of low-molecular organic components in the diffusion of radionuclides in OPA – a literature study

Rock material from the opalinus clay formation contains approximately one weight percent of organic carbon [Courdouan et al., 2007]. This organic matter is partly dissolved in the pore water of the clay material. Its composition is highly heterogeneous, showing large and complex molecules like humic and fulvic acids as well as small organic acids (e.g. formate (up to 2 μM), acetate (up to 203 μM), propionate (up to 27 μM) and lactate (up to 9 μM)). These different organic molecules are potential ligands for radionuclides which may leach into the pore water of the clay formation.

Natural clay formations show a very low hydraulic conductivity. Thus, the main transport mechanism, which will determine the migration or retention of radionuclides in clay rocks is the diffusion process [Nagra, 2002; Andra, 2005]. In order to model the long term migration of radionuclides in a nuclear waste repository in clay formations, a distinct understanding of their diffusion is mandatory. The question arises, whether the above mentioned organic complexing agents will influence this process. Thus, a detailed knowledge of the ternary systems radionuclide-organics-clay is needed. However, the modeling of such complex ternary systems is a very difficult task. Therefore, a distinct understanding of the binary systems clay-organics, clay-radionuclide and radionuclide-organics is required first.

The aim of the present work is to give a basic overview of the binary system actinide-organic ligand. Studies with ligands like actetate, propionate or lactate are of direct relevance for the natural system. Furthermore, systematic studies with more uncommon ligands like oxalic and phtalic acid are important for gaining a deeper insight into the mechanism of the complexation of actinides with organic ligands. Also, these ligands serve as model ligands for binding sites of more complex ligands like humic or fulvic acids.

In the past, numerous studies on the complexation of different actinides with organic ligands were performed, using a broad series of experimental techniques (mainly indirect methods like potentiometry or solvent extraction). Due to the large quantity of available data, several important ligand systems are selected within the scope of this work. In the following, the literature data on the respective actinide complexes is discussed with respect to their oxidation states.

8.1 Complexation of trivalent actinides with organic ligands

Experimental data on the interaction of trivalent actinides with small organic ligands is scares. More common are studies with trivalent lanthanides. Due to the similarity of their chemical properties, selected literature data on Eu(III) and Nd(III) is also discussed within the present work. The thermodynamic log β^0_n values for the complexation of Ln(III) and An(III) with different organic ligands are summarised in Table 8-1. The molecular structures of these ligands in their acid form are displayed in Figure 8-1.

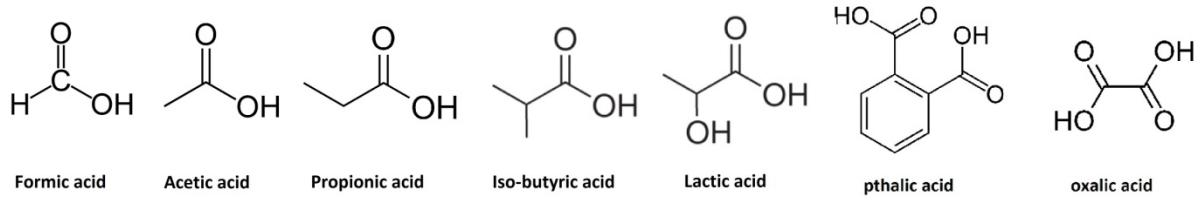

Figure 8-1: Molecular structures of formic-, acetic-, propionic-, iso-butyric-, lactic-, pthalic-, and oxalic acid

The formic-, acetic- and propionic acid differ only by the length of their aliphatic alkyl chain. The carbon chain of iso-butyric- and lactic acid is the same as for propionic acid, with an additional methyl or hydroxyl group in α-position, respectively. The alkyl chain length of oxalic acid is similar to acetic acid, but the molecule shows two carboxylic acid functional groups. Pthalic acid is a derivative of benzoic acid with an additional COOH group in ortho position.

Table 8-1: log β_n values for the formation of Ln(III) and An(III) acetate/propionate/iso-butyrate and lactate complexes.

Complex	pK_a ligand	log β^0_1	log β^0_2	Ionic strength	method	Ref
$Eu(formate)_n^{3-n}$	3.70	1.83	2.84	0	Pot.	a
$Eu(acetate)_n^{3-n}$	4.76	2.58	4.52	0	Pot.	a
		2.20 ± 0.50	-	0.1 M ($NaClO_4$)	TRLFS	b
		2.80 ± 0.30	5.90 ± 0.60	10^{-3} M	ESI-MS	b
		2.00	3.80	0.1 ($NaClO_4$)	Spec.	c
$Am(acetate)_n^{3-n}$	4.76	2.49 ± 0.08	-	0	Solv.Ex.	d
$Eu(propionate)_n^{3-n}$	4.88	2.70	4.65	0	Pot.	a
$Cm(propionate)_n^{3-n}$		3.34 ± 0.04	4.51 ± 0.26	0	TRLFS	e
$Cm(phtalate)_n^{3-n}$	2.95 and 5.41	3.62 ± 0.02	-	0.1 ($NaClO_4$)	TRLFS	f
$Eu(iso\text{-}butyrate)_n^{3-n}$	4.85	2.32	4.13	0	Pot.	a
$Eu(lactate)_n^{3-n}$	3.87	3.27	5.81	0	Pot.	a
		2.99 ± 0.17	5.09 ± 0.23	1.05 m ($NaClO_4$)	Spec.	g
$Nd(lactate)_n^{3-n}$	3.87	2.58 ± 0.05	4.60 ± 0.06	1.05 m ($NaClO_4$)	Spec.	g
		2.60 ± 0.01	4.66 ± 0.02	1.00 M (NaTf)	Pot.	h
$Am(oxalate)_n^{3-n}$	1.23 and 4.19	5.20	9.20	0.0	Solv.Ex.	i

a: [Wood, 1993]; b: [Plancque et al., 2005]; c: [FAR64]; d: [Moore et al., 1999]; e: [Höhne, 2010]; f: Panak et al., 1995]; g: [Tian et al., 2010]; h: [Zalupski et al., 2010]; i: [Choppin&Chen, 1996]

The stability constants of the Eu(III)-formate, -acetate and -propionate complexes increase according to the increasing pK_a of the ligands. The slightly smaller value of log β^0_n(Eu(iso-butyrate)$_n^{3-n}$) by approximately 0.35 orders of magnitude can be attributed to a steric hindrance of the complex formation by the α-methyl group. Contrary, the log β^0_n(Eu(lactate)$_n^{3-n}$) values are by more than one order of magnitude higher, compared to log β^0_n(Eu(formate)$_n^{3-n}$), although the acidity of lactic acid is similar to formic acid. Furthermore, the log β^0_n(Am(oxalate)$_n^{3-n}$) value is by 2.5 logarithmic units higher compared to the Am(acetate)$^{2+}$ complex. These increased stability constants are explained by an additional stabilisation of the complex due to the functional group in α-position.

However, the discussed data was mainly determined by potentiometric measurements or solvent extraction. These are indirect techniques, which disturb the chemical equilibrium during the measurement. In contrary, spectroscopic methods are capable to determine the solution speciation directly at equilibrium conditions. This might be the reason for the distinctive discrepancy in themodynamic data determined by different methods. For example, the value of log β^0_n(Eu(propionate)$_n^{3-n}$ (potentriometric data) is by 0.6 orders of magnitude smaller than log β^0_n(Cm(propionate)$_n^{3-n}$), which was determined by TRLFS. A similar discrepancy is observed for the log β^0_n(Eu(lactate)$_n^{3-n}$) values determined by Wood (potentiometric data) and Tian et al (spectroscopic data). To compare these data, the conditional values given by Tian et al. are extrapolated to I_m = 0 with the SIT approach, as recommended in the NEA-TDB [Guillaumont et al. 2003]. The so calculated log β^0_n(Eu(lactate)$^{2+}$) = 4.04 ± 0.20 and log β^0_n(Eu(lactate)$_2^+$) = 6.65 ± 0.25 values are distinctively larger than the respective potentiometric data. A comparable effect is also observed for the stability constants of Ln(III)/An(III) complexes with inorganic ligands. For example, large differences of the log β^0_n(Cm(SO$_4$)$_n^{3-2n}$) values determined by indirect methods and spectroscopic techniques are found, which are beyond experimental uncertainty of the two different experimental methods. [Guillaumont et al. 2003] These findings point toward a general difference of the data demined by indirect methods and spectroscopy.

8.2 Complexation of tetravalent actinides with organic ligands

In case of the tetravalent actinides a few data on the complexation of Th(IV) with different organic ligands are available in the literature. Rao et al studied the complexation of Th(IV) with acetic acid by means of potentiometry and microcalorimetry [Rao et al., 2004]. The authors identified complexes with up to five acetate ligands and determined the respective log β'_n values at an ionic strength of I_m = 1.05 (NaClO$_4$). The stepwise stability constants log K'_n decrease with increasing n. This effect is expected as the complex is more and more negatively charged as ligands are introduced into the first coordination sphere. Furthermore, data on the complexation of Th(IV) with different dicarboxylic acids are available in the literature. In the following, the literature data on the Th(IV) complexes with malonate, succinate, glutarate and oxydiacetate is summarized (Table 8-2). For a better comparison, exclusively condi-

tional stability constants valid for an ionic strength of I_m ~ 1.0 ($NaClO_4$) and determined by potentiometric methods are discussed. The structure of the respective ligand molecules in their acid form are shown in Figure 8-2.

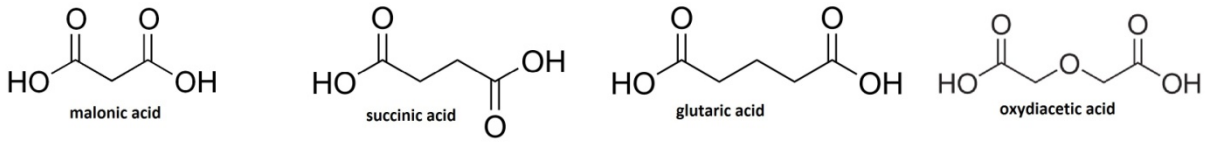

Figure 8-2: Molecular structures of malonic-, succinic-, glutaric- and oxydiacetic acid

The malonic-, succinic- and glutaric acids differ only by the length of the carbon-chain between the two terminal carboxylic acid groups. The oxydiactic acid has the same chain length as the glutaric acid, but shows an additional ether function in β-position to both COOH groups.

The complexation of Th(IV) with dicarboxylic ligands is distinctively stronger compared to ligands with only one COOH functional group. The complexation of Th(IV) with malonic acid was studied by [DiBernardo et al., 1977], [Srinivasan et al., 2006] and [Rawat et al., 2011]. The formation of up to 1:3 complexes is confirmed by all authors and the respective conditional log β'_n values are determined. The given stability constants are by several orders of magnitude larger than the respective values for the acetate complexes. The increased complexation strength of dicarboxylic acids results from the chelating effect of the second COO^--group, similar to functionalized monocarboxylic acids. Obviously, the length of the aliphatic chain has a distinct impact on the size of the chelate ring.

Table 8-2: log β'_n for the complexation of Th(IV) with actetate, malonate, succinate, glutarate and oxydiacetate

ligand	pK_a ligand	log β'_1	log β'_2	log β'_3	I_m ($NaClO_4$)	method	Reference
acetate	4.76	3.81 ± 0.02	6.79 ± 0.02	8.71 ± 0.13	1.05	Pot.	a
malonate	2.85 and 5.69	7.25 ± 0.07	12.78 ± 0.17	16.74 ± 00.30	1.00	Pot.	b
		7.47	12.79	16.28	1.00	Pot.	c
		7.47 ± 0.04	12.84 ± 0.04	16.54 ± 0.06	1.05	Pot.	d
succinate	4.21 and 5.64	6.4 ± 0.2	8.8 ± 0.4	-	1.00	Pot.	b
glutarate	4.33 and 5.57	6.2 ± 0.1	-	-	1.00	Pot.	b
oxydiacetate	2.96 and 4.43	8.15 ± 0.08	14.82 ± 0.21	18.16 ± 0.33	1.00	Pot.	e

a: [Rao et al., 2004]; b: [Rawat et al., 2011]; c: [DiBernardo et al., 1977]; d: [Srinivasan et al., 2006]; e: [[DiBernardo et al., 1983]

The log β'_n for the Th(oxydiacetate)$^{2+}$ complex is by one order of magnitude larger than the corresponding stability constant for the Th(IV) complex with the other dicarboxylic acids. This is due to the formation of a chelat complex with an additional contribution of the ether oxygen atom.

8.3 Complexation of pentavalent actinides with organic ligands

A broad variety of literature data on the complexation of Np(V) with small organic ligands is available. Within the scope of the present overview, the data for the Np(V)-actetate, -oxalate and -lactate systems are discussed. The conditional stability constants for the formation of the 1:1 complexes of Np(V) with the respective ligands are summarized in Table 8-3. Unfortunately, the data are given for different ionic strengths and ionic media in some cases. Thus the comparison of the single log β' values is difficult. No data on the formation of higher Np(V) complexes with the ligands is available in the literature.

Table 8-3: log β'_1 for the complexation of Np(V) with actetate, oxalate, lactate and α-hydroxy-isobutyrate

ligand	pK_a ligand	log β'_1	I_m (NaCl)	Method	Reference
acetate	4.76	1.13	1.0	Solv.Ex.	a
		0.99 ± 0.10	1.0 ($NaClO_4$)	Solv.Ex.	b
		1.70 ± 0.04	5.0	Spect.	c
		1.93 ± 0.01	0.3 (NH_4ClO_4)	Spect.	d
oxalate	1.23 and 4.19	3.35 ± 0.06	1.0 ($NaClO_4$)	Solv.Ex.	b
		3.55	<0.1	Solv.Ex.	e
		3.04 ± 0.08	5.0	Spect.	c
lactate	3.87	1.11	2.0	Solv.Ex.	e
		1.48 ± 0.05	2.0	Solv.Ex.	a
		0.76 ± 0.03	5.0	Spect.	c

a: [Moore et al., 1999]; b: [Pokrovsky&Choppin, 1997]; c: [Borkovsky et al., 1996]; d: [Takai et al., 2009]; e:[Inoue&Tochiyama, 1983]

The value of log $\beta'_{1,25°C}(NpO_2(acetate))$ is by almost 3 logarithmic units smaller than the corresponding value for the Th(IV)-acetate complex. The introduction of an additional carboxylate group results in an increase of the stability constant by several orders of magnitude [Moore et al., 1999; Pokrovsky&Choppin, 1997]. This increase in the stability constant is in good agreement with the increase observed for Am(III)-complexes.[Choppin&Chen, 1996; Moore et al., 1999] Due to the large discrepancies of the data presented in Table 8-3, an increase of log β'_1 in presence of an α-hydroxyl-group is not observable.

The available data shows rather large scattering of the values. For example the log β'_1 (NpO_2Lac) (I_m = 2.0) determined by [Inoue&Tochiyama, 1983] and [Moore et al., 1999] by solvent extraction differ by almost 0.4 orders of magnitude. Additionally, a distinct difference between data determined by indirect methods and spectroscopy is observed. For this comparison, the available conditional stability constants for the NpO_2Ac complex are extrapolated to

I_m = 0, using the SIT approach [Guillaumont et al., 2003]. The so calculated spectroscopic values (log β^0_1 (NpO_2Ac) = 1.92 ± 0.05 [Borkovsky et al., 1996]; log β^0_1 (NpO_2Ac) = 1.94 ± 0.03 [Takai et al., 2009]) are by almost one order of magnitude higher than the respective data from indirect methods (log β^0_1 (NpO_2Ac) = 1.16 ± 0.05 [Moore et al., 1999]; log β^0_1 (NpO_2Ac) = 1.02 ± 0.12 [Pokrovsky&Choppin, 1997]). These findings are in very good agreement with the data discussed for trivalent actinides.

8.4 Complexation of hexavalent actinides with organic ligands

Numerous studies have been conducted on the complexation of UO_2^{2+} with organic ligands. In the following, only the data on U(VI)-acetate, -malonate, -oxalate, -oxydiacetate and -thiodiacetate complexes are summarised (see Table 8-4). The structures of the ligands are given in Figure 8-1and Figure 8-2. The thiodiacetate ligand has a similar structure to oxydiacetic acid, but with a thioether bridge between the two terminal carboxylic acid groups.

The conditional stability constants of the U(VI)-acetate complexes are similar to Ln(III)/An(III) complexes [Choppin&Rizkalla, 1994]. The log β'_n values for the U(VI)-oxalate complexes are by several orders of magnitude higher than the corresponding log β'_n for the U(VI)-acetate complexes, whereas the log $\beta'_n(UO_2(malonate)_n^{2-2n})$ is by 0.7 logarithmic units lower compared to log $\beta'_n(UO_2(oxalate)_n^{2-2n})$, despite the higher p$K_a$ values of malonate.

Table 8-4: log β'_1 for the complexation of U(VI) with actetate, oxalate, malonate, oxydiacetate and thio-diacetate (T = 25°C)

ligand	pK_a ligand	log β'_1	log β'_2	log β'_3	I_m	method	Reference
acetate	4.76	2.58 ± 0.03	4.37 ± 0.14	6.86 ± 0.04	1.0 ($NaClO_4$)	Pot.	a
		1.68 ± 0.02	3.18 ± 0.03	-	5.0 (NaCl)		b
oxalate	1.23	7.44 ± 0.07	12.07 ± 0.10	13.40 ± 0.25	0	Spect.	c
	and 4.19	6.06 ± 0.01	10.76 ± 0.02	13.27 ± 0.22	1.0 ($NaClO_4$)	Spect.	c
malonate	2.85 and 5.85	5.36 ± 0.01	9.39 ± 0.01	11.22 ± 0.06	1.0 ($NaClO_4$)	Pot.	d
oxy-diacetate	2.96 and 4.43	5.01 ± 0.04	7.64 ± 0.11	-	1.0 ($NaClO_4$)	Pot.	e
thio-diacetate		2.89 ± 0.03	-	-	1.0 ($NaClO_4$)	Pot.	f

a: [Jiang et al., 2002]; b: [Borkovsky et al., 1996]; c: [DiBernado et al., 2009]; d: [Rao et al., 2002]; e: [Rao et al., 2003]: f: [DiBernado et al., 2006]

Introduction of an ether bridge between the two carboxylic acid groups results in even further decrease of the log β'_n values. This finding is in contradiction to the analogous Th(IV)-

oxydiacetate system. There, the ether functionality supports the complexation. A reasonable explanation may be a steric hindrance of the complexation due to the two oxygen atoms of the UO_2^{2+} entity. Also, the log β'_n value for the U(VI)-thioacetate complex is by about 2 orders of magnitude lower than the respective value for the oxydiacetate complex. This is expected, since sulfur shows weaker complexation properties towards actinides.

8.5 Summary

The present work gives a short overview of the complexation of actinides in different oxidation states with small organic ligands. Due to the availability of numerous studies and a broad set of data, only chosen ligand systems with systematic variations of their molecular structure are discussed to give a basic insight into the complexation mechanism. The comparison of the given stability constants showed, that the complex formation is influenced by a number of factors, like the alkalinity of the ligand and its molecular structure. In the case of aliphatic carboxylic acid ligands, functional groups in α-,β- or γ-position to the coordinating COOH group increase the stability constants of the complexes distinctively. This effect is attributed to an additional contribution of the additional functional group, resulting in a partial chelating effect.

However, the available thermodynamic data is determined by various methods. The present overview shows a distinct discrepancy between literature data from indirect methods (e.g. potentiometry and solvent extraction) and spectroscopic techniques, which is far beyond experimental uncertainties of these two different types of methods. The difference is rather attributed to the general problem, that indirect methods disturb the chemical equilibrium during the measurement, which might provide biased results. Furthermore, indirect methods are unable to distinguish between inner- and outer-sphere complexes and thus changes in activity coefficients may be misinterpreted for changes in log β values.

Hence, application of spectroscopic methods (e.g. TRLFS and UV/Vis) for the precise determination of thermodynamic data is of major importance to validate the available literature data and to establish a reliable thermodynamic database for actinides under natural conditions.

9 Measurement of pH values at elevated temperatures

Many chemical reactions in aqueous solutions (e.g. complexation, dissolution/precipitation or adsorption) are a function of the proton activity. Thus, the pH can be considered as a master variable in an aquatic system, and its precise measurement is one of the key issues in a detailed understanding and description of an aqueous system [Pankow,1991] At ambient temperatures, the pH is usually monitored with good accuracy by potentiometric measurement, using a hydrogen ion sensitive glass electrode. However, this approach is accompanied by various experimental difficulties, such as electrode drift, susceptibility to electromagnetic interferences and problems with reference electrodes. Also, glass electrodes are limited mainly to solutions with low salt concentrations, since the liquid junction potential is depending on the ionic strength (Dickson, 1993). Furthermore, due to uncertainties in the liquid junction potential and lack of reference electrode stability at high temperatures and pressures, the IUPAC has recommended to use potentiometric methods only in a temperature range of 5 to 50°C [Buck et al., 2002]. An alternative to potentiometric methods is the spectroscopic measurement of the pH. This approach is a well established experimental technique at ambient temperatures. Also, it can be applied for pH measurements of solutions at high temperatures and pressures [Raghuraman et al., 2006; Millero et al., 2009; Vogel, 1961; Bates, 1964; Seok et al., 1995].

9.1 Theory

Spectroscopic pH measurement techniques use UV/Vis absorption spectroscopy of pH sensitive dyes. These dyes are weak acids, with their dissociation equilibrium defined as follows (the charge of the dye depends on the respective molecule and is omitted here).

$$HDye \rightleftharpoons Dye + H^+ \qquad \text{Equation 9-1}$$

The acid (HDye) and base form (Dye) of the dye show different absorption bands. The absorption spectrum of a dye in a solution with the pH in the range of the pK'_a(dye) is a linear combination of these single component spectra with respect to the molar fractions of the acid and base form of the dye. By fitting the measured spectrum with the individual absorption spectra of the respective species, the speciation of the dye can be obtained directly from the integral of the respective absorption bands (peak deconvolution). The pH is then calculated by using the Henderson-Hasselbalch equation $pH = pK_a^0(T) + \log\left(\frac{\chi(Dye)}{\chi(HDye)}\right) + \log\left(\frac{\gamma_{Dye}}{\gamma_{HDye}}\right)$,

$$pH = pK_a^0(T) + \log\left(\frac{\chi(Dye)}{\chi(HDye)}\right) + \log\left(\frac{\gamma_{Dye}}{\gamma_{HDye}}\right) \qquad \text{Equation 9-2,}$$

where K^0_a is the temperature dependent thermodynamic equilibrium constant of Equation 9-1. χ(Dye) and χ(HDye) are the molar fractions of the acid and base form of the dye and γ_{Dye} and γ_{HDye} are the respective activity coefficients. For solutions with an ionic strength of $I_m \leq 0.2$ mol/kg H_2O, the activity coefficients are calculated with the Davies-equation Equation 9-3 [Pankow, 1991]:

$$\log\gamma_i = -A \cdot z_i^2 \cdot \left(\frac{\sqrt{I_m}}{1 + Ba_j \cdot \sqrt{I_m}}\right) - 0.2 \cdot I_m$$

Equation 9-3

The individual absorption spectra of the acid and base form are obtained from reference solutions at a pH value which is at least one order of magnitude higher or lower than the pK'_a of the dye. Under such conditions complete protonation or deprotonation of the dye can be assumed. Also, in order to determine the pH of a unknown solution, the dissociation constant of the respective dye must be known. The pK^0_a of an indicator dye can be determined at room- as well as at increased temperatures by calibration versus reference solutions with known pH(T). Such reference solutions are for example commercially available buffer solutions. An overview of the reference solutions used within the present work is given in Table 9-1.

Table 9-1 Composition of the used reference solutions and their pH(T) from 25 to 90°C

	Buffer pH 2	Buffer pH 4	Buffer pH 11
	c($C_6H_8O_7$) = 0.030 m c(HCl) = 0.069 m c(NaOH) = 0.061 m	c($C_6H_8O_7$) = 0.056 m c(HCl) = 0.044 m c(NaOH) = 0.11 m	c(H_3BO_4) = 0.094 m c(KCl) = 0.048 m c(NaOH) = 0.091 m
T [°C]	pH	pH	pH
25	2.00	4.00	11.00
30	2.00	4.01	10.81
40	2.00	4.01	10.64
50	2.00	4.01	10.48
60	2.00	4.00	10.45
70	2.01	4.00	10.19
80	2.01	4.00	10.06
90	2.01	4.00	9.93

The major drawback of the spectroscopic pH measurement the limited available pH window of pK'_a(Dye) ± 1, since at higher or lower pH the dye is completely protonated or deprotonated and no information can be derived from peak deconvolution.

9.2 Technical equipment

The experiments were performed in a custom build high temperature cell for spectroscopic measurements [Skerencak et al., 2009] The region which is exposed to high temperatures (hot region) is made of Ti with 0.2 wt% Pd, which has a very high resistance towards corrosion. The cold region of the cell consists of PEEK (polyetheretherketone). The overall sample volume is about 2 ml. The temperature range for spectroscopic studies is 25 to 200°C. The pressure of the cell can be increased with an external pressure pump up to 13 - 15 bar (p_{max} = 30 bar). Four optical quartz windows are embedded into the central body (diameter = 8 mm, thickness = 2 mm). The cell is coupled with optical waveguides (quartz) to a UV/Vis spectrometer (Cary 50, Varian Inc.). A first test with the optical indicator dye acridin showed a very good agreement of the measured absorption spectra with literature data in the temperature range from 20 to 150°C. Also, the change of the spectra was fully reversible with decreasing temperature. Above 150°C an irreversible decrease of the absorption intensity was observed leading to a complete bleaching of the solution. A possible explanation for this is a catalytic decomposition of the dye molecule of the titanium cell walls.

9.3 Measurement of the pH

In the following, the results on the application of two different indicator dyes are described.

Indicator dye bromocresol green

Bromocresol green is an optical indicator dye of the triphenylmethane family, with a pK'$_a$,25°C value of about 4.90 (I_m = 0.05 m). Thus it can be applied to monitor the pH in the region of 4 to 6. The dye molecule in its acid and base form is displayed in Figure 9-1.

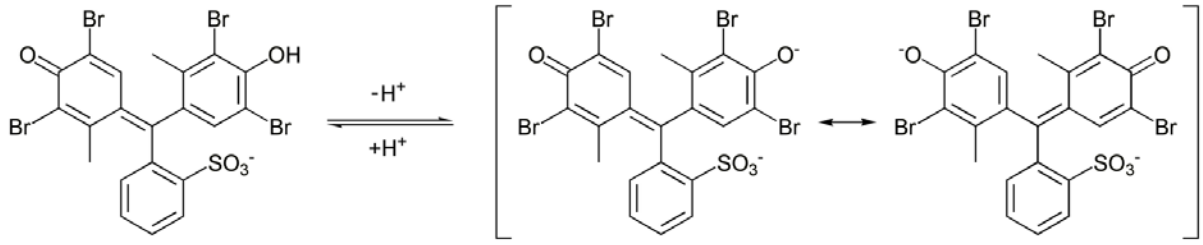

Figure 9-1: Bromocresol green in its acid (left) and base (right) form

To determine the temperature dependency of the pK^0_a of bromocresol green, the dye is calibrated against the reference solutions given in Table 9-1 Composition of the used reference solutions and their pH(T) from 25 to 90°C. The absorption spectra of bromocresol green in the buffer solutions at T = 25 °C are displayed in Figure 9-2a. At pH = 2 the dye exist in its acid form, showing an absorption band at 440 nm. At pH = 11 an absorption band at 620 nm is observed, which is attributed to the base form of the dye molecule. These assignments are in excellent agreement with the literature [Lee et al., 2001]. At pH = 4 the proton activity is in

a region corresponding to $pK^0_{a,25°C} \pm 1$ of bromocresol green. Hence, the acid and the base form of the dye coexist in solution and both bands are observed in the absorption spectrum.

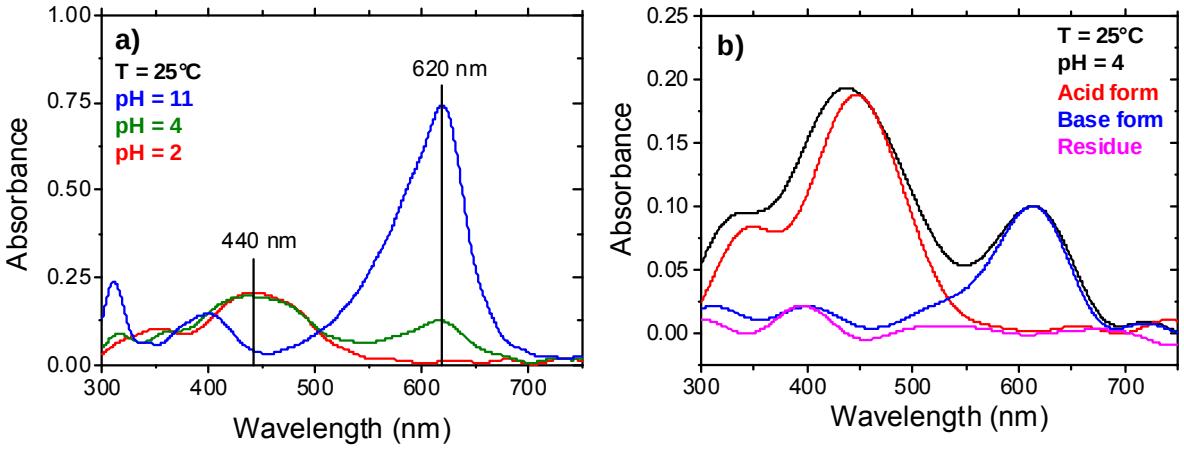

Figure 9-2: Absorption Spectra of bromocresol green at pH = 2, 4 and 11 (T = 25°C) b) exemplary peak deconvolution at T = 25°C

The measured spectrum is fitted with the previously determined absorption bands of the individual species. An exemplary peak deconvolution of an absorption spectrum of bromocresol green at pH = 4 (T = 25°C) is displayed in Figure 9-2b. Thus, the respective molar fractions are determined as function of the temperature and the $pK'_a(T)$ is calculated according to Equation 9-2. The so determined $pK'_a(T)$ values are displayed in Figure 9-3a.

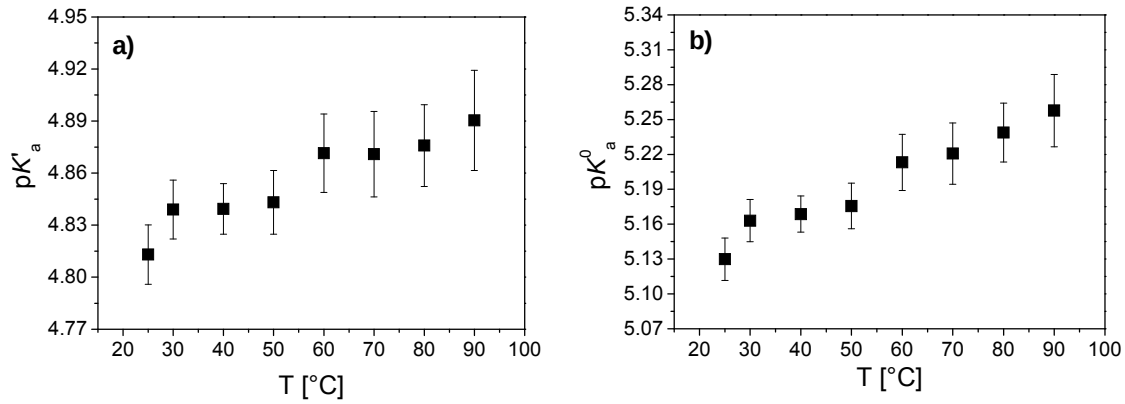

Figure 9-3: a) conditional pK'a(T) values of bromocresol green (valid for Im = 0.2 m) b) respective thermodynamic pK0a(T) values (valid for Im = 0 m)

The thermodynamic $pK^0_a(T)$ values (valid for $I_m = 0$) are related to the conditional $pK'_a(T)$ by the following equation

$$pK^0_a = pK'_a - \log\left(\frac{\gamma_{H^+} \cdot \gamma_{Dye^-}}{\gamma_{HDye}}\right)$$

Equation 9-4

The so calculated temperature dependent thermodynamic stability constants of bromocresol green are shown in Figure 9-3b.

At T = 25°C, the pK^0_a value determined in this work is in good agreement with literature data ($pK^0_{a,25°C,Lit}$ = 4.98) [Meloun et al., 1977]. With increasing temperature the pK^0_a increases by about 0.15 orders of magnitude, yielding a pK^0_a of 5.26 ± 0.04 at 90°C. A comparison of the temperature effect with literature data is not possible, since no data are available on the temperature dependency of the pK^0_a of bromocresol green.
Bromocresol green is applied to measure the pH(T) of solutions containing propionate ions. The results are used to calculate the temperature dependency of the pK^0_a of propionic acid. Since the pK^0_a(T) of propionic acid is known from the literature, this system can be used for validating the here applied experimental setup. Four sample solutions are prepared with a $pH_{25°C}$ of about 4.8, corresponding to the pK^0_a propionate (see Table 9-2).

Table 9-2: Samples for the spectroscopic pH measurement with bromocresol green

No.	$[NaProp]_{total}$	$[HClO_4]_{total}$	$[NaClO_4]_{total}$	I_m
P1	0.005	0.0025	0.193	0.2
P2	0.01	0.005	0.185	0.2
P3	0.025	0.012	0.163	0.2
P4	0.05	0.025	0.125	0.2

Using the previously determined single component spectra, the dye speciation of the four samples is determined by peak deconvolution. The pH of the four samples is then calculated as function of the temperature with the pK'_a(T) values of bromocresol green using Equation 9-3. The so determined pH(T) values are displayed in Figure 9-4a. The results are consistent for all four samples, yielding an average value of $pH_{25°C}$ = 4.73 ± 0.05 which increases by about 0.25 orders of magnitude in the studied temperature range. The temperature dependent pK^0_a of propionic acid is calculated according to Equation 9-5,

$$pK_c^{\theta} = -\log\left(\frac{([H^+]_{eq})^2 - [H^+]_{eq}\cdot[H^+]_{total} + [H^+]_{eq}\cdot[Prop^-]_{total}}{[H^+]_{total} - [H^+]_{eq}}\cdot\gamma_{H^+}\cdot\gamma_{Prop^-}\right)$$

Equation 9-5

where $[H^+]_{eq}$ is the proton concentration in solution, $[H^+]_{total}$ is the total proton concentration, $[Prop^-]_{total}$ is the total sodium propionate concentration and γ_{H^+} and γ_{Prop^-} are the respective activity coefficients. Hereby, the protons originating from the dissociation of water are neglected, since their concentration is by two orders of magnitude lower than the concentration of the protons in solution. The $[H^+]$ concentration at equilibrium is related to the pH by the following equation.

$$[H^+]_{sc} = 10^{-pH} \cdot (\gamma_{H^+})^{-1}$$ Equation 9-6

The $pK^0_a(T)$ values of propionate are shown in Figure 9-4b.

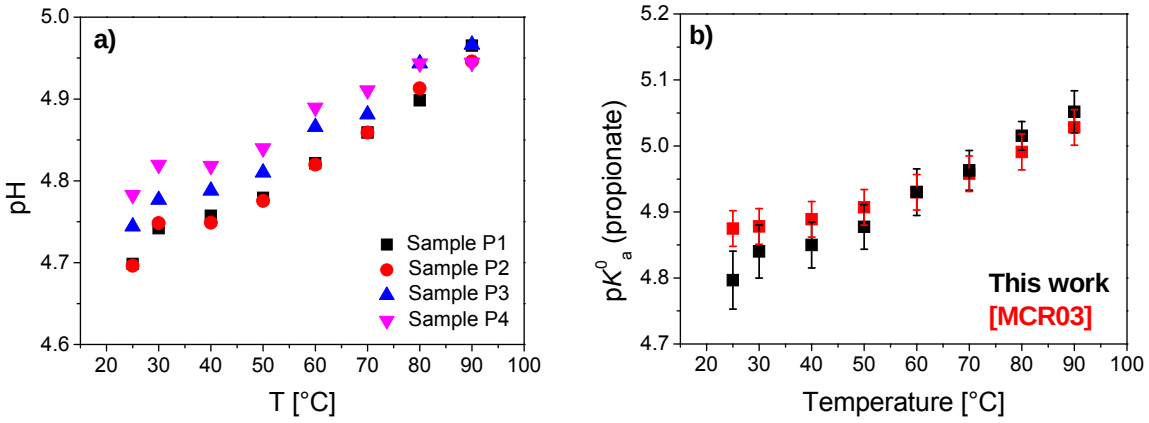

Figure 9-4: a) pH(T) values of four sample solutions (see **Table 9-2**), b) pK0a(T) values of propionate

The $pK^0_a(T)$ values of propionic acid determined in the present work are in good agreement with literature data [McRae et al., 2003]. This shows that our newly designed experimental setup is very well suitable for pH measurements at increased temperature.

X.3.1 Indicator dye bromophenol blue

Similar to bromocresol green, bromophenol blue is an indicator dye of the triphenylmethane family. The dye has a $pK^0_{a,25°C}$ of 4.171, making it suitable for pH-measurements in a region of 3 to 5 [Manohar & Atkinson, 1993] The acid and base form of bromophenol blue is displayed in Figure 9-5.

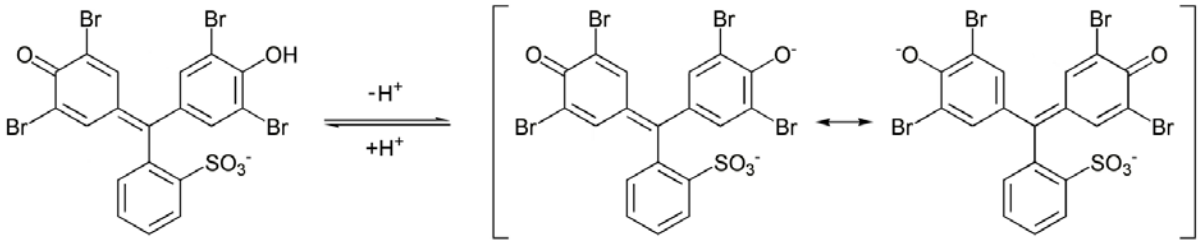

Figure 9-5: Bromophenol blue in its acid (left) and base (right) form

The temperature dependency of the pK^0_a of bromophenol blue is determined by calibration versus the reference solutions given in Table 9-1. The respective absorption spectra at $pH_{25°C}$ = 2, 4 and 11 and T = 25°C are shown in Figure 9-6a. The absorption spectra at $pH_{25°C}$ = 2 and 11 display maxima at 440 nm and 591 nm, attributed to the acid and base form of the dye, respectively. The assignment of the absorption bands is confirmed by comparison with literature data [Abdel-Fattah, 1997]. At $pH_{25°C}$ = 4 both species are present in solution, and the

measured absorption spectrum is a linear combination of the respective absorption bands. The molar fractions of the acid and base form of the dye in the buffer solution at $pH_{25°C}$ = 4 are determined as function of the temperature by peak deconvolution. An exemplary fit of the spectrum at $pH_{25°C}$ = 4 and T = 25°C is shown in Figure 9-6b.

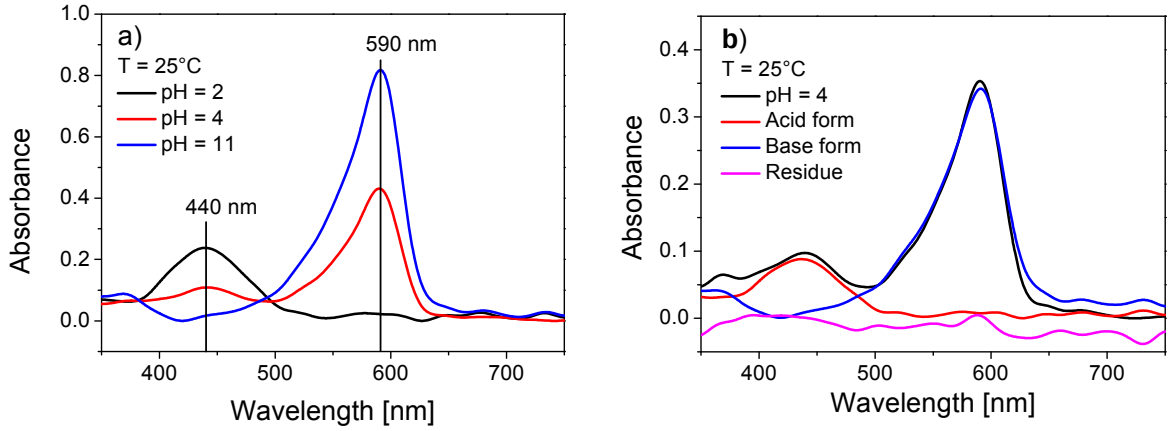

Figure 9-6: a) Absorption Spectra of bromophenol blue at pH25°C = 2, 4 and 11 (T = 25°C) b) peak deconvolution of the spectrum at pH25°C = 4 and T = 25°C

The conditional $pK'_a(T)$ values are determined using the dye speciation and Equation 9-2 (Figure 9-7a). By calculating the respective activity coefficients with the Davies equation (Equation 9-3) the thermodynamic $pK^0_a(T)$ values of bromophenol blue are obtained (Figure 9-7b).

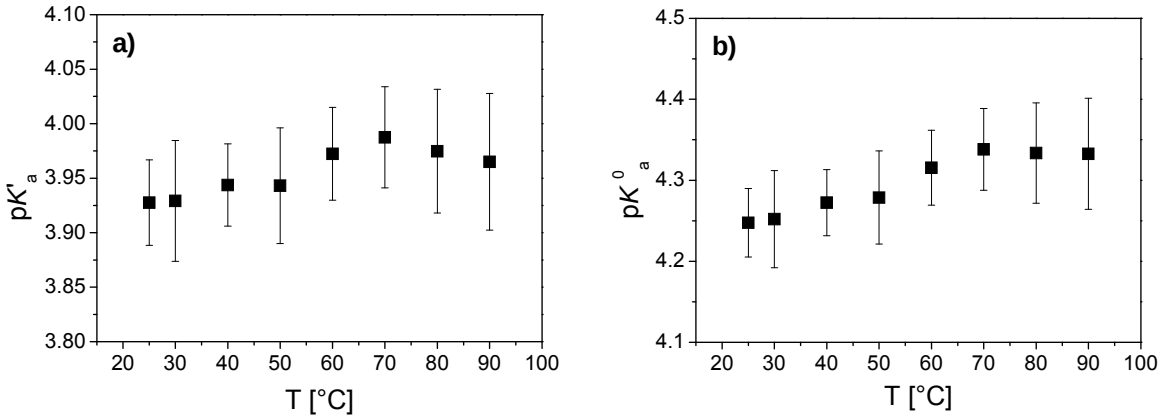

Figure 9-7: a) conditional pK'a(T) of bromophenol blue (valid for Im = 0.2 m) b) thermodynamic pK0a(T) of bromophenol blue (valid for Im = 0 m)

The pK^0_a of bromophenol blue determined in this work is in good agreement with literature data at T = 25°C [Manohar et al., 1993] No literature data is available on the temperature dependence of pK^0_a.

Due to its pK_a value, Bromophenol blue can be used to measure the pH of solutions in the range from 3 to 5. Thus, the pH(T) of three samples is measured containing defined concentrations of lactate (see Table 9-3). The $pH_{25°C}$ of these samples is adjusted to approximately 3.7, corresponding to the pK^0_a of lactic acid [Larsson & Adell, 1931].

Table 9-3: Samples for the spectroscopic pH measurement using bromophenol blue

Sample	$[NaLac]_{total}$	$[HClO_4]_{total}$	$[NaClO_4]_{total}$	I_m
L1	$1.0x10^{-3}$ m	$7.5x10^{-4}$ m	$1.98x10^{-1}$ m	0.2
L2	$1.0x10^{-2}$ m	$5.0x10^{-3}$ m	$1.85x10^{-1}$ m	0.2
L3	$2.5x10^{-2}$ m	$1.2x10^{-2}$ m	$1.63x10^{-1}$ m	0.2

The molar fractions of the acid and base form of bromophenol blue in the respective samples are determined by peak deconvolution using the previously recorded single component absorption spectra. The pH is then calculated according to Equation 9-2 (Figure 9-8a). The pH(T) values of the three samples are consistent, yielding an averaged $pH_{25°C}$ of 3.71, which increases by about 0.1 orders of magnitude in the temperature range from 25 to 90°C.

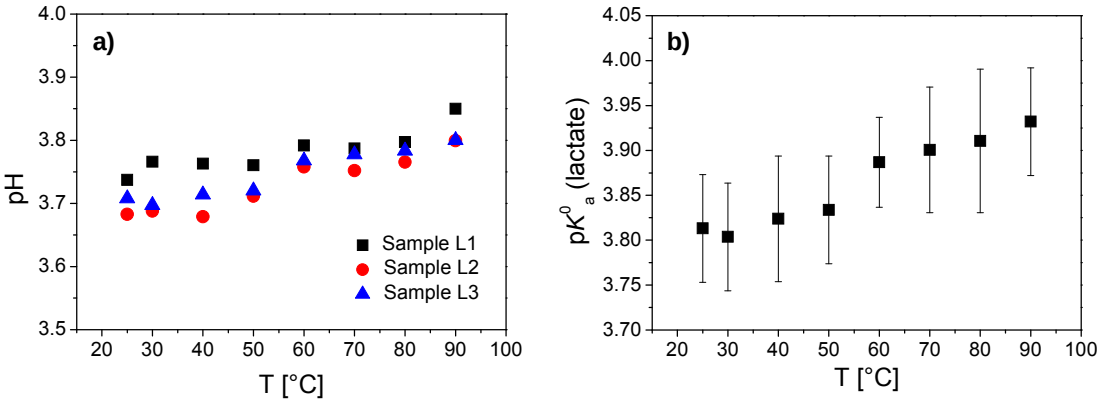

Figure 9-8: a) pH(T) values of three sample solutions (see **Table 9-3**) b) pK0a(T) values of lactate

The resulting pK^0_a(T) values of lactic acid are shown in Figure 9-8b. At T = 25°C, the results are in good agreement with literature data [Larsson & Adell, 1931]. With increasing temperature, the pK^0_a increases by about 0.15 orders of magnitude. No literature data on the temperature dependency of the pK^0_a of lactic acid is available.

The results show a very good applicability of the developed high temperature cell for spectroscopic pH measurements at increased temperatures and pressure. The experimental setup was tested by applying the optical indicator dyes bromocresol green and bromophenol blue to measure the pH of solutions containing propionate and lactate ions in the temperature range from 25 to 90°C. Thus, the temperature dependency of propionic and lactic acid was deter-

mined. These results are of major importance for the thermodynamic description of the complexation of actinide ions with small organic ligands at room as well as at increased temperatures.

10 References published from project results with INE contribution

Peer reviewed:

Grangeon, S. et al., (2011). in review. On nickel occurrence and distribution in a clay-rich formation: Implications for trace elements solubility control. Geochimica Et Cosmochimica Acta.

Grasset, L. et al., (2010). Sequential extraction and spectroscopic characterisation of organic matter from the Callovo-Oxfordian formation. Organic Geochemistry, 41(3): 221-233.

Hartmann, E., Geckeis, H., Rabung, T., Lutzenkirchen, J., and Fanghanel, T., (2008). Sorption of radionuclides onto natural clay rocks. Radiochimica Acta 96, 699-707.

Hartmann, E., Baeyens, B., Bradbury, M. H., Geckeis, H., and Stumpf, T., (2008). A Spectroscopic Characterization and Quantification of M(III)/Clay Mineral Outer-Sphere Complexes. Environmental Science & Technology 42, 7601-7606.

Hartmann, E., Brendebach, B., Polly, R., Geckeis, H., and Stumpf, T., (2010). Characterization and quantification of Sm(III)/and Cm(III)/clay mineral outer-sphere species by TRLFS in D2O and EXAFS studies. Journal of Colloid and Interface Science 353, 562-568.

Lerouge, C. et al., (2010). Comparative EPMA and µ-XRF methods for mapping micro-scale distribution of iodine in biocarbonates of the Callovian- Oxfordian clayey formation at Bure, Eastern part of the Paris Basin. Physics and Chemistry of the Earth, Parts A/B/C, 35(6-8): 271-277.

Schäfer, T. and Denecke, M.A., (2010). Nuclear waste repository research at the micro- to nanoscale. In: M.A. Denecke and C.T. Walker (Editors), X-Ray Optics and Microanalysis, Proceedings. AIP Conference Proceedings. Amer. Inst. Physics, Melville, pp. 181-187.

Schäfer, T., Michel, P. and Claret, F., (2009a). The application of STXM and µFT-IR to characterize sedimentary organic matter in the Opalinus clay. Journal of Physics: Conference Series, 186: 012095.

Schäfer, T. et al., (2009b). Radiation sensitivity of natural organic matter: Clay mineral association effects in the Callovo-Oxfordian argillite. Journal of Electron Spectroscopy and Related Phenomena 170: 49-56.

Vilas, V.V. et al., (2010). Synthesis and Characterization of the Hybrid Clay-Based Material Montmorillonite–Melanoidin: A Potential Soil Model. Soil Sci. Soc. Am. J., 74(6): 2239-2245.

11 References

Abdel-Fattah, A.A., El-Kelany, M., Abdel-Rehim, F., El Miligy, A.A., (1997). *UV-sensitive indicators based on bromophenol blue and chloral hydratedyed poly (vinyl butyral)*, Journal of Photochemistry and Photobiology A: Chemistry, **110**, 291-297,.

Acholla, F.V. and Orr, W.L., (1993). Pyrite Removal from Kerogen without Altering Organic-Matter - the Chromous Chloride Method. Energy & Fuels, 7(3), 406-410.

Allen, P. G., Bucher, J. J., Shuh, D. K., Edelstein, N.M., Reich, T., (1997). Investigation of aquo and chloro complexes of UO_2^{2+}, NpO_2^{+}, Np^{4+}, and Pu^{3+} by X-ray absorption fine structure spectroscopy. Inorg. Chem. **36**, 4676.

Altmann, R. S., Buffle, J., (1988). Geochim. Cosmochim. Acta 52, 1505.

Amayri, S., Jermolajev, A., Reich, T., (2011). Radiochim. Acta **99**, 349–357.

Andra Dossier 2005 – Référentiel du site de Meus/Haute Marne, (2005). C.R.P.ADS.04.0022; Andra: Paris, France.

Ankudinov, A.L., Ravel, B., Rehr, J.J., Conradson, S.D., (1998). Real-space multiple-scattering calculation and interpretation of x-ray-absorption near-edge structure. Physical Review B 58(12), 7565-7576.

Antonio, M. R., Soderholm, L., Williams, C. W., Blaudeau, J.-P., Bursten, B. E., (2001). Neptunium redox speciation. Radiochim. Acta 89, 17.

Arfaioli, P., Ristori, G.G., Bosetto, M. and Fusi, P., (1997). Humic-like compounds formed from L-tryptophan and D-glucose in the presence of Cu(II). Chemosphere, 35(3), 575-584.

Artinger, R., Marquardt, C. M., Kim, J. I., Seibert, A., Trautmann, N., Kratz, J. V., (2000). Radiochim. Acta 88, 609.

Banik, N. L., Buda, R. A., Bürger, S., Kratz, J. V., Trautmann, N., (2007). Journal of Alloys and Compounds, 444, 522-525.

Bates, R., (1964). *Determination of pH: Theory and Practice.* John Wiley & Sons, New York,.

Beitz, J.V., Hessler, J.P., (1981). Oxidation state specific detection of transuranic ions in solution. Nuclear Technology 51, 169-177.

Beitz, J.V., Bowers, D.L., Doxtader, M.M., Maroni, V.A., Reed, D.T., (1988). Detection and speciation of trans-uranium elements in synthetic groundwater via pulsed-laser excitation. Radiochimica Acta 1988, 44-45, 87-93.

Benzing-Purdie, L.M., Ripmeester, J.A. and Ratcliffe, C.I., (1985). Effects of temperature on Maillard Reaction Products. J. Agric. Food Chem., 33, 31-33.

Bolt, G.H., Bruggenwert, M.G., Kamphorst, A., (1976). Adsorption of cations by soils. In: Soil chemistry A. Basic element. Hrsg. G.H. Bolt, M.G. Bruggenwert, Elsevier, Amsterdam, p. 54-90.

Bonin, L., Guillaumont, D., Jeanson, A., Auwer, C. D., Grigoriev, M., Berthet, J. C., Hennig, C., Scheinost, C., Moisy, P., (2009). Thermodynamics and Structure of Actinide(IV) Complexes with Nitrilotriacetic Acid, Inorg. Chem. 48, 3943-3953.

Borkowski, M., Lis, S., Choppin, G.R., (1996). Complexation study of NpO_2^{+} and UO_2^{2+} Ions with several organic ligands an aqueous solutions of high ionic strength,Radiochim. Acta, 74, 117-121.

Bosetto, M., Arfaioli, P. and Pantani, O.L., (2002). Study of the Maillard reaction products formed by glycine and D-glucose on different mineral substrates. Clay Minerals, 37, 195-204.

Bosetto, M., Arfaioli, P., Pantani, O.L. and Ristori, G.G., (1997). Study of the humic-like compounds formed from L-tyrosine on homoionic clays. Clay Minerals, 32(3), 341-349.

Bouchet, A., Rassineux, F., (1997). Echantillons d'argiles du forage EST104: Etude mineralogique approfondie. Rapport final DR-P- 0ERM-98-007A, ANDRA Agence nationale pour la gestion des d´echets radioactifs, Chatenay-Malabry, p. 107.

Bradbury, M.H. and Baeyens, B., (2009). Sorption modelling on illite. Part II: Actinide sorption and linear free energy relationships, Geochim. Cosmochim. Acta 73, 1004–1013

Bradbury, M.H., Baeyens, B., (2005a). Modelling the sorption of Mn(II), Co(II), Ni(II), Zn(II), Cd(II), Eu(III), Am(III), Sn(IV), Th(IV), Np(V) and U(VI) on montmorillonite: Linear free energy relationships and es-timates of surface binding constants for some selected heavy metals and actinides. Geochim. Cosmochim. Acta 69(4), 875-892.

Bradbury, M.H., Baeyens, B., (2005b). Experimental and modelling investigations on Na-illite: Acid-base behaviour and the sorption of strontium, nickel, europium and uranyl. Paul Scherrer Institut, PSI-Bericht 05-02, Villigen.

Bradbury, M.H., Baeyens, B.A. (2003). Comparison of Apparent Diffusion Coefficients Measured in Compacted Kunigel V1 Bentonite with Those Calculated from Batch Sorption Measurements and De (HTO) Data: A Case Study for Cs(I), Ni(II), Sm(III), Am(III), Zr(IV) and Np(V). PSI Bericht Nr. 03-02, Villigen, Switzerland.

Bradbury, M.H., Baeyens, B., (2003a). Far field sorption data bases for performance assessment of a high-level radioactive waste repository in an undisturbed Opalinus Clay host rock. Paul Scherrer Institut, PSI-Bericht 03-08, Villigen, 128 p.

Bradbury, M.H., Baeyens, B., (2002). Sorption of Eu on Na- and Ca-montmorillonites: Experimental investigations and modelling with cation exchange and surface complexation, Geochim. Cosmochim. Acta, 66(13), 2325-2334.

Bradbury, M.H., Baeyens, B., (1999). Modelling the sorption of Zn and Ni on Ca-montmorillonite. Geochim. Cosmochim. Acta 63(3-4), 325-336.

Bradbury, M.H., Baeyens, B., (1997). A mechanistic description of Ni and Zn sorption on Na-montmorillonite. Part 2, Modelling. Journal of Contaminant Hydrology 27(3-4), 223-248.

Bradbury,M. H., Baeyens, B., (1995). A Quantitative Mechanistic Description of Ni, Zn and Ca Sorption on Na-Montmorillonite. Part III, Modelling. Technical Report NTB 95-06, NAGRA Nationale Genossenschaft für die Lagerung radioaktiver Abfälle, Wettingen/Schweiz, p. 75.

Bradbury, M.H., Baeyens, B., Geckeis, H., Rabung, T., (2005). Sorption of Eu(III)/Cm(III) on Ca-montmorillonite and Na-illite. Part 2: Surface complexation modelling. Geochim. Cosmochim. Acta 69(23), 5403-5412.

Brendebach, B., Banik, N. L., Marquardt, Christian M., Rothe, J., Denecke, M., Geckeis, H., (2009). Radiochimica Acta 97,12, 701-708.

Buck, R.P., Rondini, S., Covington, A.K., Baucke, F.G.K., Brett, C.M.A., Camoes, M.F., Milton, M.J.T., Mussini, T., Naumann, R., Pratt, K.W., Spitzer, P., Wilson, G.S., (2002). *Measurement of pH, Definition, Standards and Procedures,* Pure & Appl. Chem., **74(11)**, 2169-2200,

Bulemela, E., Trevani, L., Tremaine, P.R., (2005). *Ionization Constants of Aqueous Glycolic Acid at Temperatures up to 250°C Using Hydrothermal pH Indicators and UV-Visible Spectroscopy*, Journal of Solution Chemistry, **34**, 769-788,.

Choppin, G.R., (2003). Actinide speciation in the environment, Radiochim. Acta 91, 645-649.

Choppin, G.R., Chen, J.F., (1996). Complexation of Am(III) by oxalate in NaClO4 media, Radiochim Acta, 74, 105-110.

Choppin, G.R., Rizkalla, E.N., (1994). Solution chemistry of actinides and Lanthanides, in Handbook on the physics and chemistry of rare earths, K.A.a.E. Gschneider, L., Editor, Elsevier Science B. V. p. 559-590.

Claret, F., Sakharov, B. A., Drits, V. A., Velde, B., Meunier, A., Griffault, L., Lanson, B., (2004). Clay minerals in the Meuse-Haute marne underground laboratory (France): Possible influence of organic matter on clay mineral evolution. Clays Clay Minerals **52**(5), 515.

Claret, F., Schäfer, T., Bauer, A., Buckau, G., (2003). Generation of humic and fulvic acid from Callovo-Oxfordian clay under high alkaline conditions, Science of the Total Environment 317(1-3), 189-200.

Claret, F., Bauer, A., Schäfer, T., Griffault, L., Lanson, B., (2002). Experimental investigation of the interaction of clays with high-pH solutions: A case study from the Callovo-Oxfordian formation, Meuse-HauteMarne underground laboratory (France). Clays Clay Mineral 50(5), 633

Cohen, D. (1961). Electrochemical studies of plutonium ions in perchloric acid solutions, Journal of Inorganic Nuclear Chemistry, 18, 207.

Conradson, S.D., et al., (2003). Higher order speciation effects on plutonium L-3 X-ray absorption near edge spectraInorganic Chemistry, Vol. 43, No. 1, 116-131.

Courdouan, A., Christl, I., Rabung, Th., Wersin, P., Kretzschmar, R., (2008). Proton and Trivalent Metal Cation Binding by Dissolved Organic Matter in the Opalinus Clay and the Callovo-Oxfordian Formation. Environ. Sci. Technol. 42, 5985-5991.

Courdouan, A., Christl, I., Meylan, S., Wersin, P., Kretzschmar, R., (2007). Characterization of dissolved organic matter in anoxic rock extracts and in situ pore water of the opalinus clay, Appl. Geochem., 22, 2926-2939.

Davies, C.W., (1962). Ion association., London, Butterworths, 190 p.

Deniau, I., Devol-Brown, I., Derenne, S., Behar, F. and Largeau, C., (2008), Comparison of the bulk geochemical features and thermal reactivity of kerogens from Mol (Boom Clay), Bure (Callovo-Oxfordian argillite) and Tournemire (Toarcian shales) underground research laboratories. Science of The Total Environment, 389(2-3), 475-485.

Denecke, M.A., (2006). Actinide speciation using X-ray absorption fine structure spectroscopy. Coordination Chemistry Reviews, 250(7-8), 730-754.

Denecke, M. A., Dardenne. K., Marquardt, C.M. (2005). Np(IV)/Np(V) valence determinations from Np L3 edge XANES/EXAFS, Talanta 65,1008-1014.

Denecke, M.A., Janssens, K., Proost, K., Rothe, J. and Noseck, U., (2005a). Confocal micrometer-scale X-ray fluorescence and X-ray absorption fine structure studies of uranium speciation in a tertiary sediment from a waste disposal natural analogue site. Environmental Science & Technology, 39(7), 2049-2058.

Denecke, M.A., Rothe, J., Dardenne, K., Blank, H. and Hormes, J., (2005b). The INE-Beamline for Actinide Research at ANKA. Physica Scripta T115, 1001-1003.

Denecke,M. A., Marquardt, C. M., Rothe, J., Dardenne, K., Jensen, M. P., (2002). XAFS study of actinide coordination structure in Np(IV)-fulvates. J. Nucl. Sci. Technol., Suppl. 3, 410.

Deniau, I., Devol-Brown, I., Derenne, S., Behar, F. and Largeau, C., (2008). Comparison of the bulk geochemical features and thermal reactivity of kerogens from Mol (Boom Clay), Bure (Callovo-Oxfordian argillite) and Tournemire (Toarcian shales) underground research laboratories. Science of The Total Environment, 389(2-3), 475-485.

DiBernardo, P., Zanonato, P., Tian, G., Tolazzi, M., Rao. L., (2009). Thermodynamics of the complexation of uranium(VI) with oxalate in aqueous solution at 10-70°C, Dalton Trans., 4450-4457.

DiBernardo, P., Zanonatp, P., Bismondo, A., Jiang, H., Garnov, A.Yu., Jiang, J., Rao, L., (2006). Complexation of Uranium(VI) with Thiodiacetic Acid in Solution at 10–85 °C, Eur. J. Inorg. Chem., 4533.

DiBernardo, P., Cassol, A., Tomat, G., Bismondo, A., Magon, L., (1983). Thermodynamics of the complex formation between Thorium(IV) and some Polydentate Ligands in aqueous Solution, J. Chem Soc. Dalton Trans., 733-735.

DiBernardo, P., DiNapoli, V., Cassol, A., Magon, L., (1977). J. Inorg. Nucl. Chem., 39, 1659.

Dickson, A.G., (1993). The *measurements of sea water pH*, Marine Chemistry, 44, 131-142.

Edelstein, N.M., Klenze, R., Fanghänel, T., Hubert, S., (2006). Optical properties of Cm(III) in crystals and solutions and their application to Cm(III) speciation. Coordination Chemistry Reviews 2006, 250(7-8), 948-973.

Eglizaud, N., Miserque, F., Simoni, E., Schlegel, M., Descostes, M., (2006). Uranium(VI) interaction with pyrite (FeS_2): chemical and spectroscopic studies, Radiochim. Acta 94, 651-656.

Elie, M. and Landais, P., (1997). Identification et comportement thermique des matières organiques du Callovo-Oxfordien. Journées Scientifiques ANDRA-CNRS, 27 et 28 Octobre 1997, Bar-le-Duc, 35-58.

Fairhurst, A.J., Warwick, P., (1998). The influence of humic acid on europium-mineral interactions. Colloids and Surfaces a-Physicochemical and Engineering Aspects, 145(1-3), 229-234.

Fanghänel, T., Kim, J.I., Klenze, R., Kato, Y., (1995). Formation of Cm(III) chloride complexes in $CaCl_2$ solutions. Journal of Alloys and Compounds 225(1-2), 308-311.

Fox, P.M., Davis, J.A., Zachara, J.M., (2006). The effect of calcium on aqueous uranium(VI) speciation and adsorption to ferrihydrite and quartz. Geochimica Et Cosmochimica Acta 70(6), 1379-1387.

Freyer, M., Walther, C., Stumpf, T., Buckau, G., Fanghänel, T., (2209). Formation of Cm humate complexes in aqueous solution at pHc 3 to 5.5: The role of fast interchange. Radiochimica Acta 97, 547-558.

Fröhlich, D.R., Amayri, S., Drebert, J., Reich, J., (2011). Radiochimica Acta Vol. 99, No. 2, pp. 71-77.

Gadel, F. and Bruchet, A., (1987). Application of pyrolysis-gas chromatography-mass spectrometry to the characterization of humic substances resulting from decay of aquatic plants in sediments and water. Water Research, 21, 1195-1206.

Gaines, G.L.J., Thomas, H.C., (1953). Adsorption studies on clay minerals. II. A formulation of the thermody-namics of exchange adsorption. The Journal of Chemical Physics 21(4), 714-718.

Gaucher, E., Robelin, C., Matray, J. M., Negral, G., Gros, Y., Heitz, J. F., Vinsot, A., Rebours, H., Cassagnabere, A., Bouchet, A., (2004). ANDRA underground research laboratory: interpretation of the mineralogical and geochemical data acquired in the Callovian-Oxfordian formation by investigative drilling. Phys. Chem. Earth **29**(1), 55-77.

Geckeis, H., (2010). Modellrechnungen zur Speziation von Cm(III) bzw. Am(III) in Gorlebengrundwasser auf der Grundlage des NICA-Donnan-Modells, Institut für Nukleare Entsorgung, KIT, Karlsruhe, Persönliche Mitteilung.

Giaquinta, D.M., Soderholm, L., Yuchs, S.E. and Wasserman, S.R., (1997). The speciation of uranium in a smectite clay: evidence for catalysed uranyl reduction. Radiochimica Acta, 76, 113- 121.

Grangeon, S. et al., (2011), in review. On nickel occurrence and distribution in a clay-rich formation: Implications for trace elements solubility control. Geochimica Et Cosmochimica Acta.

Grasset, L. et al., (2010). Sequential extraction and spectroscopic characterisation of organic matter from the Callovo-Oxfordian formation. Organic Geochemistry, 41(3), 221-233.

Griffault, L., (1999). Référentiel géologique du site de l'Est, Technical Report A RP ADS 99-005, ANDRA Agence nationale pour la gestion des d´echets radioactifs, Chatenay-Malabry.

Grim, R.E., (1953). Clay mineralogy. New York, McGraw-Hill, p. 587

Guillaumont, R., Fanghänel, T., Fuger, J., Grenthe, I., Neck, V., Palmer, D.A., Rand, M.H., (2003). Update on the chemical thermodynamics of uranium, neptunium, plutonium, americium and technetium. 1. Aufl. Chemical Thermodynamics, Hrsg. F.J. Mompean, M. Illemassene, C. Domenech-Orti, K. Ben-Said. Vol. 5., Amsterdam, Boston, Heidelberg, ELSEVIER, 918 p.

Hartmann, E., (2010). Sorption von Ln(III)/An(III) und U(VI) an Tonmineralien und natürlichen Tongesteinen, PhD thesis, Fakultät für Bauingenieur-, Geo- und Umweltwissenschaften des Karlsruher Instituts für Technologie (KIT), Karlsruhe.

Hartmann, E., Geckeis, H., Rabung, T., Lutzenkirchen, J., Fanghanel, T., (2008). Sorption of radionuclides onto natural clay rocks. Radiochimica Acta 96, 699-707.

Hartmann, E., Baeyens, B., Bradbury, M., Geckeis, H., Stumpf, T., (2008a). A Spectroscopic Characterization and Quantification of M(III)/Clay Mineral Outer-Sphere Complexes, Environ. Sci. Technol. 42, 7601–7606.

Heberling, F., Denecke, M.A., Bosbach, D., (2008). Neptunium(V) coprecipitation with calcite. Environ. Sci. Technol. 42, 471-476.

Höhne, S.,(2010). Spektroskopische und thermodynamische Untersuchungen des Komplexierungsverhaltens vonCm(III) mit Propionat bei erhöhten Temperaturen, Bachelor-Arbeit, Universität Heidelberg.

Huh, Y., Lee, J.-G., McPhail, D.C., Kim, K., (1993). *Measurements of pH at elevated temperatures using the optical indicator acridine*, J. Sol. Chem., **22**, 651-661.

Inoue, Y., Tochiyama, O., (1983). Polyhedron, 2, 627.

Jacquot, E., (2002). Composition des eaux interstitielles des argilites du Callovo-Oxfordien non perturb´ees. Rapport ANDRA No. D NT ASTR 02-041, ANDRA Agence nationale pour la gestion des d´echets radioactifs, Châtenay-Malabry, p. 13.

Janssens, K., Proost, K. and Falkenberg, G., (2004). Confocal microscopic X-ray fluorescence at the HASYLAB microfocus beamline: characteristics and possibilities. Spectrochimica Acta Part B-Atomic Spectroscopy, 59(10-11), 1637-1645.

Janos, P., (2003). Journal of Chromatography A 983, 01.

Jeanson, A., Dahou, S., Guillaumont, D., Moisy, P., Auwer, C. D., Scheinost, C., Hennig, C., Vidaud, C., Subra, G., Solari, P. L., (2009). A comparative study of actinide complexation in three ligand systems with increasing complexity, Journal of Physics: Conference Series 190 012185.

Jeanson, A., Ferrand, M., Funke, Harald., Hennig, C., Moisy, P., Solari, P. L., Vidaud, C., Den Auwer, C., (2010). The Role of Transferrin in Actinide(IV) Uptake: Comparison with ACHTUNGTRENUNGIron(III), Chem. Eur. J. 16, 1378 – 1387.

Jiang, J., Rao, L., DiBernardo, P., Zanonato, P., Bismondo, A., (2002). J. Chem. Soc., Dalton Trans., 9, 1832.

Jokic, A., Wang, M.C., Liu, C., Frenkel, A.I. and Huang, P.M., (2004). Integration of the polyphenol and Maillard reactions into a unified abiotic pathway for humification in nature: the role of □-MnO2. Org. Geochem., 35, 747-762.

Jung, A.-V. et al., (2005). Synthesis of amino-phenolic humic-like substances and comparison with natural aquatic humic acids: A multi-analytical techniques approach. Org. Geochem., 36, 1252-1271.

Kaszuba, J. P., Runde, W. H. (1999). The aqueous geochemistry of neptunium: Dynamic control of soluble concentrations with applications to nuclear waste disposal. Environ. Sci. Technol., 33, 4427–4433.

Keeney-Kennicutt,W. L., Morse, J. W., (1984). Marine Chem. 15, 133.

Keeney-Kennicutt,W. L., Morse, J. W., (1985). Geochim. Cosmochim. Acta 49, 2577.

Keizer, M.G., van Riemsdijk, W.H., (1999). ECOSAT Equilibrium Calculation Of Speciation And Transport 4.8 (user manual), Universität Wageningen, 76 p.

Kim, J. I., Czerwinski, K. R., (1996) Radiochimica Acta **73**, 5.

Kim, J. I., Buckau, G., Li, G. H., Duschner, H., Psarros, N., (1990). Fres. J. Anal. Chem., 338, 245–252.

Kimura, T., Choppin, G.R., (1994). [349]

Kinniburgh, D. G., van Riemsdijk,W. H., Koopal, L. K., Borkovec, M., Benedetti, M. F., Avena, M. J., (1999). Colloids Surf. A 151, 147.

Kowal-Fouchard, A., Drot, R., Simoni, E., Marmier, N., Fromage, F., Ehrhardt, J.J., (2004). Structural identification of europium(III) adsorption complexes on montmorillonite. New Journal of Chemistry 28(7), 864-869.

Krause M. O., Haire R. G., Keski-Rahkonen O. and Peterson J. R. (1988). Photoelectron spectrometry of the actinides from Ac to Es. J. Electron Spectrosc. Relat. Phenom. 47, 215–226.

Křepelová, A. (2007). Influence of humic acid on the sorption of uranium(VI) and americium(III) onto kaolinite, Dissertation, Fakultät Mathematik und Naturwissenschaften, Technische Universität, Dresden.

Kuczewski, B., Marquardt, C. M., Seibert, A., Geckeis, H., Kratz, J. V., and Trautmann, N., (2003). Separation of Plutonium and Neptunium Species by Capillary Electrophoresis-ICP-MS and Application to Natural Ground Water Samples. Anal.Chem. 75, 6769-6774.

Larsson, E., Adell, B., (1931). Z. Phys. Chem, **157**, 342-362.

Latrille, C., Ly, J. and Herbette, M., (2006). Retention of Sn(IV) and Pu(IV) onto four argillites from the Callovo-Oxfordian level at Bure (France) from eight equilibrated sedimentary waters. Radiochimica Acta, 94(8), 421-427.

Lee, T.S., Gin, J., Nampoori, V.P.N., Vallabhan, C.P.G., Unnikrishnan, N.V., Radhakrishnan, P., (2001). *A sensitive fibre optic pH sensir using multiple sol-gel coatings,* J. Opt. A: Pure Appl. Opt., **3**, 355-359.

Lerouge, C. et al., (2010). Comparative EPMA and μ-XRF methods for mapping micro-scale distribution of iodine in biocarbonates of the Callovian-Oxfordian clayey formation at Bure, Eastern part of the Paris Basin. Physics and Chemistry of the Earth, Parts A/B/C, 35(6-8), 271-277.

Lujaniene, G., Motiejunas, S., and Sapolaite, J., (2007). Sorption of Cs, Pu and Am on clay minerals. Journal of Radioanalytical and Nuclear Chemistry 274, 345-353.

Luckscheiter, B., Kienzler, B., Bosbach, D., (2004). Literaturstudie zum Korrosionsverhalten von HAW-Gläsern in Ton: Tongestein und Versatzmaterial, Institut für Nukleare Entsorgung, FZKA 7068, Karlsruhe.

Maillard, L.C., (1912a). Action des acides aminés sur les sucres ; formation des mélamoidines par voies méthodique. Comptes Rendus de l´Académie des Sciences, Séance du 8 janvier 1912, 66-68.

Maillard, L.C., (1912b). Formation d´humus et de combustibles minéraux sans intervention de l´oxygène atmosphérique, des microorganismes, des hautes températures, ou des fortes pressions. Comptes Rendus de l´Académie des Sciences, Séance du 23 décembre 1912, 1554-1556.

Manohar, S., Atkinson, G., (1993). *The effect of high pressure on the ion pair equilibrium constant of alkali metal fluorides: A spectrophotometric study,* J. Sol. Chem., **22**, 859-872.

Marignac, C. and Cuney, M., (1999). Ore deposits of the French Massif Central: insight into the metallogenesis of the Variscan collision belt. Mineralium Deposita, 34(5-6), 472-504.

Marquardt, C. M., Seibert, A., Artinger, R., Denecke, M. A., Kuczewski, B., Schild, D., Fanghänel, Th., (2004). The redox behaviour of plutonium in humic rich groundwater . Radiochimica Acta 92, 617-623.

Marquardt, C.M., Kim, J. I., Pirlet, V., (2001). Complexation of tetravalent neptunium with fulvic acid, Book of Abstracts, Actinide-2001 Conference, Hayama, Japan, p. 140.

Marquardt, C. M., Pirlet, V., Kim, J. I., (2000). Initial studies on the complexation of tetravalent neptunium with fulvic acid, in Scientific Report, FZKA 6524, Karlsruhe, 45-70.

Marques Fernandes, M., (2010). Ternäre Eu(III)/Carbonat-Oberflächenkomplexe an Illit. LES Labor für Endlagersicherheit, PSI, Villigen, private communication, 2010.

Marques Fernandes, M., Baeyens, B., Bradbury, M., (2008). The influence of carbonate complexation on lan-thanide/actinide sorption on montmorillonite. Radiochimica Acta 96, 691-697.

Marques Fernandes, M., (2006). Spektroskopische Untersuchungen (TRLFS und XAFS) zur Wechselwir-kung von dreiwertigen Lanthaniden und Actiniden mit der Mineralphase Calcit. Dissertation, Naturwissenschaftlich-Mathematische Gesamtfakultät, Ruprecht-Karls-Universität Heidelberg, 174 p.

Mathis, V., Robert, J.-P. and Saint, M., (1990). J Chron. Rech. Min., 499(31-40).

Mavrik Zavarin, S. K. Roberts, N. Hakem, A. M. Sawvel, and A. B. Kersting, (2005). Eu(III), Sm(III), Np(V), Pu(V), and Pu(IV) sorption to calcite. Radiochim. Acta, Vol. 93, Issue 2, pp. 93-102.

McRae, B.R., Patterson, B.A., Origlin-Luster, M.L., Sorenson, E.C., Woolley, E.M., (2003). *Thermodynamics of proton dissociation from aqueous 1-propanoic and 1-butanoic acids at temperatures 278.15□(T/K)□393.15 and pressure p=0.35 MPa: apparent molar volumes and apparent molar heat capacities of aqueous solutions of the acids and their sodium salts,* J. Chem Thermodynamics, 35, 301-329.

Meloun, M., Kotrly, S., Collect., (1977). Czech. Chem. Commun., **42**, 2115.

Michot, L. J., Bihannic, I., Porsch, K., Maddi, S., Baravian, C., Mougel, J., Levitz, P., (2004). Phase diagrams of Wyoming Na-montmorillonite clay. Influence of particle anisotropy. Langmuir **20**(25), 10829-10837 .

Millero, F.J., DiTrolio, B., Suarez, A.F., Lando, G.,(2009). *Spectroscopic measurements of the pH in NaCl brines,* Geochim. et. Comsochim. Acta, **73**, 3109-3114.

Milne, C.J., Kinniburgh, D.G., van Riemsdijk, W.H., Tipping, E., (2003). Generic NICA-Donnan model pa-rameters for metal-ion binding by humic substances, Environ. Sci. Technol., 37,, 958-971.

Milne, C.J., Kinniburgh, D.G., Tipping, E., (2001). Generic NICA-Donnan model parameters for proton bind-ing by humic substances, Environ. Sci. Technol., 35(10), 2049-2059.

Montes-H, G., Fritz, B., Clement, A., Michau, N., (2005). Modelling of geochemical reactions and experimental cation exchange in MX80 bentonite. J. Env. Management **77**(1), 35.

Moore, R.C., Borkowski, M., Bronikowski, M.G., Chen, J., Pokrovsky, O.S., Xia, Y., Choppin, G.R., (1999). Thermodynamic modeling of actinide complexation with acetate and lactate at high ionic strength, J. Sol. Chem., 28(5), 521-531.

Morse, J.W., Choppin, G.R., (1986). Laboratory studies of plutonium in marine systems, Mar. Chem. 20, 73– 89.

Motellier, S., Ly, J., Gorgeon, L., Charles,Y., Hainos,D., Meier, P., Page, J., (2003). Modelling of the ion-exchange properties and indirect determination of the interstitial water composition of an argillaceous rock. Application to the Callovo-Oxfordian low-water-content formation. Appl. Geochem. **18**(10), 1517.

Nagra, (2002a). Projekt Opalinuston – Synthese der geowissenschaftlichen Untersuchungsergebnisse, Entsorgungsnachweis für abgebrannte Brennelemente, verglaste hochaktive sowie langlebige mittelaktive Abfälle. Technischer Bericht NTB 02-03, NAGRA Nationale Genossenschaft für die Lagerung radioaktiver Abfälle, Wettingen/Schweiz, p. 659.

Nagra, (2002b). Nagra Project Opalinus Clay – safety report: Demonstration of disposal feasibility for spent fuel, vitrified-high level waste and long-lived intermediate level waste (Entsorgungs-nachweis); NTB 02-05; Nagra: Wettingen, Switzerland.

Neck, V., Altmaier, M., Seibert, A., Yun, J. 1., Marquardt, C. M., Fanghanel, T., (2007). Solubility and redox reactions of Pu(IV) in hydrous oxide: evidence for the formation of PuO_{2+x}(s, hyd.). Radiochim. Acta 95, 193-207.

Newville, M., Livins, P., Yacoby, Y., Stern, E.A., Rehr, J.J., (1993). Near-edge x-ray-absorption fine-structure of Pb - A comparison of theory and experiment. Physical Review B 47(21), 14126-14131.

Nitsche, H., Roberts, K., Xi, R., Prussin, T., Becraft, K., Mahamid, I. A., Silber, H. B., Carpenter, S. A., Gatti, R. C. (1994). Long term plutonium solubility and speciation studies in a synthetic brine. Radiochim. Acta, 66, 3-7.

Panak, P., Klenze, R., Kim, J.I., Wimmer, H., (1995). A study of intramolecular energy transfer in Cm(III) complexes with aromatic ligands by time-resolved laser fluorescence spectroscopy, J. Alloys Comp., 225, 261-266.

Pankow, J.F., (1991). *Aquatic Chemistry Concepts*, Lewis Publisher, Inc.

Pirlet, V., (2003). The investigation of the neptunium complexes formed upon interaction of high-level waste glass and Boom Clay medium, PhD thesis, Faculté des Sciences, Universite de Liege, Liege.

Plancque, G., Maurice, Y., Moulin, V., Toulhoat, P., Moulin, C., (2005). On the use of spectroscopic techniques for interaction studies, part I: complexation between europium and small organic ligands, Applied Spectroscopy, 59, 432-441.

Plaschke, M., Rothe, J., Altmaier, M., Denecke, M.A. and Fanghanel, T., (2005). Near edge X-ray absorption fine structure (NEXAFS) of model compounds for the humic acid/actinide ion interaction. Journal of Electron Spectroscopy and Related Phenomena, 148(3), 151-157.

Pokrovsky, O.S., Choppin, G.R., (1997). Neptunium(V) complexation by acetate, oxalate and citrate in NaClO4 media at 25°C,Radiochim. Acta, 79, 167-171.

Pompe, S. et al., (2000). Investigation of humic acid complexation behavior with uranyl ions using modified synthetic and natural humic acids. Radiochim. Acta, 88, 553-558.

Powell, J.E., Karraker, R.H., Kolat, R.S., Farrell, J.L., (1964). Rare earth research II, proceedings of the third conference on rare earth research, R.S. Vorres, New York.

Preston, C.M. and Schmidt, M.V.I., (2006). Black (pyrogenic) carbon: a synthesis of current knowledge and uncertainties with special consideration of boreal regions. Biogeosciences, 3(397-420).

Rabung, T., (1997). Einfluß von Huminstoffen auf die Europium(III)-Sorption an Hämatit. Dissertation, Ma-thematisch-Naturwissenschaftliche Fakultät, Universität des Saarlandes, Saarbrücken.

Rabung, T., Pierret,M. C., Bauer, A., Geckeis, H., Bradbury, M. H., Baeyens, B., (2005). Sorption of Eu(III)/Cm(III) on Ca-montmorillonite and Na-illite. Part 1: Batch sorption and time-resolved laser fluorescence spectroscopy experiments. Geochim. Cosmochim. Acta **69**(23), 5393-5402.

Rabung, T., Geckeis, H., Kim, J.I., Beck, H.P., (1998). The influence of anionic ligands on the sorption behav-iour of Eu(III) on natural hematite. Radiochimica Acta 82, 243-248.

Raghuraman, B., Gustavson, G., Mullins, O.C., Rabbito, P., (2006). *Spectroscopic pH measurement for High Temperatures, Pressures and Ionic Strengths,* AIChE Journal, **52**, No.9, 3257-3265.

Rao, L, (2007). Thermodynamics of actinide complexation in solution at elevated temperatures: application of variable-temperature titration calorimetry, Chem. Soc. Rev., 36, 881-892,.

Rao, L., Zhang, Z., Zanonato, P., DiBernardo, P., Bismondo, A., Clark, S.B., (2004). Complexation of thorium(IV) with acetate at variable temperatures, Dalton Trans., 2867-2872,

Rao, L., Garnov, A.Yu., Jiang, J., DiBernardo, P., Zanonato, P., Bismondo, A., (2003). Inorg. Chem., 42, 3685.

Rao, L., Jiang, J., Zanonato, P., DiBernardo, P., Bismondo, A., Yu, A., (2002). Radiochim. Acta, 90, 581.

Ravel, B., Newville, M., (2005). ATHENA, ARTEMIS, HEPHAESTUS: data analysis for X-ray absorption spectroscopy using IFEFFIT. J. Synchrotron Rad. 12, 537.

Rawat, N., Sharma, R.S., Nishad, A., Tomar, B.S., Manchanda, V.K., Thermodynamic study of Th(IV) complexes with dicarboxylates py potentiometry and calorimetry, Radiochim. Acta, 99, 341-347, (2011).

Rehr, J. J., Albers, R. C., Zabinsky, S. I., (1992). High-order multiple-scattering calculations of x-ray-absorption fine structure. Phys. Rev. Lett. 69, 3397.

Reiller, P.E., Evans N.D.M., Szabo G., (2008). Complexation parameters for the actinides(IV)-humic acid system: a search for consistency and application to laboratory and field observations Radiochim. Acta, 96, 345-358.

Rothe, J., Steppert, M., Walther, C., INE-Beamline, Karlsruher Institute of Technology, unpublished data (2011)

Rothe, J., Denecke, M. A., Dardenne, K., Fanghänel, Th., (2006). Radiochim. Acta 94, 691.

Rundle, R.E., Baenziger, N.C., Wilson, A.S. and McDonald, R.A., (1948). The structures of carbides, nitrides, and oxides of uranium. Journal of the American Chemical Society, 70, 99-105.

Sakuragi, T., Sato, S., Kozaki, T., Mitsugashira, T., Hara, P., Suzuki, Y., (2004). Am(III) and Eu(III) uptake on hematite in the presence of humic acid. Radiochim. Acta, 92(9-11), 697-702.

Sasaki, T., Takaoka, Y., Kobayashi, T., Fujii, T., Takagi, I., Moriyama, H., Hydrolysis constants and complexation of Th(IV) with carboxylates, Radiochim. Acta, 96

Schäfer, T. and Denecke, M.A., (2010). Nuclear waste repository research at the micro- to nanoscale. In: M.A. Denecke and C.T. Walker (Editors), X-Ray Optics and Microanalysis, Proceedings. AIP Conference Proceedings. Amer. Inst. Physics, Melville, pp. 181-187.

Schäfer, T., Michel, P. and Claret, F., (2009a). The application of STXM and μFT-IR to characterize sedimentary organic matter in the Opalinus clay. Journal of Physics: Conference Series, 186, 012095.

Schäfer, T. et al., (2009b). Radiation sensitivity of natural organic matter: Clay mineral association effects in the Callovo-Oxfordian argillite. Journal of Electron Spectroscopy and Related Phenomena 170, 49-56.

Schäfer, T. et al., (2005a). Origin and mobility of fulvic acids in the Gorleben aquifer system: implications from isotopic data and carbon/sulfur XANES. Organic Geochemistry, 36(4), 567-582.

Schäfer, T. et al., (2005b). Source identification and characterization of humic and fulvic acids from Oxfordian argillite and Opalinus Clay. In: E.A. Ghabbour and J. Davies (Editors), Humic Sustances: Molecular Details and Applications in Land and Water Conservation. Taylor & Francis, New York, pp. Chapter 4.

Schild, D., Marquardt , C. M., (2000). Radiochim. Acta 88, 587–591.

Schlepp, L., Landais, P., Elie, M. and Faure, P., (2001). Influence of paleoenvironment and radiolytic alteration on the geochemistry of organic matter from Autunian shales of the Lodeve uranium deposit, France. Bulletin De La Societe Geologique De France, 172(1), 99-109.

Schmeide, K., Pompe, S., Bubner, M., Heise, K.H., Bernhard, G., Nitsche, H. (2000). Uranium(VI) sorption onto phyllite and selected minerals in the presence of humic acid. Radiochim. Acta 88 (9-11), 723-728.

Schmeide, K., Reich, T., Sachs, S., Brendler, V., Heise, K. H., Bernhard, G., (2005). Neptunium(IV) complexation by humic substances studied by X-ray absorption fine structure spectroscopy, Radiochim. Acta 93, 187–196.

Seok, Y.J., Yang, K.S., Kang, S.O., (1995). *A simple spectrophotometric determination of dissociation constants of organic compounds,* Analytica Chimica Acta, **306**, 351-356.

Silva, R. J., Nitsche, H., (1995). Actinide Environmental Chemistry, Radiochim. Acta 70–71, 377.

Skerencak, A., Panak, P.J., Hauser, W., Neck, V., Klenze, R., Lindqvist-Reis, P., Fanghänel, Th., (2009). *TRLFS study on the complexation of Cm(III) with nitrate in the temperature range from 5 to 200°C*, Radiochim. Acta, 97, 385-393.

Srinivasan, T.G., Zanonato, P., DiBernardo, P., Bismondo, A., Rao, L., (2006). Complexation of thorium(IV) with malonate at variable temperatures, J. Alloys Comp., 408-412, 1252-1259.

Stern, E. A.., Newville, M., Ravel, B., Yacoby, Y., Haskel, D., (1995). The UWXAFS analysis package: philosophy and details. Physica B 208&209, 117.

Stryer, L., (1978). Fluorescence energy transfer as a spectroscopic ruler. Ann. Rev. Biochem. 47, 819-846.

Stumpf, S., (2004). Spektroskopische Untersuchungen zu Sorptionsmechanismen von dreiwertigen Actiniden an Feldspäten, Quarz und Ferrihydrit. Dissertation, Naturwissenschaftlich-Mathematische Gesamtfakultät, Ruprecht-Karls-Universität, Heidelberg.

Stumpf, T., Fanghänel, T., (2002). A time-resolved laser fluorescence spectroscopy (TRLFS) study of the inter-action of trivalent actinides (Cm(Ill)) with calcite. Journal of Colloid and Interface Science 249(1), 119-122.

Stumpf, T., Bauer, A., Coppin, F., Fanghänel, T., Kim, J.I., (2002). Inner-sphere, outer-sphere and ternary surface complexes: a TRLFS study of the sorption process of Eu(III) onto smectite and kaolinite. Radiochim. Acta 90(6), 345-349.

Stumpf, T., Bauer, A., Coppin, F., Kim, J.I., (2001). Time-resolved laser fluorescence spectroscopy study of the sorption of Cm(III) onto smectite and kaolinite. Environmental Science & Technology 35(18), 3691-3694.

Takahashi, Y., Murata, M., Kimura, T., (2006). Interaction of Eu(III) ion and non-porous silica: Irreversible sorption of Eu(III) on silica and hydrolysis of silica promoted by Eu(III). Journal of Alloys and Com-pounds 408, 1246-1251.

Takai, K., Takao, S., Scheinost, A.C., Bernhard, G., Henning, C., (2009). Complex formation and molecular structure of neptunyl(VI) and –(V) acetates, Inorg. Chem., 48, 8803-8810.

Tian, G., Martin, L.R., Rao, L., (2010). Complexation of lactate with neodymium(III) and europium(III) at variable temperatures: studies by potentiometry, microcalorimetry, optical absorption and luminescence spectroscopy, Inorg. Chem., 49, 10598-10605.

Tipping, E., (1998). Humic ion-binding model VI: An improved description of the interactions of protons and metal ions with humic substances, Aquat. Geochem. 4(1), 3-48.

Tertre, E., Berger, G., Simoni, E., Castet, S., Giffaut, E., Loubet, M., Catalette, H., (2006). Europium retention onto clay minerals from 25 to 150°C: Experimental measurements, spectroscopic features and sorption modelling. Geochimica Et Cosmochimica Acta 70(18), 4563-4578

Vandenbroucke, M. and Largeau, C., (2007). Kerogen origin, evolution and structure. Organic Geochemistry, 38(5), 719-833.

Van Loon, L. R., Eikenberg, J., (2005). A high resolution abrasive method for determining diffusion profiles of sorbing radionuclides in dense argillaceous rocks, Appl. Rad. Isotops, 11-21.

Van Loon, L. R., Soler, J. M., Bradbury, M. H., (2003). Diffusion of HTO, Cl-36(-) and I-125 in opalinus clay samples from Mont Terri - effect of confining pressure, J. Contam. Hydrol. 61,73-83.

Van Loon, L. R., Baeyens, B., Bradbury, M. H. (2005). Diffusion and retention of sodium and strontium in Opalinus clay: Comparison of sorption data from diffusion and batch sorption measurements, and geochemical calculations. Appl. Geochem., 20, 2351–2363.

Van Olphen, H., (1963), An introduction to clay colloid chemistry. New York: Interscience Publishers.

Vantelon, D., Montarges-Pelletier, E., Michot, L.J., Briois, V., Pelletier, M., Thomas, F., (2003). Iron distribu-tion in the octahedral sheet of dioctahedral smectites. An Fe K-edge X-ray spectroscopy study. Phys. Chem. Minerals 30, 44-53.

Vilas, V.V. et al., (2010). Synthesis and Characterization of the Hybrid Clay-Based Material Montmorillonite–Melanoidin: A Potential Soil Model. Soil Sci. Soc. Am. J., 74(6), 2239-2245.

Vogel, A.I., *Text-Book of Quantitative Inorganic Analysis*, 3rd ed. John Wiley & Sons, (1961).

Wersin, P., Hochella, M. F., Persson, P., Redden, G., Leckie, J. O., Harris, D. W., (1994). Interaction between aqueous uranium(VI) and sulfide minerals: spectroscopic evidence for sorption and reduction, Geochim. Cosmochim. Acta 58, 2829-2843

Wimmer, H., (1992). Laser-induzierte optische Spektroskopie zur Speziation von f-Elementen in natürlichen aquatischen Systemen. Untersuchung der Übertragbarkeit von Labordaten auf natürliche Verhältnisse. Dissertation, Institut für Radiochemie, Technische Universität München.

Wolf, M., Buckau, G., Geyer. S., (2004). Isolation and characterization of new batches of Gohy-573 humic and fulvic acids, internal report, Forschungszentrum Karlsruhe.

Wood, S.A., (1993). The aqueous geochemistry of the rare-earth elements: Critical stability constants for complexes with simple carboxylic acids at 25°C and 1 bar and their application to nuclear waste management, Engineering Geology, 34, 229 - 259..

Wu, T., Amayri, S., Drebert, J., Van Loon, L. R., Reich, T. (2009). Neptunium(V) sorption and diffusion in Opalinus clay. Environ. Sci. Technol. 43, 6567–6571.

Zalupski, P.R., Nash, K.L., Martin, L.R., (2010). Thermodynamic features of the complexation of neodynmium(III) and americium(III) by lactate in trifluoromethanesulfonate media, J. Sol. Chem, 39, 1213-1229.

Zeh, P., Kim, J. I., Marquardt, C. M., Artinger, R., (1999). The Reduction of Np(V) in Groundwater Rich in Humic Substances, Radiochim. Acta 87, 23-28.

Zuo, R., Teng, Y., Wang, J., and Hu, Q., (2010). Factors influencing plutonium sorption in shale media. Radiochim. Acta 98, 27-34.

12 List of Figures

13 List of Tables